

https://dspace.org/

Seismic analysis of thin shell catenary vaults

Surat, Daniel

2017

http://hdl.handle.net/10539/22992

Surat, Daniel (2017) Seismic analysis of thin shell catenary vaults, University of the Witwatersrand, Johannesburg, <http://hdl.handle.net/10539/22992>

Downloaded from a DSpace repository. https://dspace.org/

SEISMIC ANALYSIS OF THIN SHELL CATENARY VAULTS

Daniel Surat 381661

Research report submitted to the Faculty of Engineering and the Built Environment, University of Witwatersrand, Johannesburg, in partial fulfilment of the requirements for the degree of Master of Science in Engineering

Johannesburg 2017

Table of Contents

DECLARATION 3
Abstract 4
Acknowledgments 6
List of figures 7
List of tables 10
List of symbols 11
1 INTRODUCTION 12
1.1 The research problem 13
1.2 Objectives 13
1.3 Assumptions 14
1.4 Outline of report 15
2 LITERATURE REVIEW 16
2.1 Introduction 16
2.2 The Catenary: The Optimal Form 16
2.3 Form finding techniques for the catenary vault 21
2.3.1 Graphic Statics 21
2.3.2 Segmental Equilibrium Method 22
2.3.3 Mathematical formulation 23
2.4 The role of catenary vaults in low cost housing applications 25
2.5 Masonry as a construction material 26
2.6 Reinforcement solutions for improving seismic performance 27
2.6.1 Prestressing 27
2.6.2 Polymer Reinforcement 29
2.7 Seismic Analysis 35
2.7.1 Physical seismic testing techniques for structures 35
2.7.2 Practical ranges for seismic loading 40
2.7.3 Seismic modelling methods for unreinforced masonry arches 43
2.7.4 Previous Studies 48
2.8 The rocking response of structures 52
2.9 Requirement for further investigation 56
2.10 Summary 56
3 PREDICTIVE MODEL 58
3.1 Derivation and validation 58

3.2 Application to catenary arches 64
3.2.1 Influence of arch thickness 64
3.2.2 Influence of height to width ratio 66
4 EXPERIMENTAL SETUP 67
4.1 Shaking table 67
4.2 Data Logger and Accelerometers 69
4.3 Construction Methodology 71
4.3.1 Testing rig for masonry arch 71
4.3.2 Arch formwork 72
4.3.3 Construction Materials 73
4.3.4 Construction method for masonry arches 82
5 EXPERIMENTAL INVESTIGATION 86
5.1 Calibration of testing equipment and instruments 86
5.2 Harmonic tests (unreinforced) 89
5.2.1 Test results and discussion 90
5.2.2 Correlation with analytical model (fixed stroke tests) 95
5.2.3 Problems encountered during testing 99
5.3 Fixed frequency tests (unreinforced) 100
5.3.1 Test results and discussion 102
5.3.2 Correlation with the analytical model (fixed frequency tests) 108
5.4 Geogrid reinforcement tests (fixed frequency) 113
5.4.1 Geogrid only 114
5.4.2 Geogrid with anchors 116
5.4.3 Prestressed geogrid 118
5.4.4 Test results and discussion 122
6 CONCLUSION AND RECOMMENDATIONS FOR FUTURE STUDIES 128
6.1 Summary of findings 128
6.2 Further research to be performed 130
7 REFERENCES 132

DECLARATION

I declare that this research report is my own unaided work. It is being submitted to the Degree of Master of Science to the University of Witwatersrand, Johannesburg. It has not been submitted before for any degree or examination to and other university.

Signature ……

Daniel Surat

…….. day of …… 2017

Abstract

This report investigates the seismic response of catenary vaults. Through a series of tests, the inherent seismic resilience of catenary vaults was assessed and a number of reinforcement strategies were investigated to improve this.

An analytical model, based on the virtual work method, was developed by Ochsendorf (2002) for the assessment of circular voussoir arches. This model was adapted for catenary vaults. This model is used to calculate the minimum lateral acceleration required to cause the collapse of a catenary vault (λ_{min}) for any catenary profile.

The model indicates that there is a linear relationship between cross sectional depth of the arch and λ_{min} until the depth to ratio passes approximately 0.3, where the change in λ_{min} becomes exponential. Using the model, it is also predicted that λ_{min} decreases exponentially with an increase in the height to width ratio up to a value of approximately 1.6. After this point λ_{min} linearly decreases with increased height to width ratios and approaches zero.

The first series of tests involved subjecting unreinforced catenary vaults to seismic loading. In these tests the frequency of vibration was varied and the stroke was kept constant. From the results of the tests, it was found that there was no frequency at which the vaults underwent excessive vibration due to resonance. It was observed that during seismic loading, hinges form at locations where pre-existing cracks occur despite the higher computed λ_{min} values for these positions. The tests also indicate that the vaults' behaviour changes drastically with each hinge that forms.

In the next series of tests the frequency was set and the stroke was increased. The vaults were subjected to seismic loading at 2 Hz and 6 Hz, representative of low and high frequencies respectively. The tests indicated that the collapse acceleration of arches subjected to vibration at 2 Hz was lower than that of the vaults subjected to vibrations at 6 Hz. Despite this, the stroke, representing ground movement, required to cause collapse at 2 Hz was substantially higher than that of the 6 Hz tests. This indicates that the duration of load cycles has an effect on the collapse acceleration. In comparing the computed collapse acceleration, λ_{min}, with the actual collapse

accelerations, it was found that the computed values are highly conservative. Yet this is expected as the model is based on an infinite duration of lateral loading. It was found that the analytical model was more accurate for low frequency tests as compared to high frequency tests in terms of the predicted hinge locations.

Finally, three reinforcement strategies were investigated using basalt fibre geogrid. This was found to be an economical and viable reinforcement material. The first strategy consisted of laying the geogrid over the arch and securing it at the arch base. The second was the same as the first with the addition of anchors which held the geogrid down. The final strategy involved prestressing the arch using the geogrid. The latter 2 methods were found to be the most effective, with observed collapse accelerations being over 60% higher than that of the same unreinforced arch. The anchorage solution was found to be the most viable due to the substantially higher technical input required for the prestressing solution.

Acknowledgments

Firstly, I would like to thank my supervisor Professor Gohnert whose support and technical guidance has made this masters possible. Your vision and love of shell structures has been formative in helping my development as an engineer. Without your financial assistance this masters would not have been possible. I am most grateful for this. The sacrifices that you made to upgrade the shake table system and ensure that the equipment was running smoothly are truly appreciated.

I would like to thank Ryan Bradley who was always there to provide technical input and guidance. You have been an invaluable sounding board and voice of logic for my ideas. Thank you to Dr Li. Your guidance with regards to dynamics has been invaluable to me. All the lab staff have played a major role in this research project. A special thank you to structures lab technician, Ralph Mulder and to concrete lab technician, Dumisane Khumalo. Your assistance has been critical in making sure that my ideas could be brought into reality. Edward Pretorius must also be acknowledged for his role in developing the prestressing system used in the study. I am grateful to Dr Anne Fitchett for instilling in me a keen interest in thin-shell structures and starting me off on this avenue of inquiry.

A big thank you to Stonerod for graciously donating the geogrid used in this research project. This contribution was pivotal in the success of the project. A special thank you must go to Gordon Forrester at Stonerod for his assistance in the procurement of the material and providing technical input.

Finally I would like to thank my family and friends for all the support they have given me during my masters.

List of figures

Figure 2.1: Four hinges form where the thrust line intersects the intrados and extrados of the arch..... 17
Figure 2.2: Sketch of segment of arch used for proof (Bulovic, 2014)..... 17
Figure 2.3: The catenary arch provides greater material efficiency than the semi-circular arch..... 19
Figure 2.4: St Paul's Cathedral (Encyclopaedia Britannica ImageQuest,2015)..... 20
Figure 2.5: Sheffield Gardens (Encyclopaedia Britannica ImageQuest,2015)..... 20
Figure 2.2.6: Gateway Arch (Encyclopaedia Britannica ImageQuest, 2015)..... 21
Figure 2.7: L'Umbracle, City of Arts and Science (Encyclopaedia Britannica ImageQuest, 2015)..... 21
Figure 2.8: A funicular polygon (a) is constructed using the force polygon (b) (Block et al., 2006)..... 22
Figure 2.9: The sequential equilibrium method (Bulovic, 2014)..... 23
Figure 2.10: Inverted catenary curve..... 23
Figure 2.11: Parameters defining the catenary equation..... 24
Figure 2.12: Locally reinforced arch (Basilio, 2007)..... 31
Figure 2.13: Reinforcement spanning across the extrados and intrados respectively (Basilio, 2007)..... 32
Figure 2.14: Seismicity map of Africa (OCHA, 2007)..... 42
Figure 2.15: Seismicity map for South Africa (South African Bureau of Standards, 2011)..... 43
Figure 2.16: The masonry arch as a three-bar, four-link mechanism in the first half cycle of motion (Oppenheim, 1992)..... 44
Figure 2.17: As the arch returns to its 'initial undisplaced configuration' impact occurs (De Lorenzis et al., 2007)..... 46
Figure 2.18: The masonry arch as a 4-link 3 bar mechanism in the second half cycle of motion (De Lorenzis et al., 2007)..... 46
Figure 2.19: 3 bar mechanism with lateral components of gravitational acceleration (Ochsendorf, 2002)..... 48
Figure 2.20: The inverse relationship between impulse amplitude and period for the two tested arches (DeJong, 2009)..... 50
Figure 2.21: Results of harmonic testing (DeJong, 2009)..... 51
Figure 2.22: Reinforced and unreinforced arches during construction (Terry, 2011) 52
Figure 2.23: Time of application and constant acceleration magnitude required to cause overturning (Housner, 1963)..... 53
Figure 2.24: Period and sinusoidal acceleration magnitude required to cause overturning (Housner)..... 53
Figure 2-2.25: The natural rocking period increases with the rocking angle (Housner, 1963)..... 54
Figure 2-2.26: The probability of adding energy to the system increases with higher impulse periods (DeJong, 2009)..... 55
Figure 3.1: Three bar mechanism with lateral components of gravitational acceleration (Ochsendorf, 2002)..... 58

Figure 3.2: 2 lines are drawn through the hinges to find the centre of rotation of the arch (representation of centre of rotation adopted from De Luca et al., 2004) 60
Figure 3.3: Relative rotations may be found using compatibility (representation of rotations adopted from De Luca et al., 2004) 61
Figure 3.4: The centroids of each link are found and their displacements are calculated (representation of rotations adopted from De Luca et al., 2004) 62
Figure 3.5: Oppenheim's example arch geometry (refer to Oppenheim, 1992)..... 63
Figure 3.6: The change in λ_{min} vs thickness to span ratio..... 64
Figure 3.7: Shifting of hinge locations vs thickness to span ratio 65
Figure 3.8: Measurement of angles in arch 65
Figure 3.9: The change in λ_{min} vs height to width ratio 66
Figure 4.1: Shaking table controller..... 68
Figure 4.2: Shaking table and hydraulic actuator 68
Figure 4.3: Multipurpose Elite™ user interface 69
Figure 4.4: Nova 5000 data logger..... 70
Figure 4.5: Accelerometers connected to the Nova 5000 data logger..... 70
Figure 4.6: Arch rig..... 72
Figure 4.7: Formwork used for the construction of the arches: (a) top of formwork (b) underside of formwork..... 72
Figure 4.8: Cement stabilised earth tiles 73
Figure 4.9: A brick cut from an earth tile used in the masonry arches..... 73
Figure 4.10: Dimensions of earth bricks used 74
Figure 4.11: (a) Stabilised earth masonry and mortar cube samples (b) Tinius Olsen hydraulic press 75
Figure 4.12: Hourglass failure pattern observed for (a) mortar and (b) cement stabilised earth masonry samples 77
Figure 4.13: (a) Basalt geogrid (b) Geogrid rib is stitched together and consists of two sub-ribs..... 78
Figure 4.14: Samples were cut from the geogrid and the end transverse ribs were removed 78
Figure 4.15: Sandpaper attached on either side of the sample at the clamping points 79
Figure 4.16: Failure only encountered in one of the sub-ribs 79
Figure 4.17: Force v displacement graph for basalt fibre geogrid tests..... 80
Figure 4.18: Averaged force v extension graph for basalt fibre geogrid tests..... 80
Figure 4.19: Stress v strain graph for basalt fibre geogrid tests 81
Figure 4.20: Averaged stress v strain graph for basalt fibre geogrid tests..... 81
Figure 4.21: Arch built over formwork..... 83
Figure 4.22: Formwork removed from arch 83
Figure 4.23: Arch cured and transverse bearer bars installed..... 84
Figure 5.1: Results are closely matched for different adhesive thicknesses 86
Figure 5.2: Apparatus used for natural frequency tests..... 87
Figure 5.3: PSD plot for the first natural frequency test..... 88
Figure 5.4: Arch placed on the rig and is secured. Accelerometers placed at strategic positions..... 89

Figure 5.5: PSD plots for accelerometers on the arch apex (a) side of arch (b) and shaking table (c) 93
Figure 5.6: Hinge locations for 0.8 h/w ratio arch- first test 96
Figure 5.7: Hinge locations 0.8 h/w ratio arch- third test 96
Figure 5.8: 0.8 h/w ratio arch with pre-existing cracks..... 97
Figure 5.9: 1.0 h/w ratio arch with pre-existing cracks..... 98
Figure 5.10: Hinge locations 1.2 h/w ratio test 99
Figure 5.11: An example of the application of least square curve fitting 101
Figure 5.12: Collapse acceleration v h/w ratio for low and high frequency tests 104
Figure 5.13: Time acceleration history for the 1.0 h/w arch (6Hz) 106
Figure 5.14: PSD plot for apex accelerometer after the formation of 2 hinges 107
Figure 5.15: Hinge locations 0.8 h/w ratio test (2 Hz)..... 108
Figure 5.16: Hinge locations 1.0 h/w ratio test (2Hz)..... 108
Figure 5.17: Hinge locations 1.2 h/w ratio test (2 Hz)..... 109
Figure 5.18: Hinge locations 0.8 h/w ratio test (6 Hz)..... 111
Figure 5.19: Hinge locations 1.0 h/w ratio test (6 Hz)..... 111
Figure 5.20: Hinge locations 1.2 h/w ratio test (6 Hz)..... 112
Figure 5.21: Geogrid laid over the arch and secured on either end 115
Figure 5.22: Mortar applied over the geogrid 115
Figure 5.23: Anchors made from basalt fibre geogrid (top and bottom view) 116
Figure 5.24: (a) Predrilled bricks placed every 3 layers (b) Close-up of predrilled holed placed in the arch 117
Figure 5.25: (a) Geogrid placed over arch and secured using anchors (b) Anchors were tied to the geogrid and epoxied (c) inside face of the arch with anchors installed 117
Figure 5.26: Stages of development: (a) Rod machined down to 18mm at ends (b) thread cut into reduced end (c) hole drilled into ends and metal rod inserted, nuts added on either side of the angle support. 118
Figure 5.27: Final prestressing assembly with arch 119
Figure 5.28: Discrepancies in arch depth rectified with mortar..... 120
Figure 5.29: The effect of inconsistencies in vault thickness..... 121
Figure 5.30: Locations of failure points along arch for geogrid only test..... 122
Figure 5.31: Mortar-geogrid composite remained fairly intact after the arch failed. 123
Figure 5.32: Mortar bonded well with the arch 123
Figure 5.33: Failure points for arch reinforced with geogrid and anchors..... 124
Figure 5.34: Sliding of brick layers is the failure mechanism..... 124
Figure 5.35: Failure points of prestressed arch 125

List of tables

Table 2.1: Summary of advantages and disadvantages of prestressing solution 28
Table 2.2: Properties of glass and carbon fibre reinforced polymers (Basilio, 2007) 29
Table 2.3: Advantages and disadvantages of basalt fibre reinforcement 34
Table 2.4: Scale factors for dynamic analysis (Carvalho, 1998) 38
Table 2.5: The Modified Mercalli Intensity Scale (USGS, 1989) 40
Table 2.6: Relationship between the Modified Mercalli Intensity Scale and peak ground acceleration (adapted from Wald et al., 1999 and USGS, 2016) 41
Table 3.1: Equations to calculate vertical and horizontal displacements at the bar centroids 61
Table 4.1: Shaking table frequency ranges 67
Table 4.2: Properties of earth bricks 74
Table 4.3: Mortar mix ratios 74
Table 4.4: Results of cement-stabilised masonry compression tests 76
Table 4.5: Results of mortar compression test 76
Table 4.6: Test results for basalt fibre testing 82
Table 5.1: Accelerometer check 88
Table 5.2: Input parameters for 0.8, 1.0 and 1.2 h/w ratio arch models 95
Table 5.3: Comparison of actual vs model hinge locations for the 0.8 h/w ratio fixed stroke tests 95
Table 5.4: Comparison of actual vs model hinge locations for the 1.2 h/w ratio fixed stroke test 98
Table 5.5: Comparison of displacement commands to least square approximation of displacements at collapse 103
Table 5.6: Comparison of theoretical and actual collapse accelerations 104
Table 5.7: Comparison of actual vs model hinge locations for 2 Hz test 109
Table 5.8: Computed collapse acceleration comparison for 2 Hz tests 110
Table 5.9: Comparison of actual vs model hinge locations for 6 Hz tests 112
Table 5.10: Computed collapse acceleration comparison for 6 Hz tests 113
Table 5.11: Summary of collapse accelerations for different reinforcement strategies 126

List of symbols

Description	Symbol
Stress	σ
Axial Thrust Force	P
Cross-Sectional Area	A
Eccentricity	e
Sectional Modulus	Z
Thickness	t
Horizontal Distance From Centre Of Arch	x
Catenary Shape Factor	a
Height of Catenary Arch	H
Density	ρ
Velocity	v
Young's Modulus	E
Gravitational Acceleration	g
Length	L
Mass Per Unit Length	m
Radius from Centre of Arch	a (2nd instance)
Inertial Coefficient	M (θ)
Centrifugal and Coriolis Coefficient	L (θ)
Potential Energy Coefficient	F (θ)
Generalised Forcing Function	P (θ)
Weight of Bars	W_l
Horizontal Displacement	d_{hi}
Vertical Displacement	d_{vi}
Component of Gravitational Acceleration	λ
Rotation Between Hinges	θ

1 INTRODUCTION

Earthquakes pose a grievous threat to mankind, destroying houses and infrastructure, causing death and injuries. These losses creates severe economic strain in affected countries, especially developing nations. Earthquakes that have occurred recently in Haiti (2010), China (2008) and Pakistan (2005) highlight the devastating effects of earthquakes. The US Geological Survey (USGS) estimates that over 300 000 people died as a result of the 2010 earthquake in Haiti (USGS, 2014). In Haiti, the extensive damage caused to houses and public infrastructure was found to be due to "lack of earthquake-resistant design." (Eberhard *et al.*, 2013, pg iii). The majority of earthquake related deaths are associated to structural collapse (Bilham, 2009). This highlights the need for research into structures that are resilient to seismic loading and the development of models that may be used to understand the response of structures to seismic loading.

There has been extensive research into the response of structures to seismic loading. However, not much attention has been given to the seismic response of arches. Pivotal work by Oppenheim (1992), Ochsendorf (2002), de Lorenzis *et al.* (2007) and DeJong (2009) investigate the seismic response of circular dry-stack voussoir arches. This was done through the development of analytical models and the performing of small scale tests.

Catenary vaults are efficient structures. Under self-weight loading, all forces are contained within the middle third of the vault, resulting in purely compressive loading. Masonry is a versatile and economical construction material. It performs poorly when subjected to tensile forces, yet, it is strong in compression. Therefore it is suitable for use in catenary vaults.

However, with the introduction of lateral loads, such as seismic loading, tension will be introduced, forming hinges in the vault. When a sufficient number of hinges form, collapse occurs. In this research report, a comparative study of the seismic response and collapse mechanisms of unreinforced catenary vaults is presented. This is done by subjecting catenary vaults with varied geometric parameters to sinusoidal base motion. In addition to this, an analytical model, based on the work of Ochsendorf, was adapted to predict the behaviour of the respective catenary vaults.

In order to develop a tensile capacity in the arches, reinforcement measures must be introduced. Basalt fibre geogrid was found to be a suitable reinforcement material. Terry (2011) looked at the seismic response of geotextile reinforced catenary vaults when subjected to impulse loading. This study aims to further this work by looking at a range of reinforcement strategies to improve the seismic performance of catenary vaults when subjected to sinusoidal base acceleration.

1.1 The research problem

This study is concerned with the investigation of the seismic resilience of thin shell masonry catenary vaults. Through the testing of unreinforced vaults, their inherent seismic resilience may be assessed. Informed by these tests, the shortcomings of the vaults will be resolved through the use of remedial reinforcement measures.

This study will not be concerned with the design of an ‘earthquake-proof’ structure, which sustains no damage during seismic events. This will be prohibitively expensive and complex to construct (FEMA, 2009). Rather, the structures will be designed to be ‘earthquake resistant.’ This provides inhabitants of structures integrating catenary vaults with a fair warning before partial or full failure. This will mitigate loss of life and injury during seismic events.

1.2 Objectives

The objectives of the study are to:

- Attain a fundamental understanding of the behaviour of unreinforced catenary vaults subjected to seismic loading.
- Develop models that will help predict the methods of failure of the vaults
- Find a viable remedial reinforcement solution to increase the seismic resilience of these vaults.

1.3 Assumptions

It is assumed that:

- The supports of the arch are rigid and fixed yet undergo the same horizontal translation as the arch. This is not entirely realistic in that during earthquake loading, the support structure may move independently to the arch. This movement will cause a shift in the location of the thrust line in the arch. Consideration of this is beyond the scope of this thesis.
- The arch is fully fixed at the base. Due to inconsistency in construction and the elastic properties of soil, this may not be the case in a full scale structure.
- Global failure rather than local failure will only be considered. Global failure is 'typical of more slender structures,' such as thin shell masonry vaults (De Luca *et al*., 2004). Therefore it is assumed that at collapse two hinges will form at the respective bases and two will form in the arch.

Heyman (1966), made the following assumptions:

1. Masonry has no tensile strength.
2. Masonry has infinite compressive strength
3. Sliding failure between arch voussoirs does not occur

These assumptions have some ramifications which are discussed here. The assumption that masonry has no tensile strength is over-conservative, since in reality masonry and its binding agent (normally mortar) has some tensile capacity. As the tensile capacity of the mortar is much lower than that of the bricks, it is assumed that failure will occur at the mortar-brick interface. Furthermore, the assumption that masonry has infinite compressive stress is under-conservative in the respect that it doesn't consider failure by crushing of the masonry or mortar. Sliding is prevented by frictional forces developed at the brick-mortar interface and the shear capacity of the mortar. The latter two assumptions indicate that the critical means of failure is not material failure, but rather failure due to instability based on geometry (DeJong, 2009). For the sake of this study, these assumptions are utilised in predicting the failure of unreinforced catenary vaults. These assumptions may not hold true when the arch is reinforced.

1.4 Outline of report

The research report comprises of 6 chapters. The respective chapters contain the following:

Chapter 2 provides an overview of the literature relating the catenary arch and form finding techniques used to construct these arches. Masonry as a primary building material is then explored. The discussion then explores different reinforcement methods that may be used to improve the seismic performance of catenary arches. Subsequently, a range of seismic analysis techniques and modelling methods are discussed.

In chapter 3, a predictive model is developed to get a first order approximation of the catenary arch's behaviour under seismic loading. This model is used to investigate the effect different geometric parameters on the seismic performance of the catenary arch.

Chapter 4 provides a detailed description of experimental setup, discussing the apparatus used for testing and the arch construction methodology.

Chapter 5 pertains to the testing of the arches, presents the results of each test and provides a detailed discussion of the results. Here, a comparison between the analytical model and the observed response of the arches is discussed.

Finally chapter 6 provides conclusions and recommendations based on the findings of the study.

2 LITERATURE REVIEW

2.1 Introduction

Assessing the seismic behaviour of masonry structures has become a topic of much interest recently (DeJong, 2009). In many developing nations, masonry is used as a primary construction material. Yet, a lack of knowledge and expertise regarding the design of seismically resilient masonry structures may result in damage to property and loss of life in zones of high seismicity. Research has shown that these vaults are efficient and resilient under static loading, yet, little research has been performed in looking into their response to seismic loading.

This review first provides a broad discussion of the catenary form. Methods that have been utilised to enhance the structural performance of unreinforced masonry arches will then be explored as a means to assess which is the most viable option to improve the seismic resilience of catenary vaults. The review then investigates current seismic testing and modelling methods for unreinforced arches. Previous studies that have been performed that have investigated the seismic capacity of arches are detailed. The review discusses the rocking block as a means of understanding the fundamental behaviour of the catenary arch when subjected to base motion. Finally, gaps in the current body of knowledge that require further investigation are explored.

2.2 The Catenary: The Optimal Form

Robert Hooke (1635-1703) discovered that a hanging chain will form a catenary shape held under pure tension when subjected to self-weight loading. Through inverting the hanging chain, a form is found which is subjected to purely compressive forces (Block *et al.*, 2006). This form represents the ‘the line of action of the resultant compressive force’ acting in an arch (Harris, 2006), also known as the thrust line. As additional weights are added to the hanging chain, its form will shift, creating a new thrust line (Block *et al.*, 2006).

Heyman (1966) developed the ‘safe’ theorem which states that if the line of thrust is contained within the boundaries of a structure, the structure will be stable. In a masonry arch, hinges may form when the thrust line moves outside of the middle third of the section. A thrust line outside of the middle third will cause tensile stresses in the arch and therefore the formation of a hinge (assuming the material has no tensile capacity). Although a collapse mechanism forms, the structure may not collapse. According to Heyman, collapse only occurs when the thrust line moves outside the structure.

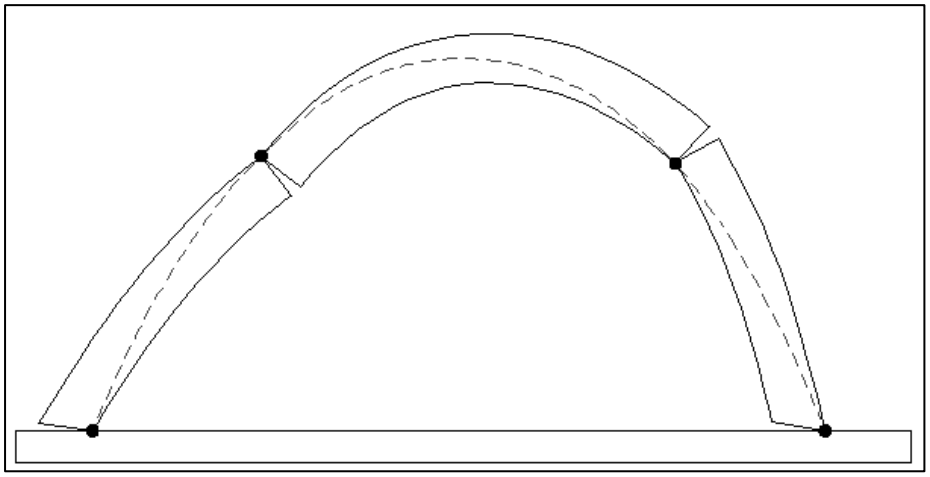

Figure 2.1: Four hinges form where the thrust line intersects the intrados and extrados of the arch

When the line of thrust is contained within the middle third of an arch, the stresses contained within it will be purely compressive. Yet, once the line of thrust falls outside this zone, tensile stresses will develop. Due to the brittle nature of masonry (i.e. weak in tension), these stresses will create cracks which may compromise the structural soundness of the arch.

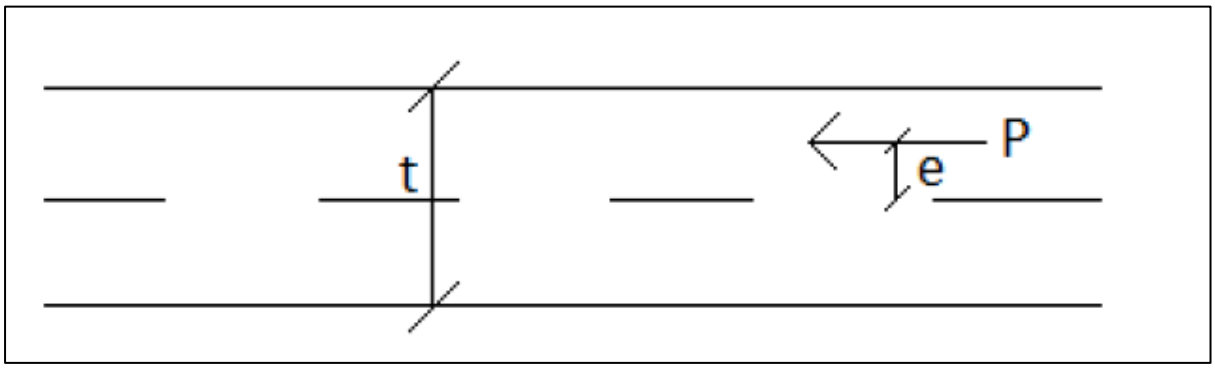

Figure 2.2: Sketch of segment of arch used for proof (Bulovic, 2014)

Bulovic (2014) provided a proof for this assertion. For a given section of the arch (assuming compression as negative[1]), the stress equation is:

$$\sigma = -\frac{P}{A} \pm \frac{Pe}{Z} \tag{2.1}$$

It is assumed that the section's width is equal to a unit width and compressive stresses are negative.

Where P=thrust force

A = cross sectional area of

e= thrust force eccentricity from centre line

t= thickness of arch

Z= section modulus =$\frac{bt^2}{6}$

Setting the stress to zero and considering the positive second term:

$$\sigma_t = \sigma_{bottom} = 0 = -\frac{P}{t} + \frac{6Pe}{t^2} \tag{2.2}$$

Simplifying and rearranging:

$$e = \frac{t}{6} \tag{2.3}$$

As this only accounts for 'one half of the middle third':

[1] Sign convention opposite to that used by Bulovic (2014), yet the same result is obtained.

$$2e = \frac{t}{3} \qquad (2.4)$$

Thus, Bulovic (2014) showed how no tensile forces will occur if the thrust line falls within the middle third of the arch.

Therefore, for a given loading, the optimal shape of a masonry arch is one that follows the form of its resultant thrust line. For arches, a catenary is optimal as is follows the form of the thrust line moving through it. This results in efficient use of materials as the line of thrust may more easily be contained within the middle third of the arch.

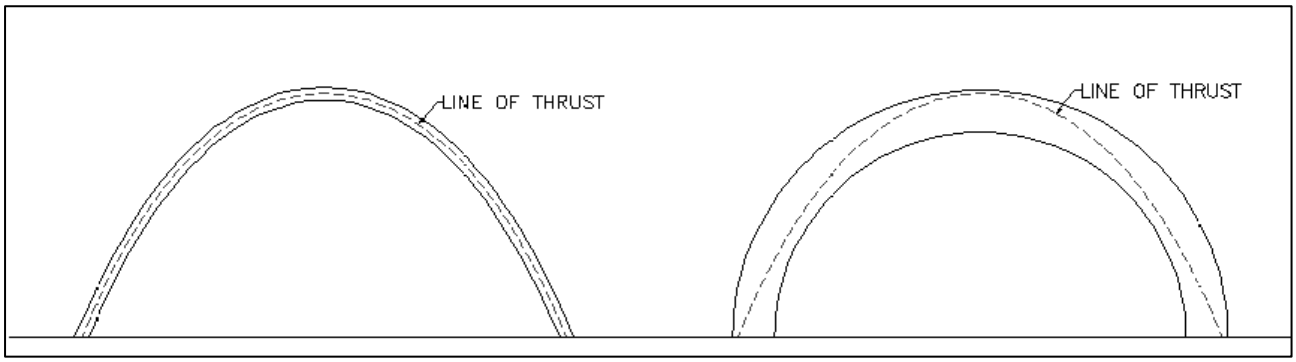

Figure 2.3: The catenary arch provides greater material efficiency than the semi-circular arch

Catenary forms are evident in many notable structures. Examples include St. Paul's Cathedral (England) where a catenary dome supports the church's lantern. The exterior and interior domes are false and merely serve an aesthetic role. Other notable uses of the catenary form includes Sheffield Gardens (England), Gateway Arch (USA) and L'Umbracle at the City of Arts and Science (Spain).

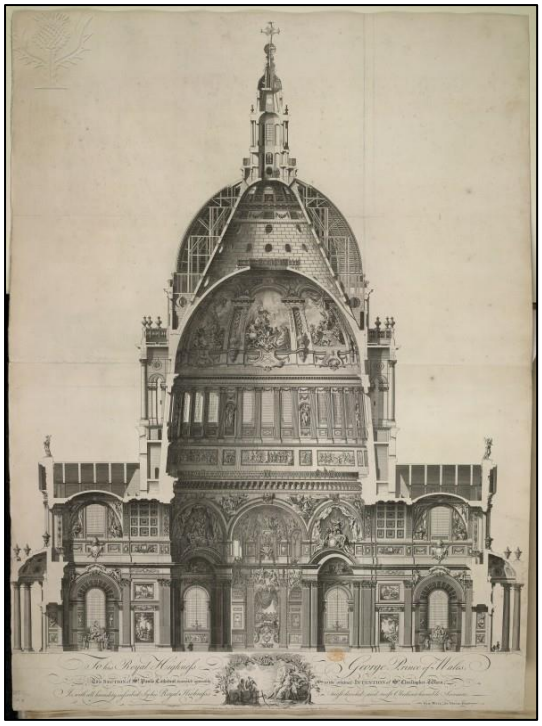

Figure 2.4: St Paul's Cathedral (Encyclopaedia Britannica ImageQuest,2015)



Figure 2.5: Sheffield Gardens (Encyclopaedia Britannica ImageQuest,2015)



Figure 2.2.6: Gateway Arch (Encyclopaedia Britannica ImageQuest, 2015)

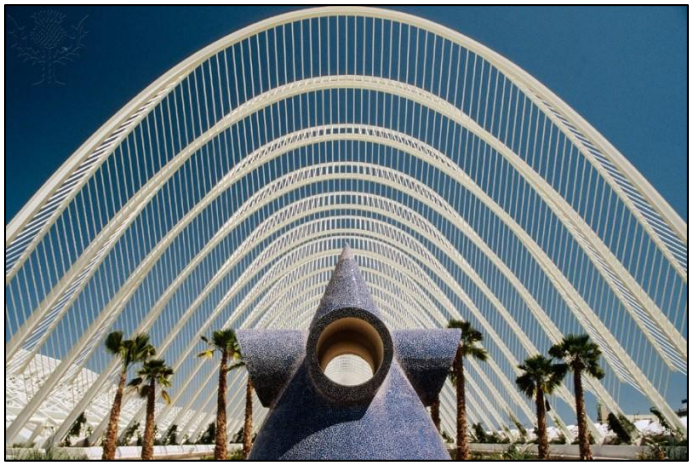

Figure 2.7: L'Umbracle, City of Arts and Science (Encyclopaedia Britannica ImageQuest, 2015)

2.3 Form finding techniques for the catenary vault

2.3.1 Graphic Statics

Graphic statics was formally developed by Culmann in 1866. In his book, Die Graphische Statik, he describes how graphic statics may be used to analyse a number of structures (Block *et al.*, 2006). More recently, Allen and Zalewski (2009) provided a methodology to find catenary curves using graphic statics methods. This method involves the reciprocal relationship of forces the structure is subjected to (in the form of the force polygon) and the thrust line or line of compressive force of a given structure (the funicular curve). With the aid of CAD (computer aided drawing)

software packages such as AutoCAD, this method may be used with a high degree of accuracy (Block *et al.*, 2006).

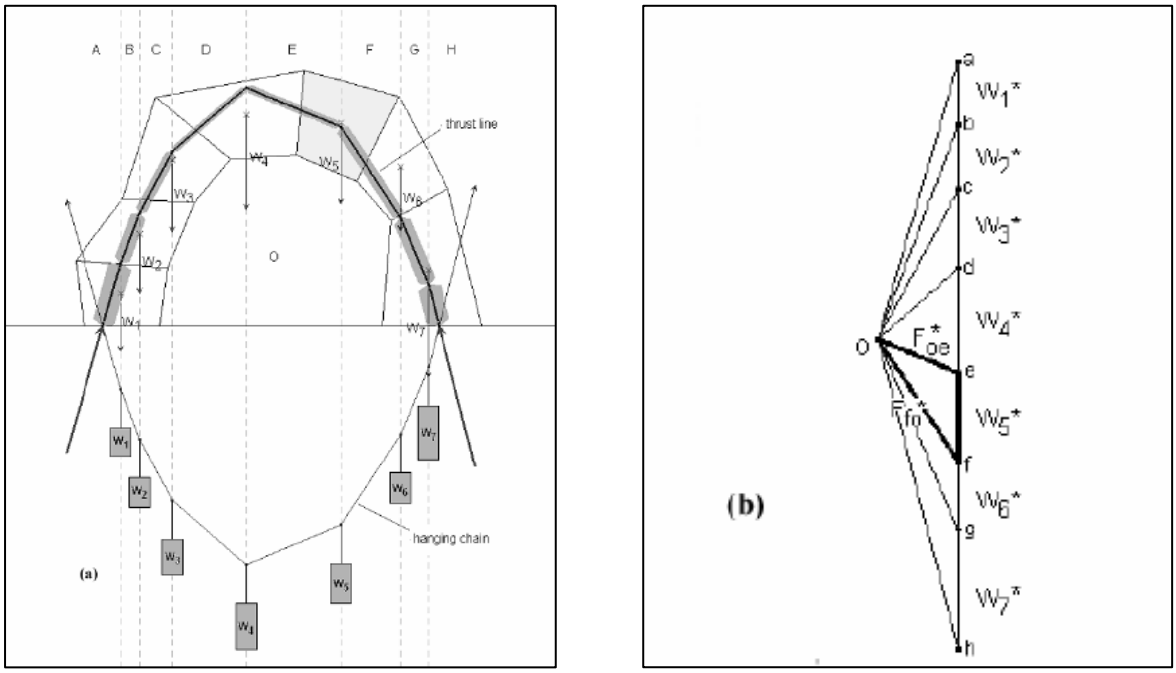

Figure 2.8: A funicular polygon (a) is constructed using the force polygon (b) (Block et al., 2006)

2.3.2 Segmental Equilibrium Method

Bulovic (2014) developed a form finding method, the sequential equilibrium method. This method can be used to find the thrust line (or funicular curve) of vaults for any given vertical and lateral loads. After calculating the reaction forces, equilibrium equations are used to calculate the magnitude of thrust and the change in the angle of the thrust line (assumed to act through the element's centre) for each element. The analysis starts at either the right or the left base. Elements are added until the arch forms. This method is versatile and highly effective form finding tool for vaults for any given static loads.

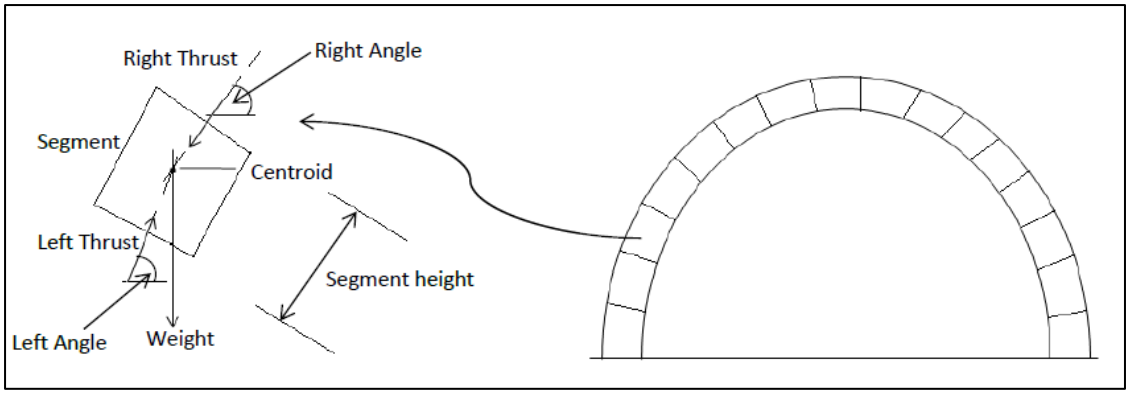

Figure 2.9: The sequential equilibrium method (Bulovic, 2014)

2.3.3 Mathematical formulation

The catenary equation is as follows:

$$y = a\cosh\left(\frac{x}{a}\right) \qquad (2.5)$$

Where a= a numerical parameter that defines the shape of the catenary

x= the horizontal distance measured from the centre of the curve

An example of the inverted curve derived from this formula is shown in figure 2.10:

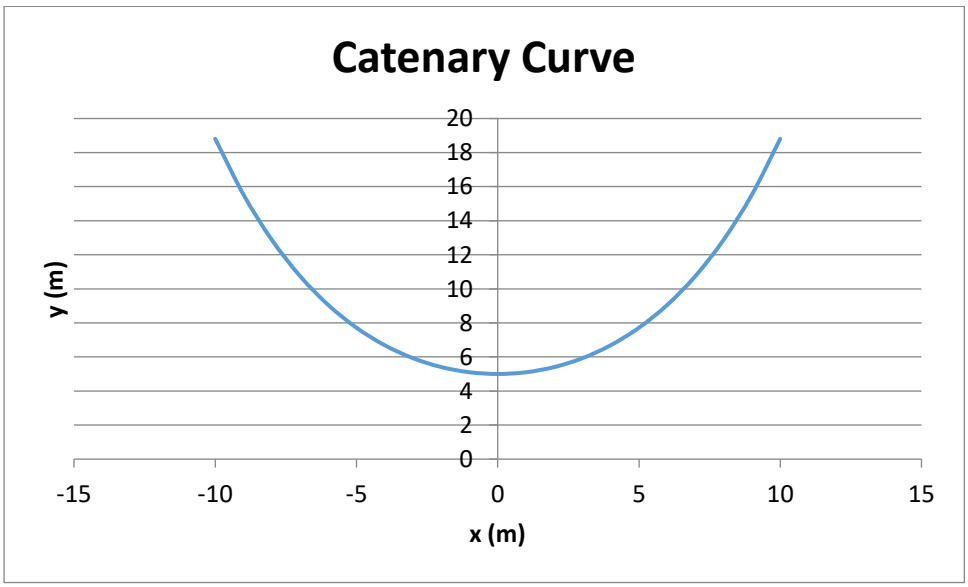

Figure 2.10: Inverted catenary curve

This equation describes the shape of a hanging chain under pure tension. Gohnert (2015) altered this equation to develop an equation describing the shape of the inverted catenary held under pure compression:

$$y = H - a\cosh\left(\frac{x}{a}\right) - a \qquad (2.6)$$

Where H=the height of the arch at midspan

Assuming that L equals to the span of the arch, using the boundary condition that:

y=0 at x= span/2 =L/2

The following may be derived from the equation above.

$$H = a\cosh\left(\frac{L}{2a}\right) \qquad (2.7)$$

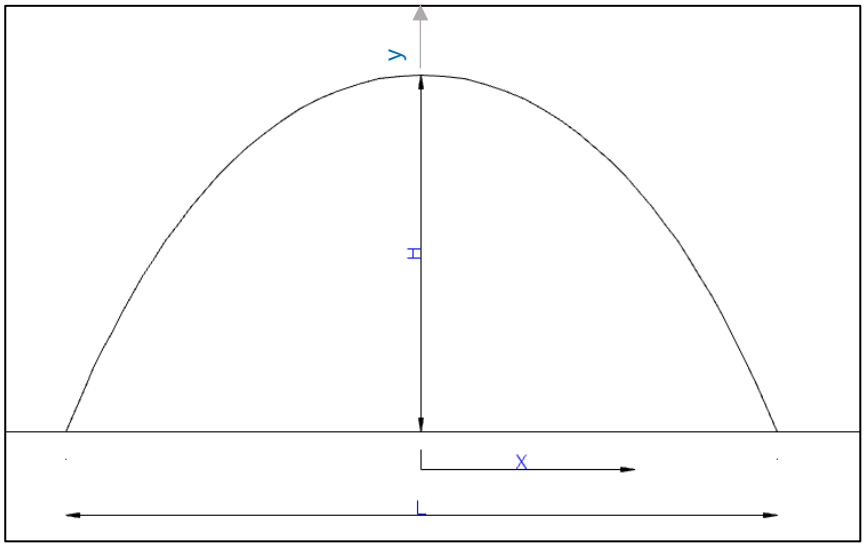

Figure 2.11: Parameters defining the catenary equation

Using this equation, with a known H and L, the parameter 'a' may be solved for iteratively. With this parameter, equation 6 may be used to define the funicular curve for a catenary arch subjected to self-weight loading. For additional loading such as wind loading and imposed loads, this method will not be sufficient. Despite this,

technique is sufficient to get the initial geometry of the arch to be constructed and analysed.

2.4 The role of catenary vaults in low cost housing applications

Although this study is not directly concerned with the low-cost housing model, catenary vaults have been studied from this perspective. Fitchett (2009) describes how low cost housing requires 'design and specification that maximizes the use of local materials, locally manufactured components, local suppliers and transport, local energy sources, as well as local labour at all levels of expertise.' In addition to this, importing of costly materials, such as cement and steel reinforcement must be minimized.

This definition informs the mainstream paradigm of low-cost housing. Bulovic (2014) found that utilising unreinforced masonry catenary vaults in low-cost housing applications, namely for roofing, proves to be cost-effective and viable solution. Minke (2009) furthers this idea, listing the following advantages: 'Vaults and domes require less building material to enclose a given volume,' are cheaper to construct than conventional roofs in developing countries and have good thermal properties. As discussed above, the inverted catenary is the optimised shape for a vault subjected to self-weight loading, making efficient use of materials.

Yet with the introduction of seismic loading and associated tensile forces, the structural integrity of the masonry catenary vault is undermined. In order to rectify this, methods to increase the seismic capacity of this vault need to be developed.

Low-earning communities and developing nations in seismically active zones may benefit from a study looking into improving the seismic resilience of catenary vaults in the following ways:

i. Reduction in deaths due to sudden collapse of structures that are unfit for use in seismically active zones.
ii. As construction becomes more regulated in developing countries, construction of unreinforced masonry structures may be prohibited. [2] This

[2] In the USA for example, building code regulations ban the use of unreinforced masonry in areas of known seismicity. For more information refer to pp. 2-3 of *Unreinforced Masonry Buildings and Earthquakes: Developing Successful Risk Reduction Programmes* (FEMA, 2009)

may result in the necessity to demolish unreinforced masonry structures creating an economic burden on the government and home-owners. Through looking at reinforcement strategies that are cost-effective, solutions may be found that still align with the low-cost housing model.

2.5 Masonry as a construction material

Masonry is an ancient and versatile construction material. Masonry units may be created in a number of ways using various materials. In this study, cement stabilised earth blocks are used. Stabilised earth blocks and tile are made from in-situ earth stabilised with cement, lime, fly-ash or other additives. The stabiliser to soil ratio used is low[3], making it more economical and energy efficient than conventional brickwork. Tiles may be made using a hand-press which does not require a large initial capital investment, is mobile and simple to use (Fitchett, 2009). Adam and Agib (2001) discuss the advantages and disadvantages of earth as a construction material. Its advantages are as follows:

- Earth is an abundant material, making it highly accessible procurement and cost perspective.
- Good fire performance
- Has a 'high thermal capacity, low thermal conductivity and porosity' making it highly effective at passive cooling and heating. Internal temperatures in buildings that are constructed using earth materials are less susceptible to sudden changes in ambient temperature.
- The processing and handling of earth requires a substantially lower amount of energy as compared to concrete (approximately 1% of the energy required for concrete production).
- Less harmful to the environment. Since cement production is a large contributor to the production of greenhouse gas, namely CO2 (Gibbs *et al.*, n.d.), a lower cement content also makes the earth blocks more environmentally friendly.

[3] This ratio varies from 4-9 %, depending on the soil type used and the extent of stabilisation required (Adam and Agib, 2001)

Despite its many advantages, building with earth materials has some disadvantages:

- Needs to be protected and maintained to prevent degradation.
- Like all masonry, earth bricks have a low tensile capacity
- Poor public perception
- Lack of standards and building codes for earth construction.

Despite its disadvantages, stabilised earth proves to be a viable and economical construction material.

2.6 Reinforcement solutions for improving seismic performance

Three options are considered as solutions to improving the seismic capacity of masonry vaults; namely, post-tensioning, polymer reinforcement and basalt fibre reinforcement. It must be noted that as structural steel reinforcement is expensive to purchase and transport, is prone to corrosion (decreasing its maintainability) and is hard to bend in order to conform to the profile of a catenary vault it has not been considered as a viable solution.

2.6.1 Prestressing

The aim of prestressing and post-tensioning is to create a tensile force in a high strength materials such as steel tendons and cables, such that the counteracting reaction force in the tendon will induce compression in a structure. This force will reduce or totally remove internal tensile stresses in the structure (Gilbert and Mickleborough, 1990).

Through the tensioning of tendons or elements that rest on the extrados of the arch, a distributed force is applied over the arch. The application of this force will not shift the original thrust line of the arch, yet the magnitude of the thrust will increase. The prestressing force must be low enough such that the internal stresses in the arch remain below the masonry's compressive strength limit. If a lateral load is introduced, such as seismic loading, the thrust line will shift. Yet, the introduction of prestressing will prevent this shift, thereby reducing the movement of the thrust outside the middle-third of the arch's cross section. This prevents the development of

tensile stresses in the arch. In doing so, the seismic capacity of the arch is increased.

The design process must include an allowance for loss of prestressing force in the tendons due to creep, elastic shortening and anchorage losses.

The design of prestressing solutions requires greater technical input. Considerations include the correct placement of anchorage points, jacking sequences, calculations of prestressing losses and measurement of the applied prestressing force.

Prestressing tendons are held under high tension. In case of demolition, special care must be taken to release this tension carefully so as to prevent damage to adjacent structures and injury. This may require bringing in experts for demolition. The same risk is also associated with fire, which may lower the integrity of the tendons, resulting in catastrophic failure of the prestressed structure and risk to human life.

A summary of the advantages and disadvantages of prestressing is presented in Table 2.1.

Table 2.1: Summary of advantages and disadvantages of prestressing solution

Advantages	Disadvantages
• Consolidates the arch and prevents movement. • Increases the arch's capacity under static and seismic loading • May prevent the formation of hinges outright under a given seismic load.	• Manufacturing of specialised anchors and tendons may prove to be costly. • Needs to be installed and maintained by a competent person. • Problems with fires and demolition (i.e. sudden release of high tensile forces in tendons is a hazard) • High cost of system • Cables need to be protected from corrosion (if steel cables are used). • Bonding issues

2.6.2 Polymer Reinforcement

Fibre Reinforced Polymer

Numerous studies have looked into the strengthening of existing structures with FRP (fibre reinforced polymer) used in place of steel reinforcement. The bulk of research has looked into the use of FRP in reinforced concrete, rather than masonry structures (Shrive, 2005). Shrive (2005) explains that 'FRP's consist of high strength fibres embedded in a resin matrix.' The most commonly used are carbon, glass and aramid FRP's. The strength of FRP's varies substantially, depending on its constituent material. Two commonly used types are glass and carbon FRP's. Basilio (2007) performed tests of both glass and carbon fibre reinforced polymers. The material properties of GFRP and CFRP are given in Table 2.2.

Table 2.2: Properties of glass and carbon fibre reinforced polymers (Basilio, 2007)

Parameter	**Glass fibre reinforced polymer (GFRP)**	**Carbon fibre reinforced polymer (CFRP)**
Young's Modulus (GPa)*	79.85	216.25
Strain (%)	36.58	12.38
Ultimate tensile stress (MPa)	1473.1	2534.6

*Results according to ISO 527-1

From this data, it may be seen that carbon fibre is substantially stronger than glass fibre, despite being less ductile. The Young's modulus of carbon fibre is comparable to that of steel (approximately 200-210 GPa). Both have high tensile stress capacities.

In addition to having high tensile strength, FRP's are lightweight and therefore they are more easily transported. In seismic applications, they are useful as the 'strength and stiffness of a structure can be increased with very little increase in mass,' thus producing little change in inertial force generated by seismic loading. As FRP is not susceptible to corrosion, it may be used in more aggressive environments (Shrive,

2005). FRP is flexible, therefore it can conform to the shape of the structure it is reinforcing.

However, FRP's also have some disadvantages. The resin of FRP's is sensitive to UV light and may become brittle with prolonged exposure. They also degrade under heat and therefore behave poorly when subjected to fires (Shrive, 2005). A key consideration is the bond of the FRP to the structure that it reinforces (Valuzzi *et al*., 2001). Delamination of the FRP from the structure can occur during loading, limiting its ability to resist loads. In arches, this normally occurs when FRP is bonded to the intrados. FRP's failure is sudden (not ductile), therefore their 'stress-strain behaviour is taken as linear elastic until failure' (Shrive, 2005). There is also a danger that if the material is loaded over its elastic limit, that sudden failure will occur. Therefore, it is critical that the loading of structures utilising these materials is within this limit. Glass fibre also reacts with concrete. This reaction degrades the glass fibres down, drastically reducing its strength (Sheffler et al, 2009).

When FRP reinforcement is placed at either the intrados or extrados of a masonry arch, the behaviour of the arch changes substantially as the tensile capacity of the reinforcement is mobilised. Under these conditions failure occurs, not due to instability, but rather due to Crushing of the masonry, delamination of the adhesion system or sliding between bricks (Valuzzi *et al.*, 2001).

This change in structural behaviour is illustrated by tests performed by Basilio (2007). Basilio performed a series of static tests on unreinforced and FRP reinforced circular masonry arches. The FRP was attached to prepared surfaces on the arches using bonding adhesives. The first tests involved the static testing of unreinforced arches. FRP was then placed over portions of the arch where hinges had occurred in the previous tests. Rather than preventing the formation of hinges, the local reinforcement just caused the relocation of the hinges.

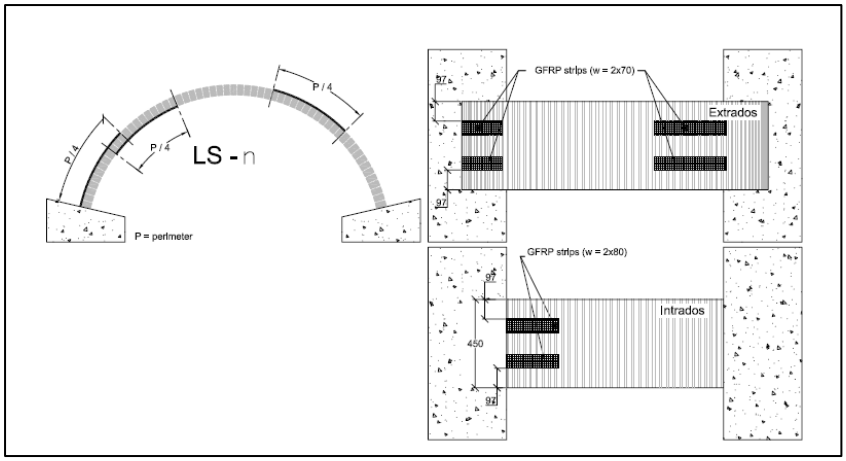

Figure 2.12: Locally reinforced arch (Basilio, 2007)

When FRP was placed over the length of the arch's extrados, substantial increases in the ductility of the structure was observed (measured displacements before failure was 20 times greater than that of unreinforced arches). Failure in these tests was characterised by sliding between blocks. When FRP was placed over the length of the arch's intrados with anchorage spikes located along its length, ductility increased substantially (35 times the displacement of unreinforced arches). Failure was characterised by the formation of three hinges, followed by collapse when the fourth hinge formed with the delamination of the FRP from the arch. Placing the FRP along the intrados also resulted in the highest increase in load capacity. These tests indicate that the location of FRP reinforcement is a critical concern. (Basilio, 2007). The final method was the most effective with regards to improvement of structural performance and highlights the efficacy of using anchors. Through increasing the ductility of unreinforced masonry vaults, sudden catastrophic failure during seismic events is prevented. By providing additional time and warning before collapse occurs, many lives could be saved during earthquake events.

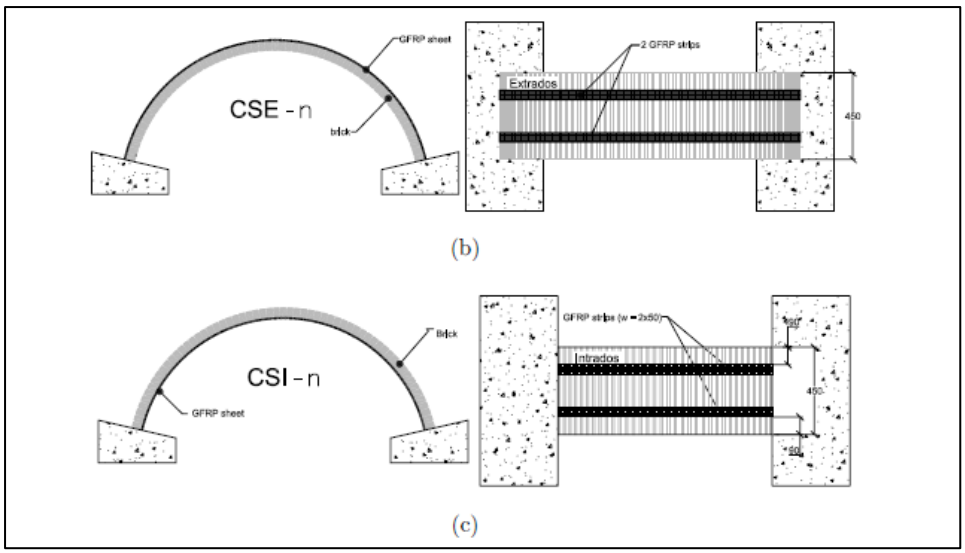

Figure 2.13: Reinforcement spanning across the extrados and intrados respectively (Basilio, 2007)

Polymer geogrid

DeJong *et al.* (2011) conducted dynamic tests on catenary vaults reinforced with Tensar Triax, a geogrid polymer. The geogrid was positioned over the length of the arch's extrados, embedded in a mortar layer between two layers of tiles. The geogrid was secured at the base of the arch. An unreinforced and reinforced arch was tested harmonically and then subjected to a series of cosine wave impulse with linearly increasing frequencies. At lower frequencies, rigid body motion of the entire arch was encountered yet at higher frequencies, hinges formed and rocking motion of the arch was observed. When this occurred, the frequency measured on the shaking table diverged from the frequency measured on the arch, characteristic of rocking motion.

Failure was characterised by global collapse of the arch and delamination and failure of the geogrid reinforcement. The reinforced vault was subjected to accelerations 2.5 times higher than those subjected to the unreinforced vault at collapse. This points to the efficacy of geogrid reinforcement in improving the seismic performance of unreinforced masonry vaults.

Basalt Fibre Reinforcement

Despite FRP's versatility in strengthening applications, it is prone to UV light and fire degradation. Exposure results in rapid loss of volumetric stability and strength (Sim *et al.*, 2005). A material that overcomes problem whilst retaining the benefits of FRP is basalt fibre reinforcement (BFR). BFR consists of strands extruded from basalt rock, which is abundant on Earth (Colombo *et al.*, 2012). To produce the material, the rock is heated to 1400-1500 degrees Celsius in a furnace and is then forced through bushings to form fibres. This process is less energy intensive than that used to make glass and carbon fibre. As no additives need to be added to the material, it is cheaper to produce than both glass and carbon fibre (Fiore et al, 2015). Basalt fibre can be used in numerous ways. BFR can be used to strengthen structural elements, make reinforcing bars, manufacture of automotive and aeroplane parts and form geo-composites which are used in environmental applications (Saravanan, 2006).

Basalt fibres have excellent thermal performance properties. Sim *et al.* (2005) found that basalt fibre retains 90% of its strength after being exposed to 600°C for 2 hours. They also have better mechanical performance than glass fibres (Fiore *et al.*, 2015). The literature gives varying views on the alkali resistance of BFR. Sim measured the degradation and strength loss of immersed basalt, carbon and glass fibres in a NaOH solution. In the tests, the main constituent of basalt fibres, SiO_2, reacted with the alkali solution resulting in a significant volume reduction in the fibres. The result was that the basalt fibres lost 50% of their strength after 7 days and 80% of their strength after 28 days of immersion. Sheffler *et al.* (2009) looked deeper into this problem, by comparing the degradation of glass and basalt fibres in a NaOH solution and a cement solution, over a range of exposure times and temperatures. These two solutions have comparable pH values. Similarly to Sim's findings, extreme corrosion was observed when the fibres were immersed in the NaOH solution. When immersed in the cement solution, the formation of small holes on the fibre surface was observed. Despite this, it was found that the fibres in the cement solution did not 'reveal decreasing failure stresses over a vast interval of temperature and time.' Therefore if the arch is covered by a layer of mortar for aesthetic or protective purposes, degradation of the BFR should not be a concern.

Garmendia *et al.* (2011) performed static loading tests on circular masonry arches similar to those performed by Basilio (2007). Here basalt fibre geogrids were used as reinforcement. In these tests, the geogrids were placed over the length of the arches' extradoses and secured by anchorage spikes. As in Basilio's tests, failure was characterised by masonry crushing and debonding of the reinforcement rather than instability. Substantial increases in load capacity (13 times that of the unreinforced arches) and ductility were observed in the basalt reinforced arches.

With high durability, a relatively low price, ease of transportability and installation, ease of conforming to the shape of structural elements and good mechanical properties BFR is a good solution for strengthening the arch in a low-cost housing applications. By possessing all the good qualities of FRP reinforcement and the additional benefits as discussed above, BFR is a feasible solution for the reinforcement of catenary masonry vaults. A summary of the benefits of BFR from the above discussion is shown in Table 2.3:

Table 2.3: Advantages and disadvantages of basalt fibre reinforcement

Advantages	Disadvantages
• Durable • No prone to UV or fire degradation • Good mechanical properties • Lightweight and easily transportable. • Low weight, therefore does not contribute substantially towards inertial forces generated by seismic activity (reference). • Many basalt fibre products are flexible. Can conform to the shape of unreinforced structures easily • Better mechanical performance than glass fibre.	• May be prone to alkaline attack in aggressive environments. • Problems associated with delamination. • May shift the position of the hinges (if placed incorrectly). • Different types of basalt rocks will produce BFR with different mechanical properties. (Lopresto, *et al.*, 2011). • Material failure is not ductile. If not designed correctly, sudden catastrophic collapse may occur.

Advantages • Cheaper to produce than glass and carbon fibre • Doesn't require high level of skill to install. • Structural system can be maintained easily. • Resistant to UV light and high temperatures. • Gives the unreinforced arch a tensile capacity. • Can increase the ductility of structures.	

2.7 Seismic Analysis

Extensive research has been done into the seismic analysis of structures, yet, masonry arches have not received much consideration. This discussion first explores the primary physical model testing techniques to assess the response of structures to seismic loading, namely, static, pseudo dynamic or dynamic tests (Carvalho, 1998). It then presents practical ranges of seismic loading. The discussion then focussed on the seismic response of unreinforced masonry arches. Analytical models that have been developed to model the behaviour of unreinforced arches are explored and previous studies that have investigated seismic analysis of arches are discussed.

2.7.1 Physical seismic testing techniques for structures

The various testing methods are discussed below. This discussion will guide why certain methodologies will be employed in the study and other disregarded.

‘Pure’ Static Testing

Static testing consists of applying discrete displacements along the structure. This aims to mimic the effect of induced inertial loads induced by seismic activity. As this method does not require ‘complex testing equipment’, it is less cost intensive than other testing methods. Despite this, selection of a suitable displacement-time history that models the dynamic response of the structure and accounts for the changes in the structures response due to non-linearity can prove to be difficult using this method. Additionally, this test does not truly simulate true dynamic behaviour which is characterised by material changes (with regards to damage to the model) and the effect of impact, damping and changes in momentum (Carvalho, 1998).

Pseudo-dynamic testing

Pseudo-dynamic (PsD) testing was developed to overcome the shortfalls of static testing. This method involves the application of static loads on the structure via actuators which are connected and controlled by a computer. This models the response of a structure to dynamic loading via creating a series of discrete displacements. An algorithm converts a given acceleration-time history into corresponding displacements by iteratively solving for the equations of motion. This provides a more accurate representation of the structure’s response, taking into account restoring, inertial and damping forces. This method is far more effective than pure static tests, where the structure is subjected to cyclical loading, which measures fatigue more so than seismic capacity. Despite this, pseudo-dynamic load test do have some disadvantages. As the process uses input from previous time steps to calculate displacement values for subsequent time steps, errors will increase exponentially, resulting in unreliable data. Another disadvantage is that the timescale for testing is drastically increased, making it impractical when time constraints are present. Finally, PsD tests are most suited for structures where ‘mass is concentrated in certain locations’ of the structure (Carvalho, 1998). In catenary vaults, mass is spread out. This may make this method less conducive to testing these structures.

Shaking Table Tests

Shaking table tests allow the designer to assess the seismic response of a structure in real time. Although an effective manner of analysis, it can prove to be impractical in certain instances. The testing of full-scale structures gives a complete and realistic picture of a structure's response to seismic loading, yet this can be prohibitively expensive. Therefore, reduced scale models are often used for this type of testing. As most shaking tables do not have the capacity to assess 'full-scale structures,' scale models need to be used in most cases (Carvalho, 1998). In order to model the behaviour of the full-scale structure, similitude need to be respected, namely, Cauchy Similitude and Froude Similitude. Equations 2.8 and 2.9 describe the two similitude conditions (Carvalho, 1998):

$$\text{Cauchy value} = \frac{\rho\, v^2}{E} \qquad (2.8)$$

$$\text{Froude value} = \frac{v^2}{Lg} \qquad (2.9)$$

Where: ρ= density

v= velocity

E=Young's modulus

g= gravitational acceleration

L=length

A number of parameters that are not variables in equations 2.8 and 2.9 are affected by these similitude requirements and must be scaled accordingly. Table 2.4 presents parameter scaling requirements when applying Cauchy Similitude and combined similitude.

Table 2.4: Scale factors for dynamic analysis (Carvalho, 1998)

Parameter	Symbol	Scale Factor (Cauchy Similitude only)	Scale Factor (Cauchy and Froude Similitude)
Length	L	$L_p/L_m = l$	l
Modulus of Elasticity	E	$E_p/E_m = 1$	1
Specific Mass	ρ	1	l^{-1}
Area	A	l^2	l^2
Volume	V	l^3	l^3
Mass	m	l^3	l^2
Displacement	d	l	l
Velocity	v	1	$l^{1/2}$
Acceleration	a	l^{-1}	1
Weight	w	l^3	l^2
Force	F	l^2	l^2
Moment	M	l^3	l^3
Stress	σ	1	1
Strain	ε	1	1
Time	t	l	$l^{1/2}$
Frequency	f	l^{-1}	$l^{1/2}$

* Where p denotes the prototype (full-scale) and m denotes the model

It may be seen from Table 2.4 that in the respecting of combined similitude, the density or specific mass of the model structure is ‘inversely proportional to the geometric scale.’ This means that the density of the material used in the model structure would have to be substantially denser than that used in the prototype. This problem is rectified by the distribution of masses along the structure, normally concrete blocks or steel ingots. These masses must be connected in a way such that it does not affect the stiffness of the model structure (Carvalho, 1998). In the literature, most shaking table tests are performed with the application of Cauchy Similitude alone (for example Yang, 2010 and Mendes *et al.*, 2010). In addition to this constraint, the ability to model seismic loads is limited to the capabilities of the shaking table used, which is defined by its maximum stroke and frequency range. This study is concerned with providing a comparative analysis between unreinforced and reinforced arches rather than providing a predictive model that can be applied to large scale structures.

Although similitude is not applied in the study, the overall behaviour of the arches is the primary matter of interest, which will not be affected by scaling. Although material crushing may be more of a concern for larger arches, the expected failure mechanism is instability of the unreinforced arches. In assuming that masonry and mortar have no tensile capacity, the failure mechanisms and hinge locations of the tested arches should mimic those of larger arches. The purpose of the reinforced tests is to assess the effect of various reinforcement strategies on the behaviour and capacity of the arches. The arches are ‘over-reinforced’ in that failure due to crushing of the masonry and mortar rather than failure of the reinforcement is expected. These tests look at the failure mechanisms and behaviour of the arch when reinforced and provide a comparison of the relative efficacy of different reinforcement strategies. This too will not be affected substantially by scaling effects.

On this basis, the lack of scaling will not affect achieving the overall objective of this study. This method provides the most realistic simulation of the seismic response of structures and is relatively simple to carry out using the apparatus available at the University of Witwatersrand. Therefore, it was decided to use this method to test the arches.

2.7.2 Practical ranges for seismic loading

There are a number of scales used to assess the extent of seismicity. The most well-known scales being the Richter and Modified Mercalli Intensity Scales.

The Richter Scale uses the logarithm of an earthquake's wave amplitude adjusted by a number of parameters including and the distance of the measuring device to the earthquake epicentre to assess the magnitude of an earthquake. As the scale is logarithmic, each whole number increment in the scale represents a tenfold increment in the earthquake wave amplitude (Spall &Schnabel, 1989). The Modified Mercalli Intensity Scale is more quantitative and assesses the magnitude of earthquakes according to their effect on people, vehicles, furniture and structures. The Scale describes the increasing severity of seismic loading using 12 different intensity levels (refer to Table 2.5) (USGS, 1989).

Table 2.5: The Modified Mercalli Intensity Scale (USGS, 1989)

Intensity	Effect
I	Not felt except by a very few under especially favourable conditions.
II	Felt only by a few persons at rest, especially on upper floors of buildings. Delicately suspended objects may swing.
III	elt quite noticeably by persons indoors, especially on upper floors of buildings. Many people do not recognize it as an earthquake. Standing motor cars may rock slightly. Vibration similar to the passing of a truck. Duration estimated.
IV	Felt indoors by many, outdoors by few during the day. At night, some awakened. Dishes, windows, doors disturbed; walls make cracking sound. Sensation like heavy truck striking building. Standing motor cars rocked noticeably.
V	Felt by nearly everyone; many awakened. Some dishes, windows broken. Unstable objects overturned. Pendulum clocks may stop.
VI	Felt by all, many frightened. Some heavy furniture moved; a few instances of fallen plaster. Damage slight.
VII	Damage negligible in buildings of good design and construction; slight to moderate in well-built ordinary structures; considerable damage in poorly built or badly designed structures; some chimneys broken.
VIII	Damage slight in specially designed structures; considerable damage in ordinary substantial buildings with partial collapse. Damage great in poorly built structures. Fall of chimneys, factory stacks, columns, monuments, walls. Heavy furniture overturned.
IX	Damage considerable in specially designed structures; well-designed frame structures thrown out of plumb. Damage great in substantial buildings, with partial collapse. Buildings shifted off foundations.
X	Some well-built wooden structures destroyed; most masonry and frame structures destroyed with foundations. Rail bent.

Intensity	Effect
XI	Few, if any (masonry) structures remain standing. Bridges destroyed. Rails bent greatly.
X	Damage total. Lines of sight and level are distorted. Objects thrown into the air.

Wald et al. (1999) developed a relationship between peak ground acceleration (as a percentage of gravitational acceleration) and the Modified Mercalli Intensity Scale (MMIS). This is indicated in Table 2.6. This relationship serves as a basis to assess the severity of seismic loading in the tests performed in this study.

Table 2.6: Relationship between the Modified Mercalli Intensity Scale and peak ground acceleration (adapted from Wald et al., 1999 and USGS, 2016)

Modified Mercalli Intensity Level	I	II-III	IV	V	VI	VII	VIII	IX	X+
Shaking	Not felt	Weak	Weak	Light	Moderate	Strong	Very strong	Severe	Extreme
Peak Ground Acceleration (% g)	<0.17	0.17-1.4	1.4-3.9	3.9-9.2	9.2-18	18-34	34-65	65-124	>124

Case study: Africa, the Middle-East and South Africa

As mentioned in section 2.4, masonry catenary vaults have been found to be sustainable and cost effective for use in low-cost housing applications. Due to this, these vaults could be of great benefit to developing countries. In order to assess the needs of developing countries with regards to design for seismic loading, Africa, the Middle-East and South Africa are used as a case study.

Using the relationship between developed by Wald (1999) (refer to Table 2.6 above) and Figure 2.14 (OCHA, 2007), it is possible to assess practical ranges of seismicity in Africa and the Middle-East with regards to peak ground accelerations. As indicated in Figure 2.14, most seismicity in Africa is experienced in eastern Africa. Zones with significant seismicity (Modified Mercalli Scale of VIII) include Ethiopia and northern Botswana, Algeria and Morocco. The associated peak ground acceleration for this MMIS level is 34-65 % of gravitational acceleration (0.34-0.65 g). Zones of lower seismicity (MMIS levels VI-VII) have associated peak ground accelerations of 9.2-34% of gravitational acceleration (0.092-0.34 g). Included in this range is South Africa (with an exception of a small area in the Western Cape Province). In the Middle-East, seismicity in countries such as Iran and Turkey, the MMIS level range is IX-XII, which correlates with peak ground accelerations between 0.65 to greater than 1.24 g (Wald, 1999).

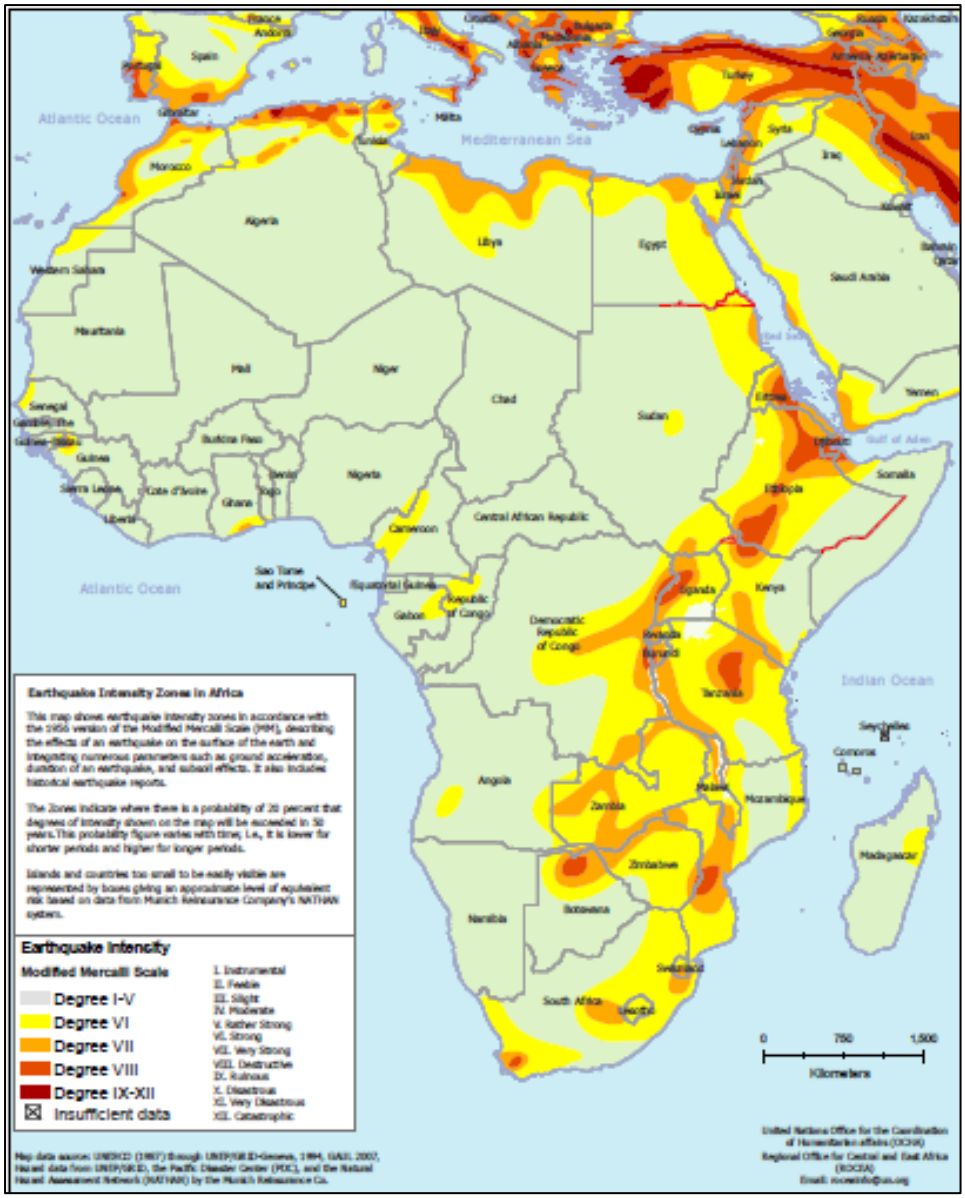

Figure 2.14: Seismicity map of Africa (OCHA, 2007)

As a means to validate the map in Figure 2.14, the South African Bureau of Standards code for seismic loading (SANS 10160-4: 2011) was investigated. Figure 2.15 demarcates two different zone types (I and II), which correlate to zones of natural seismicity and zones of mining induced and natural seismicity respectively. The map indicates that in central South Africa, zones of significant seismicity are mostly mining related with peak ground accelerations ranges between 0.1-0.2 g. In the Western Cape, North-West and Kwa-Zulu Natal Provinces, zones of significant seismicity are mostly natural, with peak ground accelerations ranging between 0.1-0.15 g. As per Figure 2.14, MMIS levels range between degrees VI-VII for most of South Africa, which corresponds to peak ground accelerations between 0.09-0.34 g, which roughly correlates with the values indicated in Figure 2.15. The only significant difference between the two maps is that Figure 2.14 does not indicate seismicity in the North-West Province.

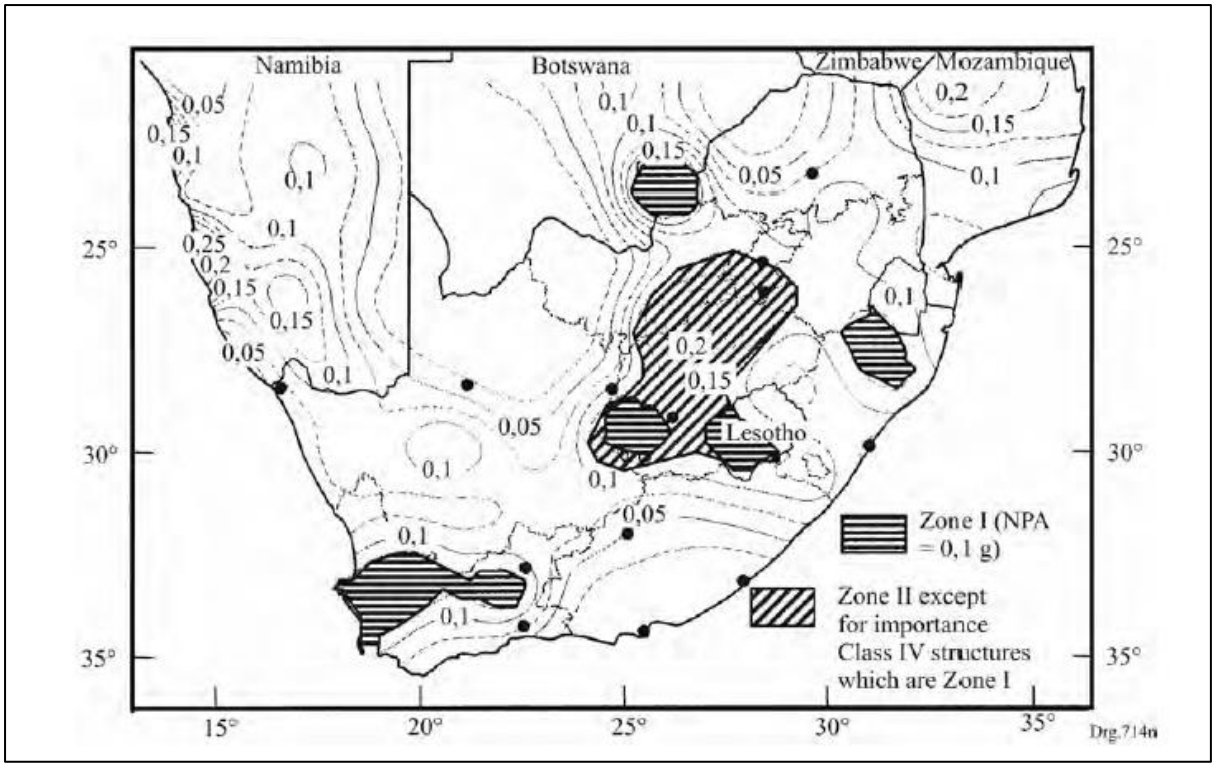

Figure 2.15: Seismicity map for South Africa (South African Bureau of Standards, 2011)

Using these maps as a reference, it can be seen if the tests performed in this study correlate to actual seismic conditions in the developing world.

2.7.3 Seismic modelling methods for unreinforced masonry arches

There are a number of methods with which the seismic response of a masonry arch may be modelled. Yet, only two methods relevant to the scope of this dissertation are discussed below.

Analytical Model

Oppenheim (1992) was the first to develop an analytical model for the response of arches to seismic loading. His model focussed on a circular masonry voussoir arch. Oppenheim looks at the condition where four hinges form a mechanism, causing collapse. The arch is modelled as a three-bar, four-link mechanism (see Figure 2.14).

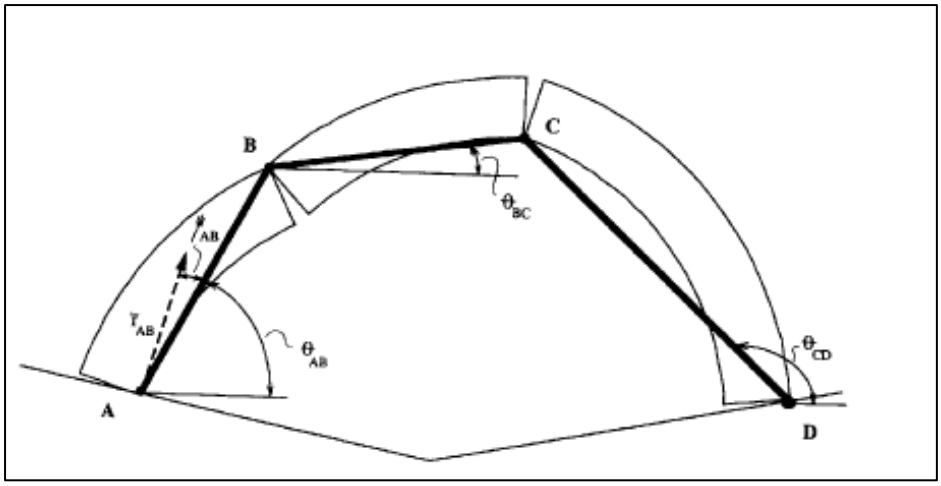

Figure 2.16: The masonry arch as a three-bar, four-link mechanism in the first half cycle of motion (Oppenheim, 1992)

As the rotations and rotational velocities of the links may be described by a single Lagrangian parameter, the mechanism is a single degree of freedom (SDOF) system. The rotation of links BC and CD (θ_{BC} and θ_{CD}) are defined relative to θ_{AB} (the rotation of link AB). Likewise, the rotational velocity of links BC and CD (θ'_{BC} and θ'_{CD}) are defined by θ'_{AB} (the rotational velocity of link AB). Using displacement and velocity analysis, relative rotations and rotational velocities of the other links may be found. The derivation of the equation of motion was performed using Lagrange's equation and Hamilton's principle and is presented in equation 2.10:

$$M(\theta)ma^3\ddot{\theta} + L(\theta)ma^2\dot{\theta}^2 + F(\theta)ma^2g = P(\theta)ma^2\ddot{x}_g \quad (2.10)$$

Where m =mass per unit length

a= radius from the origin of the arch to the centre of the arch

$\theta=\theta_{AB}$

$\dot{\theta}=\dot{\theta}_{AB}$

M(θ)= coefficient accounting for inertial effects

L(θ)= coefficient accounting for centrifugal and coriolis acceleration

F(θ)= coefficient accounting for gravitational force/ potential energy of the system

P(θ)= the generalised forcing function

This may be simplified to:

$$M(\theta)a\,\ddot{\theta} + L(\theta)\,\dot{\theta}^{2} + F(\theta)g = P(\theta)\ddot{x}_g \qquad (2.11)$$

The solution for the equation may be found by evaluating the system at the onset of motion where the initial conditions are as follows:

$\theta(0) = \theta_0$

$\dot{\theta}_{AB}(0)=0$

Where $\theta_0 = \theta_{AB}$ in the undisplaced arch configuration

$\dot{\theta}_0 = \dot{\theta}_{AB}$ in the undisplaced arch configuration

By solving this, equation the 'governing collapse mechanism and the corresponding minimum horizontal ground acceleration necessary to cause collapse' can be solved for.

Oppenheim only assessed the seismic response of the masonry arch under the first half cycle of motion the arch (as depicted in Figure 2.14). De Lorenzis *et al.* (2007) developed this model further. If the induced base acceleration is not sufficient to cause collapse during this cycle, the arch will first return to its 'initial undisplaced configuration' (Figure 2.15), where impact occurs and causes the dissipation of energy in the system as well as the development of impact induced forces in the arch. Using the equations of linear and angular momentum, the coefficient of restitution, a measure of energy lost during each impact may be calculated. For each impact event, this coefficient is applied to account for energy losses (De Lorenzis *et al.*, 2007).

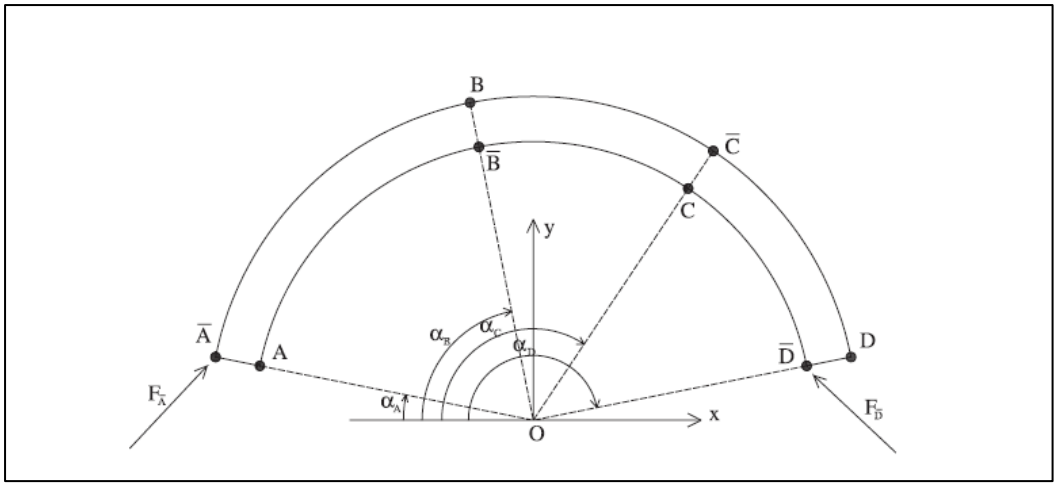

Figure 2.17: As the arch returns to its 'initial undisplaced configuration' impact occurs (De Lorenzis et al., 2007)

It is assumed that the location of the hinges in the arch will not move from one half cycle of motion to another. Therefore, after impact, the arch will enter into the second half cycle of motion, forming an inverse or mirror image mechanism to that encountered in the first cycle of motion. The point of hinge rotation changes to the other side of the respective hinges (refer to Figure 2.16) (De Lorenzis *et al.*, 2007).

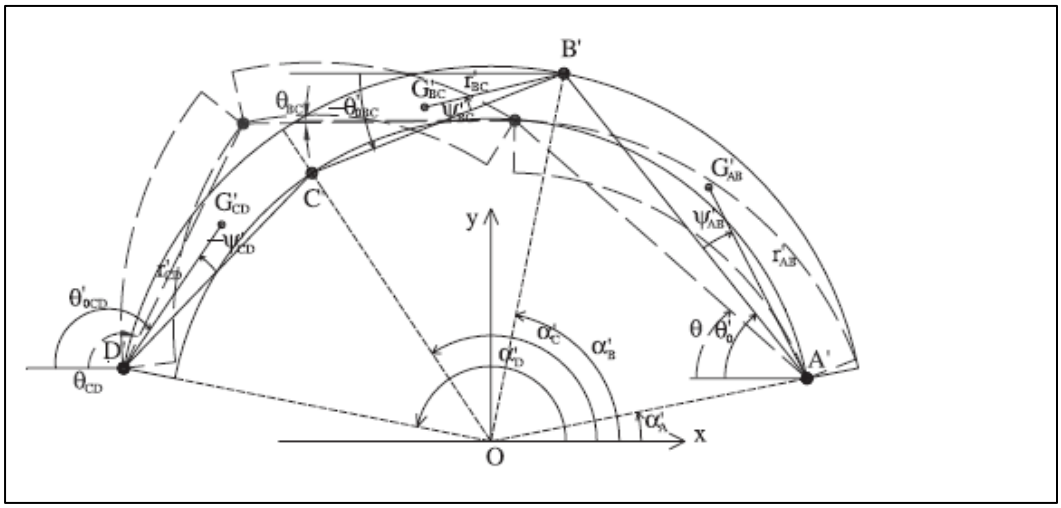

Figure 2.18: The masonry arch as a 4-link 3 bar mechanism in the second half cycle of motion (De Lorenzis et al., 2007)

De Lorenzis *et al.* (2007) developed the equation of motion for this cycle of motion.

$$M(\theta')R\ddot{\theta}' + L(\theta')\dot{\theta}'^{2} + F(\theta')g = -P(\theta')\ddot{x}_g \qquad (2.12)$$

Where R= the radius from the origin of the arch to the centre of the arch

All coefficients in equation 2.12 are the same as that in equation 2.10, but for the second half cycle of motion. Rotations and rotational velocity in now measured in the opposite direction.

Similarly, the equation of motion may be solved using the initial conditions:

$\theta'(0) = \theta_0' = \theta_0$

$\dot{\theta}_{AB}'(0) = \theta_{\varphi}'$

Where θ_{φ}'= rotational velocity of link A'B' immediately after impact.

Using the equations above, the motion of the arch with time and a given base motion may be fully described.

Tilt analysis

Stability methods can provide a first-order assessment of an arch's seismic capacity. This method models seismic loading as a constant lateral ground acceleration. If the arch is tilted, a lateral component of gravitational acceleration will develop. As the tilt angle increases, this component increases.

At collapse, the arch forms a 4-link, 3-bar mechanism. As discussed above, the mechanism is a single degree of freedom system and therefore the rotation of one bar may be used to describe the relative rotations of the remaining bars. By applying a virtual rotation to one bar and calculating the relative rotations of the other bars and the virtual displacements of the forces, the horizontal component of acceleration that causes collapse may be calculated using the principle of virtual work. Through iteration the critical collapse mechanism may be found (Ochsendorf, 2002).

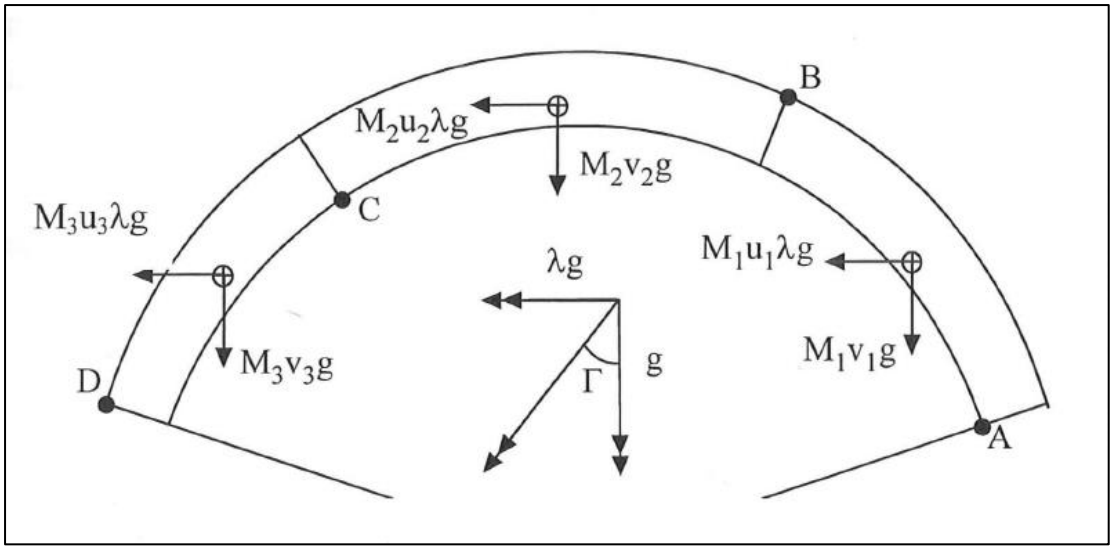

Figure 2.19: 3 bar mechanism with lateral components of gravitational acceleration (Ochsendorf, 2002)

This method is conservative in the regard that most earthquakes occur over a short period of time and are not subjected to constant ground acceleration. It is also unconservative in that it does not consider the effects of resonance and energy dissipation on the structure. However, this method provides a good first order approximation of the arch's seismic response and can be used to approximate the locations where hinges will form in the physical models (DeJong, 2009). Although Ochsendorf developed this method for circular arches, it may be adapted for a catenary arch.

2.7.4 Previous Studies

DeJong (2009)

DeJong performed a series of physical tests on dry stack, circular arches. The arch was constructed with aerated concrete blocks. The tests consisted of static tilt tests, based on the work of Ochsendorf (2002) (refer to Tilt Analysis above), seismic testing (subjecting arches to different earthquake time histories) and harmonic testing (subjecting arches to base motion of linearly increasing amplitude). Two arches of varying angles of embrace (152 and 162 degrees respectively) were used for testing. The collapse acceleration results from the tests were compared to the results of the expanded analytical model developed by De Lorenzis *et al.* (refer to section 2.72). During testing, it was observed that the locations of the hinges in the arch were not fixed. Rather they shifted from one half cycle of motion to another.

For the tilt tests, base of the respective arches was rotated until failure occurred. These tests model mode 2 type of failure (Zhang and Makris, 2001), where the

induced seismic loading is of sufficient duration and amplitude to cause collapse within the first cycle of motion. This approach is conservative.

The results of the tilt test experiments correlated closely to theoretical collapse acceleration values. The maximum percentage difference was approximately 4%.

For the seismic tests, the arches were subjected to earthquake time histories from records of five different earthquakes. These various earthquakes were selected as they represented a vast range of loading frequencies and amplitudes. The acceleration-time histories were scaled down and varied in even increments from 2%-100% of the full-scale amplitude of the respective earthquakes. The scale was increased until collapse occurred. Using the least square method, the maximum sine-wave amplitude and period at collapse was extracted from the respective acceleration-time histories.

The test results indicate that the impulse acceleration required to cause collapse decreases exponentially with an increase in the impulse period. They also indicate that there is a fairly good correlation with the analytical model. The results of the seismic testing are indicated in Figure 2.20.

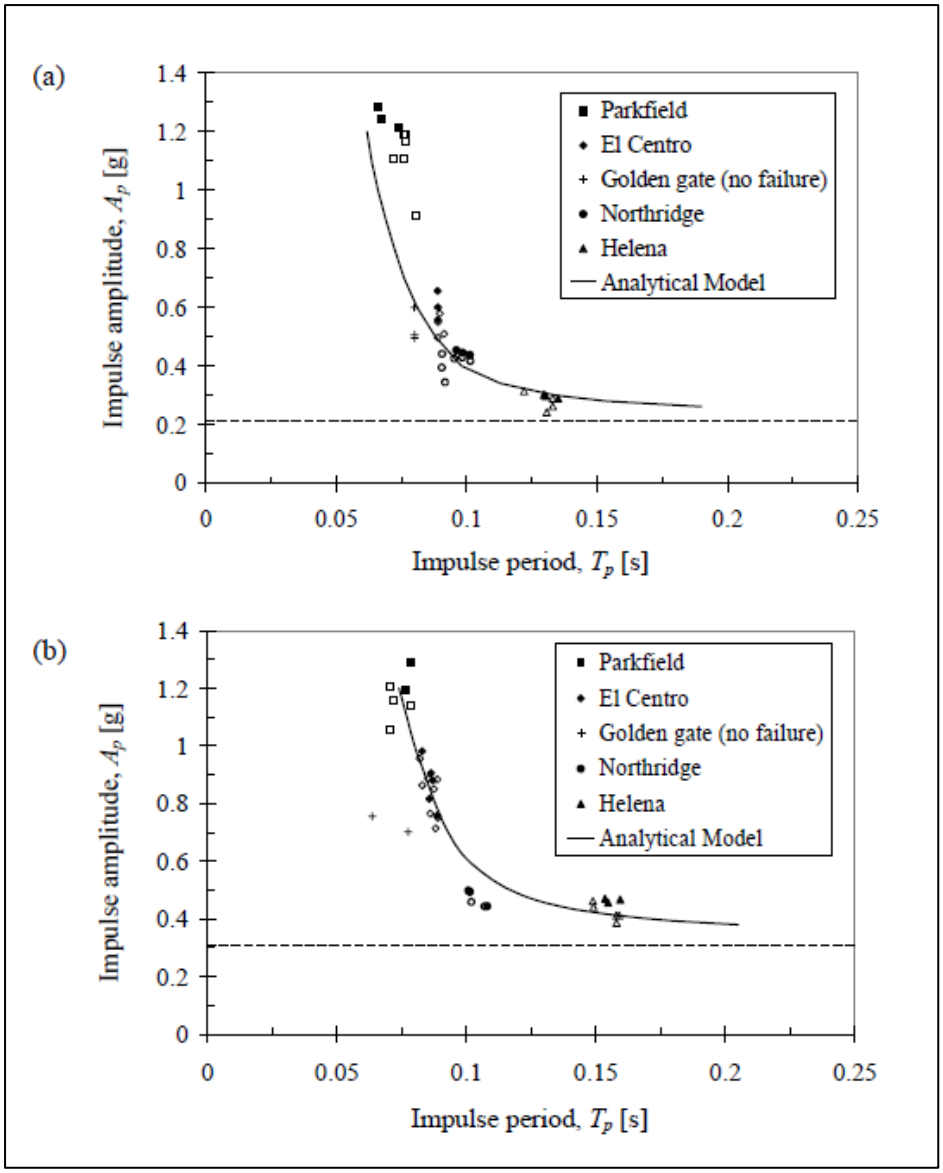

Figure 2.20: The inverse relationship between impulse amplitude and period for the two tested arches (DeJong, 2009)

The aim of the harmonic tests was to find the seismic response of the arches when subjected to sinusoidal base motion of linearly increasing amplitude. The reason for this test was to investigate the 'effect of repeated impulses on the arch response' as compared to single impulse loading. In these tests the frequencies of loading were 2,4,6,8 and 10 Hz respectively. The results of the tests indicate that the collapse is overpredicted for low frequency tests and underpredicted for higher frequency tests.

Collapse for the 2Hz tests was characterised by instability (i.e. due to the formation of a 4 hinge mechanism). During the 6 Hz tests, the seismic loading had a 'stabilising effect.' This is characterised by less pronounced rotation of the hinges during testing until a certain amplitude where rocking motion ensues and collapse occurs. This effect is attributed to the fact that at higher frequencies the number of impacts that occur when the arch goes from one half-cycle to the next increases substantially, accounting for a higher rate of energy dissipation. At higher frequencies (8-10 Hz), during collapse the arch 'vibrated apart' rather than failing due to instability. Figure

2.21 indicates the results of these tests. A trend can be observed that as the frequency of seismic loading increases, so too does the acceleration required to cause collapse. This provides the same result as the seismic tests.

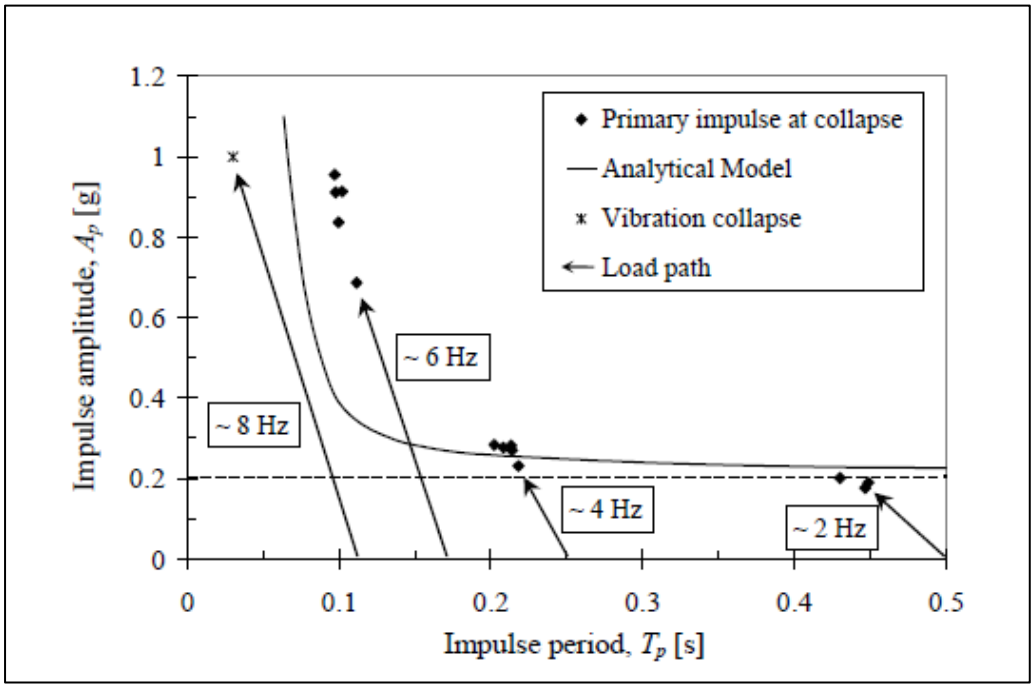

Figure 2.21: Results of harmonic testing (DeJong, 2009)

Terry, 2011

Terry (2011) conducted a test to compare the seismic performance of an unreinforced and triaxial polymer geogrid reinforced masonry catenary arch. This is the first study that investigated the seismic performance of thin shell catenary vaults using physical testing. The two arches were both 2m in span and 0.73m high. The arch consisted of two layers. The first and second layers was constructed using plaster and mortar respectively. In between these layers was a mortar layer, in which the geogrid was embedded. The two arches used in Terry's test are shown in Figure 2.22. A single later of bricks was added to the top of the arch for mass scaling purposes. The geogrid was held down at the base of the reinforced arch to prevent slippage during testing.



Figure 2.22: Reinforced and unreinforced arches during construction (Terry, 2011)

The arches were subjected to cosine wave ground acceleration impulses. During testing, the unreinforced arch failed at an impulse acceleration amplitude of 0.5g (i.e. 0.5x9.81 m/s^2=4.91 m/s^2) and the reinforced arch failed at 1.4g. This indicates that the seismic resilience increases substantially with the addition of reinforcement. For both tests, failure was due to instability (the formation of a four hinge mechanism). Collapse of the reinforced arch was also characterised by the failure of the geogrid, located at the position of the second hinge.

2.8 The rocking response of structures

Housner (1963) was the first to investigate the rocking response of a block subjected to ground motion. He developed and solved for the equations of motion for both half cycles of motion for different types of base motion and discussed the role of impact on dissipation of energy induced by ground motion.

For rocking blocks and all rocking structures, there are two possible modes of failure (in the form of collapse or overturning). Mode 1 is defined by failure that occurs after multiple impacts and mode 2 is defined by failure caused by a base acceleration of a sufficient magnitude and duration to cause failure without impacts (Zhang and Makris, 2001).

Housner (1963) first looked at mode 1 type failure. He found that with for both rectangular and sinusoidal base accelerations that there is a ‘relationship between the impulse acceleration and duration which causes overturning’ (DeJong 2009).

Error! Reference source not found. The relationship between the frequency of a single sinusoidal impulse and the magnitude of peak acceleration that causes overturning of a block is shown in Figures 2.21 and 2.22. Both of these graphs point to the fact that longer durations of base accelerations require lower amplitudes to cause failure.

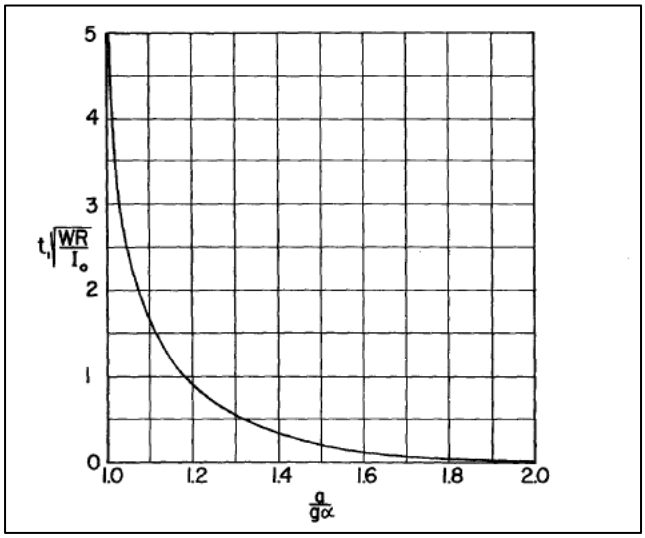

Figure 2.23: Time of application and constant acceleration magnitude required to cause overturning (Housner, 1963)

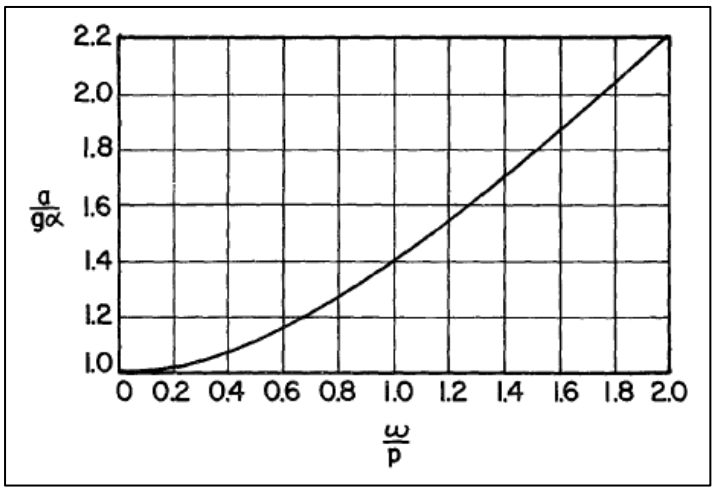

Figure 2.24: Period and sinusoidal acceleration magnitude required to cause overturning (Housner)

A vital finding in Housner (1963) was that the 'dynamic response of rocking structures and typical elastic structures' varies substantially. In elastic structures, the natural frequency is static and resonance will be encountered at this frequency (DeJong, 2009). Housner found that rather than being static, the natural rocking period of the block is dependent on its rocking angle (refer to Figure 2.19). When the

block moves from one cycle of motion to another, impact occurs and the ‘energy of vibration’ decreases which results in an increasing rocking period with the each half-cycle of motion (Housner, 1963).

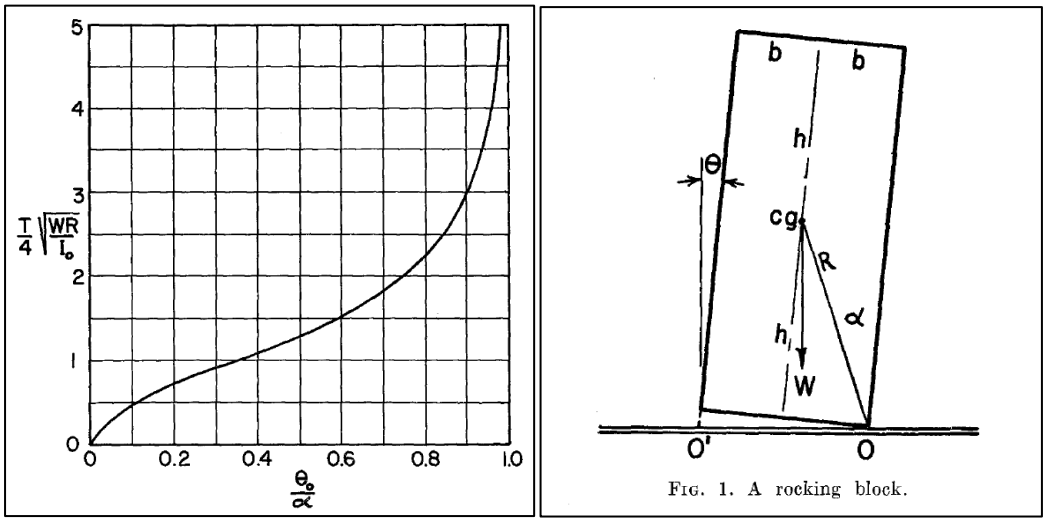

Figure 2-2.25: The natural rocking period increases with the rocking angle (Housner, 1963)

Therefore an optimised ground motion that would cause ‘rocking resonance’ is one where the period of induced acceleration increases with time. Yet such a ground motion is not likely to occur. DeJong (2009) found that the ability of the ground motion to add energy to the system is dependent on the relative relationship between the natural rocking frequency of block at a given moment in time (T_n) and the induced acceleration impulse’s duration or period. In Figure 2.20, it may be seen that likelihood of and magnitude of energy increment increases when ratio of the impulse period to T_n is higher. The time at which the impulse starts (t_{start}), relative to T_n, is also an important factor (DeJong, 2009). Using the analytical model developed, the seismic response of the rocking block to a set of generated earthquakes was studied. A trend was found that as the duration of the generated earthquakes increased, rocking amplification is encountered until a certain point where the induced impulses become relatively short in comparison to the large natural rocking frequency of the block, resulting in a little increases in amplification.

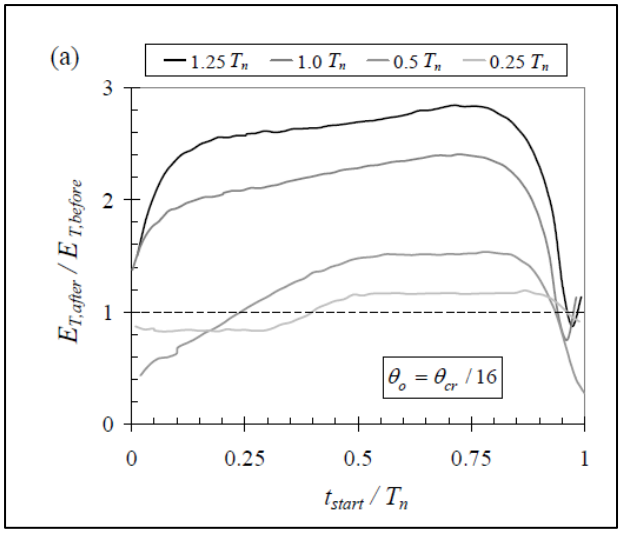

Figure 2-2.26: The probability of adding energy to the system increases with higher impulse periods (DeJong, 2009)

DeJong further considers the energy of the rocking block. He states that when 'the total energy input between impacts exceeds the energy dissipated at impact, collapse will eventually occur.' As less energy is dissipated at impact with slender blocks, they are more likely to collapse at lower accelerations. Additionally he found that with more initial energy in the system, marked by larger rotation of the block, the time taken for impact to occur will increase. This results in a slower rate of energy dissipation. Therefore, with a higher initial energy the rocking block will collapse at a lower accelerations.

This points to the complexity of predicting the rocking response of structures. The occurrence of 'rocking resonance' becomes a question of the probability of the ideal conditions that will result in the increased energy of the system and eventual collapse. These findings were applied to the rocking arch model and the variability encountered in the single block's response were also encountered for the arch

From this study, it may be seen that the rocking response of an arch is highly variable and is sensitive to the rate of application of seismic load and the spacing, magnitude and duration of subsequent impulses.' (DeJong, 2009).

2.9 Requirement for further investigation

Previous research has provided critical insight into the seismic response of arches. Yet, there are certain aspects that were not covered that warrant further investigation.

In both DeJong and Terry's investigations, a limited array of arch geometries were tested. The effect of the height to width ratio of arches on collapse acceleration has not yet been investigated using physical testing. DeJong performed a number of tests on dry stack masonry arches looking at various types of seismic loading. Yet, is unclear if the characteristic behaviour of dry stack masonry arches is similar or different to that of mortared masonry arches for different types of seismic loading.

Terry investigated the effect of introducing geogrid reinforcement on the seismic capacity of mortared masonry arches. In the study only one type of reinforcement strategy (anchoring geogrid at the base) was investigated. In section 2.6, it was shown that the use of geogrid anchors substantially improved the load capacity of masonry arches. The efficacy of anchors in improving the seismic capacity of masonry arches has not yet been investigated. Prestressing of arches as a means of improving seismic capacity of masonry arches has also not been investigated. In addition to this, only single impulse seismic loading was investigated in Terry's study. The effect of sinusoidal harmonic base motion on catenary vaults still needs to be investigated for both reinforced and unreinforced thin shell catenary arches.

This study aims to fill these gaps in the current body of knowledge. This will be done by investigating the effect of varying height to width ratios on the seismic capacity and response of catenary arches. The arches will be subjected to an array of sinusoidal base accelerations. Finally, various reinforcement strategies will be investigated to improve the seismic performance of the arches.

2.10 Summary

This chapter has explored the catenary arch and the various techniques that may be used to develop the catenary form. The role of catenary vaults and improving their seismic performance in the low-cost housing model was then considered using various reinforcement techniques. Although unreinforced catenary vaults perform

well under static loading, the introduction of lateral seismic loading severely affects their performance. Therefore a range of interventions were explored as a means on improving the catenary vault's seismic performance. Through exploring the benefits and disadvantages of each intervention, the use of basalt fibre geogrids was found to be the most effective and viable in low-cost housing applications.

There are many ways to perform physical seismic testing of structures. In this chapter, a review of several methods was performed and it was found that shaking table tests provide the most accurate means of assessing the seismic response of catenary vaults. A host of modelling methods have been developed to assess the seismic response of circular masonry arches. These methods may be adapted for catenary vaults to provide predict their seismic response.

Finally, the rocking block model and its application to masonry arches was considered. This model provides the designer with a basis for understanding the non-intuitive seismic behaviour of rocking structures, which is fundamentally different to that of conventional elastic structures. There a number of gaps in the current body of knowledge that require investigation that this study aims to investigate.

3 PREDICTIVE MODEL

3.1 Derivation and validation

This method, based on the principle of virtual work, was developed by Ochsendorf (2002). It is used to calculate the minimum lateral component of acceleration that is required to cause collapse of an unreinforced circular masonry arch. This component is represented as a percentage of g, gravitational acceleration (λmin). This calculation is iterative, assessing all possible hinge locations in order to find the critical lateral acceleration. As discussed above, this method assesses the arch at collapse, where a 4-hinge, 3-bar mechanism has formed. The hinges will alternate between the extrados and intrados of the arch. For each bar, there will be a self-weight load. If the arch is tilted, a lateral component of vertical acceleration (gravity) will develop. These forces act at the centroid of each bar (Figure 3.1).

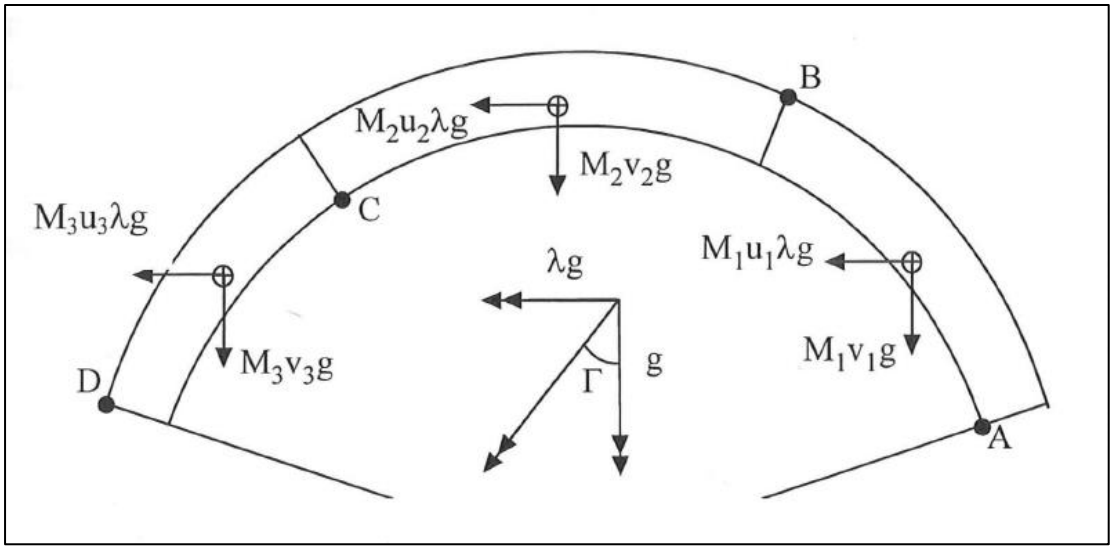

Figure 3.1: Three bar mechanism with lateral components of gravitational acceleration (Ochsendorf, 2002)

The three bar arch mechanism is a single degree of freedom system. Therefore, if a virtual displacement is subjected to one bar, the relative rotations of the other bars may be calculated. Using these rotations, the virtual horizontal and vertical displacement of all forces may be calculated. The principle of virtual work states that the sum of external work must equal to internal work when an arbitrary virtual displacement is performed on a body (W_E=W_I) (Ochsendorf, 2002). This method

assesses the arch at collapse, where each bar in the mechanism will undergo rigid-body motion. This method is simplified by not considering the moment capacity of the structure, primarily the mortar joint. Megson (2005) states that 'the internal work produced by a virtual displacement in a rigid body is zero'. Therefore, setting W_I to zero, the virtual work formula reduces to:

$$\sum_{i=1}^{n} W_i \cdot d_{vi} + \lambda \cdot \sum_{i=1}^{n} W_i \cdot d_{hi} = 0 \qquad (3.1)$$

Where W_i = the weight of the respective bars

d_{hi} and d_{vi} = the horizontal and vertical displacements of the respective forces

λ = lateral component of gravitational acceleration

The formula may be rearranged to solve for λ:

$$\lambda = \frac{-\sum_{i=1}^{n} W_i \cdot d_{vi}}{\sum_{i=1}^{n} W_i \cdot d_{hi}} \qquad (3.2)$$

Using this method, the 'the relative stability of various arch geometries' may be assessed. As discussed above, this method is conservative because it models a constant lateral acceleration, which will not occur in reality. As Housner (1963) showed, the longer the time of application of lateral load, the lower the amplitude of acceleration to cause collapse. At a certain duration of application of lateral acceleration, the collapse curve will tend toward a straight line, forming an asymptote under which no lateral accelerations will cause failure. Therefore, this method provides the designer with the minimum value of acceleration that will cause collapse (Ochsendorf, 2002). This provides the designer with a baseline for seismic assessment with which they can generate preliminary designs based on regional seismicity.

Firstly, the steps used for Ochsendorf's method are discussed, followed by the findings made using the adapted model.

Methodology:

1. Select 4 locations where hinges will occur in the arch. The respective locations will be referred to as hinges A, B, C and D. Hinges A and C form at the arch's intrados and hinges B and D form at the arch's extrados.
2. Draw two lines. One will pass through hinges A and B. The other will pass through hinges C and D. Find the coordinates of the intersection of these two lines. This line represents the centre of rotation of the arch.

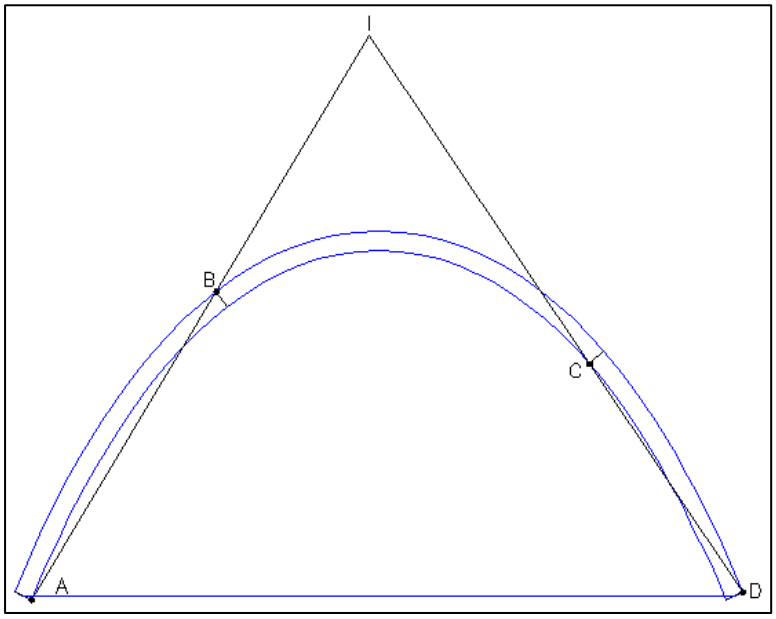

Figure 3.2: 2 lines are drawn through the hinges to find the centre of rotation of the arch (representation of centre of rotation adopted from De Luca et al., 2004)

3. The mechanism is a SDOF system, which means that the rotation of all links may be described by 1 rotation. Here, the rotation of bar AB (θ_1) is chosen as the controlling parameter. Using geometric compatibility and assuming small angles, θ_2 and θ_3 may be found as follows:

$$\theta_1 (X_B - X_A) = \theta_2 (X_I - X_B) \quad (3.3)$$

$$\theta_2 = \theta_1 \times \frac{(X_B - X_A)}{(X_I - X_B)} \quad (3.4)$$

$$\theta_3 = \theta_2 \times \frac{(X_D - X_C)}{(X_C - X_B)} \quad (3.5)$$

Where X_A, X_B, X_C, X_D and X_I are the x-coordinates of hinges A, B, C and D and the centre of rotation respectively

θ_3 may be calculated in a similar manner. It must be note that any rotation may be used as the controlling parameter.

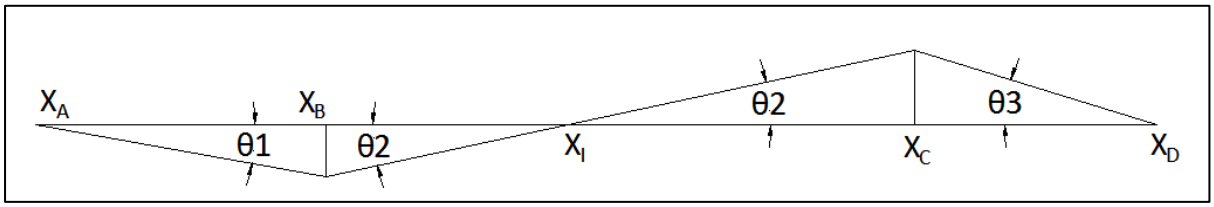

Figure 3.3: Relative rotations may be found using compatibility (representation of rotations adopted from De Luca et al., 2004)

4. Calculate the centroids and masses of the respective bars.
5. Calculate the virtual horizontal and vertical displacements at the centroids.

Table 3.1: Equations to calculate vertical and horizontal displacements at the bar centroids

	Vertical Displacements	Horizontal Displacements
Bar 1	$d_{v1} = \theta_1 \cdot (X_{\overline{AB}} - X_A)$	$d_{h1} = \theta_1 \cdot (Y_{\overline{AB}} - X_A)$
Bar 2	For $X_{\overline{BC}} > X_I$ $d_{v2} = -\theta_2 \cdot (X_{\overline{BC}} - X_I)$ For $X_{\overline{BC}} < X_I$	$d_{h2} = \theta_2 \cdot (Y_I - Y_{\overline{BC}})$

	Vertical Displacements	Horizontal Displacements
	$d_{v2} = \theta_2 \cdot (X_I - X_{\overline{BC}})$	
Bar 3	$d_{v3} = -\theta_3 \cdot (X_{\overline{CD}} - X_D)$	$d_{h3} = \theta_3 \cdot (Y_{\overline{CD}} - Y_D)$

Where $X_{\overline{AB}}$, $X_{\overline{BC}}$ and $X_{\overline{CD}}$ are the x-coordinates of the respective bars' centroids

$Y_{\overline{AB}}$,$Y_{\overline{BC}}$ and $Y_{\overline{CD}}$ are the y-coordinates of the respective bars' centroids.

(Sign convention: Displacements in the direction of force (+ve), in opposite direction (-ve)).

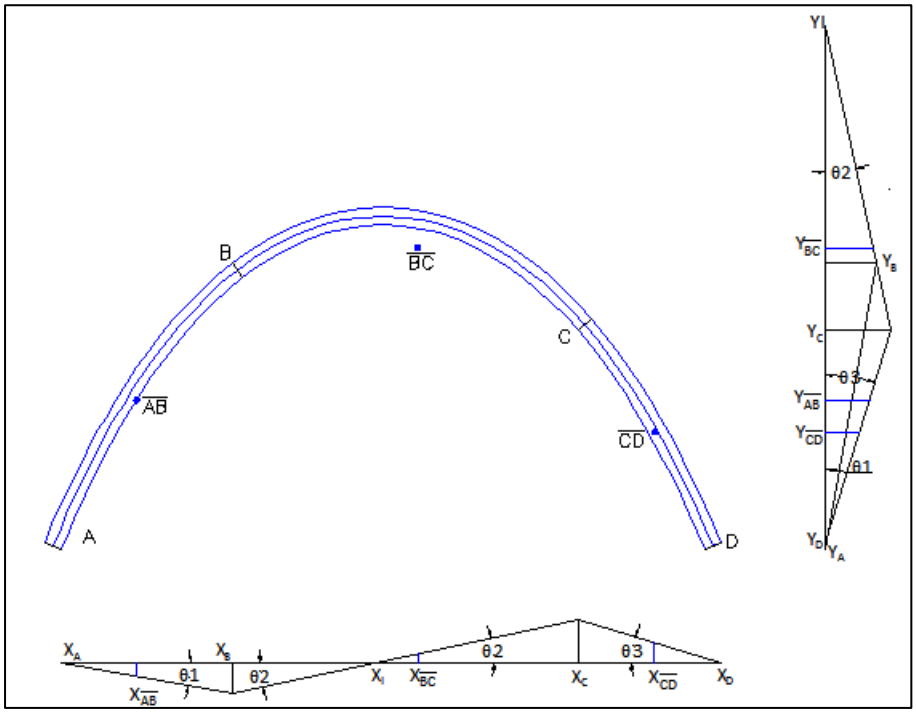

Figure 3.4: The centroids of each link are found and their displacements are calculated (representation of rotations adopted from De Luca et al., 2004)

6. Use the following formula to calculate λ (the horizontal component of gravitational acceleration that will cause collapse):

$$\lambda = \frac{-\sum_{i=1}^{n} W_i \cdot d_{vi}}{\sum_{i=1}^{n} W_i \cdot d_{hi}} \qquad (3.6)$$

7. Iterate through all possible hinge locations to find the minimum value of λ (λ_{min}).

In this study, the iterative computation was performed in Excel. The spreadsheet first finds the optimal catenary form for the inputted geometric parameters (using the Segmental Equilibrium Method developed by Bulovic). The spreadsheet then performs an iterative computation as described above. In order to confirm the validity of the method, the geometry of Oppenheim's example arch[4] (refer to Figure 3.5) was inputted. The value of λ_{min} calculated 0.3707 is 0.2% higher than Oppenheim's value of 0.370, which is accepted as a negligible margin of error. Refer to appendix B to see an example of the use of this model for catenary vaults and the validation model used for the circular arch in addition to the VBA code used.

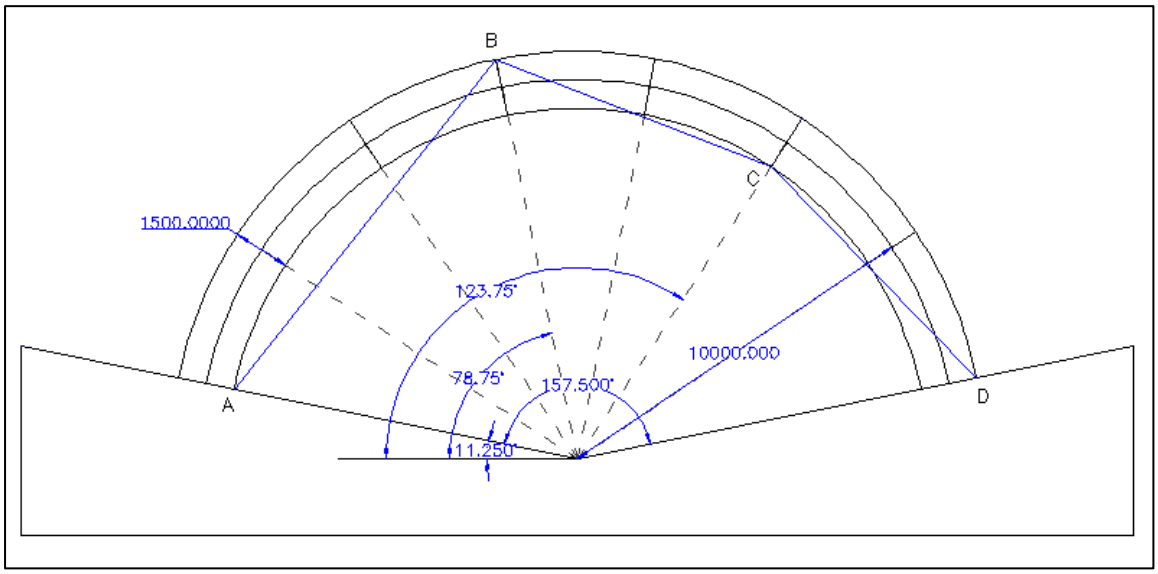

Figure 3.5: Oppenheim's example arch geometry (refer to Oppenheim, 1992)

[4] This geometry was used to provide a numerical example in Oppenheim,1992 p. 1009

3.2 Application to catenary arches

This method was used to find the value of λ_{min} for catenary arches. In order to assess the effect of changing geometric parameters on the stability of the arches and critical horizontal accelerations, two sensitivity analyses were performed. The analyses looked at the influence of the arch's thickness and height to width ratio respectively.

3.2.1 Influence of arch thickness

In the first analysis, the effect of changing the thickness of the arch was investigated. The arch span was set at 7.5m and the height to width ratio was set at to 1.0 (height=3.75m). Figure 3.6 indicates the change in the λ_{min} with the thickness to span ratio.

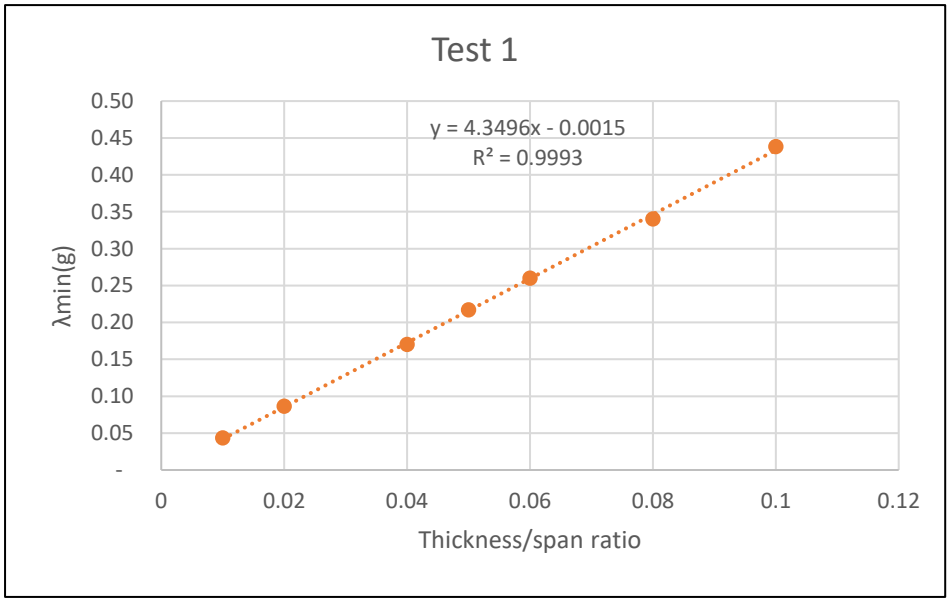

Figure 3.6: The change in λ_{min} vs thickness to span ratio

Figure 3.6 indicates that there is a linear relationship between thickness and λ_{min}. A mechanism forms when the thrust line exits the arch's thickness at four points. Therefore, with a larger arch thickness, the distance the thrust line will have to shift in order for a mechanism to be formed increases, translating to greater stability.

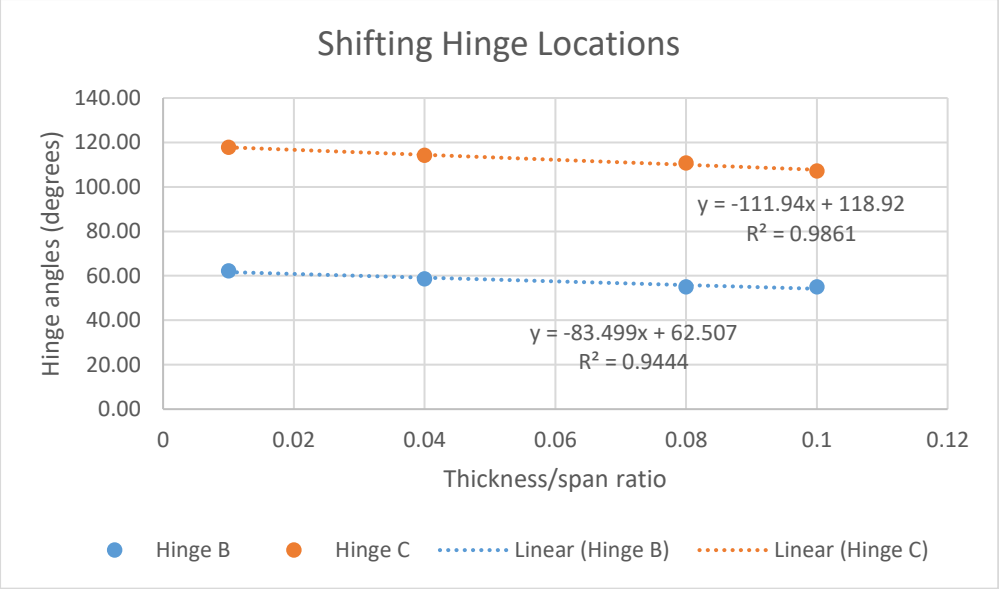

Figure 3.7: Shifting of hinge locations vs thickness to span ratio

The model indicates that the thickness of span affects the locations of hinges. Figure 3.7 indicates that as the thickness of the arch increases, so too does the position of the hinges in the arch (hinges B and C- refer to Figure 3.2). Angles are measured anti-clockwise from the centre of the arch (Figure 3.8). This relationship is approximately linear and indicates that the locations of the hinges shift in an anticlockwise direction as the thickness to span ratio is increased.

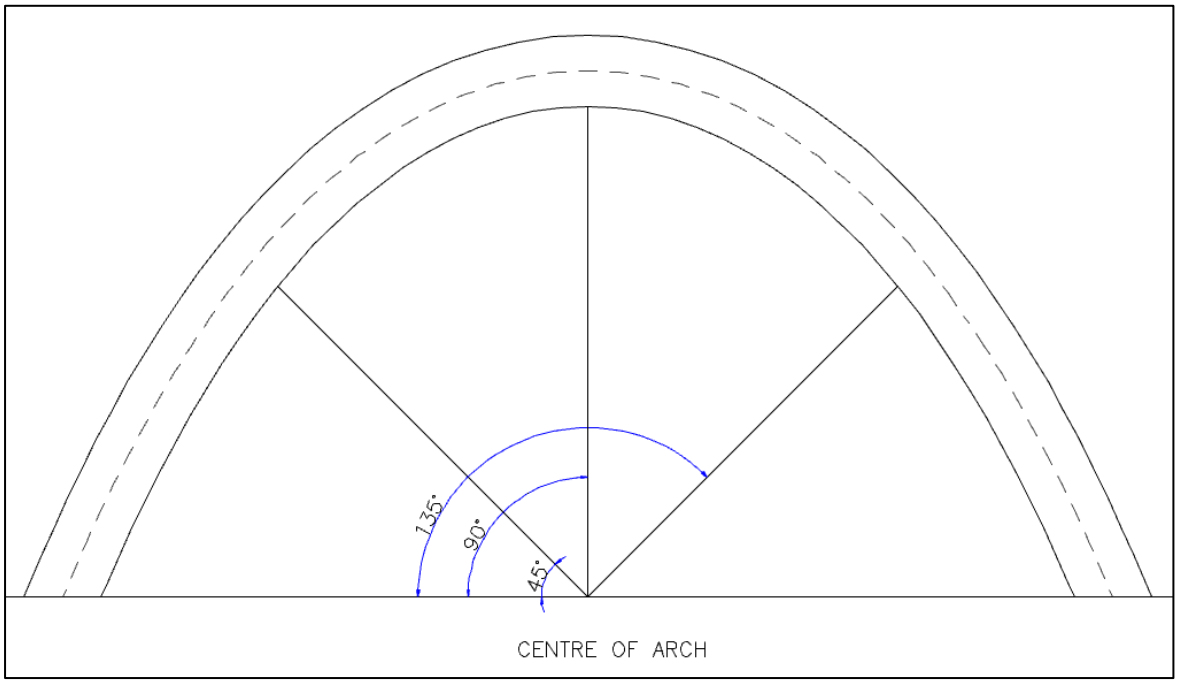

Figure 3.8: Measurement of angles in arch

It must be noted that for all computations, λ_{min} was lowest when the hinges A and D were located at the arch base (0 and 180 degrees respectively). Therefore their locations are not depicted in Figure 3.7.

3.2.2 Influence of height to width ratio

In the second analysis, the effect of changing the height to width ratio was investigated. The arch span was set at 7.5m and the arch thickness was set at to 0.1m. The change in the critical component of gravitational acceleration (λ_{min}) with varied height to width ratios is indicated on Figure 3.9.

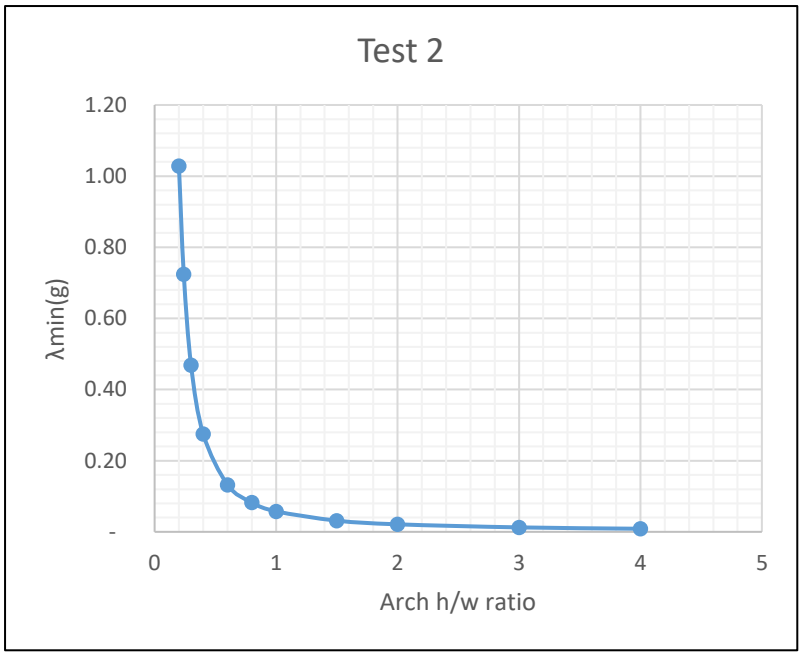

Figure 3.9: The change in λ_{min} vs height to width ratio

Figure 3.9 indicates that the value of λ_{min} is initially very sensitive to changes in the height to width ratio and decreases exponentially up to a value of approximately 1.6. After this point λ_{min} linearly decreases with increased height to width ratios and approaches zero. This indicates that lower h/w ratio arches are preferable from a seismic perspective (in terms of earthquake resistance). Despite this, as the h/w ratio is increased, the greater the magnitude of horizontal thrust forces at the arch's base. These forces, which cause instability, need to be resisted by either using tension ties or buttressing (Seedat and Surat, 2012). Additionally, the lower the h/w ratio, the lower the overhead space provided. Therefore designers need to balance out these considerations in order to develop an economical and resilient design.

4 EXPERIMENTAL SETUP

4.1 Shaking table

The shake table consists of a 0.82m^2 shake table and a hydraulic ram that is powered by hydraulic actuators.

For the first stage of tests (static stroke, increasing frequency for unreinforced arches- see section 5.2), the shake table movement was controlled by a MTS 458.10 micro console (see Figure 4.1). The console can induce both sin wave and impulse acceleration time histories. The acceleration of the shaking table is controlled by two parameters, frequency and span. The frequency output is controlled by a 458.90 function generator on the micro console. The frequency can be set in the following ranges:

Table 4.1: Shaking table frequency ranges

Range Number	Frequency Range (Hz)
1	0.01-0.11
2	0.1-1.1
3	1-11
4	10-110
5	100-1100



Figure 4.1: Shaking table controller

Span was adjusted using the span pot using a 458.14 AC Controller. This defines the distance through which the shaking table's hydraulic actuator moves through during one cycle of motion. Therefore, by adjusting the span and frequency settings, induced acceleration may be modulated.



Figure 4.2: Shaking table and hydraulic actuator

The span was initially set to 3mm. A dial gauge was used in order to ensure that the required span was achieved.

For the second and third stage of testing, the system was upgraded and (static frequency, increasing stroke for unreinforced and reinforced arches respectively- see sections 5.3 and 5.4) was controlled using a FlexTest 40 digital controller. The interface that fed data into the controller is called Multipurpose Elite™. Figure 4.3 shows a screenshot of the program interface.

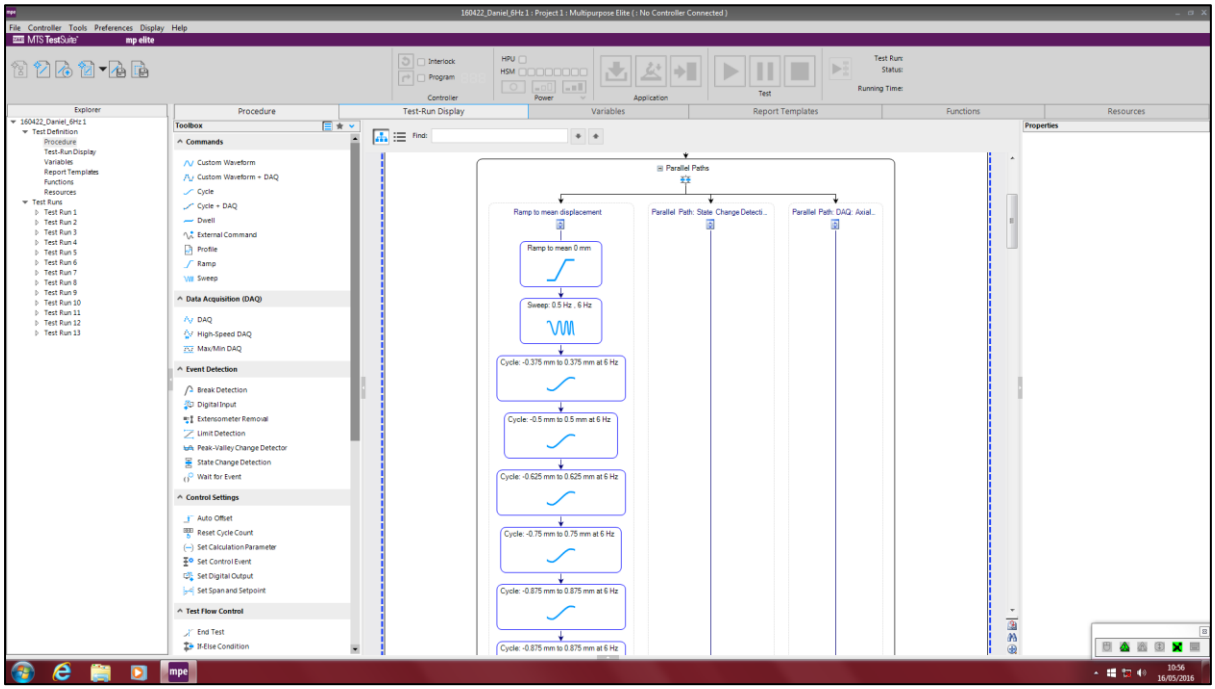

Figure 4.3: Multipurpose Elite™ user interface

Using this program, the shake table actuator's movement was controlled via a sequence of drag-and-drop commands. The control mode used for the latter stages of testing was displacement control, which allows the user to control the displacement of the hydraulic actuator. An LVDT which measures the stroke of the actuator was used to calibrate and control the actuator's movement and provide accurate displacement output readings.

4.2 Data Logger and Accelerometers

The Nova 5000 data logger was used for the testing of the arches. The logger has four sensor ports. Fourier DT138 accelerometers were used for all the arch tests. The accelerometers can capture accelerations between -5 and +5g and they

measure linear acceleration. Multilab is a software package on the Nova 5000 that processes information coming from connected sensors. This application was used to capture and log the time-acceleration histories for the respective tests.

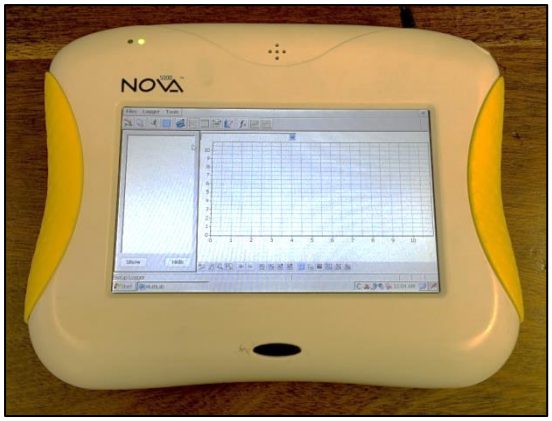

Figure 4.4: Nova 5000 data logger



Figure 4.5: Accelerometers connected to the Nova 5000 data logger

The accelerometers were calibrated in Multilab to collect 50 data points per second and to collect data continuously. The unit system was set to SI and acceleration values were measured to the 5th decimal place to ensure accuracy. It must be noted that as the maximum frequency to be subjected to the arches was 15 Hz, 50 data points per second were assumed to be sufficient (lowest requirement is that the

frequency of data capturing be at least 3 times that of the induced frequency, i.e. 45 Hz) to accurately capture the development of acceleration with time. Problems were encountered at higher data capturing frequencies as the memory capacity of the data logger was limited and the additional sensitivity resulted in excessive noise in the data.

4.3 Construction Methodology

4.3.1 Testing rig for masonry arch

The rig used for the testing of the arches was fabricated from steel square hollow sections (25 x 25 x 1.6 mm). In order to support the weight of the arch, 1.2mm steel plates were welded to the underside of the rig. Four removable steel plates were screwed on the underside of the rig. This supported the weight of the arch formwork and they were removed when removing the formwork. Removable transverse bearer bars were also installed in order to provide lateral support to the arch during seismic loading, preventing movement at the base of the structure. It was found that when screwing the bars in, some pressure was exerted on the base of the arch, which damaged the arches. Therefore it was decided to rather weld the bearer bars to the arches to prevent this. The gaps between the arch and the bars was initially filled with scrap wood and subsequently were filled with mortar, which was found to be more effective.

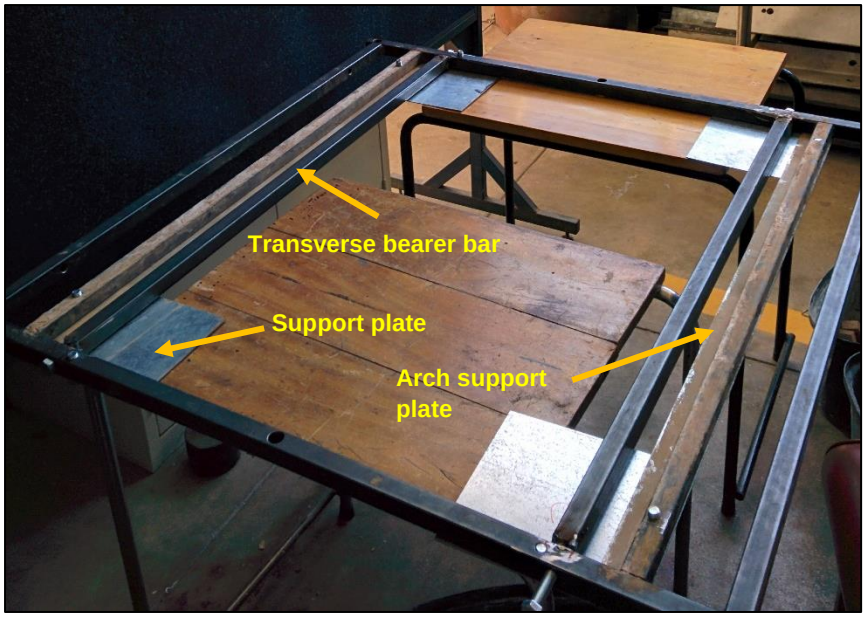

Figure 4.6: Arch rig

4.3.2 Arch formwork

Three catenary formwork units were used, namely, 0.8, 1.0 and 1.2 height to width ratio units. Two of these are indicated in Figure 4.7. They comprise of metal sheeting bent to the respective catenary profile, wooden rods that are screwed into the sheeting to maintain the profile and stabilise the sheeting. The rods are screwed into Masonite boards on either end of the arch. The profiles for the respective formwork units were generated using the spreadsheet developed by Bulovic (2014).



Figure 4.7: Formwork used for the construction of the arches: (a) top of formwork (b) underside of formwork

4.3.3 Construction Materials

Earth bricks and mortar

Cement-stabilised earth masonry was used for the construction of the arches. The bricks used to construct the arches were cut from earth tiles made in a Hydraform® hand press.



Figure 4.8: Cement stabilised earth tiles



Figure 4.9: A brick cut from an earth tile used in the masonry arches

The properties of the bricks are as follows:

Table 4.2: Properties of earth bricks

Density (kg/m^3)	1950
Young's Modulus (MPa)	3500
Poisson's Ratio (estimated)	0.2

The dimensions of the bricks used are indicated in Figure 4.10. Three different bricks sizes were used in order for the edges of the arch to be flush with the extents of the formwork.

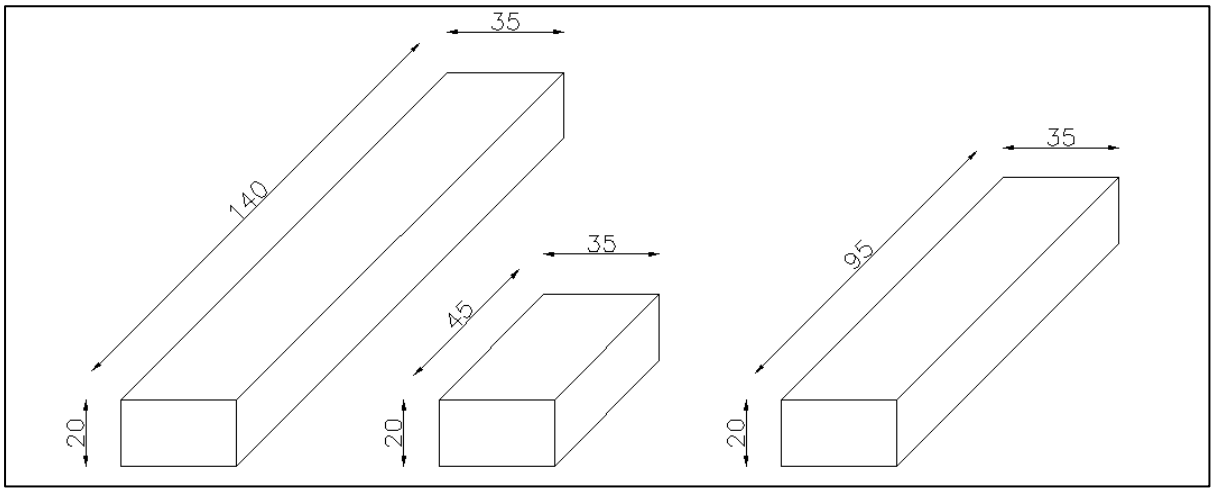

Figure 4.10: Dimensions of earth bricks used

The earth bricks that were used for the construction of the arch are hygroscopic, i.e. readily taking up moisture. In order to prevent the rapid drawing in of water from the mortar which would result in the formation of volume shrinkage cracks, the bricks were wet before being used.

A class II mortar was used in the construction of the arches. The sand to cement ratios are defined according to SANS 2001-CM1:2007. No stabilising lime was used.

Table 4.3: Mortar mix ratios

Sand	**Cement**	**Water**
4 kg	1 kg	+-1.7 kg

The code does not specify the required water content; therefore, trial and error was employed to find the water content required to achieve a suitable consistency. The mix was fairly stiff yet workable. As construction took a few hours to complete, water had to be added to the mix as time progressed in order to maintain workability.

Compression tests were conducted on both the materials using a Tinius Olsen hydraulic press. A total of 5 cement stabilised masonry and 3 mortar samples were tested.

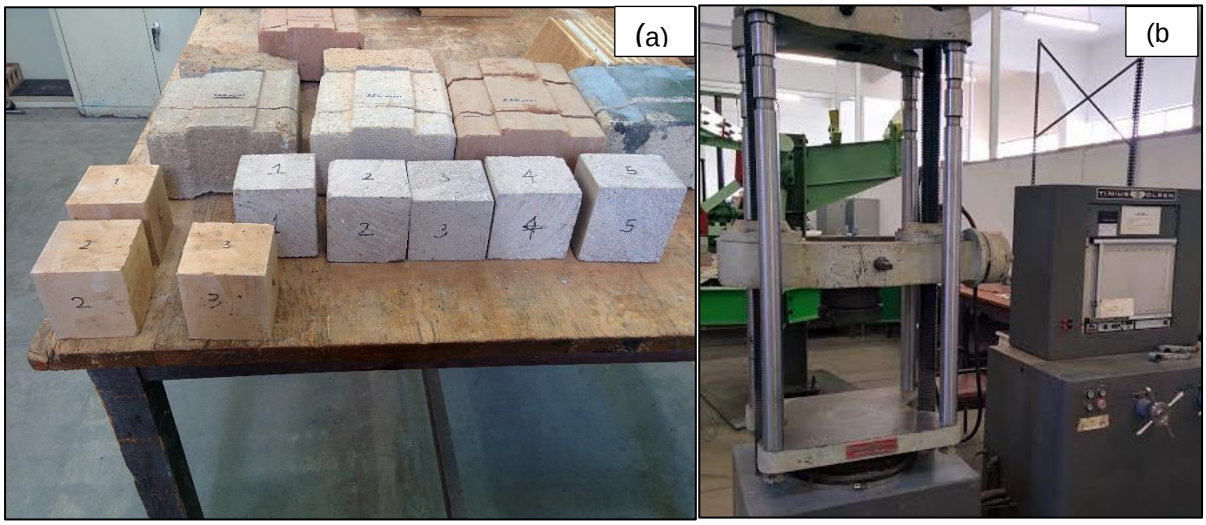

Figure 4.11: (a) Stabilised earth masonry and mortar cube samples (b) Tinius Olsen hydraulic press

The earth bricks are made by Hydraform® who made a number of cement-stabilised earth products. To find the compressive strength of the earth tiles used, initial tests involved testing individual brick units. Upon finding the results to be unsatisfactorily high, with an average compressive strength of 26.1 MPa (assumed to be due to scaling), Hydraform® interlocking blocks, which are manufactured using the same material and cement quantities, were cut into blocks for testing. One of the 5 samples displayed displaying a substantially lower failure load than the other cubes (105 kN) and did not remain intact after failure. It was therefore removed from the results. The tests indicate that the average compressive strength of the cement stabilised masonry is 14.78 MPa. The results are indicated in Table 4.4:

Table 4.4: Results of cement-stabilised masonry compression tests

Sample #	Cross-sectional area (mm^2)	Failure Load (kN)	Failure Strength (MPa)
1	10549	162.6	15.41
2	11990	165	13.76
3	11286	148	13.11
4	10438	175.5	16.81
AVERAGE			**14.78**

Three cube tests were performed to find the compressive strength of the mortar. The arches were left to cure for 1 week and under plastic sheeting (see section 4.3.4) prior to testing. Therefore, the cubes were tested 7 days after casting, and were also cured under plastic sheeting. The average compressive strength of the material was found to be 7.16 MPa. Table 4.4 indicates the results of the tests:

Table 4.5: Results of mortar compression test

Sample #	Cross-sectional area (mm^2)	Failure Load (kN)	Failure Strength (MPa)
1	9772	73.6	7.53
2	9707	68.3	7.04
3	9900	68.3	6.90
AVERAGE			**7.16**

For both the stabilised earth masonry and mortar tests, the hourglass failure pattern was observed, characteristic of cube compression tests (Figure 4.12).

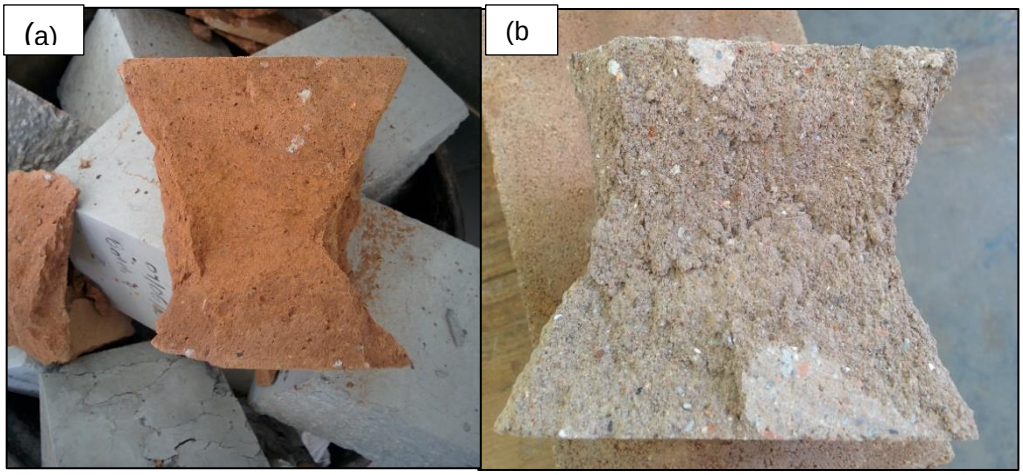

Figure 4.12: Hourglass failure pattern observed for (a) mortar and (b) cement stabilised earth masonry samples

Basalt fibre reinforcement

Some of the arches were tested with basalt fibre reinforcement. Therefore, the properties of basalt were determined. The reinforcement used for the arches is a 25x25mm basalt fibre geogrid. The fibres contained within the grid are 13 microns in diameter and are held together using a PVC binder. Each rib consists of 2, 2000 tex sub-ribs[5], consisting of 6000 fibres each, providing a total cross sectional area of 1.59mm^2 . The grid ribs are stitched together to form the grid.

[5] Tex is a measure of linear density. 2000 tex =2000 g/1000m

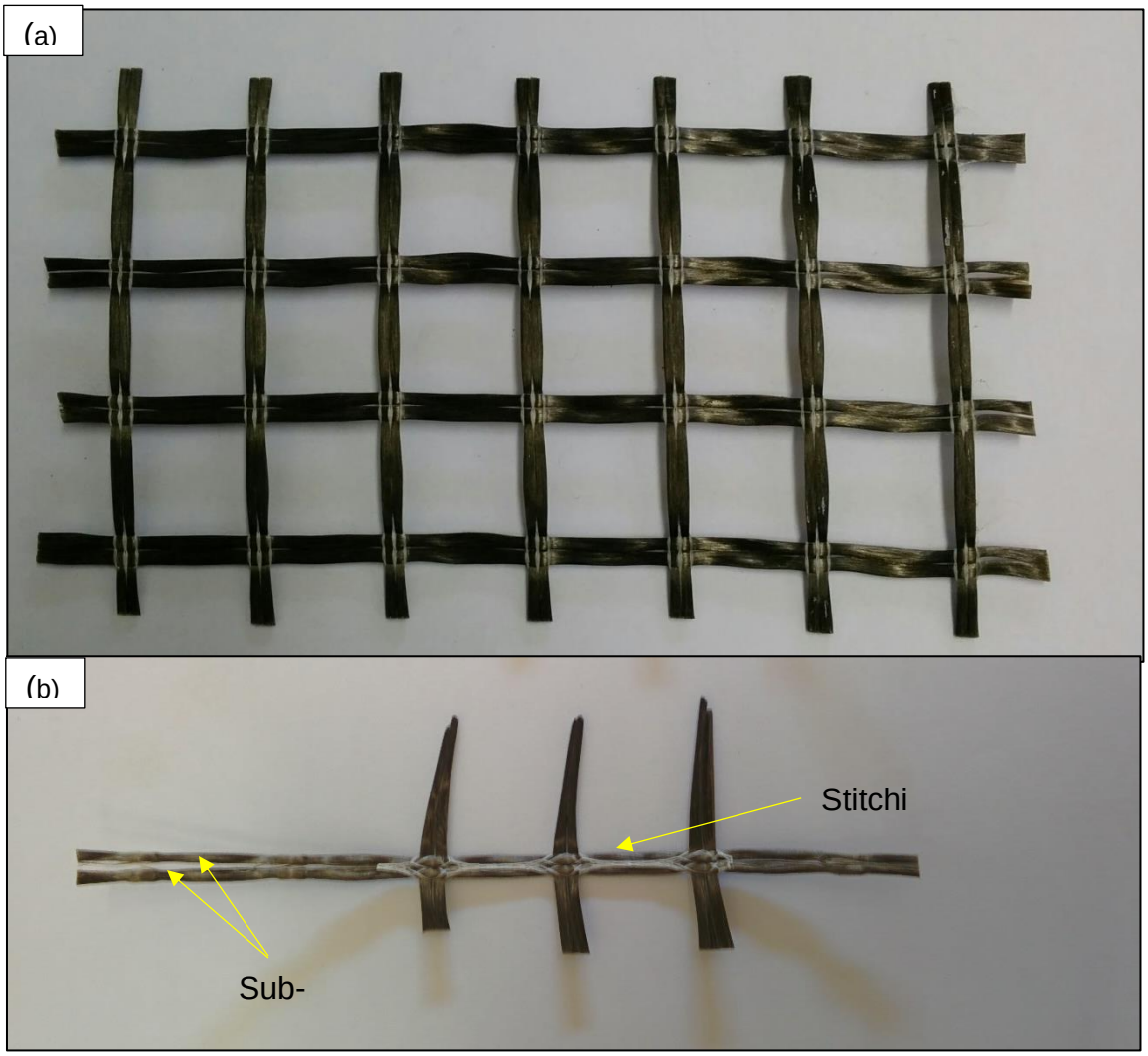

Figure 4.13: (a) Basalt geogrid (b) Geogrid rib is stitched together and consists of two sub-ribs

Tension tests were performed on the material to find the material's mechanical properties. Samples were cut from the geogrid. In order to clamp the samples, the end transverse ribs were removed (Figure 4.13).

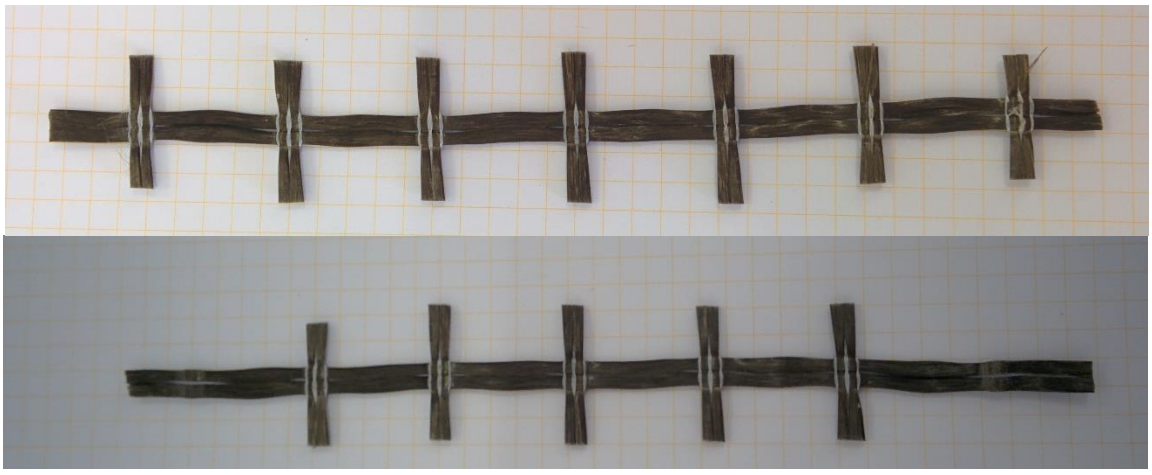

Figure 4.14: Samples were cut from the geogrid and the end transverse ribs were removed

In order to perform these tests, a tensometer in conjunction with an extensometer was used. The material was clamped into the tensometer. In order to assess strain, the extensometer was clamped to the material. However, there was difficulty attaching the clamps to the material, therefore, two pieces of sandpaper were placed on either side of the ribs at the clamping points, as shown in Figure 4.15:



Figure 4.15: Sandpaper attached on either side of the sample at the clamping points

During testing, the method of failure was problematic in that only one of the sub-ribs failed before release of tensile force (marked by the load gauge dropping back to zero). This cast doubt as to whether the full cross sectional area was being engaged in resisting the tensile force. It was feared that this would skew the data. It is postulated that this is a result of the releasing of the sample from the clamps caused by the clamps recoiling, opening up and releasing the sample when one of the sub-ribs failed.

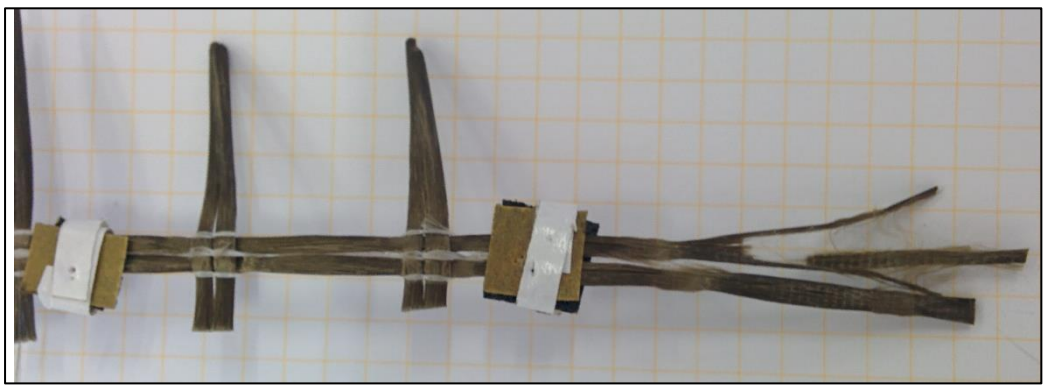

Figure 4.16: Failure only encountered in one of the sub-ribs

In order to rectify this issue, tension tests were performed on the sub-ribs. A total of 8 tests were performed on the sub-ribs. For all tests, failure occurred at the clamps. As expected from the literature, stating that fibre reinforcement is not ductile, failure was sudden with no clear yielding point. Therefore, the maximum value of tensile force for each test represents the ultimate tensile capacity of the sub-ribs. Figures

4.17-4.20 provide an indication of results of the test. Between loads of 0 and 0.2 kN, for each sample, the force v extension line has a different gradient to the rest of the graph. It is postulated that in this range the fibres in the sub-ribs were not fully engaged, requiring force to facilitate their alignment.

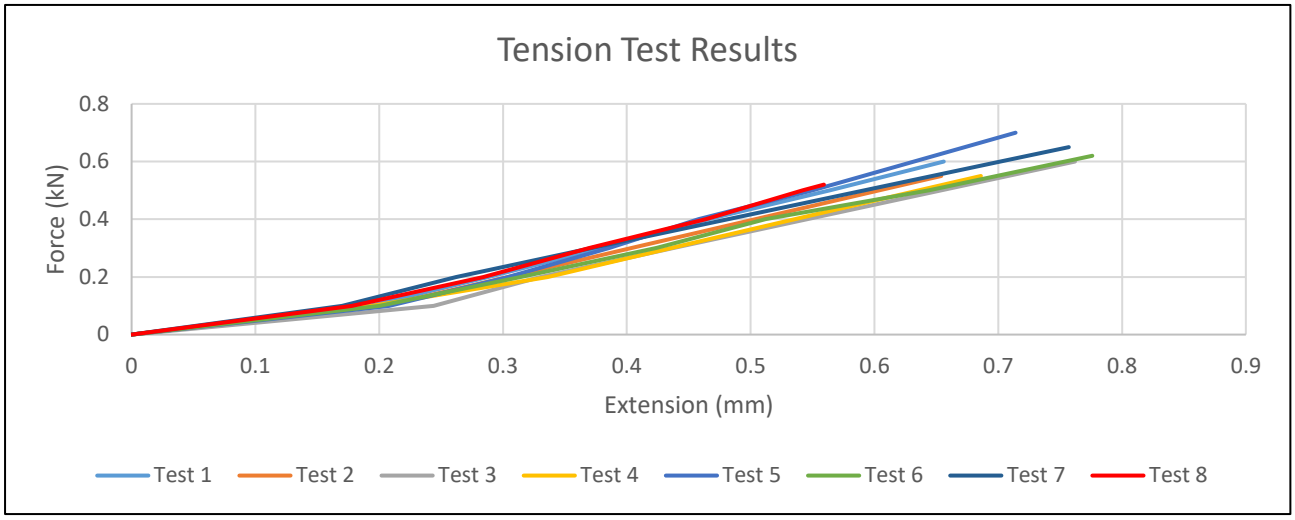

Figure 4.17: Force v displacement graph for basalt fibre geogrid tests



Figure 4.18: Averaged force v extension graph for basalt fibre geogrid tests

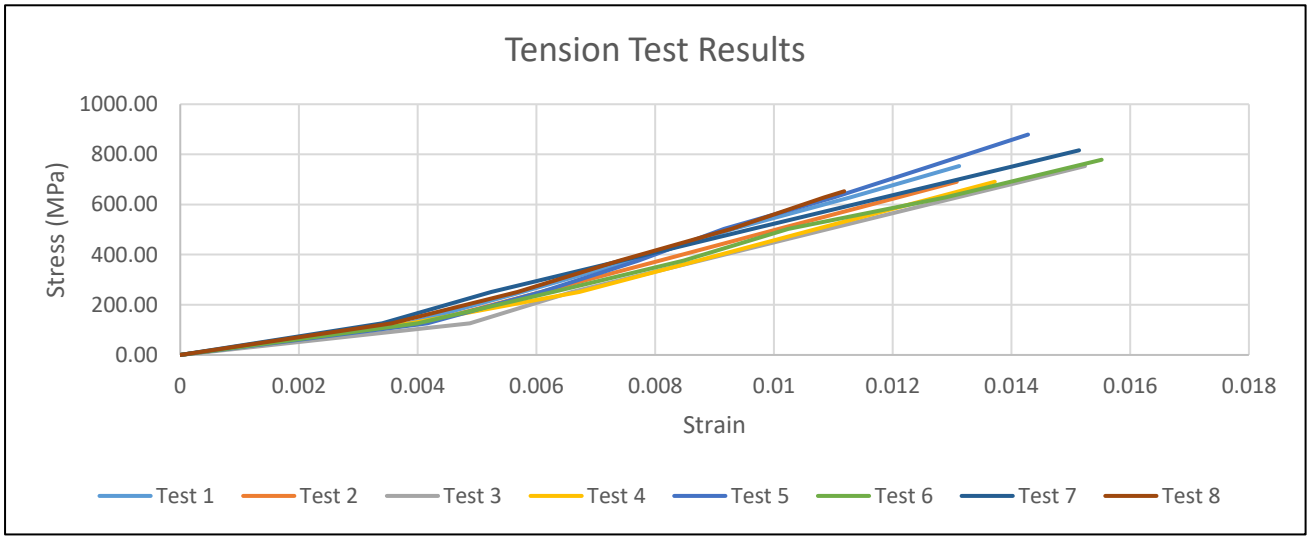

Figure 4.19: Stress v strain graph for basalt fibre geogrid tests

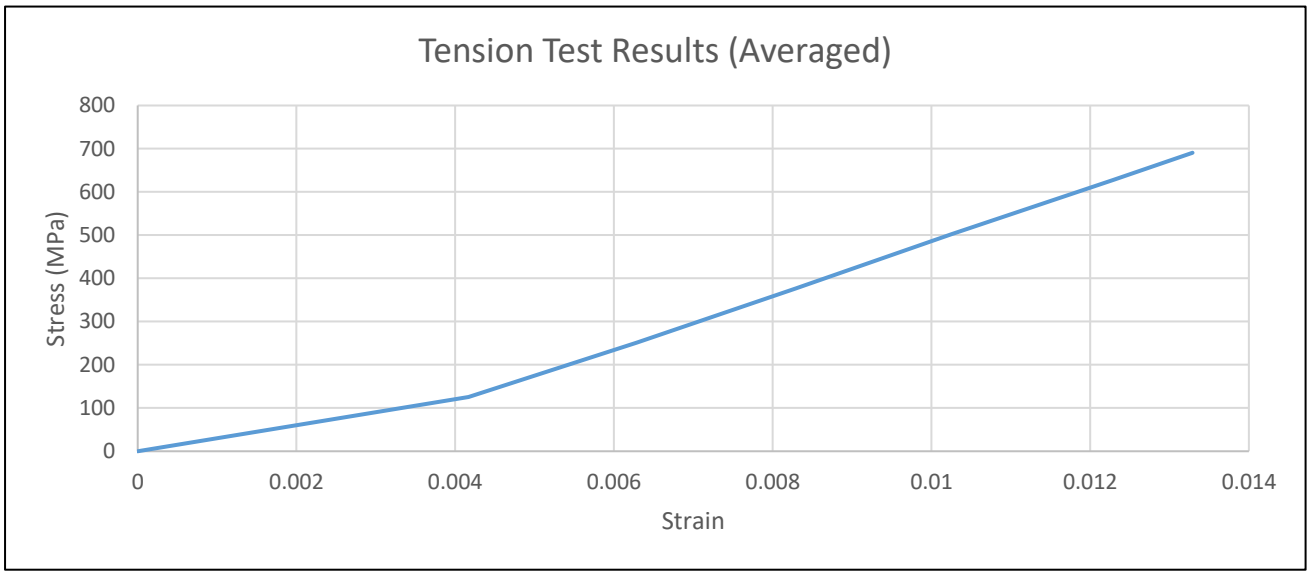

Figure 4.20: Averaged stress v strain graph for basalt fibre geogrid tests

The strains were calculated by dividing the extension readings by 50mm, the gauge length of the extensometer. The stresses were calculated by dividing the force readings by the cross sectional area of 1 sub-rib, 0.796 m^2 .The Young's modulus of the material was found from the gradient of the stress strain curves. The gradient was calculated using loads above 0.2kN in order to prevent skewing the data. The average ultimate tensile stress of the material is 752 MPa. The average Young's Modulus is 68 GPa. Table 4.5 provides a summary of the test results:

Table 4.6: Test results for basalt fibre testing

Test No	Failure force (kN)	Failure Stress (MPa)	Young's Modulus (GPa)
1	0.6	753.40	73.00
2	0.55	690.61	62.78
3	0.6	753.40	58.13
4	0.55	690.61	62.78
5	0.7	878.96	87.20
6	0.62	778.51	71.34
7	0.65	816.18	57.08
8	0.52	652.94	73.00
AVERAGE		**751.83**	**68.17**

4.3.4 Construction method for masonry arches

The following procedure was used to construct the masonry arches:

1. Removable formwork support plates are screwed into the testing rig.
2. The formwork is covered with cling-film in order to prevent bonding between the arch and formwork.
3. The formwork is placed in the rig
4. The arch is constructed over the formwork.



Figure 4.21: Arch built over formwork

5. The arch is wet and covered by plastic sheeting.
6. Approximately three hours after completing the arch construction the formwork is removed.



Figure 4.22: Formwork removed from arch

The arch is wet one more time and is covered again by plastic sheeting.

7. The arch is left to cure for 7 days in order to attain the target strength for testing.
8. Transverse bearer bars are installed at the base of the arch. Any gaps between the arch and the bars are filed in with mortar to arrest movement.



Figure 4.23: Arch cured and transverse bearer bars installed

Improvements to construction methodology (lessons learnt)

When the first arch was constructed, some cracking occurred in the arch. The arch was exposed to sunlight on one side during construction, which resulted in differential shrinkage. Initially, the formwork was left in for 24 hours before removal. It is hypothesised that as the arch lost moisture, the formwork prevented the movement of the arch as it underwent shrinkage, causing cracking. In solving this problem, the arch was constructed in a shaded area and the time for removal of formwork was changed from 24 hours to 3 hours. In three hours, it was found, the structure had sufficient strength to resist self-weight loading.

Initially grease was used to allow for the debonding of the arch from the formwork. Two arches were constructed using this technique. When removing the formwork, a suction was experienced at the arch-formwork interface. Although debonding was achieved with the structure remaining intact, this required much time to gently

remove the formwork. Subsequent to this, a test arch was built using cling-wrap to create debonding. This was successful and was used for the construction of all subsequent arches.

The transverse bearer bars were initially screwed into the arch rig for easy installation and removal. Yet due to slight eccentricity of the bar, a lateral load was induced at the base during installation, resulting in lateral cracking along the length of the bottom brick layers. In order to fix this issue, the bars were welded onto the rig. This is more labour intensive, but ensured that cracking did not occur and that the bars were flush with the inner arch face. Mortar was added to fill the voids between the arch and the bars in order to prevent lateral translation of the arch during testing.

The initial construction sequence involved building up one side of the arch at a time and finally the two sides were linked at the apex. During the curing process, visible cracking was found at the apex. Initially it was assumed that this was due to lack of compressive stresses at the apex to prevent cracking. On further consideration, it was postulated that these cracks were formed by differential shrinkage, where one side of the arch had developed strength and had already undergone shrinkage and the other still developing strength and consolidating, causing differential movement and therefore cracking. Accordingly, the construction methodology was then changed such that brick layers on both sides of the arch where built at the same time. This rectified the issue.

5 EXPERIMENTAL INVESTIGATION

5.1 Calibration of testing equipment and instruments

The first test was performed to ascertain that that no secondary effects were encountered due to the elastic nature of the double sided tape used to attach the accelerometers to the arches, a test was conducted. The three accelerometers were placed on the shaking table and were fixed in placed using 3 different tape thicknesses, namely 3.2, 1.5 and 0.9mm. The three accelerometer readings relate to these three tapes thicknesses. The shaking table was then set to vibrate at 10-14 Hz, which was assumed to produce an adequate enough acceleration to test the response of the three tapes. Under all these accelerations, a close correlation between the respective accelerations was found (refer to figure 5.1).

Isolating a small range of the test performed, it can be seen that the difference between the accelerometer readings are closely matched (removing outliers, the average difference was 6%) and therefore the change in thickness is not of concern. If larger thicknesses were used, this may have been problematic.

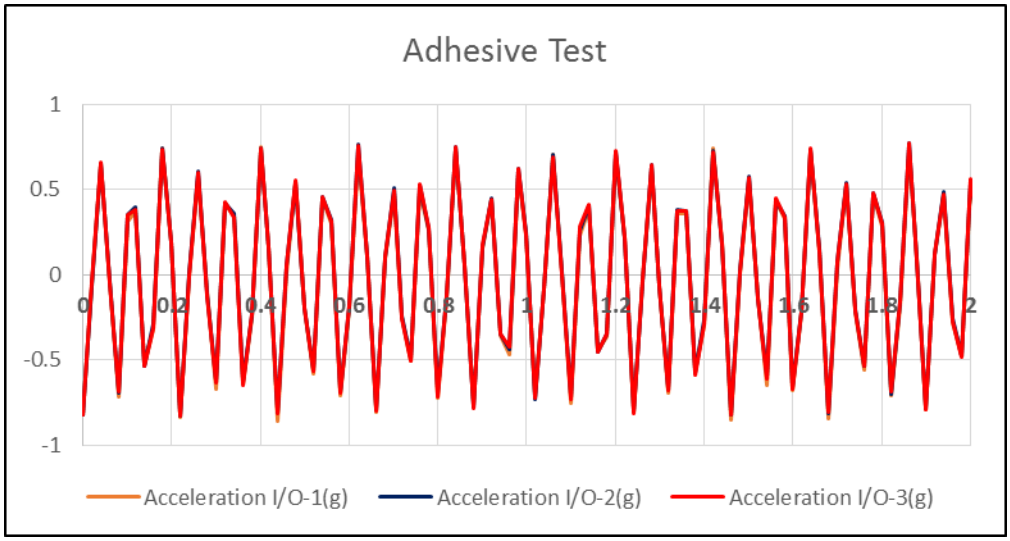

Figure 5.1: Results are closely matched for different adhesive thicknesses

A second set of tests were conducted to find the 'natural frequency' of the 0.8 h/w ratio arch. This was done by attaching accelerometers to the top of the arch and exciting it with a tap from a rubber mallet. This was only done on the 0.8 arch in

order to assess the viability of the method. Two different types of accelerometers were used in order to assess the natural frequency. This was done in order to assess if the two would provide similar results and to justify the sole use of the larger accelerometer. The smaller accelerometer can measure data to a higher degree of accuracy (can collect more data points per second). Yet, it was feared that the smaller accelerometer would be damaged during testing when the arches collapsed. Therefore, this test was performed to see if the large accelerometer could provide sufficiently accurate data readings for the purpose of this study.



Figure 5.2: Apparatus used for natural frequency tests

A total of 5 tests were performed to get the natural frequency of the arch. A power spectral density (PSD) plot was created for each test. The PSD function takes acceleration time histories and can be used to extract the natural frequency of a structure subjected to excitation (refer to appendix C for the Matlab code used to create PSD plots). The different peaks Figure 5.3 represent the modal natural frequencies of the respective arches. The first pronounced peak (i.e. the peak that has the highest value on the y-axis) represents the first natural frequency at which violent vibration is to be expected in the arch. In Figure 5.3, the first pronounced peak is at 15.27 Hz, representing the first natural frequency of the arch followed by the second natural frequency of the arch at approximately 53 Hz and so forth. As

the arch is constructed using brittle material, it was expected that if the arch was subjected to this frequency that either the structure would either collapse or vibrate violently until another hinge was created. It was postulated that when the next hinge formed that the stiffness of the entire structure would change substantially, therefore changing its natural frequency. Therefore, this first natural frequency is only valid for the arch with no hinges.

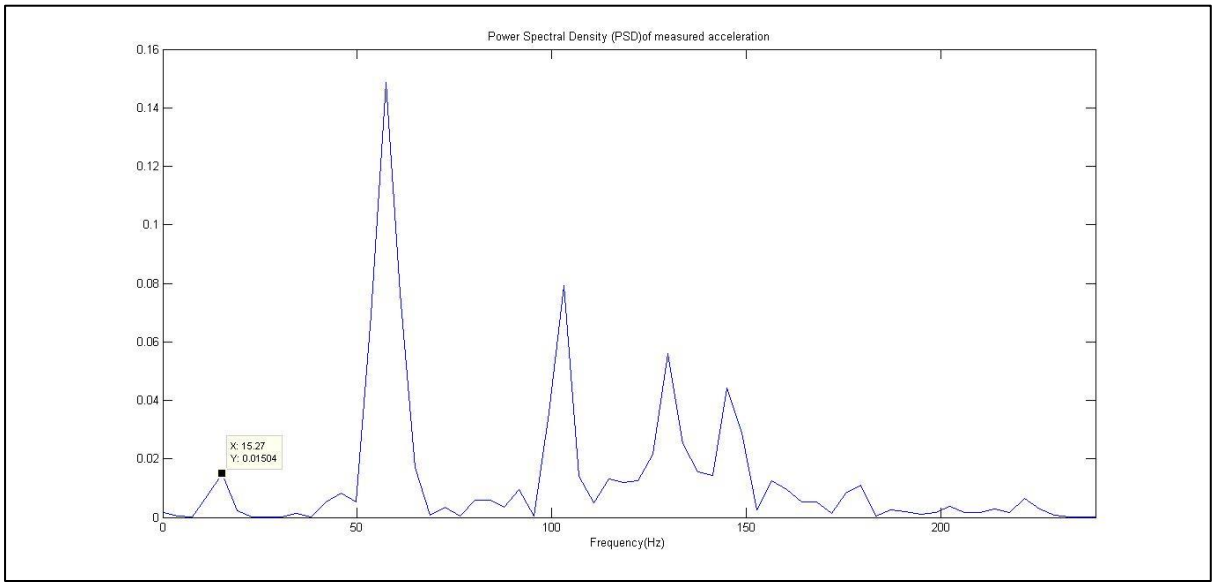

Figure 5.3: PSD plot for the first natural frequency test

The results of the test are as follows:

Table 5.1: Accelerometer check

Test No	**First Natural Frequency (Hz)**	**Accelerometer Used**
1	13.5	Small
2	15.27	Small
3	14.85	Large
4	14.18	Large
5	14.83	Large
AVG	**14.5**	

The results indicate that the first natural frequency readings for the two accelerometers correlate closely. The average first natural frequency of 14.5 Hz was considered in the harmonic tests.

5.2 Harmonic tests (unreinforced)

For the first set of tests, unreinforced arches were subjected to harmonic loading to check how the arches' behaviour changed when subjected to a range of frequencies and to investigate the effect of the formation of hinges on the seismic response of the arch. In order to find the effect of height to width (h/w) ratio on dynamic performance, three arch profiles with height to width ratios of 0.8, 1.0 and 1.2 respectively were tested. As the arches were unreinforced, it was expected that failure would be due to instability.

The arch was placed on the shaking table and was secured onto it using screws. Four accelerometers were placed on the arch. One accelerometer was placed on the shaking table to get baseline readings. One was placed on the top of the arch to get horizontal acceleration readings at the top of the structure. One accelerometer was placed at a third of the arch span to measure horizontal acceleration and another was placed on the opposite end, facing downwards, in order to capture the vertical component of acceleration during testing.

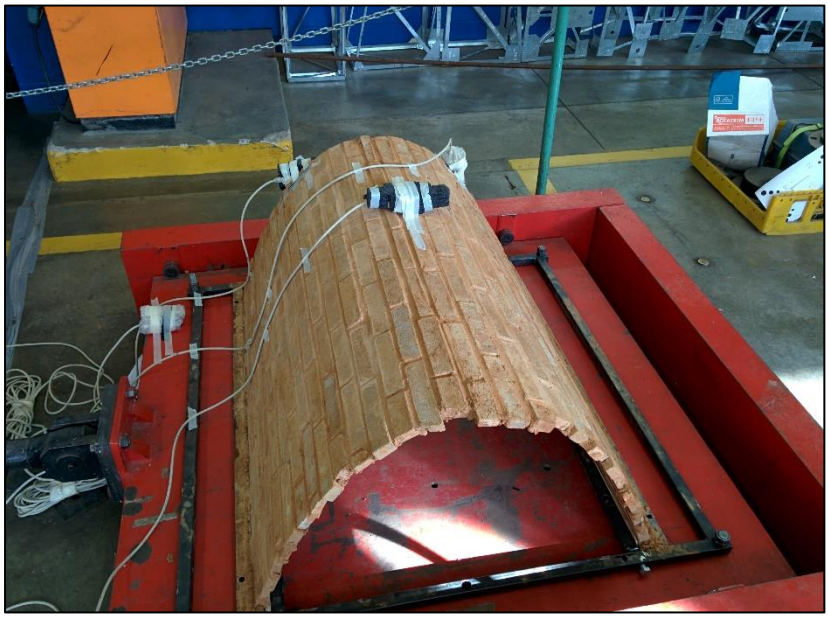

Figure 5.4: Arch placed on the rig and is secured. Accelerometers placed at strategic positions

For the tests, the frequency was first increased from 1 Hz to 11 Hz. The frequency was adjusted every 10 seconds by 0.1 Hz. This allowed the tester to observe the arch's response at specific frequencies and ensured that mode 1 failure was created (failure after multiple impacts). The actuator's stroke remained the same (3mm) throughout the duration of the tests. Once the frequency reached 11 Hz, the frequency was lowered at the same rate back down to 1 Hz and the behaviour of the arch was observed as the frequency was decreased. If collapse was not encountered in this frequency bracket, the bracket was increased to the 10-110 Hz range on the controller and the frequency was increased linearly as done in the lower frequency bracket until collapse occurred. It must be noted that this range was only considered for the lower frequencies in the range. The intention of this was to see if violent vibrations and resonance would occur at the first natural frequency of the arches, as indicated in Section 5.1.

The expected behaviour of the arch was that before the formation of a mechanism (caused by the formation of 4 hinges in the arch) there would be certain frequencies that correlated with the natural frequencies of the arch. When this occurred, it was expected that excessive vibration/ rotation between the hinges would take place such that either collapse or the formation of the next hinge would occur. As the arches' overall stiffness change substantially with each new hinge formation, it was expected that their response would change substantially with the formation of new hinges. Once a mechanism was created, it was expected that the rocking arch model would apply, where the 'rocking resonance' would play a key role in the failure of the arches. All the time-acceleration histories from these set of tests can be found in appendix A.

5.2.1 Test results and discussion

During the first 0.8 h/w ratio test, the shaking table suddenly stopped operating at a frequency of 4 Hz. This jolted the arch, resulting in the formation of 2 hinges in the arch. The following day, the test was resumed and failure occurred at 4.3 Hz, a result that was unexpected. This indicated that the prior formation of hinges critically affects the behaviour of the arch.

In the first 1.2 h/w ratio test, the 2 hinges occurred simultaneously in the arch at 5.2 Hz. Prior to this, the arch moved as a single body. The frequency was then increased to 11 Hz. As the frequency was increased, despite the formation of hinges, the rotation between the hinges was very limited. This indicates the stabilising effect at higher frequencies, where more impacts occur. Impacts reduce the energy balance of the structural system. As the frequency was lowered, the third hinge formed and at approximately 2 Hz, the rotation between the hinges increased until 1 Hz where the arch moved as a single body. The frequency range was subsequently changed to the 11-110 Hz band. This was done to assess if violent vibration was to be encountered at the first natural frequency of the arch (at 14.5 Hz). When the shaking table was started at this frequency, the arch could not withstand the sudden jolt and failure occurred upon starting the shake table. The second 0.8 h/w ratio arch was then tested. During the test at 7 Hz, the first hinge formed. At 7.5 Hz, hinges formed at the apex and the left-hand base of the arch. It is suspected that this hinge formation was a result of pre-existing cracks in the structure at the base and the apex. It is suspected that the transverse bearer bars pushed the structure outwards when inserted into the rig, resulting in cracking at the apex and base. As the frequency was lowered, the movement of the plywood on the right hand support was audible, indicating the lack of a 'fixed connection.' The final hinge that should have formed was at the base on the right hand side of the structure. It is postulated that the 'pinned connection' caused by the lack of fixity prevented this hinge from forming at this location. The frequency was lowered to 1 Hz and then the shaking table was stopped. The test was resumed and the structure failed at 2.6 Hz.

A similar result was observed during the 1.0 h/w ratio. Prior to testing, cracks had formed in a brick layer on one side of the arch. Although the crack did not extend through the entire layer, it formed a point of weakness. As a result at 6.1 Hz, in rapid succession, all four hinges formed causing collapse. The first hinge to form was located at the position of the crack.

The final 0.8 h/w ratio harmonic test was the most successful of the harmonic tests. When the frequency was increased linearly, the first hinge formed at 5.6 Hz, the second at 6.0 Hz and the third at 8.6 Hz. The frequency band peak (11 Hz) was reached and the frequency was thereafter linearly decreased. In this stage, the fourth hinge formed at 4.1Hz. During testing more pronounced rotation at the hinges

was observed at 5.6 Hz after the formation of one hinge, 2.9 Hz after the formation of the second and third hinge and 1.8 Hz with the formation of the fourth hinge. It was observed that when the fourth hinge formed, when the frequency was lowered from values higher than 1.8 Hz, that pronounced rotation between the hinges took place. When the frequency was increased from values lower than 1.8 Hz, pronounced rotation was not observed. When the fourth hinge occurred, failure did not occur immediately despite the structure being a mechanism. This aligns with the rocking arch theory, such that the energy input for the arch needs to be such that the rotation between the hinges needs to reach a critical value at which collapse will occur. It is postulated that if the stroke was increased, yielding a higher base acceleration, that collapse due to instability would occur with the at this point. Yet, this was not done. The frequency bracket was increased to the 10-110 Hz range. The stroke was slowly increased from 0mm so as not to 'shock' the arch. This proved successful and the frequency was slowly raised to 14.5 Hz, the first natural frequency value from the excitation tests. It was hoped that at this frequency that the arch would remain intact due to the effect of stabilisation at higher frequencies and that another arch could be subjected to this frequency from the outset. This would allow the tester to see how the arch would react when subjected to a known natural frequency value. At this frequency, crushing of the mortar was observed, generating collapse due to material failure, thus proving this methodology impractical.

It was expected that if the natural frequency of the arch was reached that violent vibration would occur such that collapse would occur or vibration such that the next hinge would form (for less than 4 hinges). From the test, it was observed that the when the frequencies at which more pronounced rotation between hinges was encountered, for the various hinge states, that the degree of rotation did not change even when the arch was subjected to seismic loading at that frequency for an extended period of time. When 3 hinges had formed, the arch was subjected to a frequency of 2.9 Hz for a minute and no change in the degree of rotation was observed.

In order to assess if the frequencies that generated pronounced rotation were indeed not the natural frequencies of the system, PSD graphs where plotted to find if any frequency peaks could be observed. If there was a 'natural frequency' to be encountered, then the expected result was that PSD's plotted from results of

accelerometers placed on the arch would display frequency spikes that the accelerometer attached to the shaking table would not. This was done for a number of tests in which pronounced rotation was encountered (at various hinge states). It was found that no distinct peaks could be found that correlated to the respective supposed ‘natural frequencies’. These peaks would be indicated by distinctly higher values on the y-axis as compared to the other peaks, which was not encountered in any of these graphs. Figure 5.5 demonstrates this, showing the PSD plots of various accelerometers when the arch had 3 hinges where the frequency that caused pronounced hinge rotation was 2.9 Hz. The frequency range for his test was 2.6-3.7 Hz.

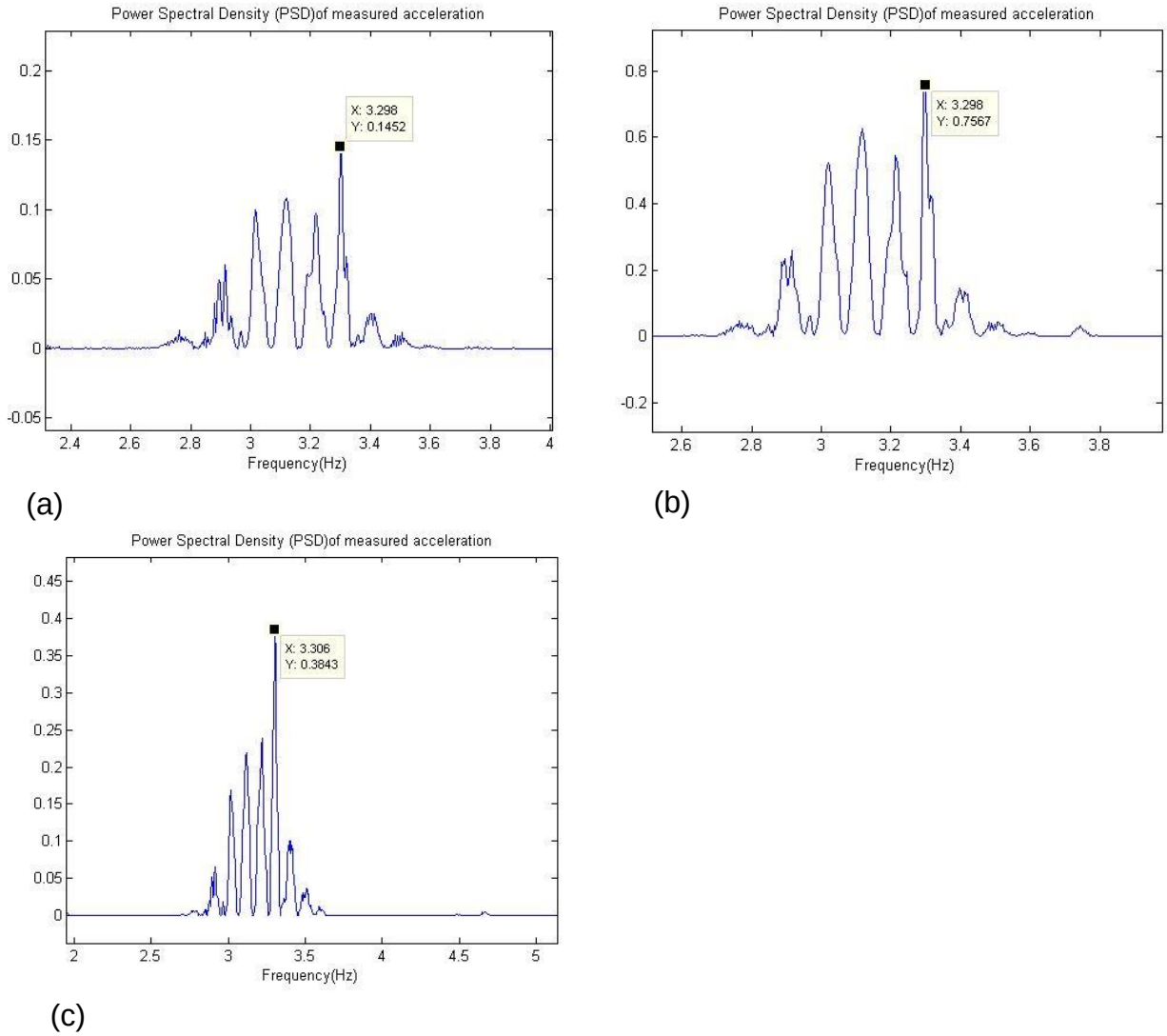

Figure 5.5: PSD plots for accelerometers on the arch apex (a) side of arch (b) and shaking table (c)

Figure 5.5 shows that there is no distinct difference in frequency peaks between the 3 different PSD's.

It was initially assumed that the structure would behave like an elastic structure (i.e. have a fixed natural frequency) before a mechanism was created with the formation of 4 hinges, at which point the rocking response would be of critical concern. The PSD's indicate that this is not the case. The rocking arch, as discussed in the literature review, does not have a fixed natural frequency, but rather is changes as a function of rotation between the hinges which is defined by the net energy input into the system.

The behaviour of the arch could be better described by the rocking block/arch model. Seismic loading introduces energy into the arch system. Yet, with the formation of hinges, there will be impact, which dissipates energy. The greater the rate of impact, the greater the rate of energy dissipation is. During testing, it was observed that at higher frequencies, where the rate of impact increased, the arches tended to stabilise, characterised by less pronounced movement of the arch and rotation between the hinges. Yet, at lower frequencies, movement generally increased as a result of fewer impacts. Rather than being 'natural frequencies', the frequencies at which more pronounced rotation between hinges was encountered are likely to be a such that the energy balance is optimised or at a maximum for a given acceleration. This may have been best illustrated in the situation where the mechanism had formed and the behaviour of the arch differed when loaded from below the frequency causing an optimised energy balance and from above.

During testing it was observed that as new hinges formed, the overall response on the structure changed substantially regarding the frequencies at which more pronounced rotation between the hinges was encountered. So too, the movement of the thrust line in the arch will change substantially with the introduction of additional hinges.

Therefore, as postulated by DeJong (refer to literature review), the concept of natural frequencies is not relevant to the study of the seismic behaviour of masonry arches. Rather their response to specific frequencies with increasing accelerations is a matter of concern. This warranted the next line of tests where set frequencies were used and the stroke was linearly increased.

5.2.2 Correlation with analytical model (fixed stroke tests)

The following input parameters were used in the virtual work model for the 0.8, 1.0 and 1.2 h/w ratio arches:

Table 5.2: Input parameters for 0.8, 1.0 and 1.2 h/w ratio arch models

h/w ratio	Span (m)	Height (m)	Thickness (m)
0.8	0.75	0.30	0.02
1.0	0.75	0.375	0.02
1.2	0.75	0.45	0.02

For the 0.8 h/w ratio test, the locations of the hinges according to the virtual work method that yielded the lowest acceleration to cause failure, were found to be at 0, 51.5, 120.9 and 180 degrees respectively. For the first 0.8 h/w ratio test, the hinge locations were at 0, 56, 128 and 180 degrees. For the third 0.8 h/w ratio test, the actual hinge locations were at 0, 53.05, 116.68 and 180 degrees. Table 5.3 indicates the correlation between the actual hinge locations and the predicted hinge locations for the 2nd and 3rd hinges in the 0.8 h/w ratio arches. The results indicate that there is a fairly good correlation between the theoretical and actual hinge locations (<10% difference).

Table 5.3: Comparison of actual vs model hinge locations for the 0.8 h/w ratio fixed stroke tests

h/w ratio	Difference- actual vs model 1st hinge location (%)	Difference- actual vs model 2nd hinge location (%)
0.8- Test 1	8	6
0.8- Test 3	3	3

When superimposing the calculated hinge locations on the respective arches, it is found that the lines intersecting the arch at these angles go through the brick rather than the mortar. Despite this, as the mortar has a substantially lower tensile capacity than the bricks, it was expected that failure will occur at the brick-mortar interface. This is a possible reason for the discrepancy in the calculated result and the actual hinge locations. It is postulated that if the bricks had a tensile capacity comparable to

the mortar, that there would be a lower discrepancy between the actual and modelled results.

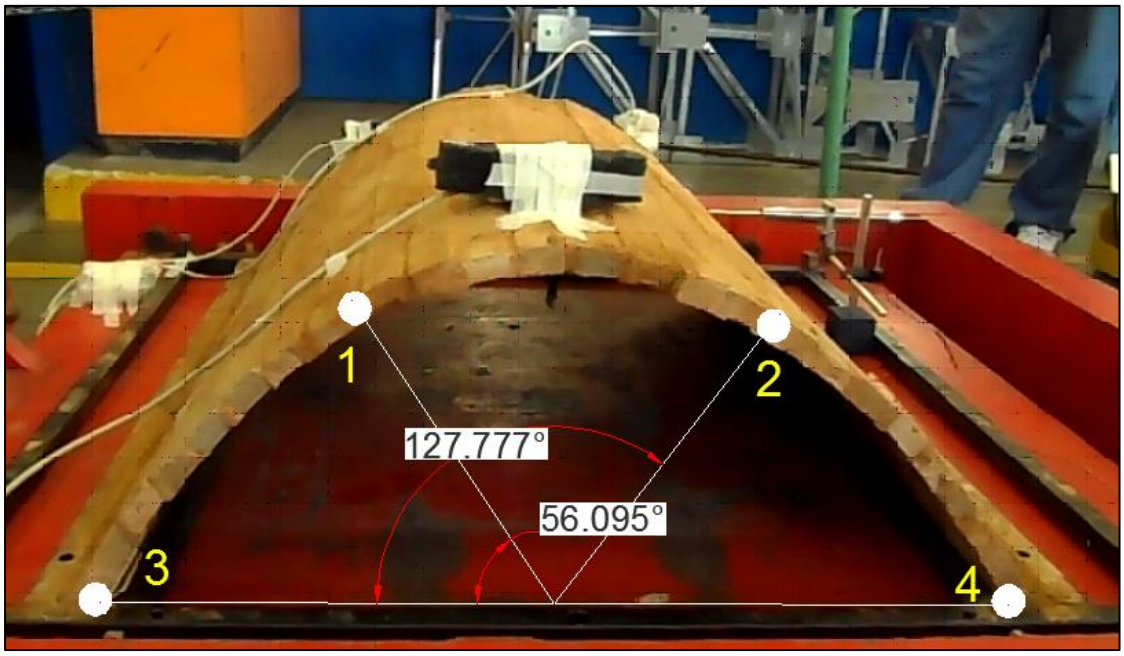

Figure 5.6: Hinge locations for 0.8 h/w ratio arch- first test

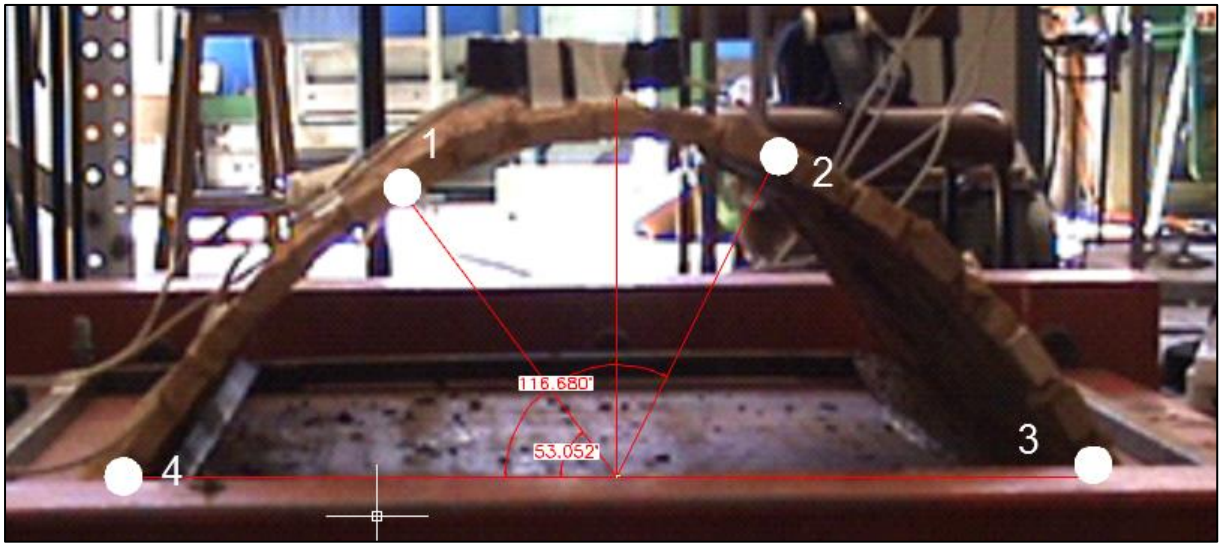

Figure 5.7: Hinge locations 0.8 h/w ratio arch- third test

For the second 0.8 h/w ratio test and the 1.0 h/w ratio test, pre-existing cracks had formed in the arches. As a result of this, hinges formed at the crack locations despite these positions yielding higher theoretical collapse acceleration. Additionally, the cracks did not go all the way through to the intrados of the arch. This indicates that the stability of these structures when subjected to seismic loading is affected by the presence of cracking. Therefore care must be taken to ensure that the extent of

cracking is minimised. From these tests it may be seen that the formation of pre-existing cracks may drastically affect the collapse mechanism of the arch. The experiments reveal that hinge locations will be forced at the position of the cracks (refer to 5.2.3). In both the 0.8 and 1.0 h/w ratio tests where pre-existing cracks were encountered, very similar failure patterns emerged. Surface cracks on the extrados of the arches (for both tests located at around 18.9 degrees) became ‘extrados opening’ hinges. It is interesting to note that the second hinge that formed for both arches were located at approximately the same location, which was close to the apex (80 to 83 degrees).

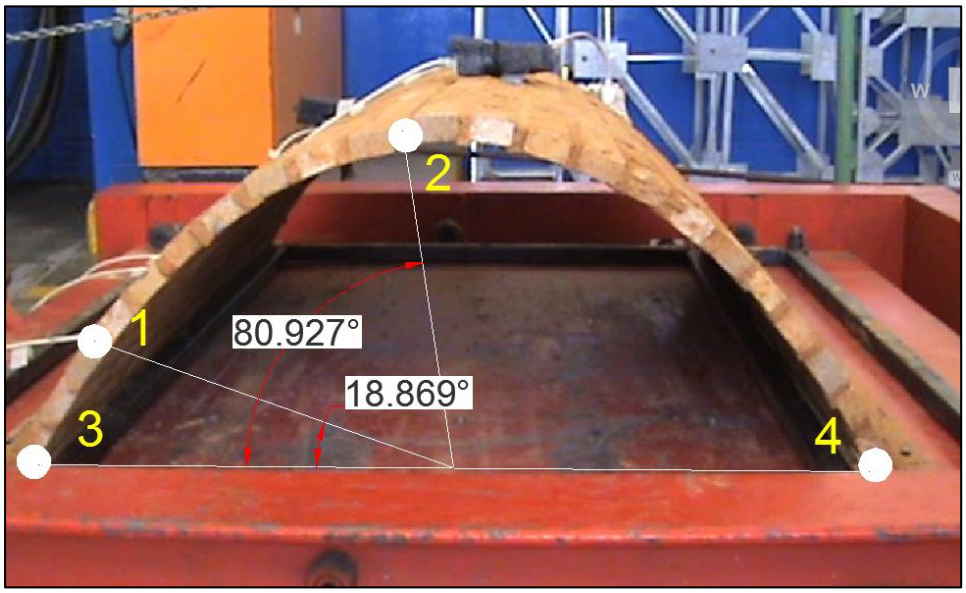

Figure 5.8: 0.8 h/w ratio arch with pre-existing cracks

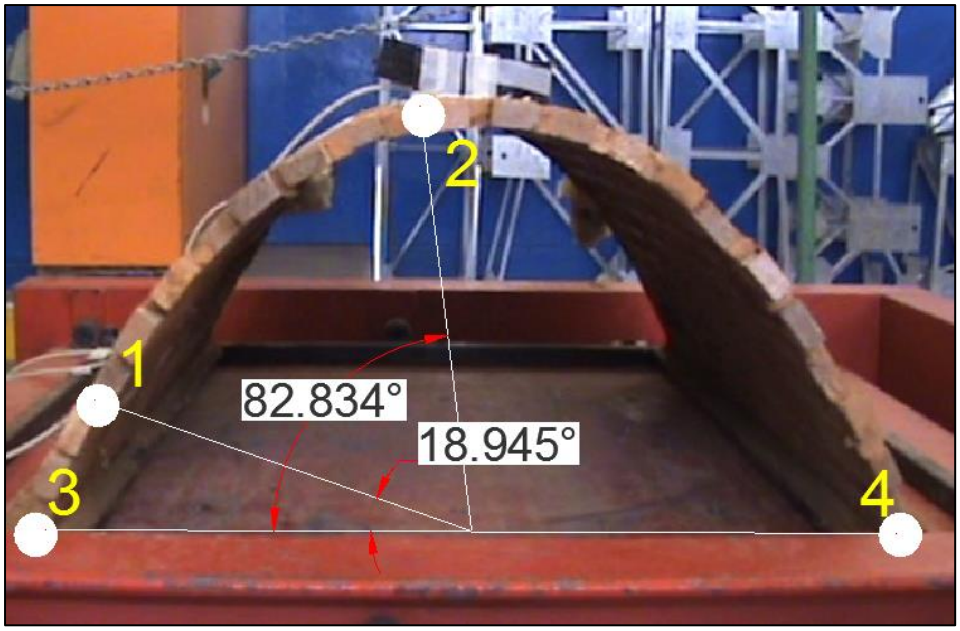

Figure 5.9: 1.0 h/w ratio arch with pre-existing cracks

For the 1.2 h/w ratio test, the locations of the hinges according to the virtual work method, that yielded the lowest acceleration to cause failure, are at 0, 68, 110 and 180 degrees respectively. For the1.2 h/w ratio test, the hinge locations were at 0, 72, 104 and 180 degrees. Table 5.4 indicates the correlation between the actual hinge locations and the predicted hinge locations for the 2nd and 3rd hinges in the 1.2 h/w ratio arch. The results indicate that there is a fairly good correlation between the theoretical and actual hinge locations (<10% difference). As stated above, the reason for the discrepancy may be a result of the brick having a greater tensile capacity than the mortar.

Table 5.4: Comparison of actual vs model hinge locations for the 1.2 h/w ratio fixed stroke test

h/w ratio	Position of 1st hinge (actual) (degrees)	Position of 2nd hinge (actual) (degrees)	Difference- actual vs model 1st hinge location (%)	Difference- actual vs model 2nd hinge location (%)
1.2 - Test 1	72	104	6	5

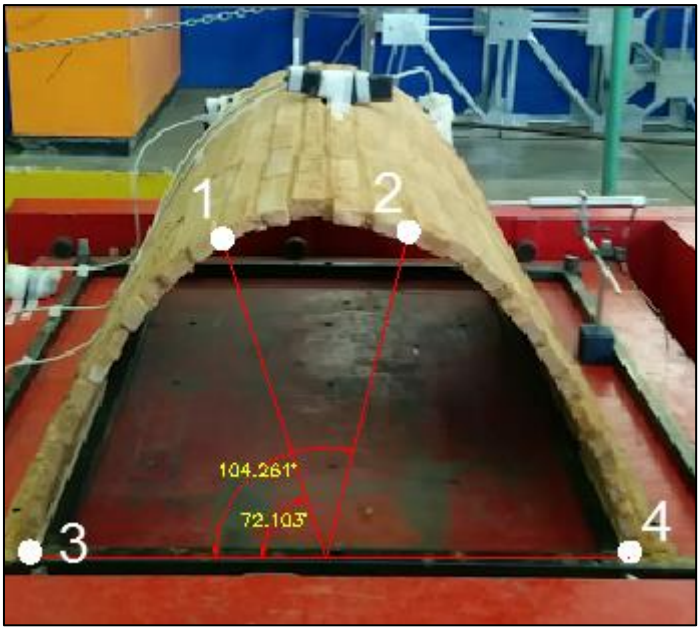

Figure 5.10: Hinge locations 1.2 h/w ratio test

5.2.3 Problems encountered during testing

The following problems were encountered during testing:

Continuous recording of acceleration data with the data logger was not possible due to hardware limitations. The full tests were therefore broken down into several periods of recording. Therefore tests were conducted in different frequency ranges within the given maximum allowable time of recording.

Recalling equation 2.2:

$$\sigma_{\text{tens}} = -\frac{\text{P}}{\text{A}} + \frac{\text{Pe}}{\text{Z}}$$

When cracking occurs prior to exposure to seismic loading, the Z value, which is a function of the thickness of the arch (Z=bt2/6) will decrease as the crack reduces the effective thickness locally. In locations of cracking, the lateral force required to induce tensile stresses is lower resulting in a higher likelihood of the formation of hinges in these locations. Therefore, prevention of cracking of the structure is of utmost importance when it comes to its ability to resist lateral seismic load.

5.3 Fixed frequency tests (unreinforced)

From the harmonic tests, it was found that the rocking arch model would better describe the seismic response of the structure before and after the formation of a mechanism in the arch. Therefore set of tests were performed for at fixed frequencies with a linearly increasing stroke. A total of 6 tests were performed. Three different arches were tested namely 0.8, 1.0 and 1.2 h/w ratio arches. Two different testing frequencies were used, namely 2 and 6Hz to investigate the behaviour of the arches at low and high frequencies respectively. This follows the methodology used by DeJong (2009). The respective frequencies were fixed and the stroke was linearly increased to intensify the induced acceleration. Like the harmonic tests, it is expected that failure will be due to instability of the arches.

In these tests only two accelerometers were used for each test. One was placed on the shaking table and the other on the apex of the arch. It was decided after the first set of tests that the other two accelerometers (on the side of the arch) used in the harmonic testing were not required. It was expected that during testing, once a mechanism formed that the rocking response would take place, characterised by divergent PSD plots from the two different accelerometer readings.

The tests were controlled by the program MTS TestSuite™ Multipurpose Elite. For the 2 Hz frequency tests, the total stroke/displacement was linearly increased from 3mm in increments of 0.5mm every 2 seconds (i.e. 4 cycles). For the 6 Hz tests, the total stroke was linearly increased from 0.5mm in increments of 0.25mm every 2.5 seconds. The timing was increased for this test such that sufficient hydraulic pressure could develop to achieve the full stroke. For both tests, a sweep function was used to gradually ramp up the frequency from 0.5 Hz to the required frequency with a 0.1Hz increment so as not to ‘shock’ the arch, which would create a mode 2 type of failure (sudden collapse) (Zhang and Makris, 2001). In order to ascertain if the correct stroke was achieved for the respective tests, the output of the LVDT connected to the program was monitored during the course of the tests.

The results from the accelerometers (especially for frequencies below 4 Hz), have a lot of ‘noise’, resulting in time acceleration curves that are not smooth. The noise could be a result of misalignment of the shake table or due small clumps of material

lying underneath the shake-table rollers. In order to smooth out the noise and get simple and accurate results with which to compare to the output from the LVDT, the least-squared curve fitting method was used.

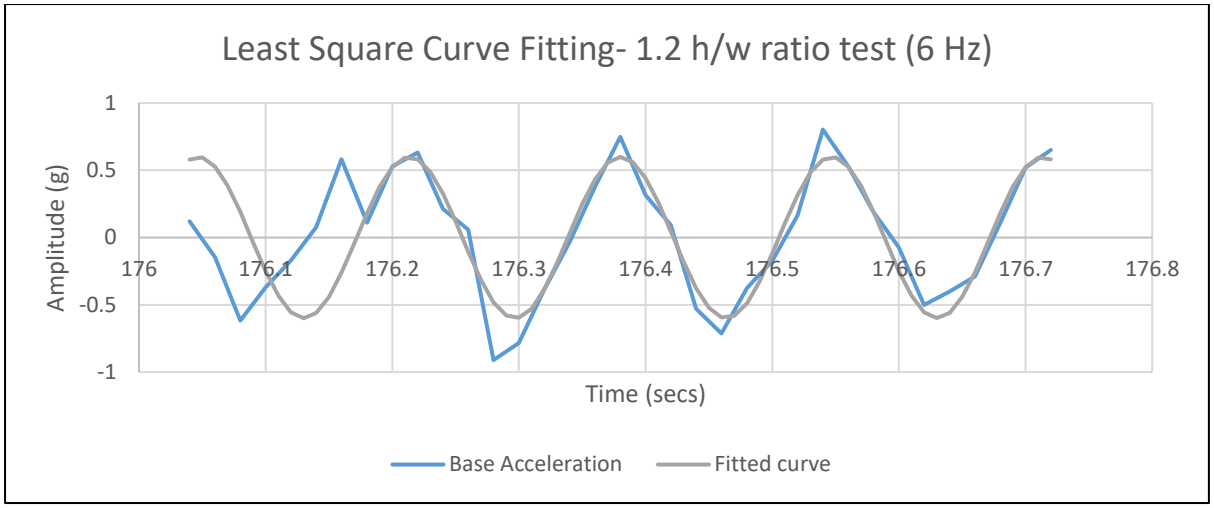

Figure 5.11: An example of the application of least square curve fitting

In order to use this method, a function had to be developed that could link displacement amplitude and frequency. For all tests, the digital controller generates a sine wave shaped seismic load. In displacement mode the output provided is in the form of a displacement v time sine graph. The following equation may be used to relate stroke to acceleration:

$$x = A\sin(\omega t) \tag{5.1}$$

$$x' = \frac{dx}{dt} = \omega A\cos(\omega t) \tag{5.2}$$

$$x'' = -\omega^2 A\sin(\omega t) \tag{5.3}$$

Where x= displacement

x'=velocity

x''=acceleration

A=half-cycle displacement (half of total stroke)

ω=angular frequency = 2π x frequency (in Hz)

t=time in seconds

Therefore expanding the terms, acceleration is given as:

$$x'' = -2\pi^2 f^2 t \times A \times \sin(2\pi ft) \qquad (5.4)$$

This function was used to smooth the acceleration readings such that they could be compared with the displacement commands. The least square curve fitting method involves finding the square of the difference between the accelerometer readings and the generated acceleration value for a time t. The square differences over the entire timeframe are then summed. Excel's Solver add-in was then used to find the value of A and frequency which provided the minimum sum of square differences. This computed stroke value may then be used to provide an approximation of the acceleration value at collapse. Refer to Appendix A to find the least square approximation graphs for the static frequency and reinforced tests in addition to a printout of the Excel worksheet and code used to compute the least square approximation.

5.3.1 Test results and discussion

Results and discussion

Multipurpose Elite ™ was used for these tests. While running the tests, on this software package, the user could ascertain what the displacement command was during collapse of the structure. These values were compared to the displacements/strokes computed at collapse found from applying least square curve

fitting method to the time acceleration-histories. This was done as there was uncertainty whether the hydraulic system could satisfactorily generate the displacements that were required as per the displacement commands. The comparison is presented in Table 5.5:

Table 5.5: Comparison of displacement commands to least square approximation of displacements at collapse

h/w ratio	2 Hz tests			6 Hz tests		
	Displacement command	**Least square displacement**	**% diff**	**Displacement command**	**Least square displacement**	**% diff**
0.8	25	23.68	5.28%	6.25	6.18	1.12%
1	21	20.44	2.67%	5.25	5.21	0.76%
1.2	8.75	8.32	4.91%	4.125	4.14	0.36%

It can be seen that the discrepancy is higher for the 2 Hz tests. This could be a result of the ‘noise’ in the data at lower frequencies. Another reason for discrepancies is that to pinpoint the point of collapse in the accelerometer readings is challenging. Despite this, the results of this comparison are satisfactory enough to use the displacement command data to make a comparison between the collapse accelerations of the respective tests.

Figure 5.12 provides an indication of the change in accelerations at which the arches collapsed with varying height to width ratios (using equivalent displacement command values at collapse).

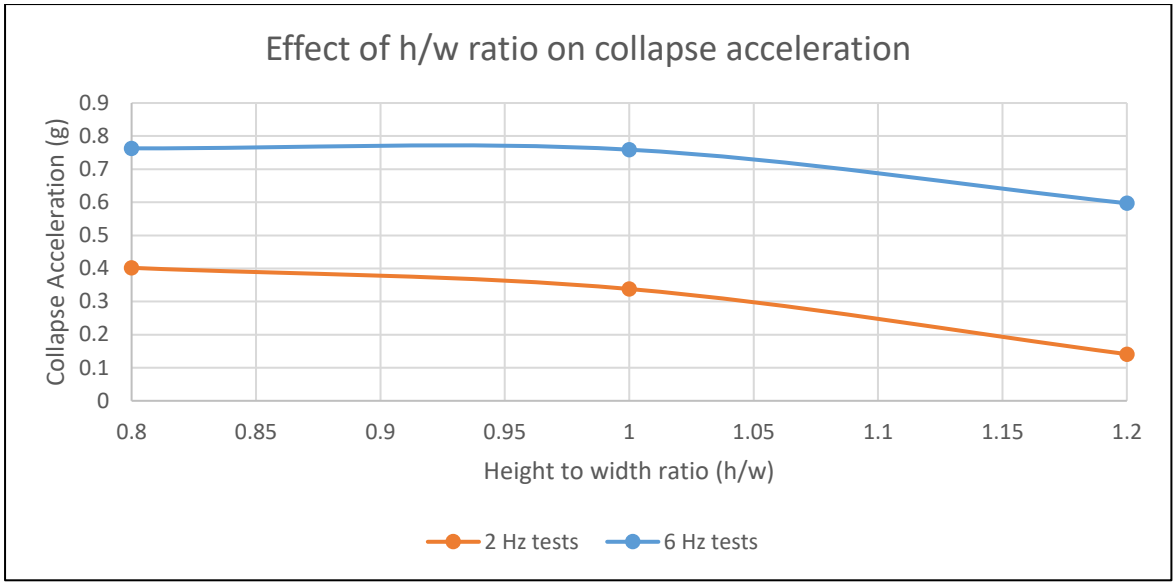

Figure 5.12: Collapse acceleration v h/w ratio for low and high frequency tests

Figure 5.12 indicates that the acceleration required to cause collapse for the 2 Hz test is lower than that of the 6Hz tests. Although this may be the case, the stroke required to cause collapse of the arches for the 2 Hz tests was substantially larger than that of the 6 Hz tests. For example, for the 1.0 h/w ratio test, the total stroke required to cause collapse was 42mm for the 2 Hz test, whereas for the 6 Hz test it was 10.5mm. When translated into full scale seismic loading, it may not be the case that the ground motion will go through such large displacements for lower frequency earthquakes.

Table 5.6 provides a comparison between the theoretically predicted (from the analytical model) and actual collapse accelerations for the respective tests:

Table 5.6: Comparison of theoretical and actual collapse accelerations

h/w ratio	Theoretical collapse acceleration (g)	2 Hz	6 Hz
		Collapse acceleration (g)	Collapse acceleration (g)
0.8	0.168	0.402	0.763
1	0.119	0.338	0.759
1.2	0.087	0.141	0.597

From Table 5.6, it can be seen that the theoretical collapse accelerations for the respective vault profiles is conservative. This model is based on a theoretically infinite duration of loading. In comparing the 2 and 6 Hz tests, it can be seen that as

the frequency of loading decreases, the acceleration required to cause collapse decreases substantially. This confirms Housner's (1963) assertion that an increase in the duration of load cycles warrant a lower acceleration required to cause collapse or failure. Therefore, it makes sense that the theoretical collapse acceleration is so low.

In reference to section 2.7.2, the peak ground accelerations required to cause the collapse of the arches for the 2 Hz tests fall in the practical range of peak ground acceleration (PGA) for Africa (0.34-0.65 g) (OCHA, 2007). For these tests, the collapse acceleration for the 1.2 h/w ratio arch falls within the practical range of PGA for South Africa (SABS, 2011). Using the relationship developed by Wald, 1999 (refer to Table 2.6). The corresponding Modified Mercalli Intensity Scale degrees that correlate to the collapse accelerations for these tests range between IV-V (light to moderate shaking).

For the 6 Hz tests, the collapse accelerations for the arches fall in the practical range of PGA for the Middle-East (0.65 to greater than 1.24 g) but not for Africa. In reference to Table 2.6, the corresponding Modified Mercalli Intensity Scale degrees that correlate to the collapse accelerations for these tests range between VIII-IX (very strong to severe shaking).

In the 2.0 Hz tests, just prior to failure, the three arches underwent rigid body motion followed by sudden collapse. During the 0.8 and1.0 h/w ratio tests, there was some rocking before the arches failed. As expected, the higher the height to width ratio, the lower the acceleration required to cause failure. For all the tests, failure was due to instability (i.e. the formation of a collapse mechanism).

In the 6 Hz tests, the arches underwent rigid body motion until the formation of the first two hinges, where pronounced rotation of the hinges occurred for a short duration before collapse with the exception of the 1.2 h/w ratio test. Again, with an increase in the height to width ratio, the acceleration required to cause collapse decreased. During the 1.0 h/w ratio test, there was some slipping between brick layers where one of the hinges formed, yet the final means of failure was due to instability. Instability was also the cause of failure for the other 2 tests in this frequency range.

During these 0.8 and 1.0 h/w ratio tests (6 Hz), the stabilising effect of higher frequency loading was observed, with the arches undergoing rocking after the formation of 2 hinges and eventually failure occurred when the rotational inertia was sufficient to cause the formation of the other two hinges to create a collapse mechanism. The 1.2 h/w ratio tests was characterised by rigid body motion until collapse.

The change of frequency of oscillation for the 1.0 h/w arch was inspected with the formation of two hinges at the apex. On the time-acceleration history for this test, it can be seen that there are two cycles of loading. During the first cycle, the displacement commands in the Multipurpose Elite procedure were exhausted. Some additional commands were added and the second cycle was initiated. In the first cycle, there is a visible point at which the two hinges form, as indicated by the substantial reduction in the apex accelerometer readings (acceleration I/0-2). This is also visible during the second cycle of loading. The accelerometers are linear in nature. Therefore as the 2 hinges formed by the apex, the linear acceleration experienced at the apex during rigid boy motion of the arch changed to rotational acceleration. Despite this, the readings allow one to ascertain if the frequency of the arch itself changes with time just after the hinges formed.

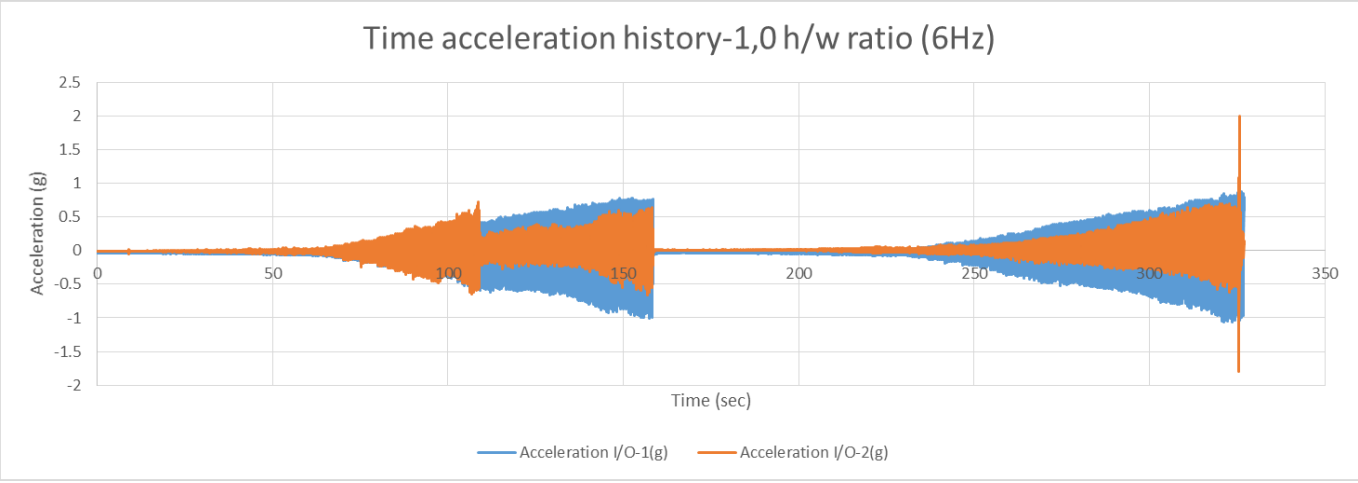

Figure 5.13: Time acceleration history for the 1.0 h/w arch (6Hz)

A PSD was plotted from the accelerometer readings after the 2 hinges formed in the first cycle of loading. The plot indicates that that the frequency remains around 6 Hz with the formation of hinges.

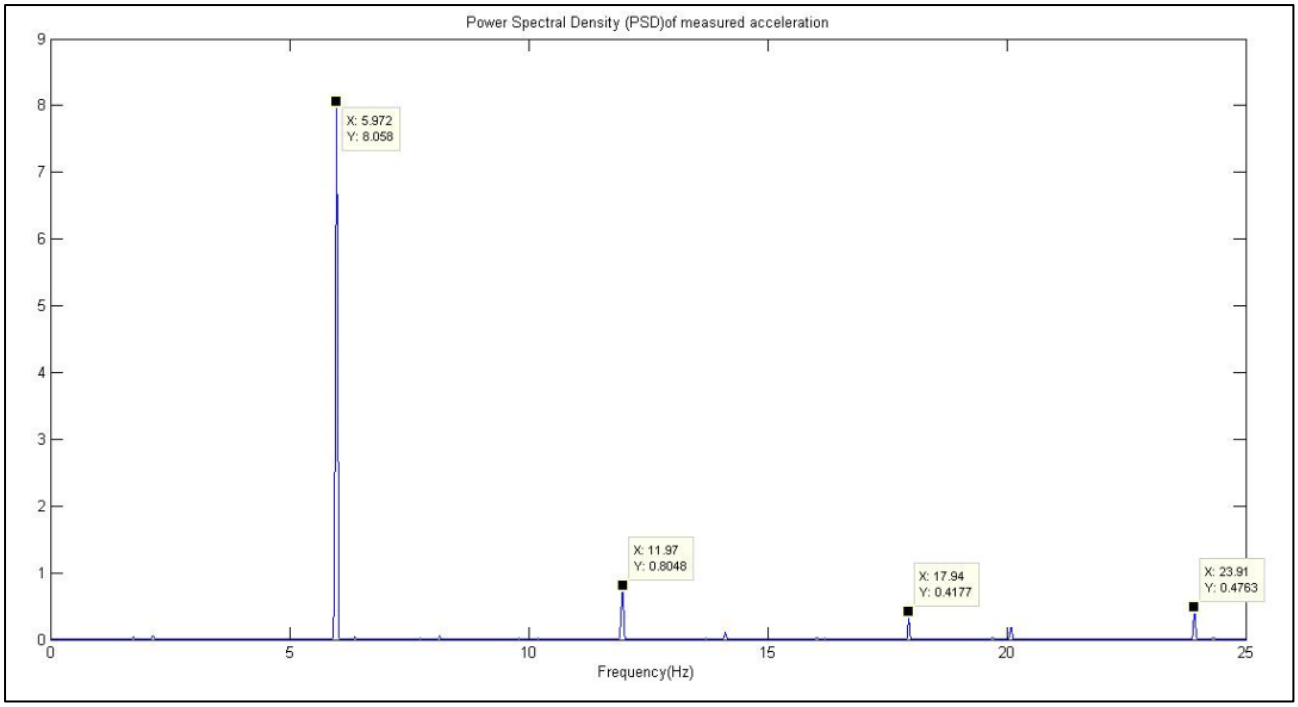

Figure 5.14: PSD plot for apex accelerometer after the formation of 2 hinges

The rocking mechanism described by DeJong (2009) and Oppenheim was not encountered during these tests. After the formation of the two hinges near the apex, the stroke was increased until the third and fourth hinges formed, causing collapse. The thickness to span ratio for DeJong's tests was approximately 0.075, whereas for these tests the ratio is approximately 0.027. It is postulated that due to this difference, that the rotational inertia required to cause the collapse of the tested arches is substantially lower than that of the ones tested by DeJong, accounting for why the rocking mechanism was not observed.

For all time acceleration histories and least square approximation graphs for these tests, please refer to Appendix A.

5.3.2 Correlation with the analytical model (fixed frequency tests)

2 Hz tests

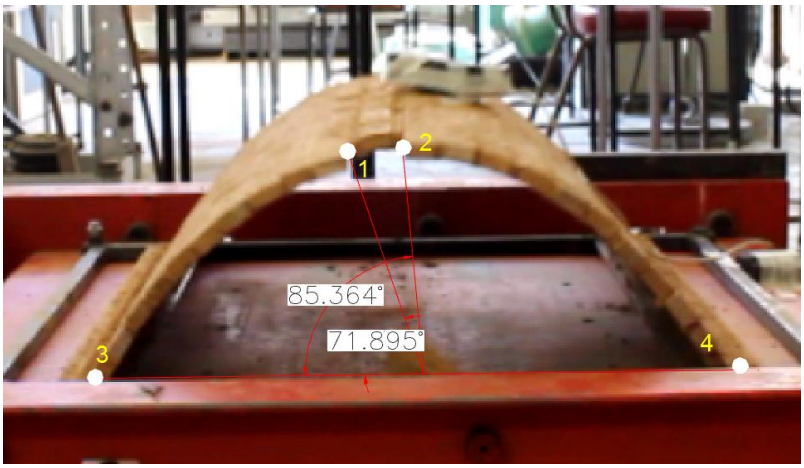

Figure 5.15: Hinge locations 0.8 h/w ratio test (2 Hz)

The 0.8 h/w ratio test (2Hz) took place in two stages. In the first stage, a few hinges had already formed when the displacement commands in the inputted procedure were exhausted, yet collapse did not occur. In the second stage of loading, the stroke range was slightly increased to cause collapse. It can be seen that during the first stage of loading that a weak point had formed in the arch. Therefore, the failure pattern was not one that was expected as per the analytical model.

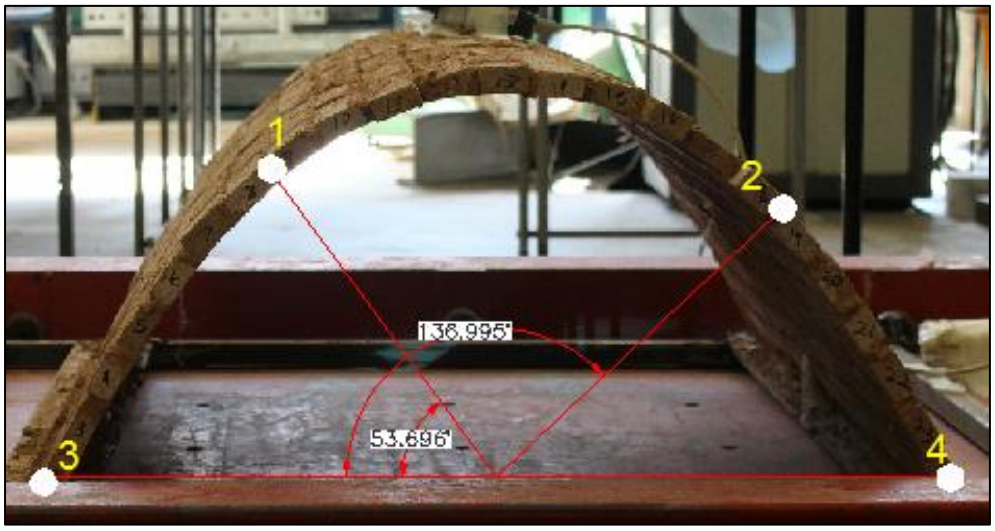

Figure 5.16: Hinge locations 1.0 h/w ratio test (2Hz)

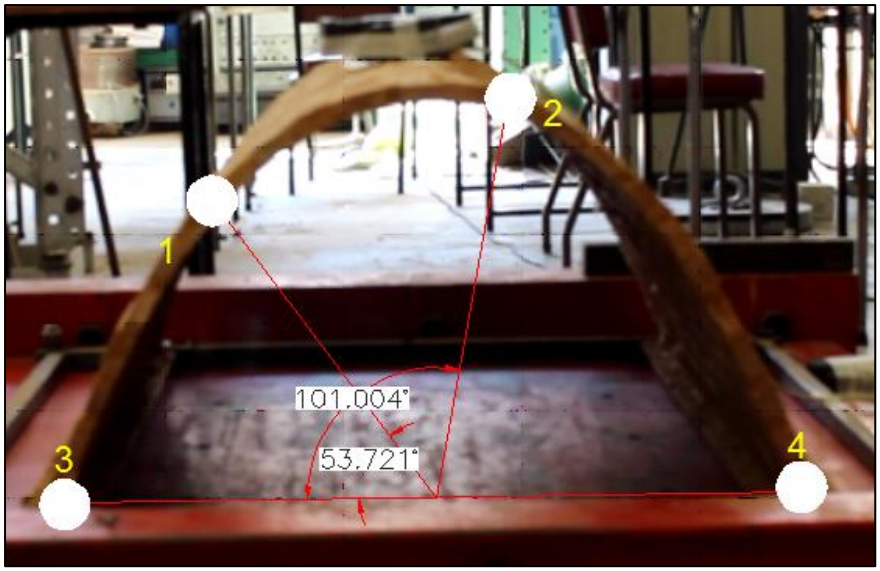

Figure 5.17: Hinge locations 1.2 h/w ratio test (2 Hz)

Table 5.7: Comparison of actual vs model hinge locations for 2 Hz test

h/w ratio	Position of 1st hinge (model) (degrees)	Position of 2nd hinge (model) (degrees)	Difference- actual vs model 1st hinge location (%)	Difference- actual vs model 2nd hinge location (%)
0.8	51.37	120.9	29	41
1.0	62.2	114.22	14	17
1.2	67.73	109	26	8

From Table 5.7, there seems to be a distinct divergence between the modelled and actual computed hinge locations. A more suitable measure than angle is a comparison between the computed minimum accelerations required to cause collapse with the computed accelerations given for the angles of the actual hinges that formed. This is presented in Table 5.8:

Table 5.8: Computed collapse acceleration comparison for 2 Hz tests

h/w ratio	Minimum computed collapse acceleration (g)	Computed collapse acceleration for actual hinge locations (g)	Percentage difference (%)
0.8	0.168	0.341	51
1.0	0.119	0.132	10
1.2	0.087	0.094	8

From Table 5.8, neglecting the 0.8 h/w ratio arch which is assumed to be an anomaly, the average percentage difference between the minimum computed collapse acceleration and computed collapse acceleration for the observed hinge locations is 8.5%. Despite this error, the results indicate that the computed trend whereby the first hinge angle increases and the second hinge angle decreases was observed in the tests. As discussed above, this model is a first order approximation and does not consider the moment capacity of the masonry and mortar. Therefore, it is a highly conservative approach.

6 Hz tests

Figures 5.18-5.20 indicate the hinge locations for the 6 Hz fixed frequency tests. It may be observed that there is a distinct change in the hinge locations between these tests and the previous tests. For the 1.0 and 1.2 h/w ratio tests, the first hinge location shifts drastically, going beyond 90 degrees, which neither the analytical model nor the previous tests could predict. This indicates that the arches' behaviour and failure mechanisms at higher frequencies are distinctly different from that observed in the lower frequency tests.

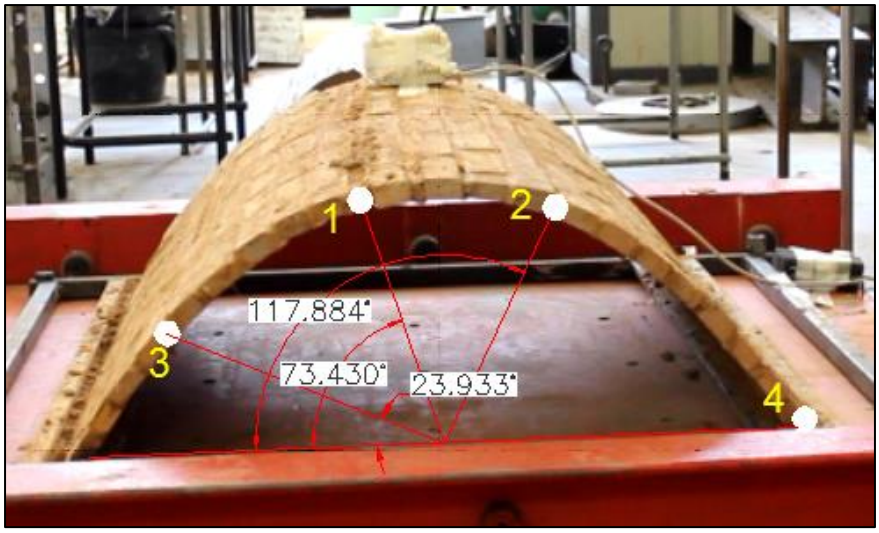

Figure 5.18: Hinge locations 0.8 h/w ratio test (6 Hz)

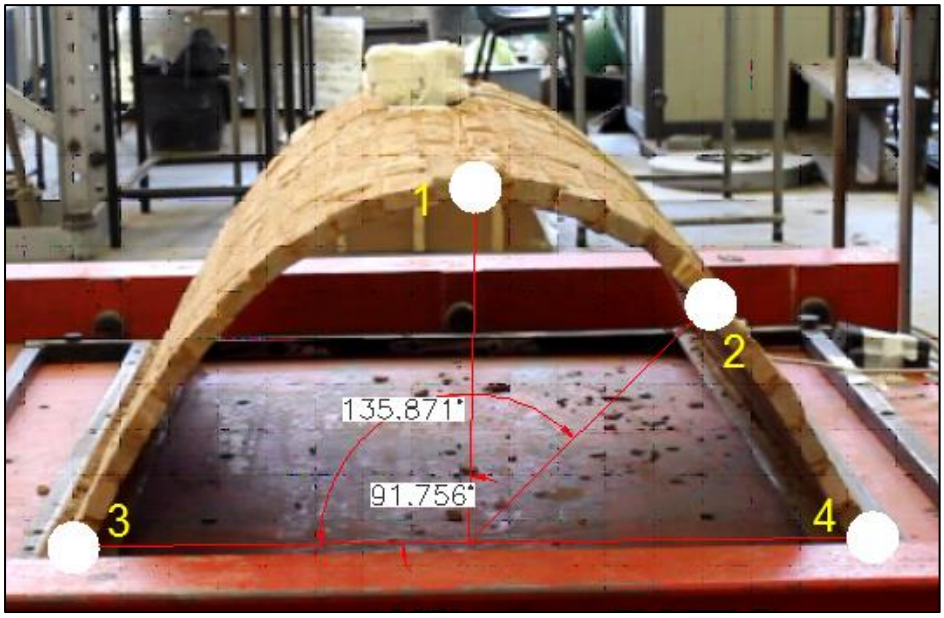

Figure 5.19: Hinge locations 1.0 h/w ratio test (6 Hz)

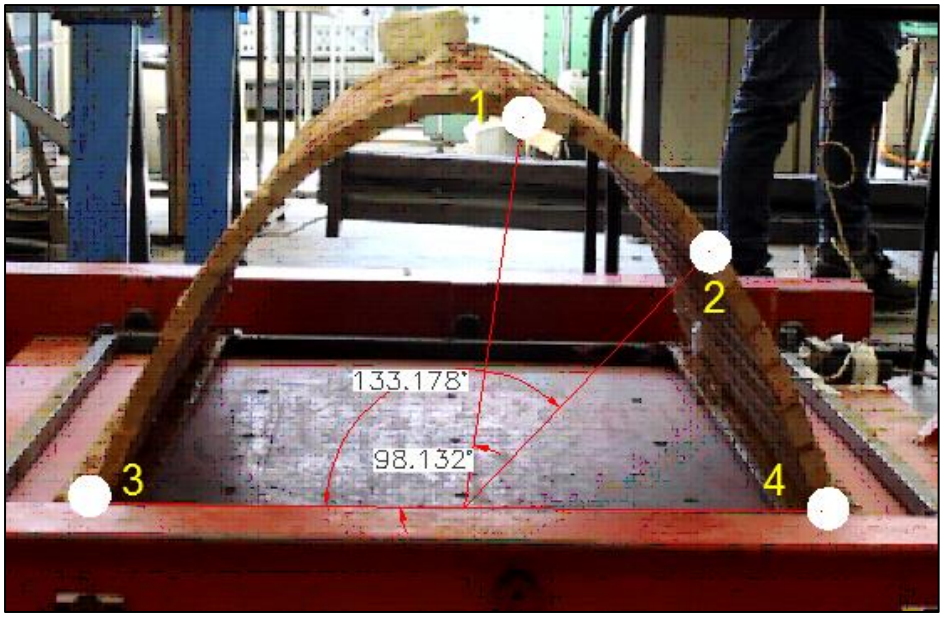

Figure 5.20: Hinge locations 1.2 h/w ratio test (6 Hz)

Table 5.6 provides a comparison between the modelled and actual hinge locations. From the results it may be seen that the higher the height to width ratio, the greater the discrepancy.

Table 5.9: Comparison of actual vs model hinge locations for 6 Hz tests

h/w ratio	Position of 1st hinge (model) (degrees)	Position of 2nd hinge (model) (degrees)	Difference- actual vs model 1st hinge location (%)	Difference- actual vs model 2nd hinge location (%)
0.8	51.4	120.9	30	3
1	62.2	114.2	32	16
1.2	67.7	109.0	31	18

Table 5.7 provides a comparison between the computed minimum accelerations required to cause collapse with the computed accelerations given for the angles of the actual hinges that formed for the 6 Hz tests.

Table 5.10: Computed collapse acceleration comparison for 6 Hz tests

h/w ratio	Minimum computed collapse acceleration (g)	Computed collapse acceleration for actual hinge locations (g)	Percentage difference (%)
0.8	0.168	0.245	31
1.0	0.119	0.178	33
1.2	0.087	0.179	105

From this comparison, it can be seen that for higher frequency tests that the analytical model does not provide a sufficiently accurate prediction of hinge locations. From previous tests, this frequency is associated with impact between the hinges, which creates damping of the motion and therefore stabilisation of the arch. The analytical model does not account for this in its assumptions. Therefore, it is postulated that this is the reason for the divergence between the computed and actual hinge locations.

5.4 Geogrid reinforcement tests (fixed frequency)

From the two tests above, it can be seen that unreinforced masonry arches are more vulnerable to seismic loading at lower frequencies as compared to higher frequencies. Failure of these structures in both sets of frequency tests resulted in the slow formation of hinges followed by sudden collapse. In practical terms, sudden structural collapse could result in loss of life. As mentioned in section 2.4, many developed nations have created laws prohibiting the construction of unreinforced masonry structures in zones of high seismicity. These regulations, with time, may become integrated into developing nations' building codes and regulations.

In order to improve the seismic performance of these vaults, prevent sudden collapse and considering existing and potential legislation prohibiting the construction of unreinforced masonry structures in zones of high seismicity, reinforcing solutions for the vaults were investigated. Three different reinforcement strategies were considered. The first measure involves laying geogrid over the entire extrados of the arch and embedding it in a mortar layer placed over the arch. The literature points out that the use of reinforcement anchors yields better structural

performance (e.g. Basilio, 2007). Therefore, the second measure is the same as the first with the addition of anchors. The third measure involves applying a prestressing force to the geogrid. The arch profile that had the lowest seismic capacity in the fixed frequency tests was the 1.2 height to width ratio arch. In order to assess the efficacy of the respective reinforcement measures, this arch profile was used for all 3 tests.

It must be noted that for these tests, there was no scaling of the strength or other properties of the geogrid reinforcement. The aim of this stage of testing was to try understand the behaviour of the catenary arch when utilising different reinforcement methods. The desired result was that the arch fails before the reinforcement and the failure mechanism be observed. As discussed above, the expected means of failure of the arches are either via sliding between blocks, delamination of the grid or material crushing.

Like the previous set of tests, the frequency was kept constant throughout the duration of testing. The frequency used for these tests was 6 Hz. With the introduction of reinforcement, it was feared that if using a frequency of 2 Hz that the stroke would have to go beyond that of the shake table limit (+-75 mm) in order for collapse to occur. It was also desired to see how the tensile capacity of the geogrid is mobilised once hinges were created and rocking is initiated. This rocking behaviour was not observed in the 2 Hz tests. Like the previous tests, the least-square method was used to find the best approximation of the collapse acceleration. The accelerometer data and least-square approximation graphs may be found in Appendix A.

5.4.1 Geogrid only

The first tests involved placing a layer of geogrid over the arch and clamping it down using hold-down bars which secured the geogrid on either end of the arch. The geogrid was placed after a week of curing the arch by covering it with plastic sheeting. Hold- down bars were screwed into the rig at 3 locations to secure the geogrid and prevent slippage during testing. The hold-down bars were made using the same hollow square section used for the testing rig. Once the geogrid was secured a layer of mortar was placed over the arch. This was done to create a bond between the arch and the geogrid. It must be noted that the additional mortar layer

adds mass to the structure, which helps stabilise it when subjected to seismic load. This is as with additional mass, there is a higher resistance to the movement of the thrust lines in the arch due to lateral loading. Therefore, the addition of the mortar layer is an additional means on improving the seismic performance of catenary arches.

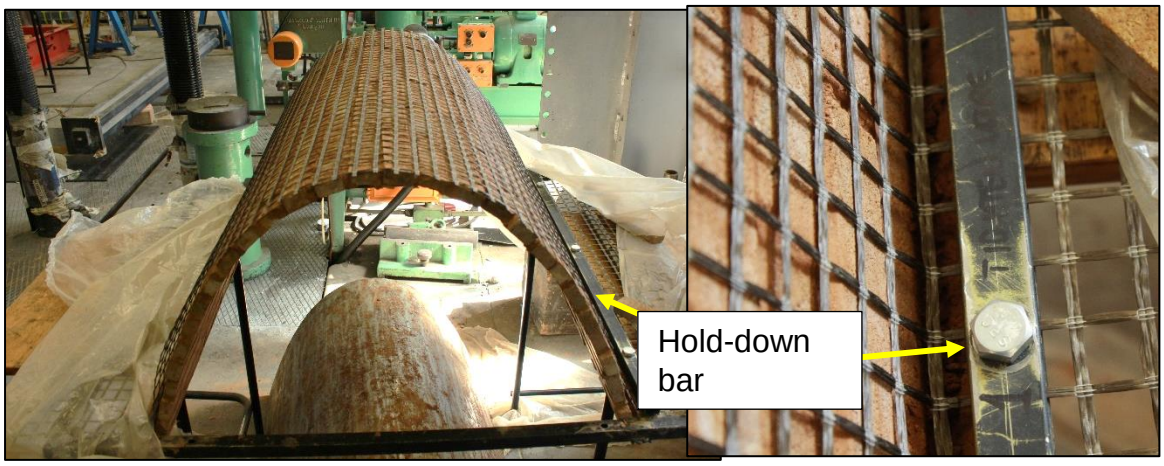

Figure 5.21: Geogrid laid over the arch and secured on either end



Figure 5.22: Mortar applied over the geogrid

For curing, the arch was covered with plastic sheeting and left for 3 days before testing. This increased the time of curing for the entire arch. Additional curing of the mortar increases the compressive strength of the mortar. Failure of the arches (due to the formation of a mechanism) is not dependent on the compressive strength of the mortar but rather on its tensile capacity. As per the assumptions stated in Section 1.3, it is assumed that the mortar has no tensile capacity. This is not unrealistic, as mortar is brittle with a very low tensile capacity. Therefore it was assumed that the additional curing time had no effect on the formation of hinges caused by induced

tensile stress in the arch. This assumption is applicable for all three reinforcement strategies.

5.4.2 Geogrid with anchors

The next test was the same as the previous test, but with the addition of anchors. This was aimed at preventing delamination of the geogrid from the arch, as observed in the previous test. The anchors were made from the basalt fibre geogrid. The ribs at the bottom of the anchor prevent the anchors from slipping during testing. The top rib is placed flush with the brick face. It was found that without the second rib, the top rib slipped off the anchor, making it a necessity.



Figure 5.23: Anchors made from basalt fibre geogrid (top and bottom view)

In order to place the anchors in the arch, holes were drilled into a number of bricks prior to construction. During construction, the predrilled bricks were placed every 3 layers. In these layers, 3 bricks with holes were positioned at either end and in the middle of the arch respectively. Figure 5.24 shows the arrangement of predrilled bricks in the arch.

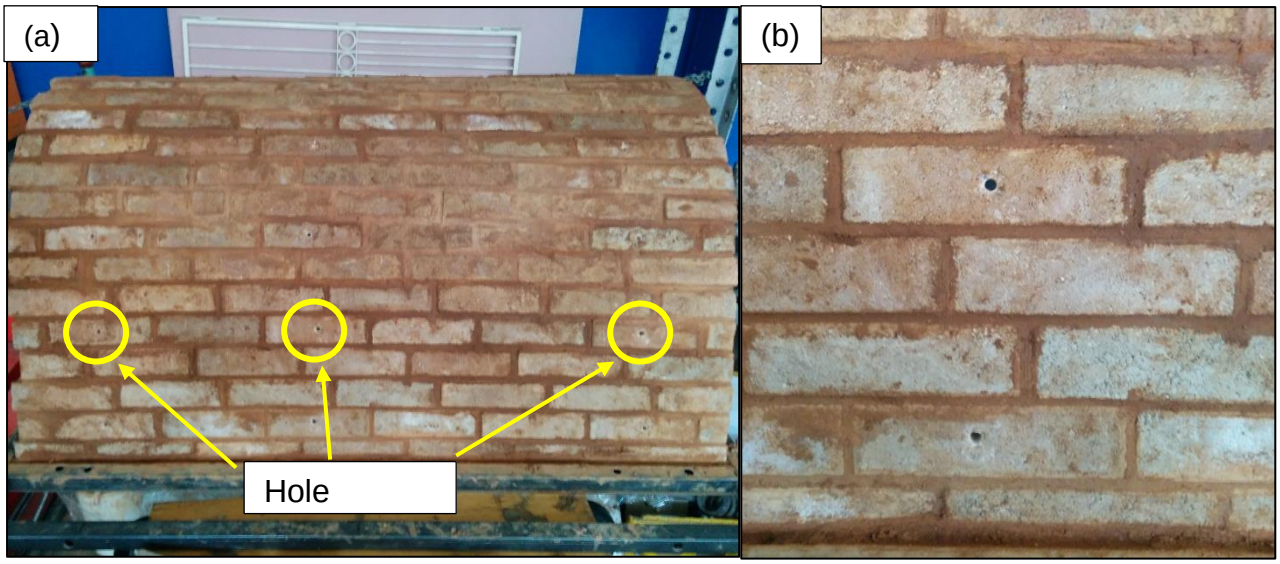

Figure 5.24: (a) Predrilled bricks placed every 3 layers (b) Close-up of predrilled holed placed in the arch

On the third day of curing, the anchors were epoxied into the arch, such that the epoxy could develop strength before testing. The geogrid was then placed over the arch after it had cured for a week. The anchors were then tied onto the grid and epoxied to ensure that they would not come loose during loading.

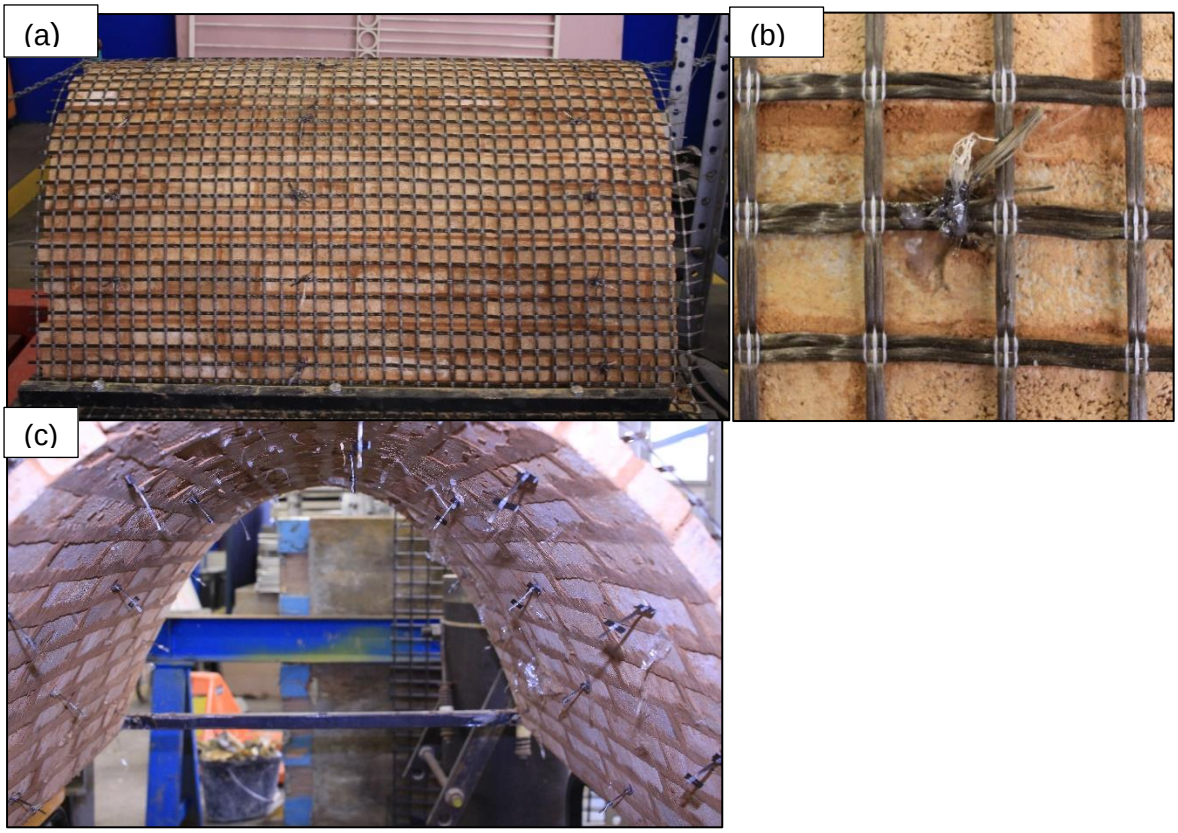

Figure 5.25: (a) Geogrid placed over arch and secured using anchors (b) Anchors were tied to the geogrid and epoxied (c) inside face of the arch with anchors installed

Like the previous test, the arch was mortared to enhance the bond between the arch and the geogrid and to ensure consistency through the reinforced tests. The mortar was covered with plastic sheeting for 3 days before testing.

5.4.3 Prestressed geogrid

The final reinforcement strategy involved the prestressing of the masonry vault using the basalt fibre geogrid. The testing rig was augmented for this test. Two shafts were attached on either side of arch rig. The shafts were supported at either ends with angle section cut-offs which were welded to the existing rig. The geogrid was attached to these shafts which were turned in order to prestress it. Shafts were placed on both ends of the arch to ensure that the prestressing load was evenly applied, despite friction between the arch and the geogrid.

The shaft used was a R25 bar, yet on either end, the shaft diameter was reduced to 18 mm and a thread was machined using a lathe. This thread was used to screw in nuts on either end of the angles such that the shaft could be secured when the desired prestressing force was achieved and to prevent slippage after tensioning. About 20mm from the respective ends of the shafts, 6mm holes were drilled in which metal rods were inserted to turn the shaft.

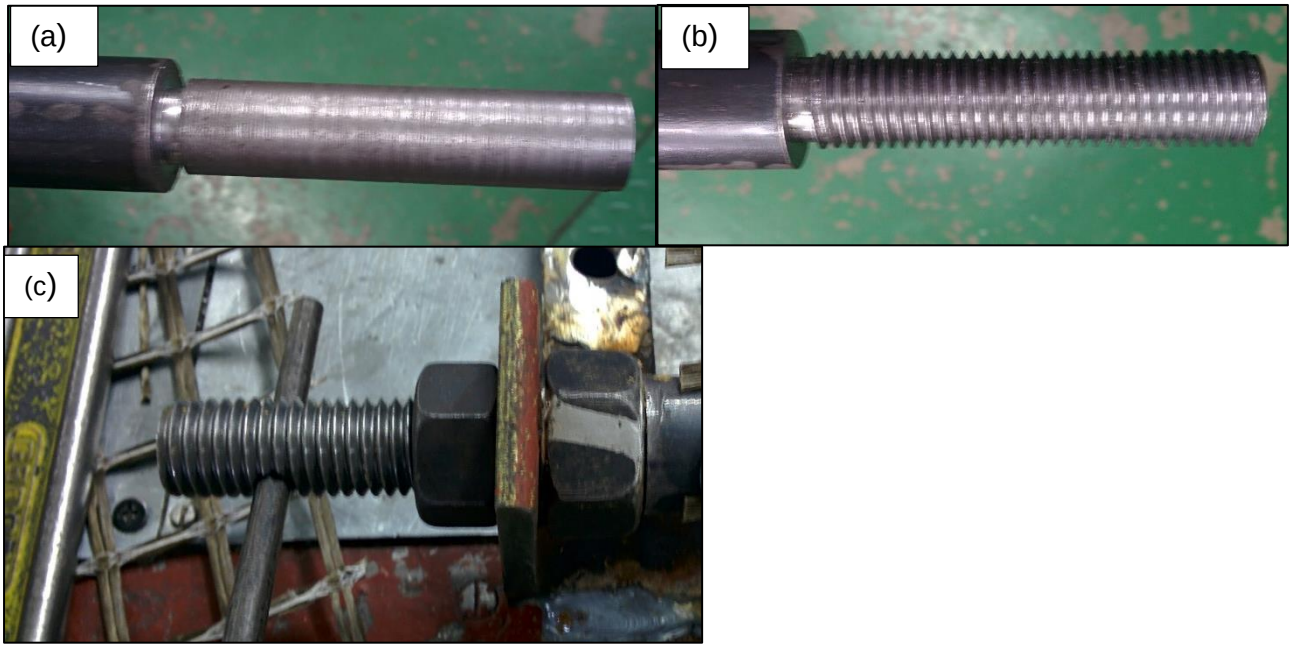

Figure 5.26: Stages of development: (a) Rod machined down to 18mm at ends (b) thread cut into reduced end (c) hole drilled into ends and metal rod inserted, nuts added on either side of the angle support.

In order to prevent slippage of the geogrid when turning the shaft, holes were drilled and tapped along the interior of the shaft. The holes were positioned such that they aligned with every 3rd to 4th vertical geogrid rib. This was done to ensure a uniform prestressing force throughout the entire geogrid. Washers were bend to the curvature of the shaft and ensured that the ribs were secured down.

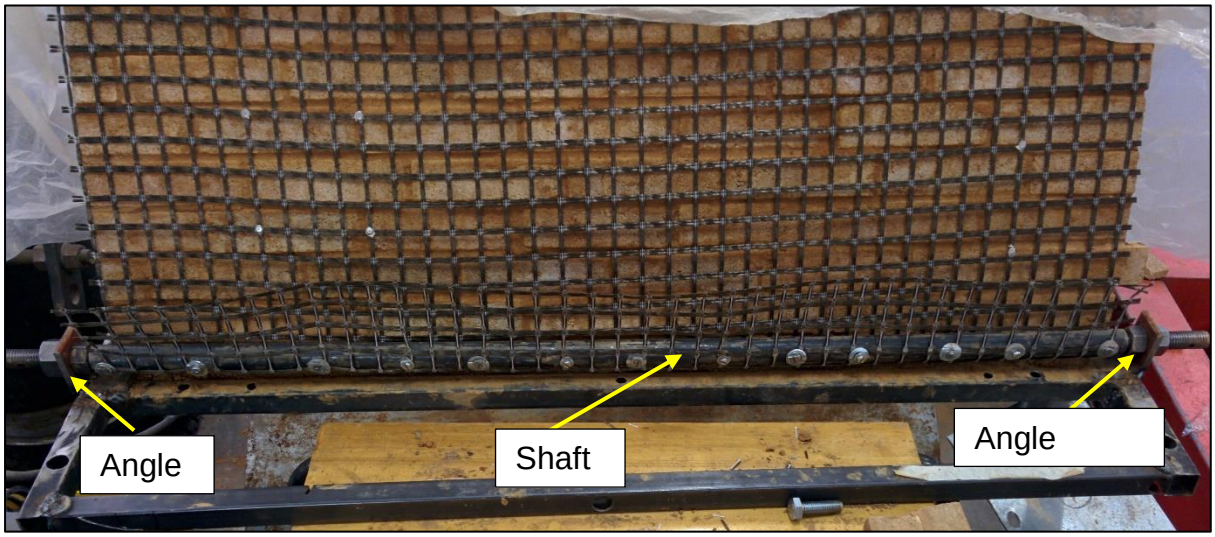

Figure 5.27: Final prestressing assembly with arch

The 1.2 h/w ratio arch was cured under plastic sheeting for a week before prestressing it. This was done such that the arch could develop some strength before loading. Demec targets were stuck to the geogrid at different locations to assess the extension of the geogrid with the application of prestressing. Firstly, a demec gauge was used to assess extension, yet after finding the results unsatisfactory, a Vernier scale was used. This was found to be more effective. The application of prestressing was gradual and done one side at a time. After each loading cycle, the extension of the prestressing was assessed. It was observed that friction plays a big role in the application of prestressing in masonry arches. When one side was prestressed, the extension on the other side was not as affected substantially.

It was also observed that the extent of prestressing is dependent on contact between the arch surface and the geogrid. While efforts were made to make sure that the depth of the arch remained constant, the nature of earth tiles warrants that there were cross-sectional depth differences in the bricks used to construct the arch. It was observed that these discrepancies created differences in the extent of

prestressing. In order to remedy this, mortar was used to fill in spaces where these discrepancies were seen (refer to .



Figure 5.28: Discrepancies in arch depth rectified with mortar

After this was done, the geogrid was laid over the arch again and prestressed. The mortar infill helped with creating a more uniform prestressing force. After three cycles of loading, the final measured extension of the fibre was found to be 0.36mm. The force-displacement curve that was developed when testing the basalt fibre (see section 4.3.3.2) was used to calculate the resultant force induced in the geogrid. This was found to be 0.48 kN or 50 kg per geogrid rib. Using a cross sectional area of 1.59 mm^2 per rib, the calculated stress in each rib is 302 MPa, close to half of the basalt fibre's ultimate tensile stress.

After the arch was loaded, a mortar layer was applied to the arch to ensure uniformity between tests. The arch was then covered for 3 days and left to cure before it was tested. In addition to adding mass to the structure, which helps stabilise the arch (refer to 5.4.1), the mortar layer was applied to create an even extrados surface, thereby ensuring that the cross sectional depth of the arch was kept consistent, avoiding the destabilising effect that these inconsistencies may have.

Inconsistencies in the brick thickness, while small, may have an effect on the stability of the structure. When there is a discrepancy in the vault thickness (refer to Figure 5.29), the centreline of the two segments will be different.

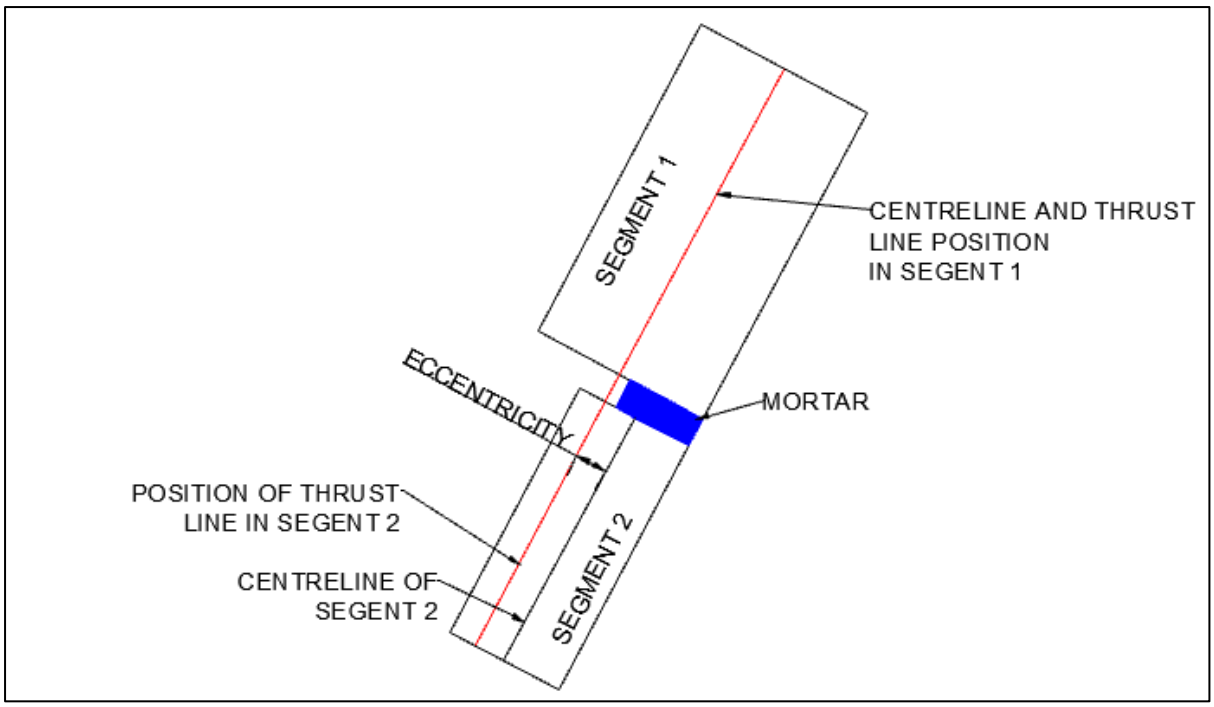

Figure 5.29: The effect of inconsistencies in vault thickness

When the thrust line moves through the middle third of an arch, the arch is loaded axially and in pure compression. When the thrust line passes from segment 1 to segment 2, which has a smaller thickness, there will be an eccentricity between the centreline of segment 2 and the thrust line (Figure 5.29). This creates moments in that segment (Moment= axial force x eccentricity). If thrust line is located outside the middle-third of segment 2's cross-section, then tensile forces causing cracking can be generated. The larger the difference between brick thicknesses from one segment to the next, the greater the eccentricity will be.

During seismic loading, lateral seismic forces cause the shifting of the thrust line. Given that inconsistencies in vault thickness result in thrust line eccentricity, less lateral force will be required to sufficiently shift the thrust line to cause the development of tensile forces. This indicates the importance of uniform vault thickness to in relation to seismic performance. When using formwork to construct catenary vaults, applying a layer of mortar to a vault's extrados to ensure a uniform arch thickness, as was done for all the reinforced arches, is one way to prevent vault thickness discrepancies.

5.4.4 Test results and discussion

Geogrid only

The failure mechanism observed during this test differed substantially from that of the unreinforced arches. Using the least square method, the displacement at collapse was found to be 5.23 mm. The displacement command was 5.275 mm. This was deemed to be satisfactory. At the collapse acceleration (using displacement command value and substituting it in to equation 16) of 0.763g or 7.48 m/s^2, one whole brick layer slid out (position 1). Subsequently, 3 brick layers slid out (position 2) and finally hinges formed at the base of the arch. Subsequently, layers of bricks fell as delamination occurred. Therefore, the means of failure for this test was delamination and sliding of the bricks.

An interesting outcome was that once the arch had collapsed, the mortar-geogrid composite remained fairly intact. On the left hand side of the arch a number of brick layers were still bonded to the composite and required some effort to remove. Once this was done, it was found that the mortar placed over the arch had bonded well with the arch.



Figure 5.30: Locations of failure points along arch for geogrid only test



Figure 5.31: Mortar-geogrid composite remained fairly intact after the arch failed



Figure 5.32: Mortar bonded well with the arch

Geogrid with anchors

Failure of the arch reinforced with geogrid and anchors is characterised by the crushing of the mortar and sliding of the bricks past one another (Figure 5.33). Just prior to failure, pieces of mortar were seen falling from the arch. In close succession, the brick layers at locations 1 and 2 slid over one another. Just prior to collapse, there was a rocking motion observed. Subsequent to this hinges formed at locations 3 and 4. Using the least square method, the displacement at collapse was found to be 6.70 mm. The displacement command was 6.75 mm. This was deemed to be satisfactory. The collapse acceleration of the arch (using the displacement

command) was 0.957g or 9.39 m/s^2. The failure points for the arch is indicated in Figure 5.32.



Figure 5.33: Failure points for arch reinforced with geogrid and anchors

It was observed that at the sliding interface, the mortar layer was completely shorn off on one side of the brick-mortar interface. After collapse, the arch was inspected and it was found that only 3 of 24 anchors used failed in tension. The remaining anchors were intact and still attached to the geogrid.



Figure 5.34: Sliding of brick layers is the failure mechanism

Prestressed geogrid

Failure of the prestressed arch was characterised by material crushing and sliding of the brick layer at location 1 shown in Figure 5.34. After sliding occurred, a hinge formed at location 2. Just prior to failure, pieces of mortar were seen falling from the arch. After testing the arch, the data logger suddenly turned off. In doing so, the data for the test was lost. However, the displacement command at which failure occurred was known. In order to recreate the test conditions (i.e. weight on the shake table), the collapsed arch was left on the shake table and the programmed procedure was run again until this point. As this series of tests is concerned with a comparison of the collapse acceleration and means of failure for the various reinforcement strategies, the available data was found to be sufficient.

Using the least square method, the displacement at collapse was found to be 6.87 mm. The displacement command was 6.875 mm. This was deemed to be satisfactory. The collapse acceleration of this arch (using the displacement command) was 0.994g or 9.75 m/s^2.

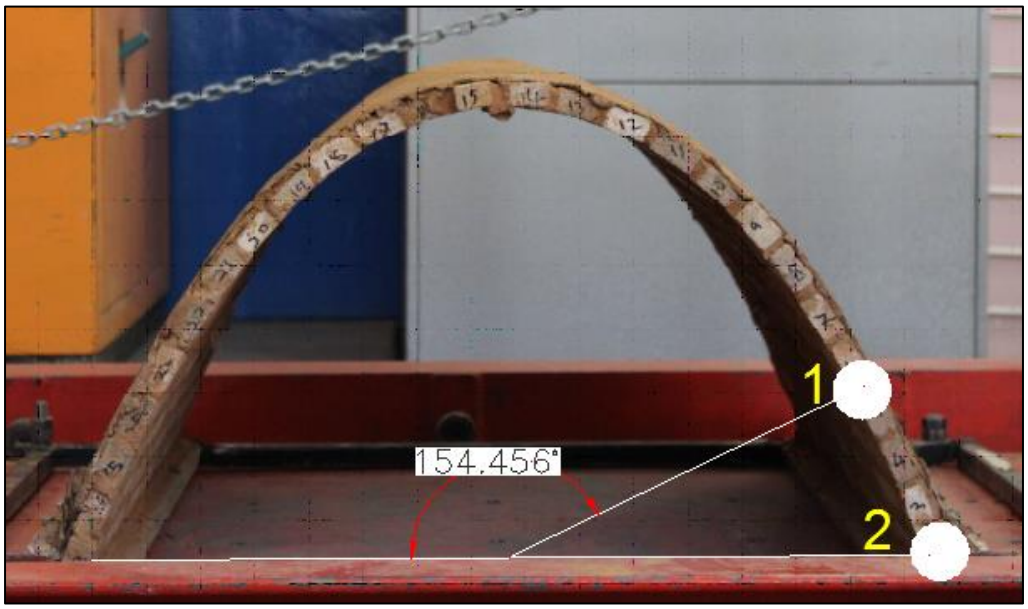

Figure 5.35: Failure points of prestressed arch

It must be noted that despite efforts to make sure that the prestressing shafts were as close as possible to the arch, that there was a slight gap between the arch and the geogrid close to the base. As prestressing force is developed through contact

between the arch and the grid, this could have reduced the prestressing force close to the base, contributing to the failure of the arch. The fact that the arch itself was already stressed prior to collapse could also have contributed to the crushing of the mortar. In addition to this, the vertical component of the induced tensile force is higher at the base than further up towards the apex. This could account for why failure due to material crushing occurred closer to the base of the arch. The collapse acceleration for this arch was close to that of the arch reinforced with the geogrid and anchors. It may be inferred that for both of these tests, the limiting factor is the mortar's compressive strength, which is less than half of that of the masonry. Yet for the prestressed test, rigid body motion was observed until the sliding of the bricks past one another, unlike the previous test.

Comparison of reinforcement strategies

Table 5.8 presents a comparison between the unreinforced and reinforced arches' seismic performance:

Table 5.11: Summary of collapse accelerations for different reinforcement strategies

Strategy	Collapse acceleration (g)	% difference to unreinforced arch
Unreinforced arch	0.597	
Geogrid only	0.763	27.81%
Geogrid and anchors	0.957	60.30%
Prestressed geogrid	0.994	66.50%

Making reference to section 2.7.2, for the reinforced vault tests, the collapse accelerations for the arches fall in the practical range of PGA for the Middle-East (0.65 to greater than 1.24 g) but not for Africa. In reference to Table 2.6, the corresponding Modified Mercalli Intensity Scale degrees that correlate to the collapse accelerations for these tests range between IX-X+ (severe to extreme shaking). These results indicate that these collapse accelerations may be practical for zones of high seismicity only but not for zones of moderate seismicity.

It is expected that when performing tests on vaults with a larger scale, that the collapse accelerations would be lower. The aim of these tests was to draw a

comparison between the seismic capacity of unreinforced and reinforced catenary vaults using different reinforcement strategies. This indicates that future studies which utilise larger scale vaults could be useful in assessing the seismic response of vaults reinforced with basalt fibre geogrid.

From Table 5.8 it can be seen that the geogrid with anchors and the prestressed geogrid provided the most satisfactory results. Despite the prestressing solution being the best, the additional technical input that is required for this strategy is substantially higher than that of the anchored geogrid solution. Therefore, for its marginally higher performance, it is not the most viable solution. It is therefore recommended that the anchored solution be used.

6 CONCLUSION AND RECOMMENDATIONS FOR FUTURE STUDIES

6.1 Summary of findings

The objectives of this study were to investigate the behaviour of unreinforced catenary vaults when subjected to seismic loading, to develop a model that can be used as a tool for a first-order analysis of the seismic resilience of catenary vaults, to predict the method of failure of the vaults and to investigate reinforcement strategies for catenary vaults that could help improve their seismic performance.

This was done by conducting a series of tests on both unreinforced and reinforced catenary vaults, developing an analytical model to predict the minimum lateral acceleration required to cause collapse of the vaults and where hinges would form.

The analytical model is based on the work of Ochsendorf (2002), who developed a model to predict the minimum lateral acceleration required to cause the collapse of circular voussoir arches. The basis of this model is the virtual work method. The model is conservative in that is only considers the mode 2 type of failure, defined by Zhang and Makris as having a base acceleration of sufficient magnitude and duration to cause failure in the first half-cycle of motion. With this mode of failure, the arch fails in the first cycle of motion due to an acceleration applied for a large amount of time. Therefore the effect of impacts between the hinges before collapse is not considered. The model also does not consider the moment capacity of the arch. The computed collapse acceleration therefore represents the minimum acceleration required to cause the failure of an arch. This model was adapted for catenary vaults. The model was then used to look at the effect of changing geometric parameters on the minimum computed collapse acceleration.

Initial tests performed on the catenary vaults looked at the effect of changing frequency on the behaviour of the vaults. From these tests, it was found that with the development of hinges in the vaults, their overall seismic response changed substantially. During these tests, it was observed that as the frequency of vibration increases a stabilisation in the form of lowered rotation between hinges occur. Although some frequencies were encountered that resulted in more pronounced

rotation between the hinges, with the use of PSD plots it was found that there were no frequencies that caused spikes in acceleration amplitude and no excessive vibrations occurred. From this result, it was inferred that the impacts between the hinges when moving from one cycle to another prevented the building up of energy, characteristic of resonance. Rather, failure is due to the movement of the thrust line outside the boundary of the arch to form a collapse mechanism. This is caused by the induced lateral motion and the generation of sufficient rotational inertia to cause collapse.

It was reported by DeJong (2009) that circular voussoir arches behave differently at different frequencies. In order to investigate this phenomenon with catenary vaults, tests looking into the response of the vaults to an induced lateral loading caused by increasing the stroke and keeping a fixed frequency were performed. The frequencies used for this test were 2 and 6 Hz, representing low and high frequencies respectively. Using 3 different catenary profiles, it was found that the acceleration required to cause collapse was lower for the 2 Hz tests as compared to the 6 Hz tests. The tests also indicated that the lower the height to width ratio of the vault, the higher the collapse acceleration. It was also found that the hinge locations for the 2 Hz tests were more closely aligned with the computed locations as compared to those observed in the 6 Hz tests. In this frequency range, rocking of the arch was observed before collapse occurred (in contrast to the sudden collapse of the arches in the 2 Hz frequency range). It is assumed that this is due to the fact that the analytical model does not consider the effects of impact between the hinges, damping and the resulting stabilisation it causes.

Finally, three reinforcement strategies were investigated to improve the seismic performance of the arches. All three of these strategies utilised basalt fibre geogrid. The first strategy consisted of laying the geogrid over the arch and securing it at the arch base. The method of failure here was characterised by the debonding of the fibre from the arch and sliding between bricks layers. The second and third strategy was to tie down the geogrid with anchors and the prestressing of the arch using the geogrid respectively. In both these tests failure was characterised by material crushing followed by sliding between brick layers. The latter two strategies were found to cause the most substantial increase in the seismic resistance of the arches. Despite the prestressing solution being slightly better than the anchorage solution, it

was found that due to the substantially higher technical requirements of the prestressing solution, that the anchorage solution was the most viable and economical reinforcement strategy.

6.2 Further research to be performed

Research on this topic may be furthered by looking into the following:

- It is assumed that there supports of the arch are rigid. In reality, the supports of the arch may move during a seismic event, which will account for a shift in the thrust line in the arch. The combined effect of ground motion and support displacement can be considered. In future studies this could be considered and integrated into predictive models.
- DeJong (2002) developed an analytical model for the seismic response of a semi-circular arch, a development of Oppenheim's (1992) analytical model. An analytical model can be developed for catenary shells subject to seismic loading. This will vary from DeJong's model as the radius of the catenary varies.
- The analytical model proved to be highly conservative in predicting the minimum collapse acceleration for arches. This is as it does not account for the moment capacity of the bricks and mortar. An analytical model integrating this consideration could be able to better predict the accelerations required to cause the collapse of mortared arches.
- It has been reported in the literature (Sim *et al.*, 2005) that basalt fibres and reinforcement may be subject to alkali degradation. Further research could look into studying this effect when the fibre is encased in mortar.
- The model tests performed did not integrate scaling. In full scale structures, issues such as material crushing or failure of the basalt reinforcement or anchors may be of concern and become critical considerations. Full-scale tests would be insightful into the investigation of these considerations.
- The equipment used for the testing did not allow for the simulation of actual earthquakes using acceleration-time histories Testing of the arches using this could provide a more insight into the behaviour of the vaults under a range of rapidly varied acceleration frequencies and amplitudes.

- The anchorage pattern of arch was arbitrarily chosen. Further research could look into the effect of increasing or decreasing the number of anchorage points in the arch on the collapse acceleration.
- The effect of varied prestressing forces was not explored in this study. This could be done in order to assess in which cases and at what loads does prestressing become the most viable reinforcement strategy for thin shelled catenary vaults.
- Although this study was extensive, the destructive nature of the tests and the time-intensive requirements imposed by the arch construction prevented the repetition of tests. Future studies could be performed to repeat certain aspects of these tests to check for consistency with the results of these tests.

7 REFERENCES

Adam, E.A. & Agib, A.R.A., 2001. Compressed stabilised earth block manufacture in Sudan. France, Paris: Printed by Graphoprint for UNESCO. Available at: https://www.sheltercluster.org/sites/default/files/docs/cebs_block_in_sudan.pdf [Accessed February 2, 2016].

Allen, E. & Zalewski, W., 2009. Form and Forces: Designing Efficient, Expressive Structures 1st edition. Hoboken, N.J: John Wiley and Sons.

Basilio, I., 2007. Strengthening of arched masonry structures with composite materials. Ph.D. University of Minho. Available at: https://repositorium.sdum.uminho.pt/.../1/2007_PhD_IsmaelBasilio.pdf [Accessed January 25, 2016].

Bhattacharya, S., Nayak, S. & Dutta, S.C., 2014. A critical review of retrofitting methods for unreinforced masonry structures. International Journal of Disaster Risk Reduction, 7, pp.51–67. Available at: http://linkinghub.elsevier.com/retrieve/pii/S2212420913000666 [Accessed February 6, 2016].

Block, P., DeJong, M. & Ochsendorf, J., 2006. As Hangs the Flexible Line: Equilibrium of Masonry Arches. Nexus Network Journal, 8(2), pp.13–24. Available at: http://link.springer.com/10.1007/s00004-006-0015-9 [Accessed March 10, 2015].

Bulovic, I., 2014. Catenary vaults: a solution to low-cost housing in South Africa. Johannesburg. MSc. University of Witwatersrand. Available at: http://wiredspace.wits.ac.za/handle/10539/17554 [Accessed November 3, 2015].

Carvalho, E.C., 1998. Seismic Testing of Structures. In: P. Bisch , P. Labbe & A. Peckers, eds. 1998. Earthquake Engineering - Invited Papers: Proceedings of the Eleventh European Conference, Paris, France, 6-11 September 1998: CRC Press. pp 53-64

Clemente, P., 1998. Introduction to dynamics of stone arches. Earthquake Engineering & Structural Dynamics, 27(5), pp.513–522. Available at: http://onlinelibrary.wiley.com/doi/10.1002/ (SICI) 1096-9845(199805)27:5<513:: AID-EQE740>3.0.CO;2-O/abstract [Accessed March 11, 2015].

Colombo, C., Vergani, L. & Burman, M., 2012. Static and fatigue characterisation of new basalt fibre reinforced composites. Composite Structures, 94(3), pp.1165–1174. Available at: http://linkinghub.elsevier.com/retrieve/pii/S0263822311003709 [Accessed November 9, 2015].

DeJong, M.J., 2009. Seismic assessment strategies for masonry structures. Ph.D. University of Cambridge. Available at: http://dspace.mit.edu/handle/1721.1/49538 [Accessed February 24, 2015].

DeJong, M.J. *et al.*, 2008. Rocking Stability of Masonry Arches in Seismic Regions. Earthquake Spectra, 24(4), pp.847–865. Available at: http://www.earthquakespectra.org/doi/abs/10.1193/1.2985763 [Accessed February 24, 2015].

DeJong, M.J., Ramage, M.H., Travers, B., Terry, S., 2011. Testing and analysis of geogrid-reinforced thin-shell masonry. In: 35th Annual Symposium of IABSE / 52nd Annual Symposium of IASS / 6th International Conference on Space Structures, Taller, Longer, Lighter - Meeting growing demand with limited resources. London, September 2011. Switzerland: IABSE / IASS.

De Lorenzis, L., DeJong, M. & Ochsendorf, J., 2007. Failure of masonry arches under impulse base motion. Earthquake Engineering & Structural Dynamics, 36(14), pp.2119–2136. Available at: http://onlinelibrary.wiley.com/doi/10.1002/eqe.719/abstract [Accessed March 30, 2015].

De Luca, A., Giordano, A. & Mele, E., 2004. A simplified procedure for assessing the seismic capacity of masonry arches. Engineering Structures, 26(13), pp.1915–1929. Available at: http://linkinghub.elsevier.com/retrieve/pii/S0141029604002263 [Accessed January 12, 2016].

Federal Emergency Management Agency, 2009. Unreinforced Masonry Buildings and Earthquakes: Developing Successful Risk Reduction Programmes. (FEMA P-774). Washington: FEMA.

Fiore, V. *et al.*, 2015. A review on basalt fibre and its composites. Composites Part B: Engineering, 74, pp.74–94. Available at: http://linkinghub.elsevier.com/retrieve/pii/S1359836815000062 [Accessed November 9, 2015].

Fitchett, A.S., 2009. Skills development and employment creation through small public buildings in South Africa. Ph.D. University of Witwatersrand. Available at: http://wiredspace.wits.ac.za/handle/10539/7217 [Accessed February 24, 2015].

Garmendia, L. *et al.*, 2011. Rehabilitation of masonry arches with compatible advanced composite material. Construction and Building Materials, 25(12), pp.4374–4385. Available at: http://linkinghub.elsevier.com/retrieve/pii/S0950061811001309 [Accessed November 20, 2015].

Gibbs, M.J., Peter Soyka & David Coneely, CO_2 emissions from cement production.

Gilbert, R.I. & Mickleborough, N.C., 1990. Design of Prestressed Concrete, CRC Press.

Gohnert, M., 2015. Interview on the equation for a catenary arch subjected to self-weight loading. Interview by Daniel Surat {verbal exchange]. University of Witwatersrand, 22 June 2015.

Harris, C.M., 2006. Dictionary of architecture & construction, McGraw-Hill.

Heyman, J., 1966. The stone skeleton. International Journal of Solids and Structures, 2(2), pp.249–279. Available at: http://www.sciencedirect.com/science/article/pii/0020768366900187 [Accessed February 24, 2015].

Housner, G.W., 1963. The behavior of inverted pendulum structures during earthquakes. Bulletin of the seismological society of America, 53(2), pp.403–417. Available at: http://www.bssaonline.org/content/53/2/403.short [Accessed January 14, 2016].

Lopresto, V., Leone, C. & De Iorio, I., 2011. Mechanical characterisation of basalt fibre reinforced plastic. Composites Part B: Engineering, 42(4), pp.717–723. Available at: http://linkinghub.elsevier.com/retrieve/pii/S1359836811000588 [Accessed November 9, 2015].

Mendes, N., Lourenço, P.B. & Costa, A.C., 2010. Shaking table tests of stone masonry buildings. Available at: http://repositorium.sdum.uminho.pt/handle/1822/19037 [Accessed April 6, 2015].

Megson, T.H., 2005. Structural and Stress Analysis, Second Edition 2 edition. Amsterdam ; Boston: Butterworth-Heinemann.

Minke, G., 2012. Building with Earth 3 Revised edition. Basel, Switzerland: Birkhaeuser.

OCHA, 2007. Earthquake Risk in Africa: Modified Mercalli Scale. OCHA Regional Office for Central and East Africa. Available at: http://www.preventionweb.net/english/professional/maps/v.php?id=7483 [Accessed December 18, 2016]

Ochsendorf, J.A., 2002. Collapse of masonry structures. Ph.D. University of Cambridge. Available at: http://www.repository.cam.ac.uk/handle/1810/244820 [Accessed February 25, 2015].

Oppenheim, I.J., 1992. The masonry arch as a four-link mechanism under base motion. Earthquake Engineering & Structural Dynamics, 21(11), pp.1005–1017. Available at: http://onlinelibrary.wiley.com/doi/10.1002/eqe.4290211105/abstract [Accessed February 24, 2015].

Pedreschi, R., The Structural Behaviour and Design of Free-Standing Barrel Vaults of Eladio Dieste. Available at: http://www.arct.cam.ac.uk/Downloads/ichs/vol-3-2451-2468-pedreschi.pdf [Accessed February 25, 2015].

Saravanan, D., 2006. Spinning the Rocks - Basalt Fibres. IE(I) Journal- TX, 86.

Scheffler, C. *et al.*, 2009. Aging of alkali-resistant glass and basalt fibers in alkaline solutions: Evaluation of the failure stress by Weibull distribution function. Journal of Non-Crystalline Solids, 355(52), pp.2588–2595. Available at: http://www.sciencedirect.com/science/article/pii/S0022309309006322 [Accessed November 19, 2015].

Seedat, H. & Surat, D., 2012. The integration of thin-shelled masonry vaults with green roof technology in the context of low cost housing. IP. University of Witwatersrand

Shrive, N.G., 2006. The use of fibre reinforced polymers to improve seismic resistance of masonry. Construction and Building Materials, 20(4), pp.269–277. Available at: http://www.sciencedirect.com/science/article/pii/S0950061805002734 [Accessed November 19, 2015].

Sim, J., Park, C. & Moon, D.Y., 2005. Characteristics of basalt fiber as a strengthening material for concrete structures. Composites Part B: Engineering, 36(6-7), pp.504–512. Available at: http://linkinghub.elsevier.com/retrieve/pii/S1359836805000454 [Accessed November 9, 2015].

South African Bureau of Standards, 2011. *SANS 10160-4:2011 Basis of structural design and actions for buildings and industrial structures: Part 4: Seismic actions and general requirements for buildings*. Pretoria: SABS.

Spall, H. and Schnabel, D.C., 1989. *Earthquakes & Volcanoes, Volume 21, Number 1, 1989: Featuring the US Geological Survey's National Earthquake Information Center in Golden, Colorado, USA*. Government Printing Office. Available at: https://pubs.er.usgs.gov/publication/70039068 [Accessed December 08,2016]

Terry, S., 2011. Seismic analysis and design of geotextile reinforced masonry vaults. MEng. Cambridge University.

United States Geological Survey. 2015. Largest and Deadliest Earthquakes by Year: 1990-2014. [ONLINE] Available at: http://earthquake.usgs.gov/earthquakes/eqarchives/year/byyear.php. [Accessed 15 March 2015].

United States Geological Survey. 1989. The Severity of an Earthquake. *USGS General Interest Publication 1989-288-913* [ONLINE] Available at: https://pubs.usgs.gov/gip/earthq4/severitygip.html. [Accessed 23 November 2016].

Valuzzi, M.R., Valdemarca, M. & Modena, C., 2001. Behaviour of brick masonry vaults strengthened with FRP laminates. Journal of Composites for Construction.

Wald, D.J., Quitoriano, V., Heaton, T.H. and Kanamori, H., 1999. Relationships between peak ground acceleration, peak ground velocity, and modified Mercalli intensity in California. *Earthquake spectra*, *15*(3), pp.557-564.

Yang, G., 2010. Dynamic analyses of a masonry building tested in a shaking table. SAHC Master, pp.1–114. Available at: http://www.msc-sahc.org/upload/docs/new.docs/2010_gyang.pdf [Accessed March 25, 2015].

Zhang, J. & Makris, N., 2001. Rocking response of free-standing blocks under cycloidal pulses. Journal of Engineering Mechanics, 127(5), pp.473–483.

Photographic references

Millennium Winter Gardens, Sheffield, Yorkshire, England, United Kingdom, Europe. [Photography]. Encyclopaedia Britannica ImageQuest. Retrieved 19 Nov 2015, from http://quest.eb.com/search/151_2591715/1/151_2591715/cite

The Gateway Arch in St. Louis, Missouri. [Photography]. Encyclopaedia Britannica ImageQuest. Retrieved 19 Nov 2015, from http://quest.eb.com/search/139_1951100/1/139_1951100/cite

Section of St. Paul's Cathedral, decorated agreeab. [Fine Art]. Encyclopaedia Britannica ImageQuest. Retrieved 19 Nov 2015, from http://quest.eb.com/search/163_2973708/1/163_2973708/cite

?Umbracle? in City of Arts and Sciences by Santiago Calatrava, Valencia. Spain. [Photo]. Encyclopaedia Britannica ImageQuest. Retrieved 19 Nov 2015, from http://quest.eb.com/search/164_3235259/1/164_3235259/cite

APPENDIX A- ACCELERATION TIME HISTORY AND LEAST-SQUARE APPROXIMATION GRAPHS

Unreinforced Tests

Fixed stroke, varying frequency

In all the fixed stroke tests, acceleration numbers relate to the following accelerometer locations:

Acceleration #	Accelerometer location
1	Base
2	Side- Horizontal
3	Side- Vertical
4	Apex

All accelerations are measured as a percentage of gravitational acceleration (g=9.81 m/s^2).

0.8 h/w ratio tests

First test

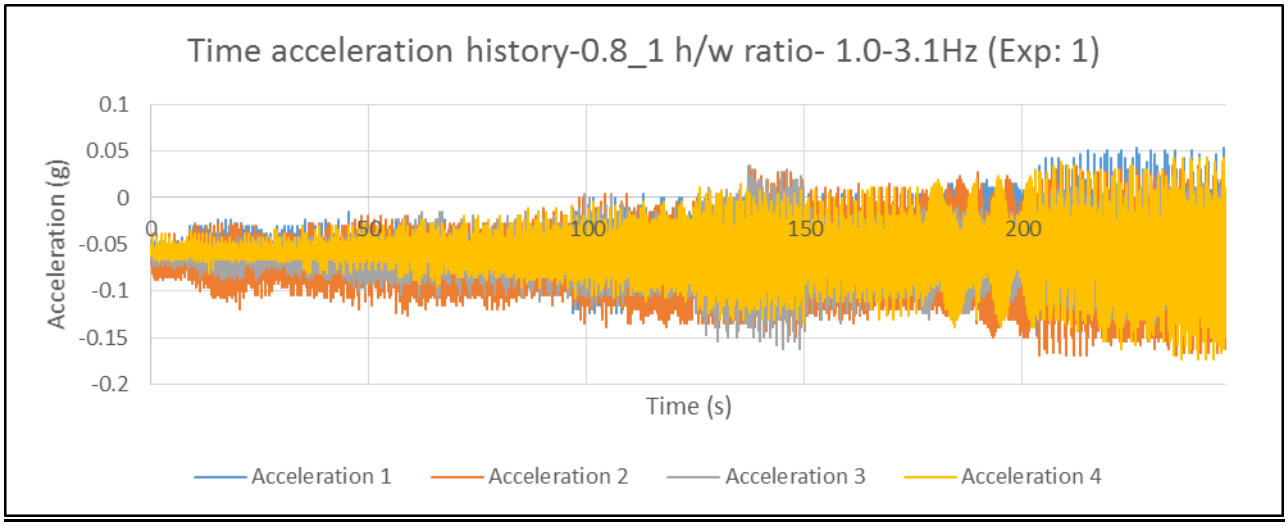

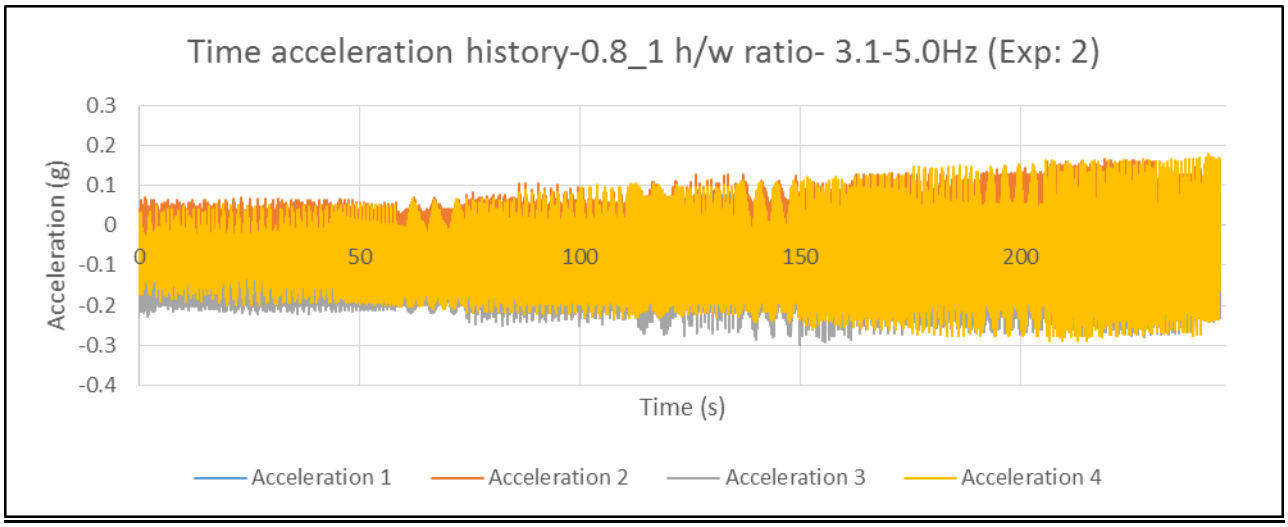

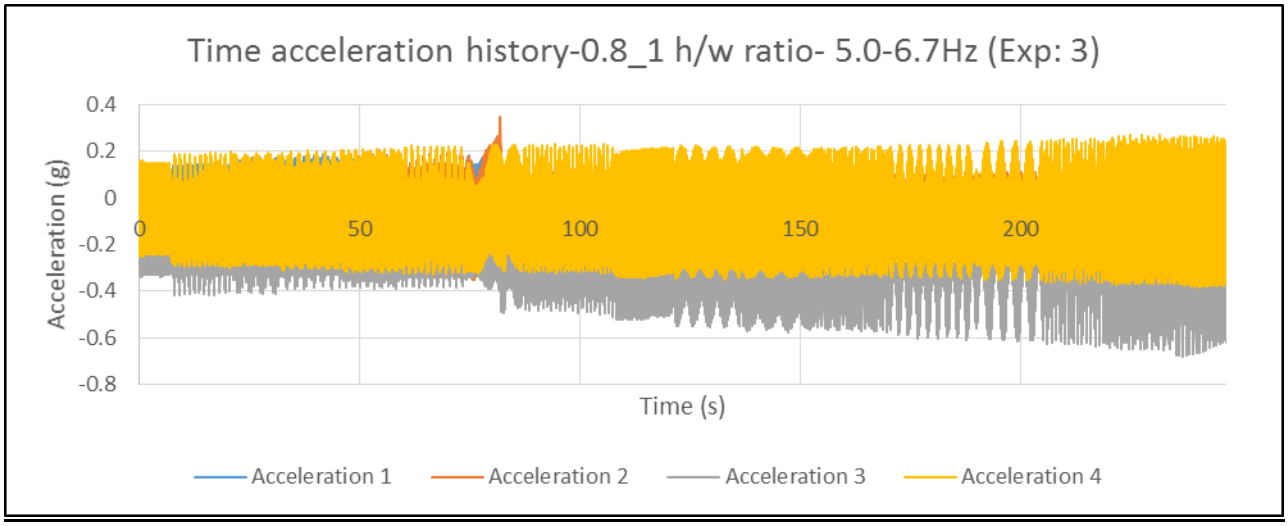
Time acceleration history-0.8_1 h/w ratio- 5.0-6.7Hz (Exp: 3)
Acceleration (g)
0.4
0.2
0
-0.2
-0.4
-0.6
-0.8
0
50
100
150
200
Time (s)
Acceleration 1
Acceleration 2
Acceleration 3
Acceleration 4

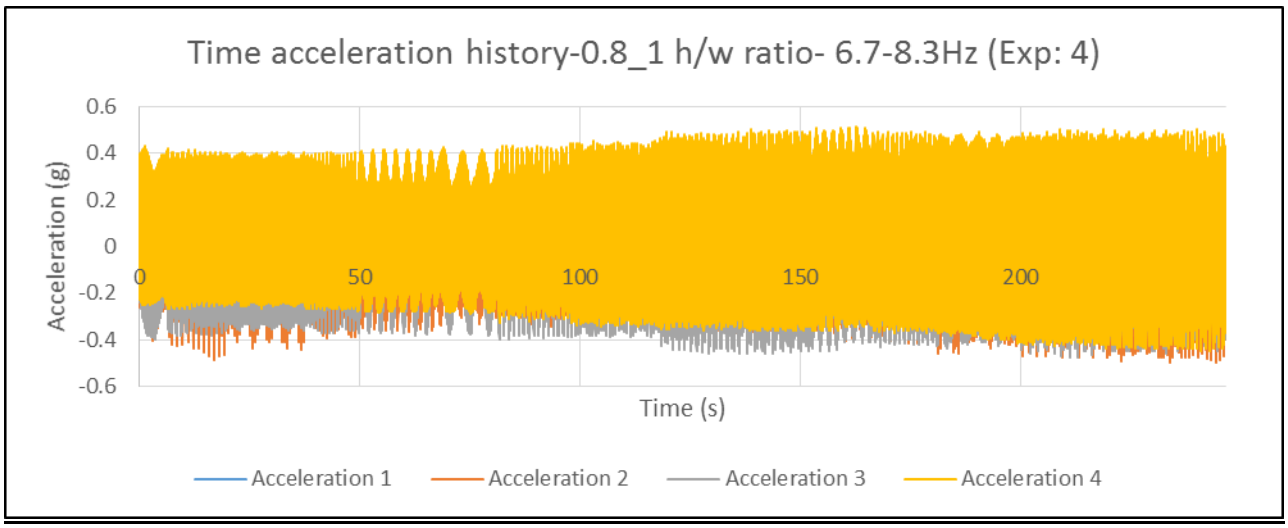
Time acceleration history-0.8_1 h/w ratio- 6.7-8.3Hz (Exp: 4)
Acceleration (g)
0.6
0.4
0.2
0
-0.2
-0.4
-0.6
0
50
100
150
200
Time (s)
Acceleration 1
Acceleration 2
Acceleration 3
Acceleration 4

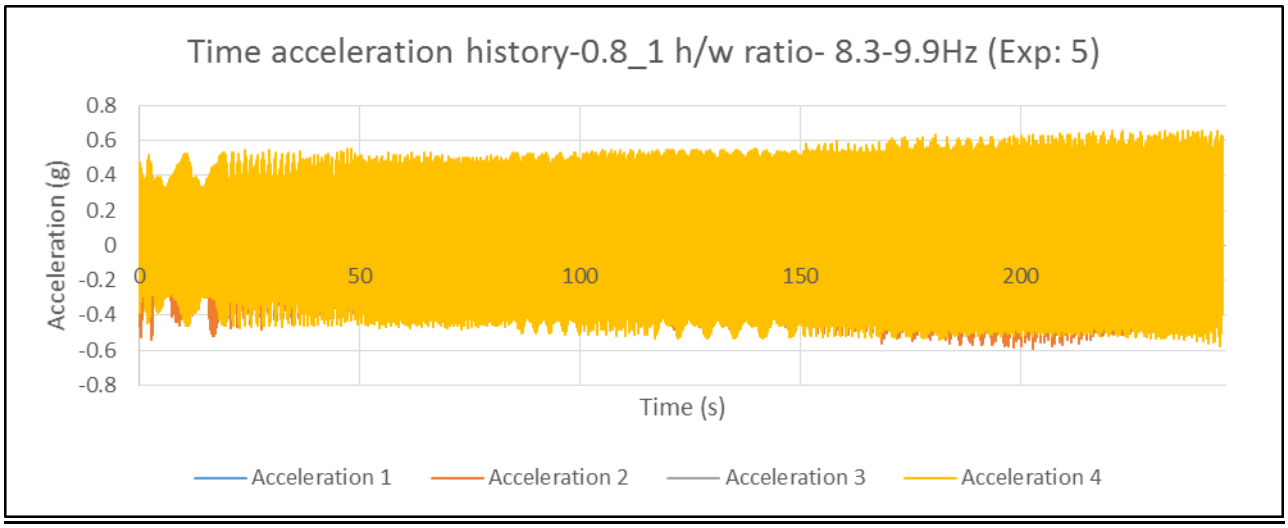
Time acceleration history-0.8_1 h/w ratio- 8.3-9.9Hz (Exp: 5)
Acceleration (g)
0.8
0.6
0.4
0.2
0
-0.2
-0.4
-0.6
-0.8
0
50
100
150
200
Time (s)
Acceleration 1
Acceleration 2
Acceleration 3
Acceleration 4

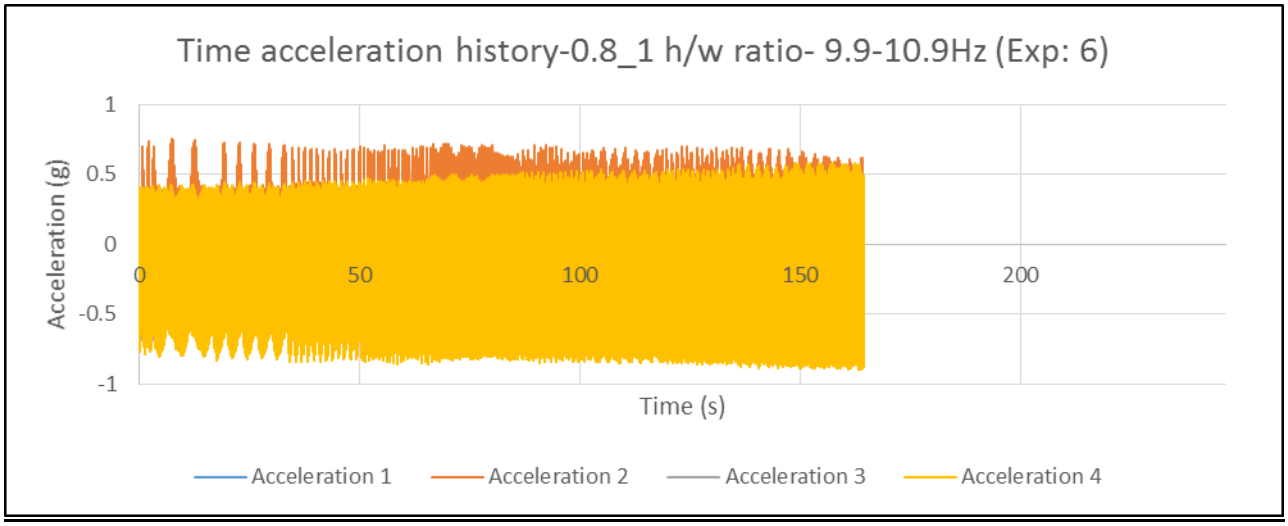
Time acceleration history-0.8_1 h/w ratio- 9.9-10.9Hz (Exp: 6)
Acceleration (g)
1
0.5
0
-0.5
-1
0
50
100
150
200
Time (s)
Acceleration 1
Acceleration 2
Acceleration 3
Acceleration 4

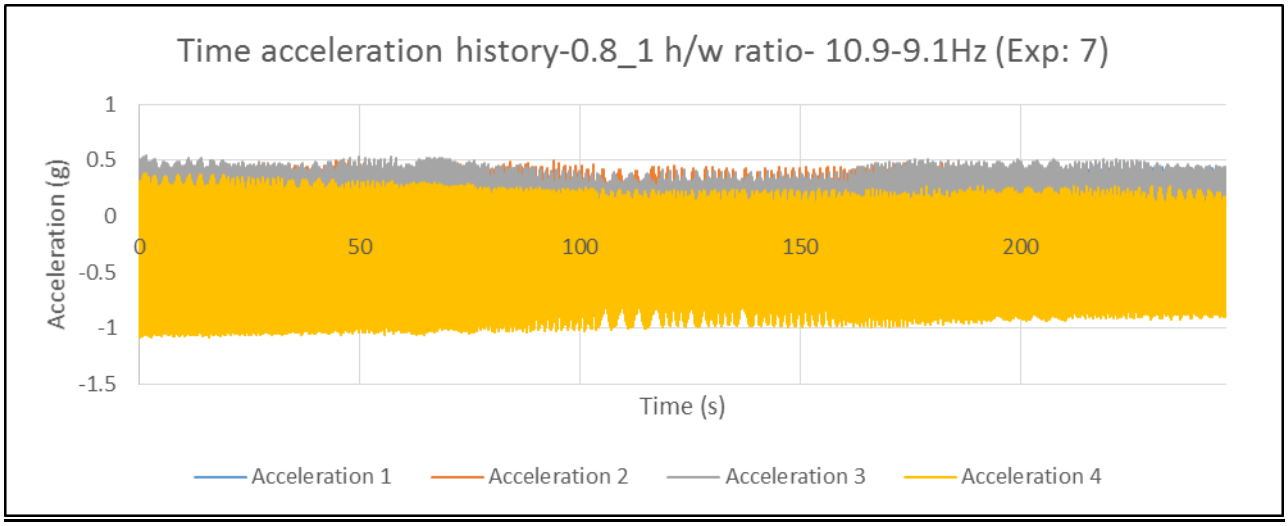
Time acceleration history-0.8_1 h/w ratio- 10.9-9.1Hz (Exp: 7)
Acceleration (g)
1
0.5
0
-0.5
-1
-1.5
0
50
100
150
200
Time (s)
Acceleration 1
Acceleration 2
Acceleration 3
Acceleration 4

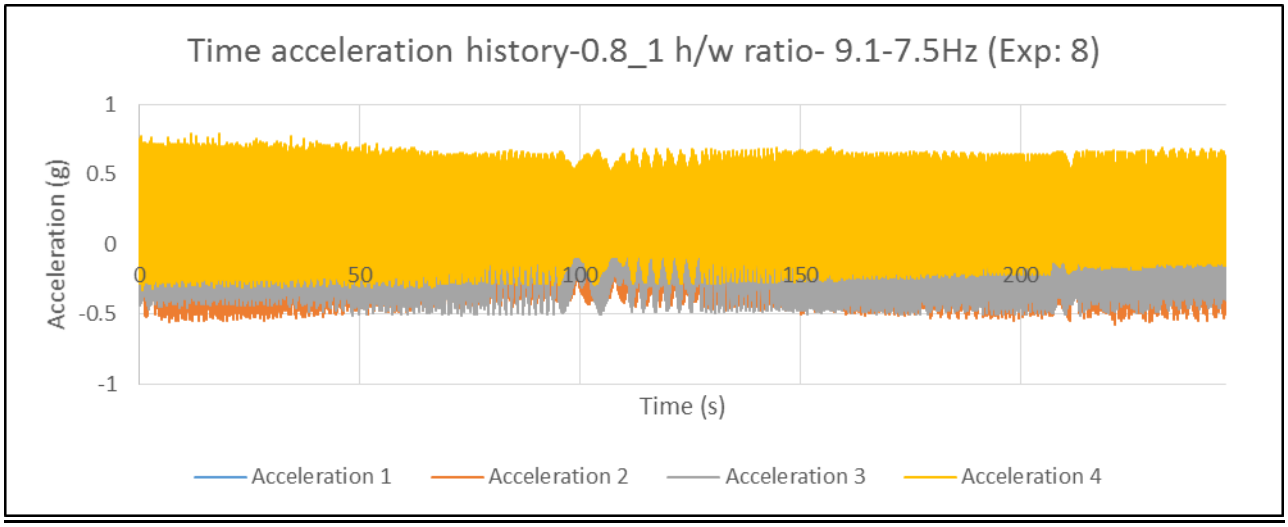
Time acceleration history-0.8_1 h/w ratio- 9.1-7.5Hz (Exp: 8)
Acceleration (g)
1
0.5
0
-0.5
-1
0
50
100
150
200
Time (s)
Acceleration 1
Acceleration 2
Acceleration 3
Acceleration 4

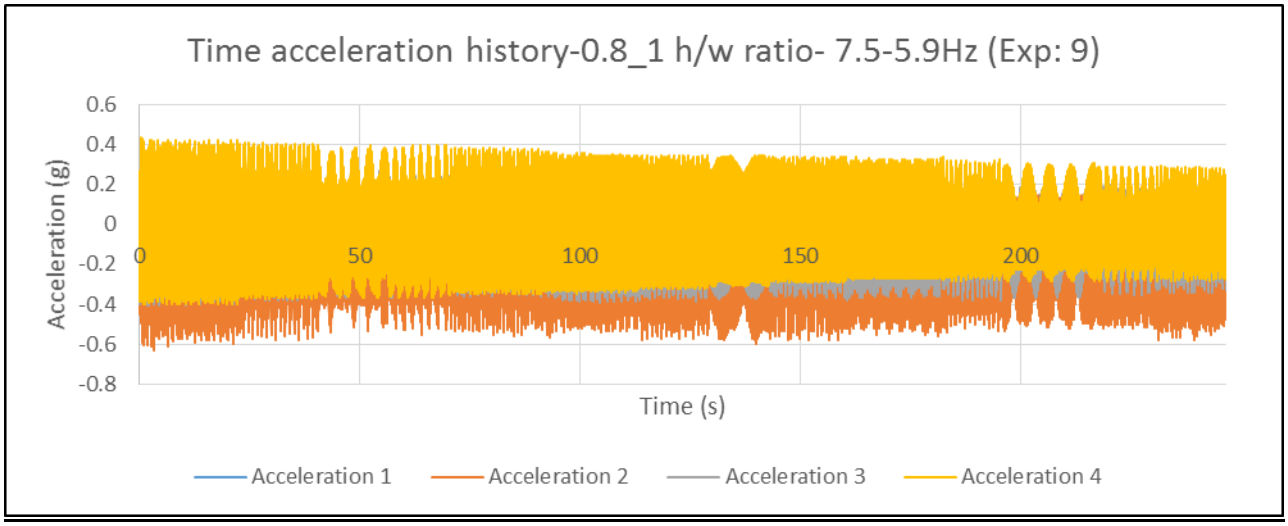
Time acceleration history-0.8_1 h/w ratio- 7.5-5.9Hz (Exp: 9)
Acceleration (g)
0.6
0.4
0.2
0
-0.2
-0.4
-0.6
-0.8
0
50
100
150
200
Time (s)
Acceleration 1
Acceleration 2
Acceleration 3
Acceleration 4

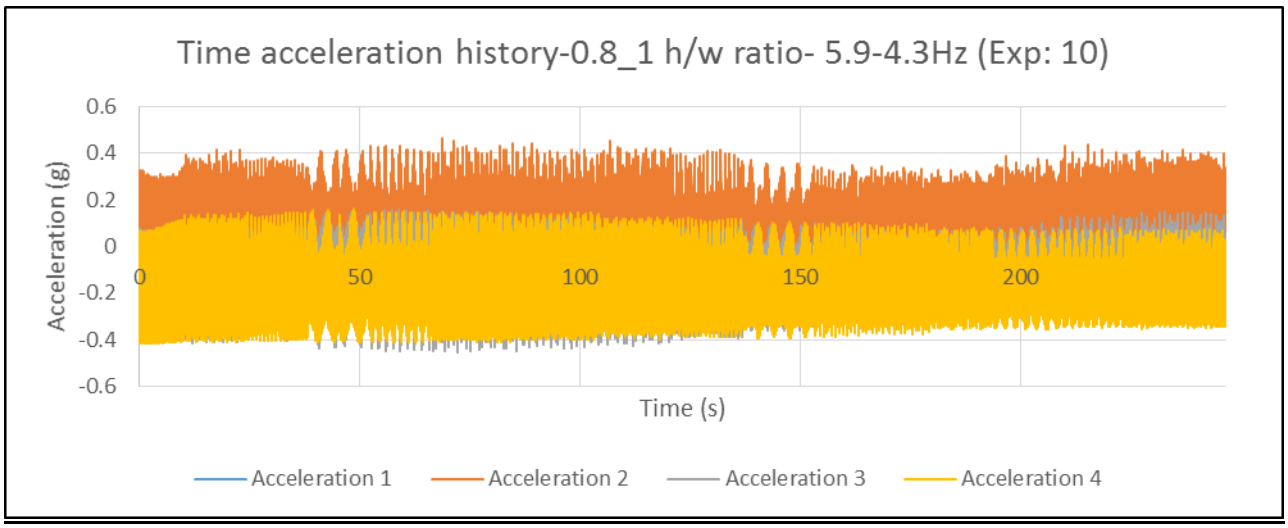
Time acceleration history-0.8_1 h/w ratio- 5.9-4.3Hz (Exp: 10)
Acceleration (g)
0.6
0.4
0.2
0
-0.2
-0.4
-0.6
0
50
100
150
200
Time (s)
Acceleration 1
Acceleration 2
Acceleration 3
Acceleration 4

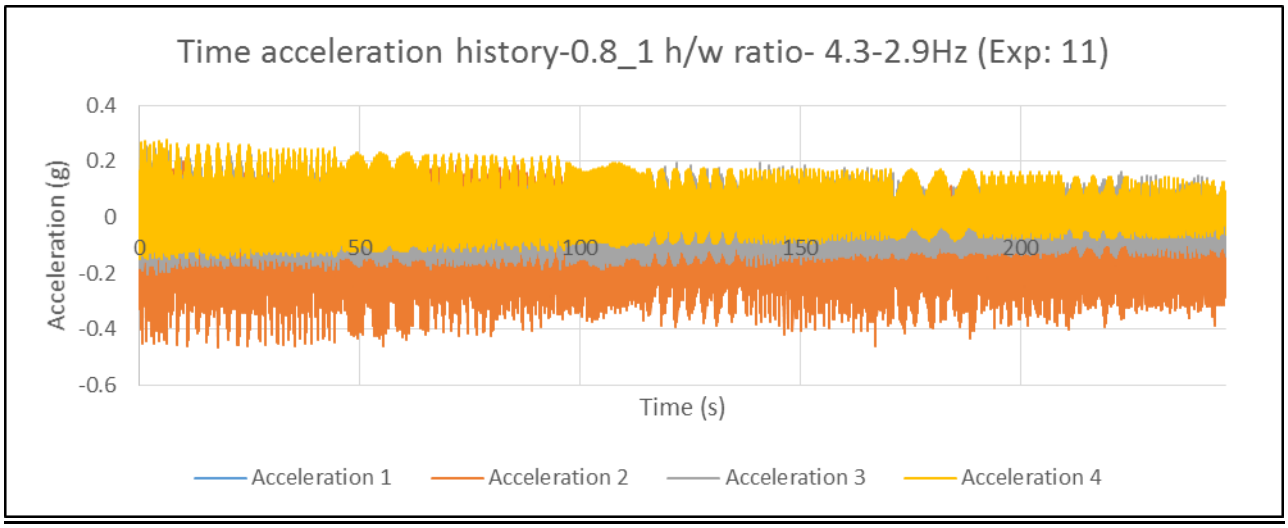
Time acceleration history-0.8_1 h/w ratio- 4.3-2.9Hz (Exp: 11)
Acceleration (g)
0.4
0.2
0
-0.2
-0.4
-0.6
0
50
100
150
200
Time (s)
Acceleration 1
Acceleration 2
Acceleration 3
Acceleration 4

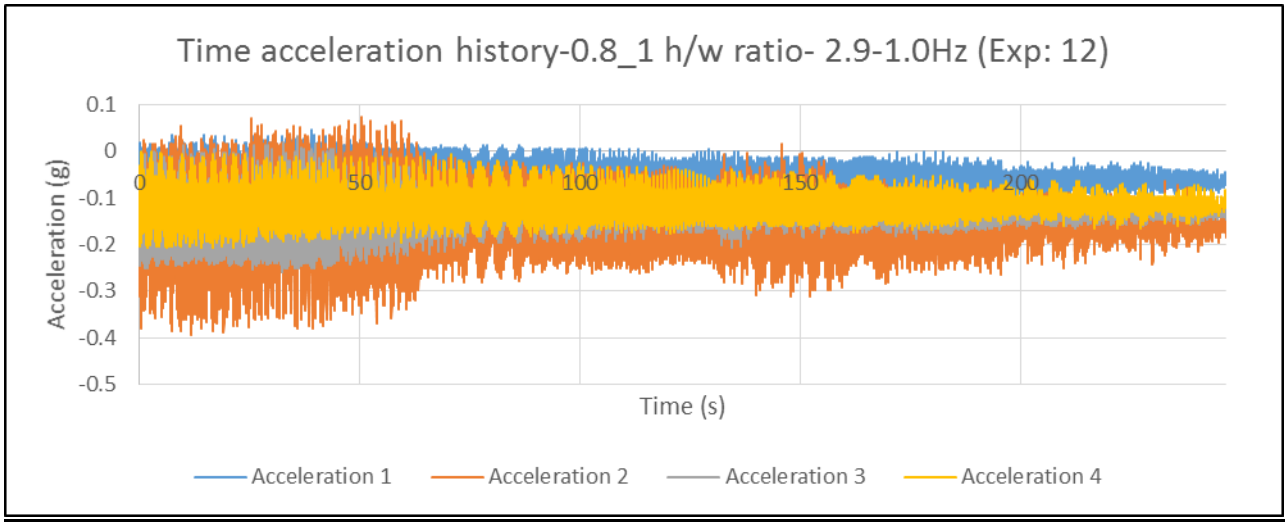
Time acceleration history-0.8_1 h/w ratio- 2.9-1.0Hz (Exp: 12)
Acceleration (g)
0.1
0
-0.1
-0.2
-0.3
-0.4
-0.5
0
50
100
150
200
Time (s)
Acceleration 1
Acceleration 2
Acceleration 3
Acceleration 4

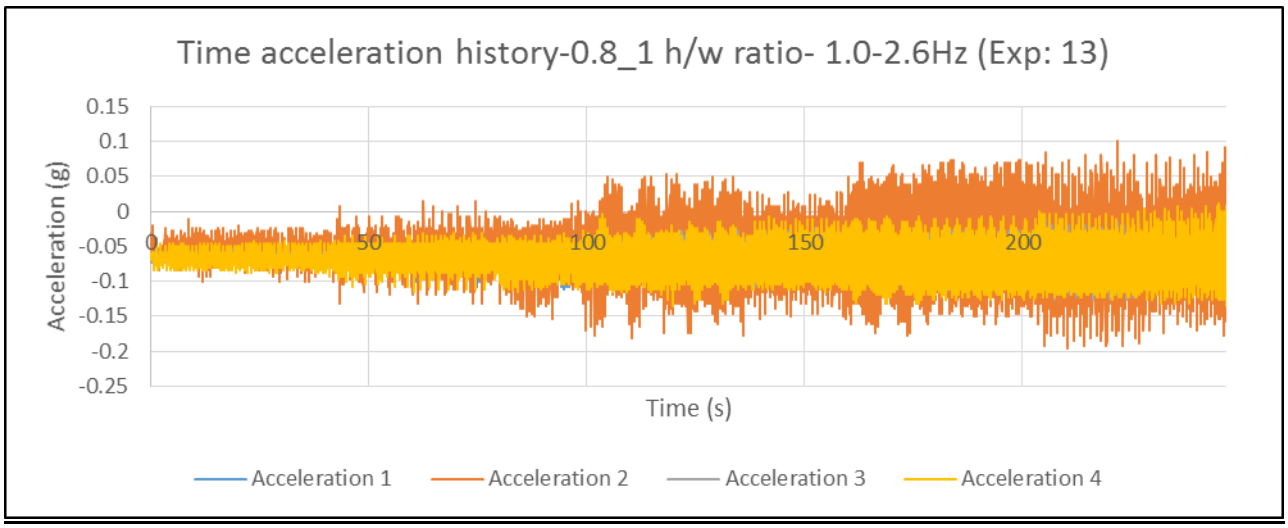
Time acceleration history-0.8_1 h/w ratio- 1.0-2.6Hz (Exp: 13)
Acceleration (g)
0.15
0.1
0.05
0
-0.05
-0.1
-0.15
-0.2
-0.25
0
50
100
150
200
Time (s)
Acceleration 1
Acceleration 2
Acceleration 3
Acceleration 4

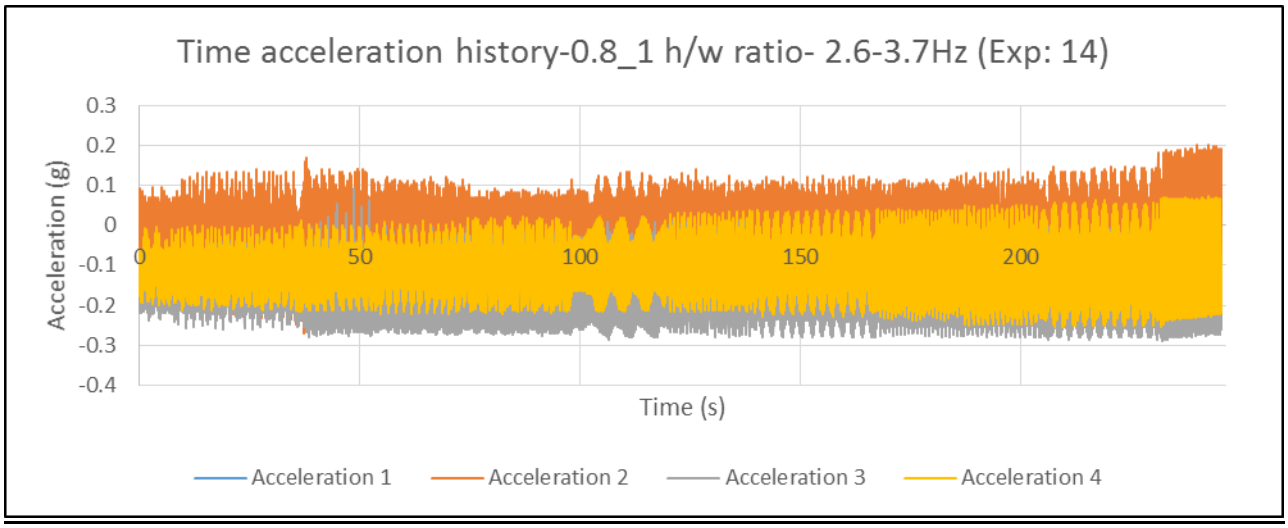
Time acceleration history-0.8_1 h/w ratio- 2.6-3.7Hz (Exp: 14)
Acceleration (g)
0.3
0.2
0.1
0
-0.1
-0.2
-0.3
-0.4
0
50
100
150
200
Time (s)
Acceleration 1
Acceleration 2
Acceleration 3
Acceleration 4

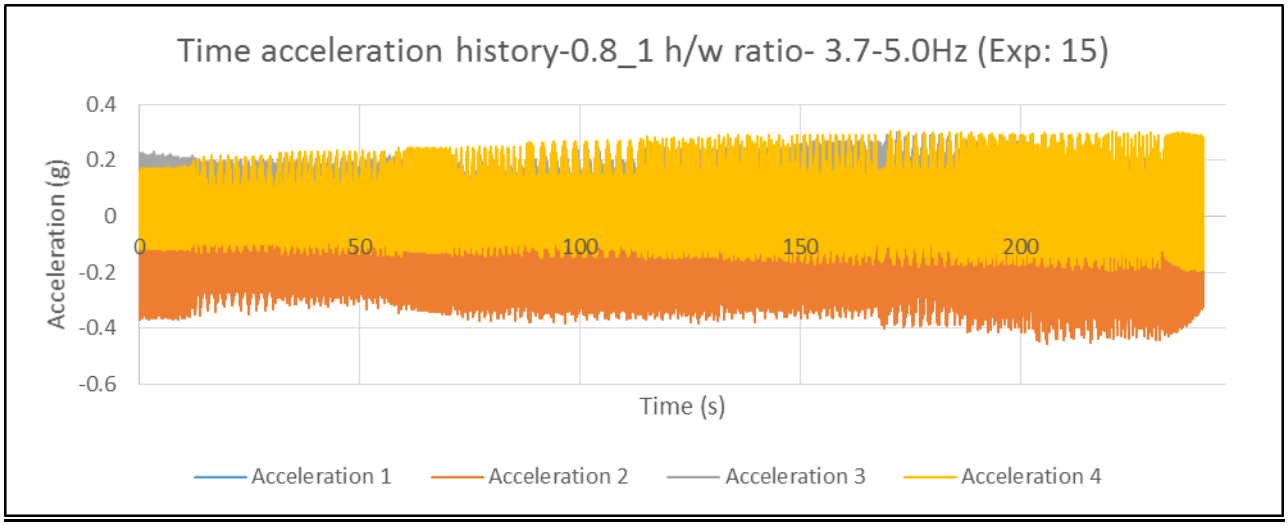
Time acceleration history-0.8_1 h/w ratio- 3.7-5.0Hz (Exp: 15)
Acceleration (g)
0.4
0.2
0
-0.2
-0.4
-0.6
0
50
100
150
200
Time (s)
Acceleration 1
Acceleration 2
Acceleration 3
Acceleration 4

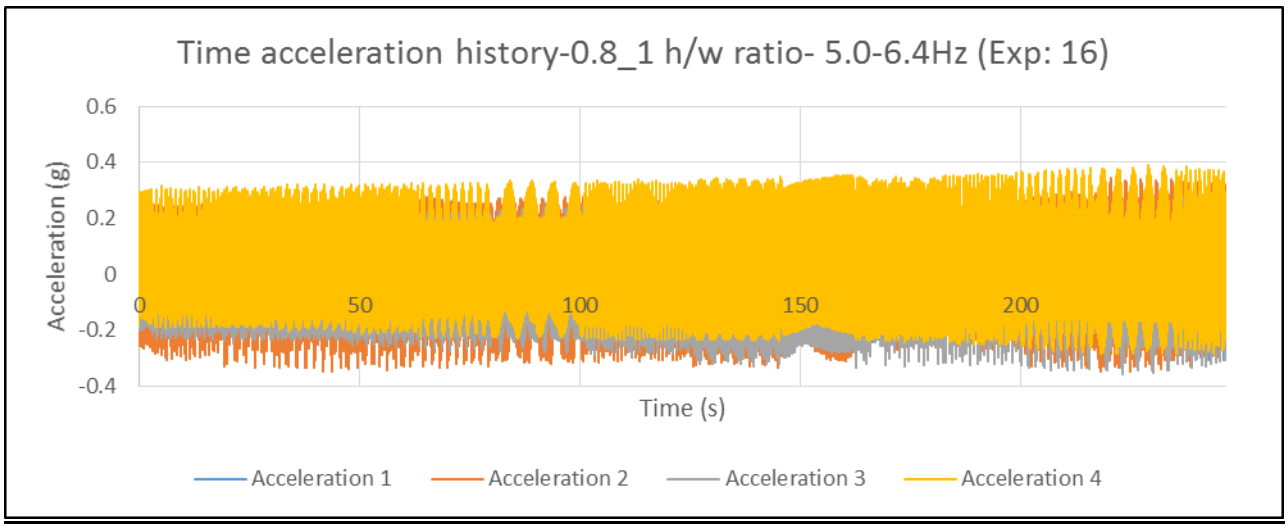
Time acceleration history-0.8_1 h/w ratio- 5.0-6.4Hz (Exp: 16)
Acceleration (g)
0.6
0.4
0.2
0
-0.2
-0.4
0
50
100
150
200
Time (s)
Acceleration 1
Acceleration 2
Acceleration 3
Acceleration 4

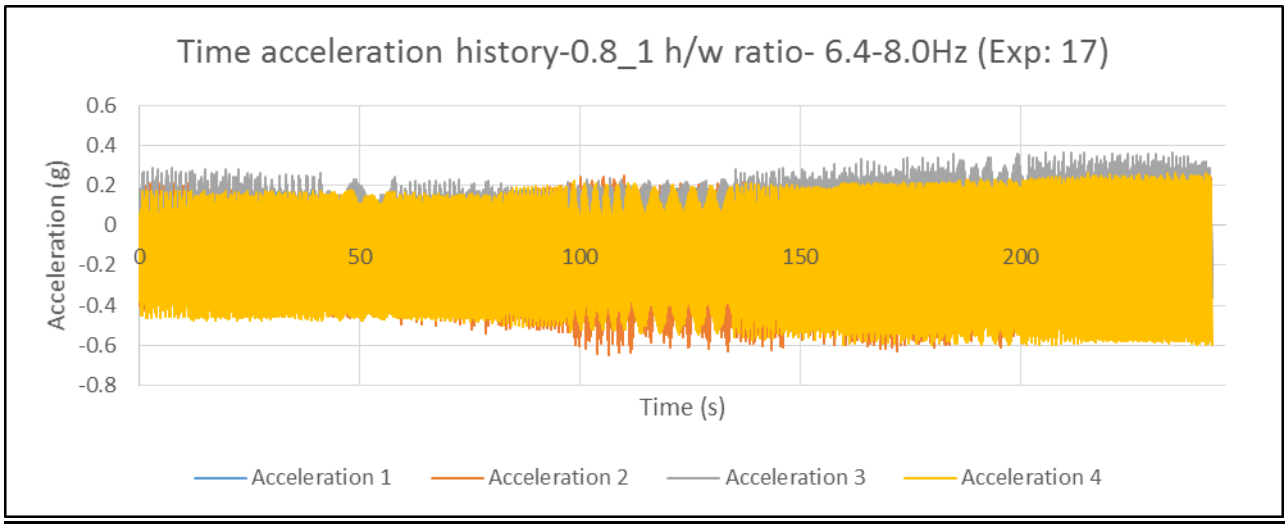
Time acceleration history-0.8_1 h/w ratio- 6.4-8.0Hz (Exp: 17)
Acceleration (g)
0.6
0.4
0.2
0
-0.2
-0.4
-0.6
-0.8
0
50
100
150
200
Time (s)
Acceleration 1
Acceleration 2
Acceleration 3
Acceleration 4

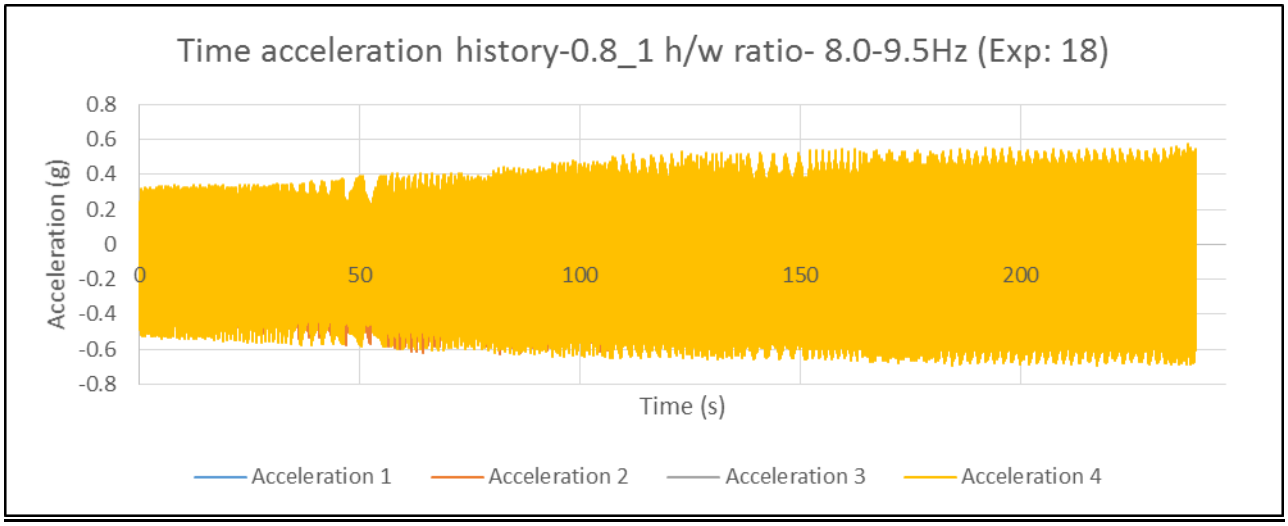
Time acceleration history-0.8_1 h/w ratio- 8.0-9.5Hz (Exp: 18)
Acceleration (g)
0.8
0.6
0.4
0.2
0
-0.2
-0.4
-0.6
-0.8
0
50
100
150
200
Time (s)
Acceleration 1
Acceleration 2
Acceleration 3
Acceleration 4

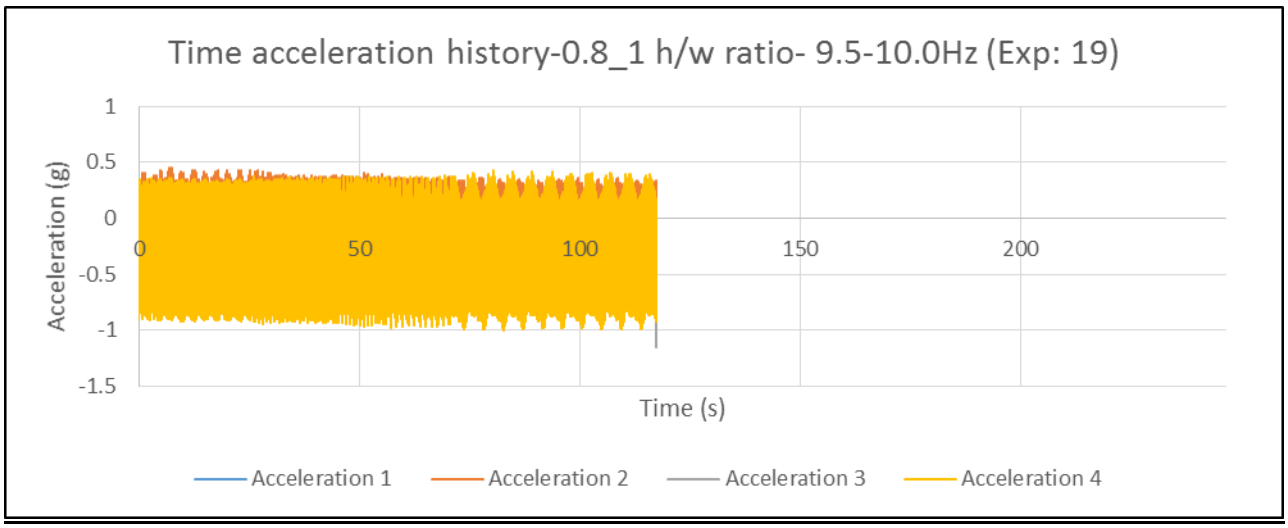
Time acceleration history-0.8_1 h/w ratio- 9.5-10.0Hz (Exp: 19)
Acceleration (g)
1
0.5
0
-0.5
-1
-1.5
0
50
100
150
200
Time (s)
Acceleration 1
Acceleration 2
Acceleration 3
Acceleration 4

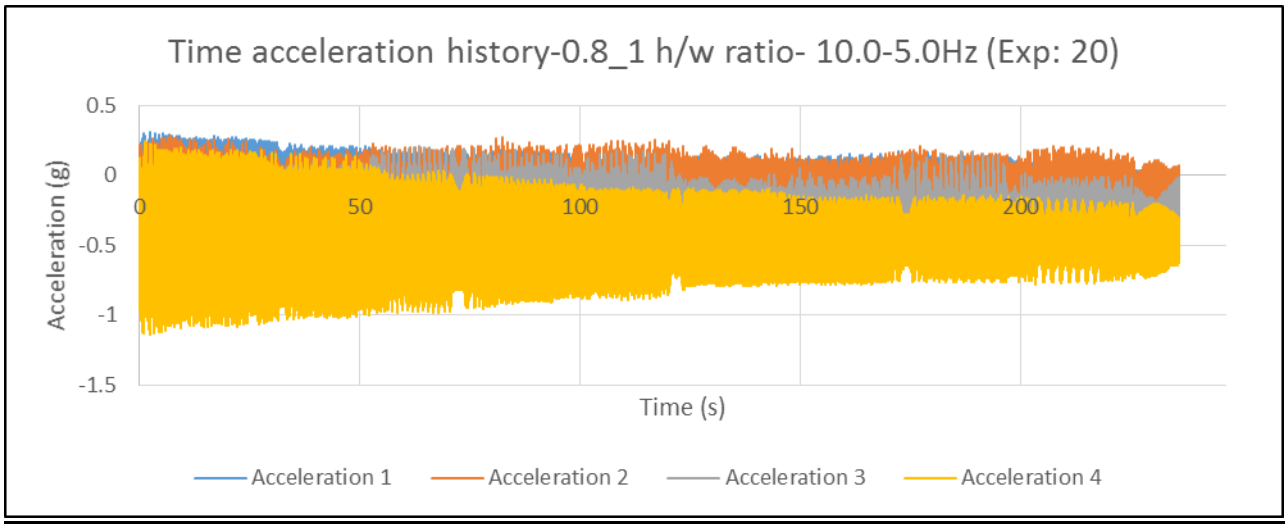
Time acceleration history-0.8_1 h/w ratio- 10.0-5.0Hz (Exp: 20)
Acceleration (g)
0.5
0
-0.5
-1
-1.5
0
50
100
150
200
Time (s)
Acceleration 1
Acceleration 2
Acceleration 3
Acceleration 4

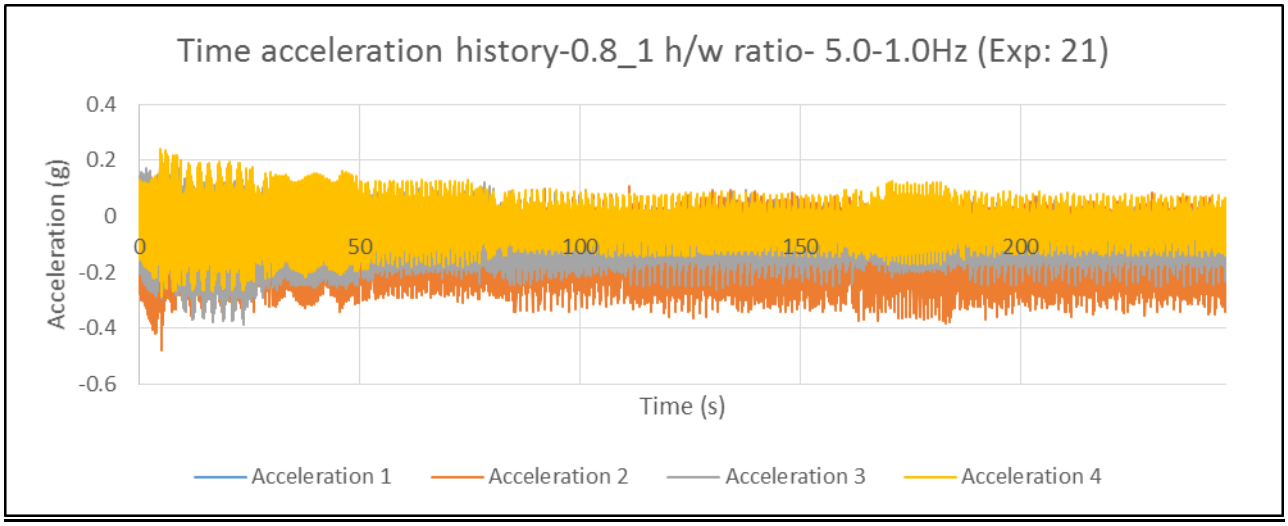
Time acceleration history-0.8_1 h/w ratio- 5.0-1.0Hz (Exp: 21)
Acceleration (g)
0.4
0.2
0
-0.2
-0.4
-0.6
0
50
100
150
200
Time (s)
Acceleration 1
Acceleration 2
Acceleration 3
Acceleration 4

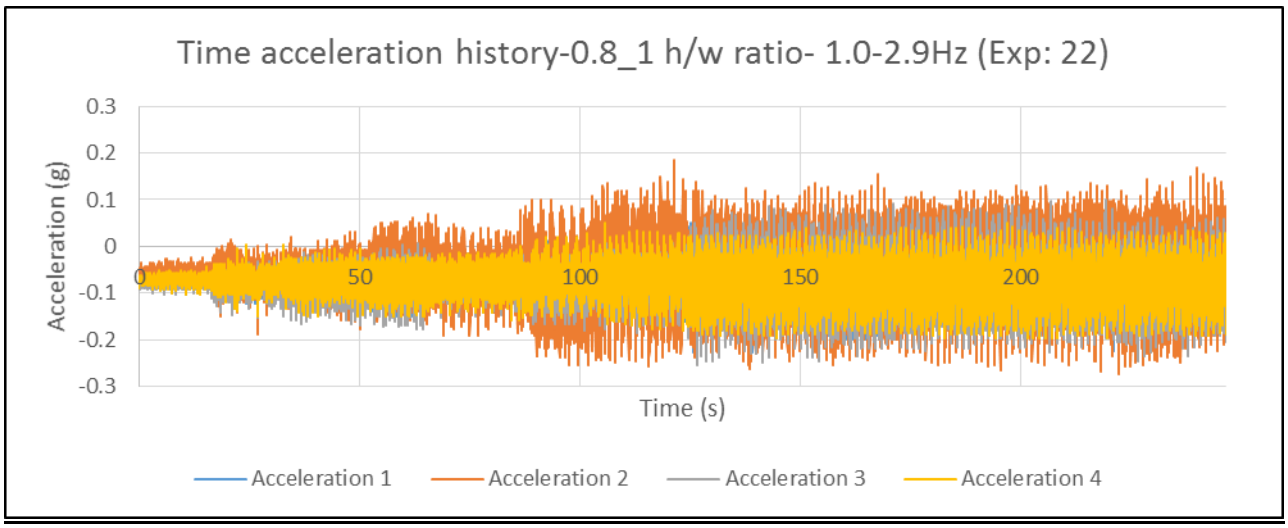
Time acceleration history-0.8_1 h/w ratio- 1.0-2.9Hz (Exp: 22)
Acceleration (g)
0.3
0.2
0.1
0
-0.1
-0.2
-0.3
0
50
100
150
200
Time (s)
Acceleration 1
Acceleration 2
Acceleration 3
Acceleration 4

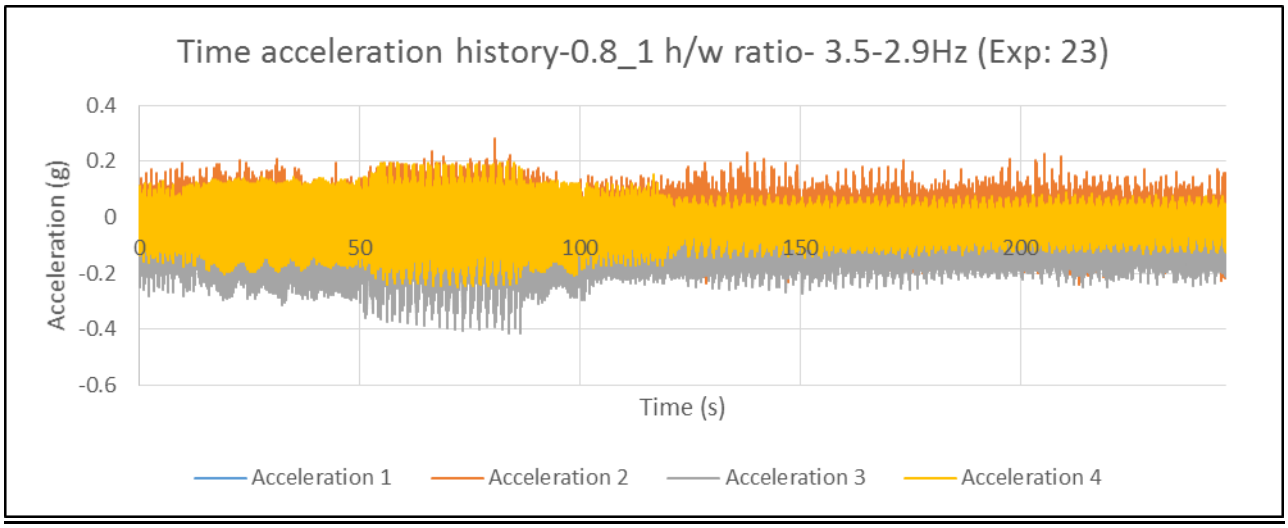
Time acceleration history-0.8_1 h/w ratio- 3.5-2.9Hz (Exp: 23)
Acceleration (g)
0.4
0.2
0
-0.2
-0.4
-0.6
0
50
100
150
200
Time (s)
Acceleration 1
Acceleration 2
Acceleration 3
Acceleration 4

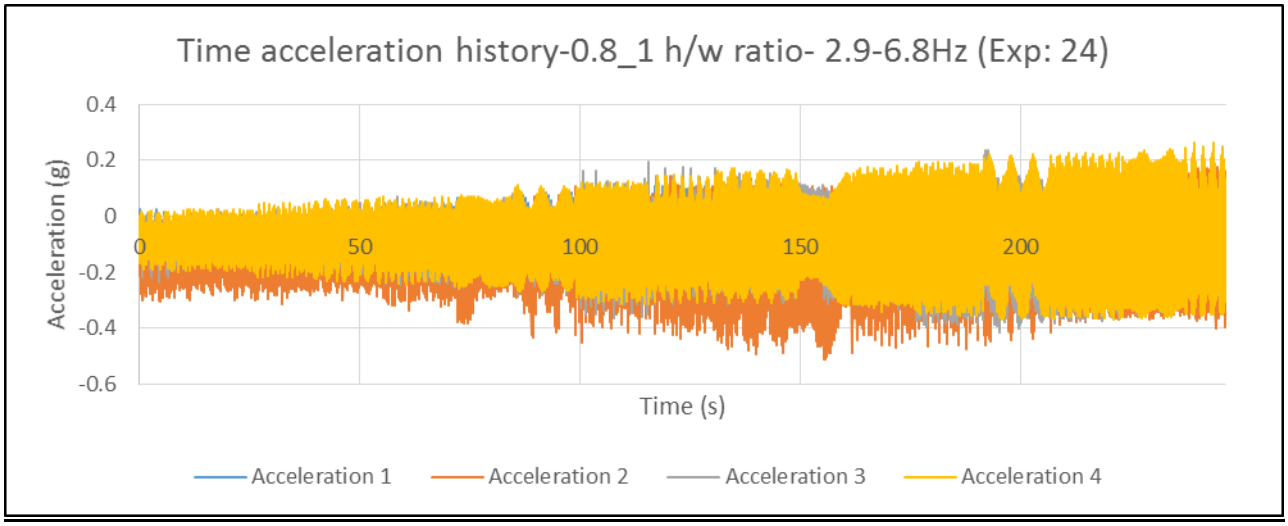
Time acceleration history-0.8_1 h/w ratio- 2.9-6.8Hz (Exp: 24)
Acceleration (g)
0.4
0.2
0
-0.2
-0.4
-0.6
0
50
100
150
200
Time (s)
Acceleration 1
Acceleration 2
Acceleration 3
Acceleration 4

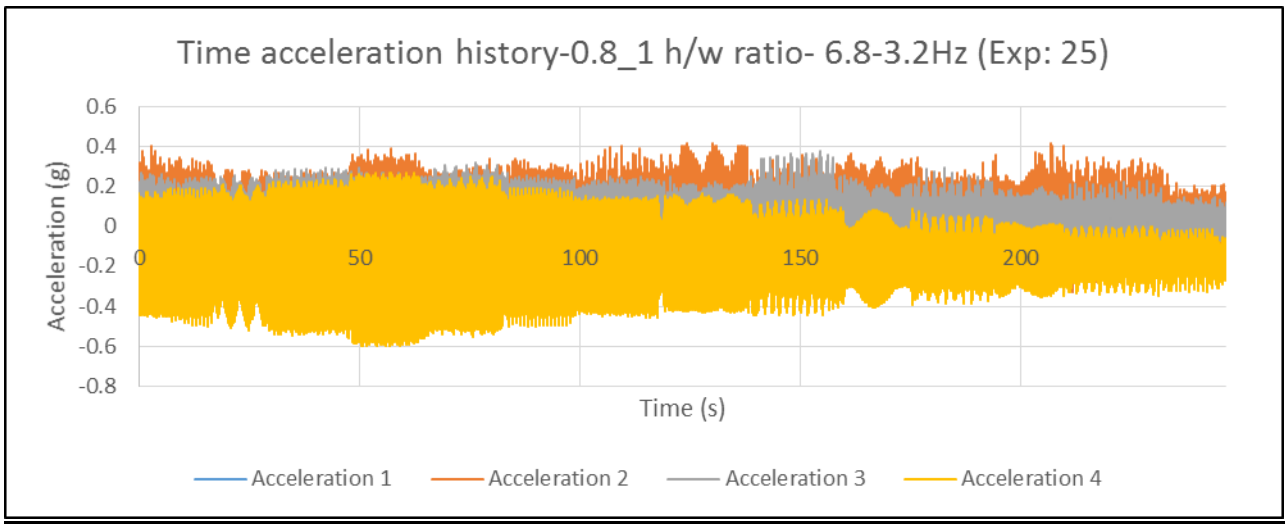
Time acceleration history-0.8_1 h/w ratio- 6.8-3.2Hz (Exp: 25)
Acceleration (g)
0.6
0.4
0.2
0
-0.2
-0.4
-0.6
-0.8
0
50
100
150
200
Time (s)
Acceleration 1
Acceleration 2
Acceleration 3
Acceleration 4

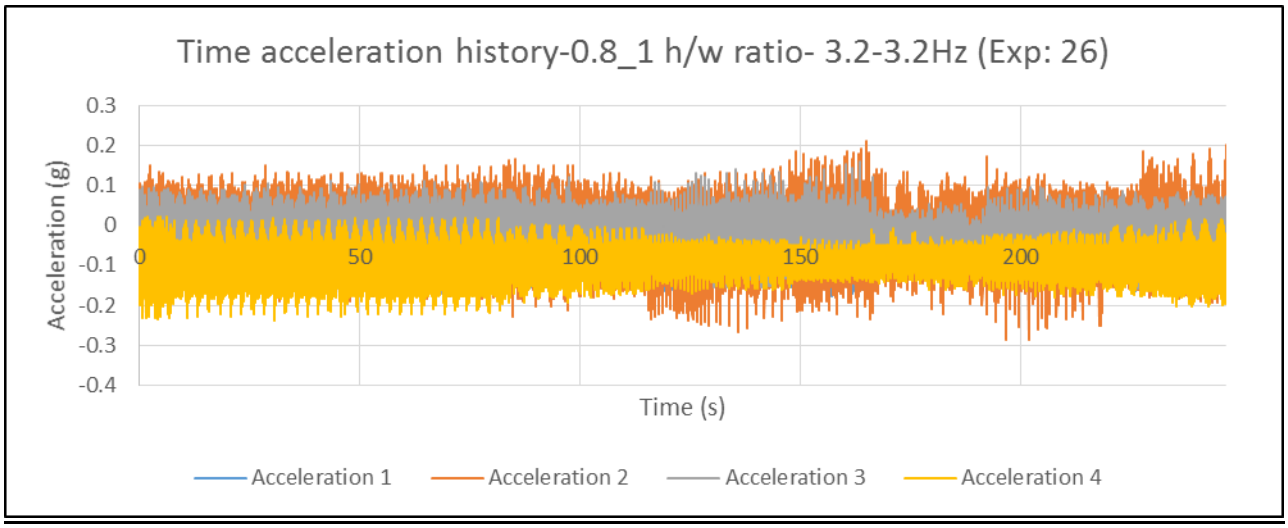
Time acceleration history-0.8_1 h/w ratio- 3.2-3.2Hz (Exp: 26)
Acceleration (g)
0.3
0.2
0.1
0
-0.1
-0.2
-0.3
-0.4
0
50
100
150
200
Time (s)
Acceleration 1
Acceleration 2
Acceleration 3
Acceleration 4

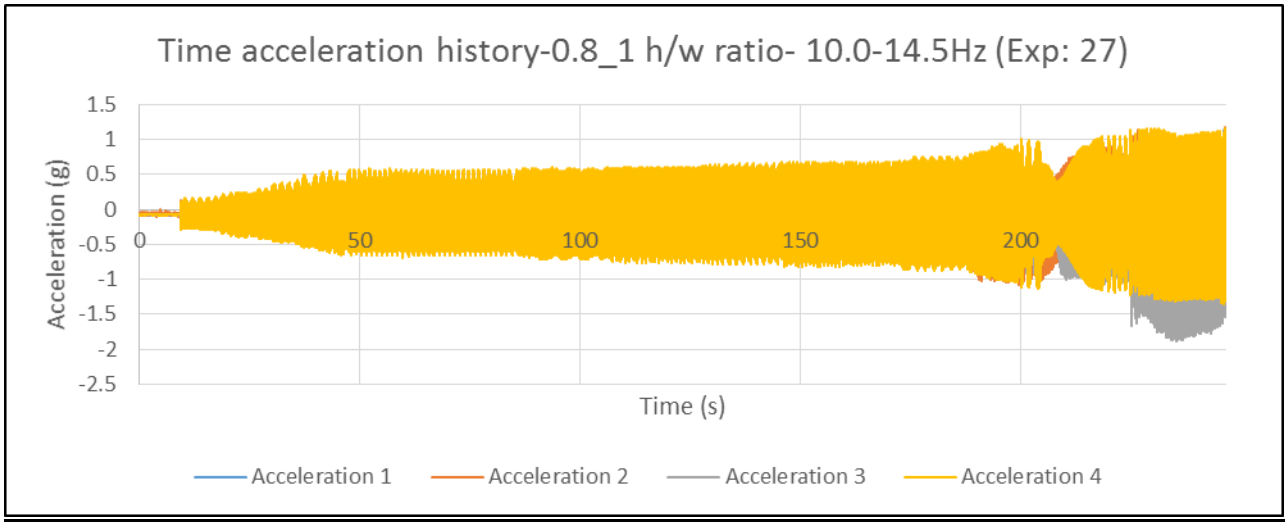
Time acceleration history-0.8_1 h/w ratio- 10.0-14.5Hz (Exp: 27)
Acceleration (g)
1.5
1
0.5
0
-0.5
-1
-1.5
-2
-2.5
0
50
100
150
200
Time (s)
Acceleration 1
Acceleration 2
Acceleration 3
Acceleration 4

Second Test

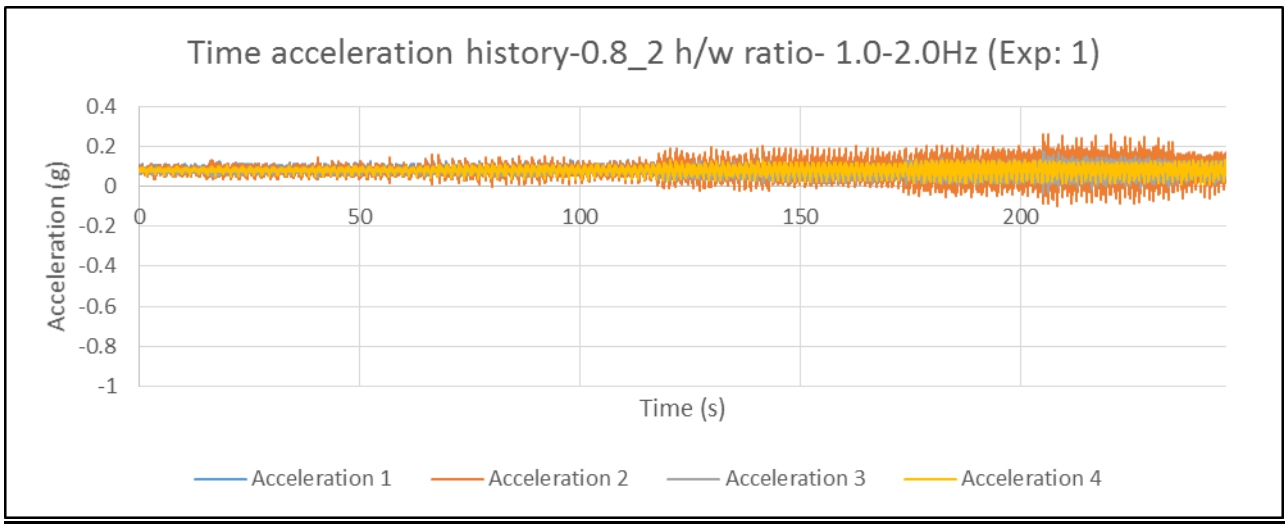
Time acceleration history-0.8_2 h/w ratio- 1.0-2.0Hz (Exp: 1)
Acceleration (g)
0.4
0.2
0
-0.2
-0.4
-0.6
-0.8
-1
0
50
100
150
200
Time (s)
Acceleration 1
Acceleration 2
Acceleration 3
Acceleration 4

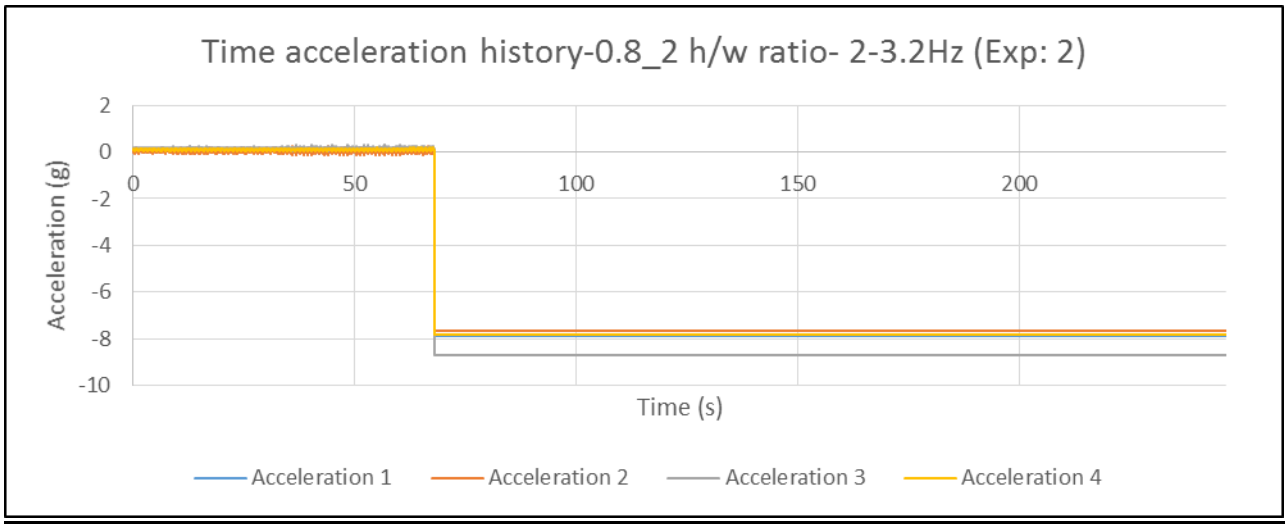
Time acceleration history-0.8_2 h/w ratio- 2-3.2Hz (Exp: 2)
Acceleration (g)
2
0
-2
-4
-6
-8
-10
0
50
100
150
200
Time (s)
Acceleration 1
Acceleration 2
Acceleration 3
Acceleration 4

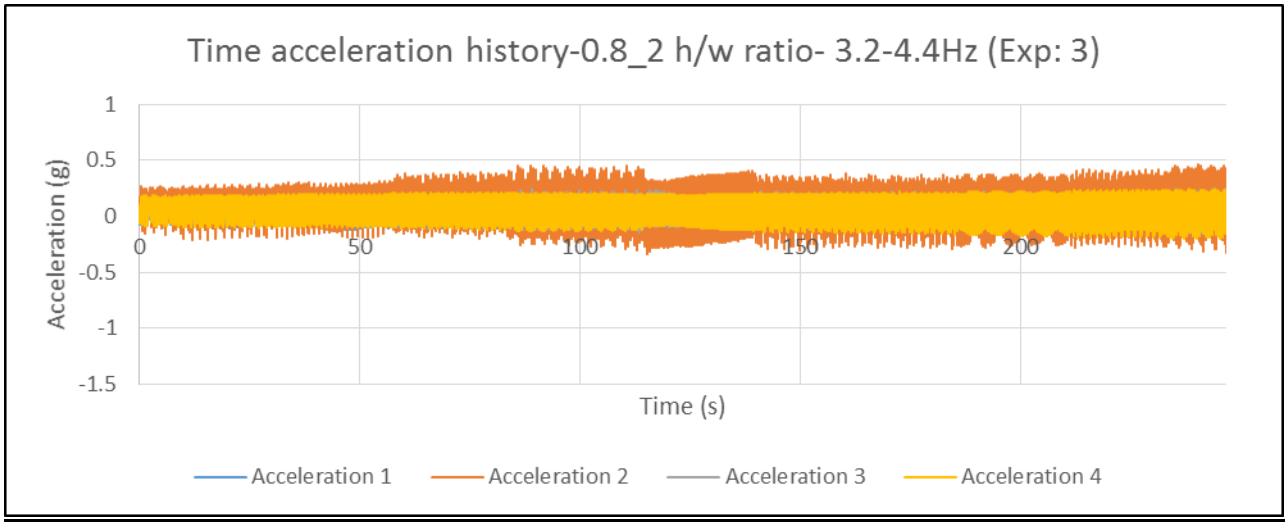
Time acceleration history-0.8_2 h/w ratio- 3.2-4.4Hz (Exp: 3)
Acceleration (g)
1
0.5
0
-0.5
-1
-1.5
0
50
100
150
200
Time (s)
Acceleration 1
Acceleration 2
Acceleration 3
Acceleration 4

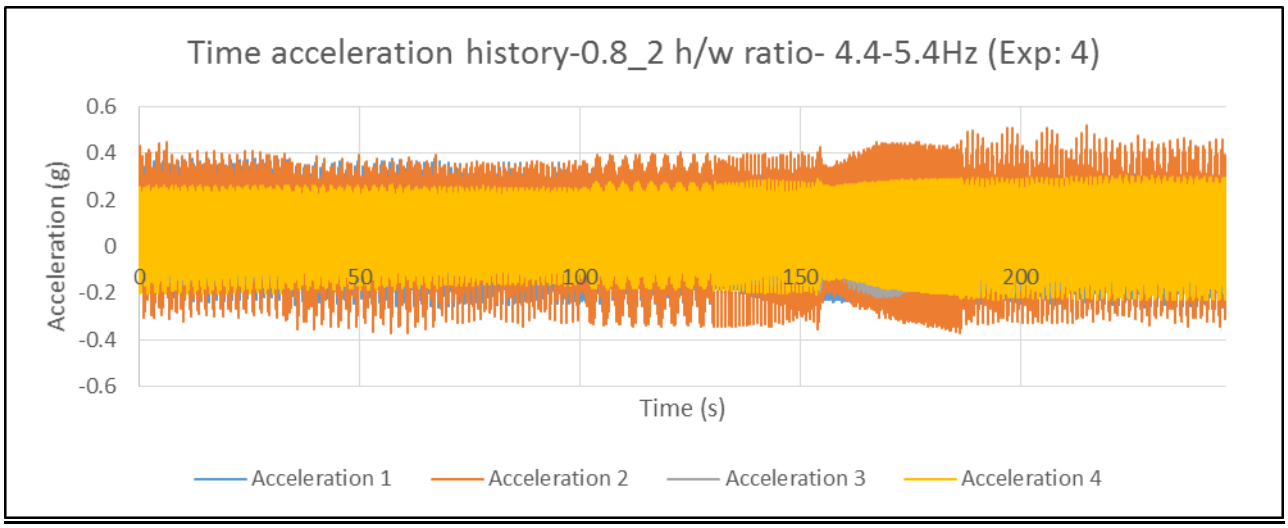
Time acceleration history-0.8_2 h/w ratio- 4.4-5.4Hz (Exp: 4)
Acceleration (g)
0.6
0.4
0.2
0
-0.2
-0.4
-0.6
0
50
100
150
200
Time (s)
Acceleration 1
Acceleration 2
Acceleration 3
Acceleration 4

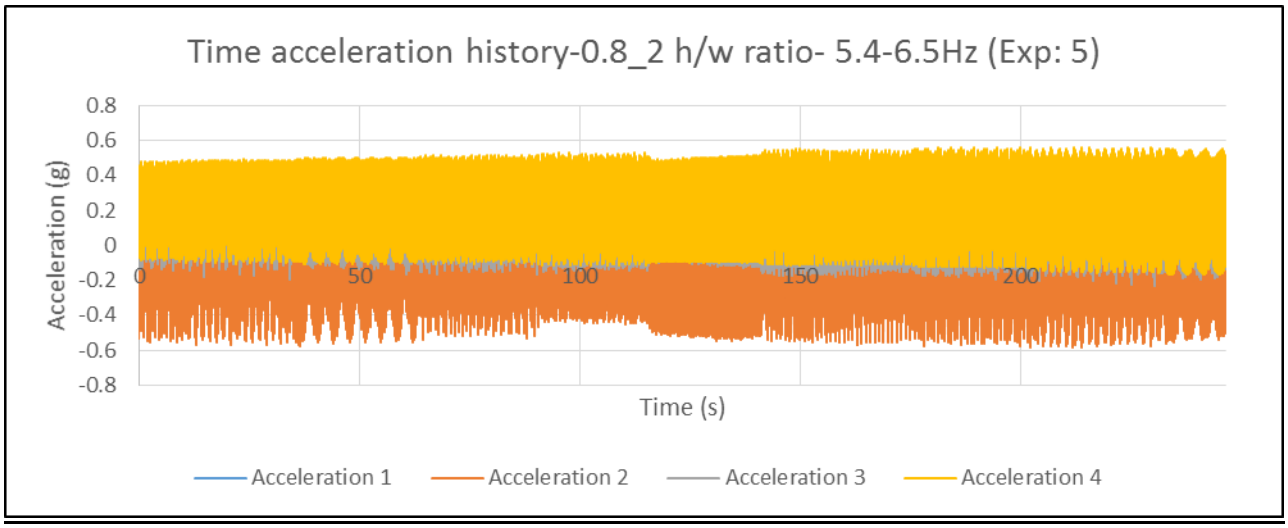
Time acceleration history-0.8_2 h/w ratio- 5.4-6.5Hz (Exp: 5)
Acceleration (g)
0.8
0.6
0.4
0.2
0
-0.2
-0.4
-0.6
-0.8
0
50
100
150
200
Time (s)
Acceleration 1
Acceleration 2
Acceleration 3
Acceleration 4

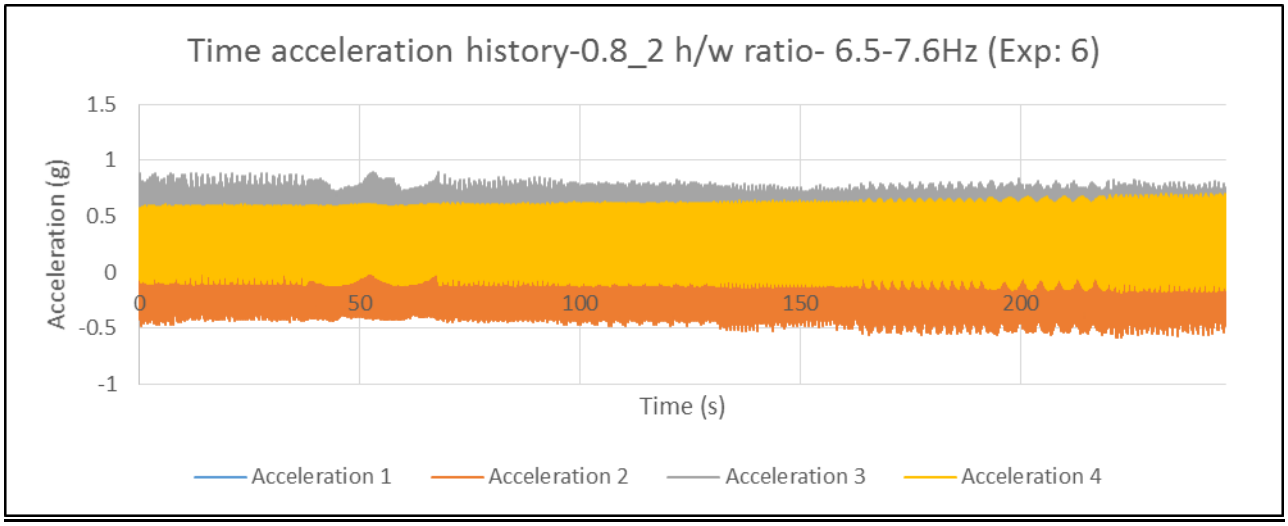
Time acceleration history-0.8_2 h/w ratio- 6.5-7.6Hz (Exp: 6)
Acceleration (g)
1.5
1
0.5
0
-0.5
-1
0
50
100
150
200
Time (s)
Acceleration 1
Acceleration 2
Acceleration 3
Acceleration 4

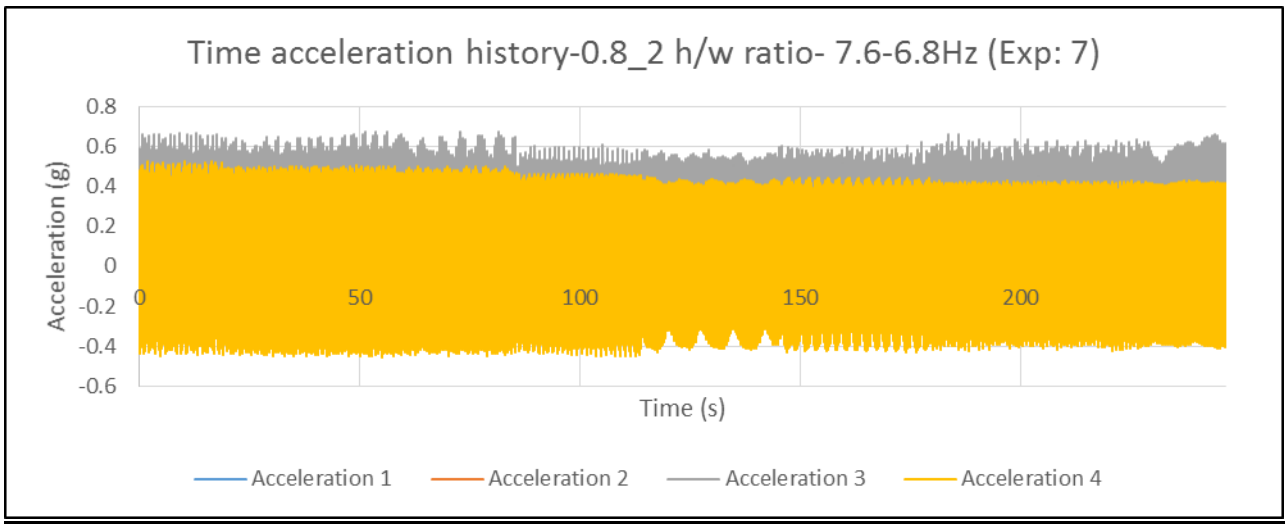
Time acceleration history-0.8_2 h/w ratio- 7.6-6.8Hz (Exp: 7)
Acceleration (g)
0.8
0.6
0.4
0.2
0
-0.2
-0.4
-0.6
0
50
100
150
200
Time (s)
Acceleration 1
Acceleration 2
Acceleration 3
Acceleration 4

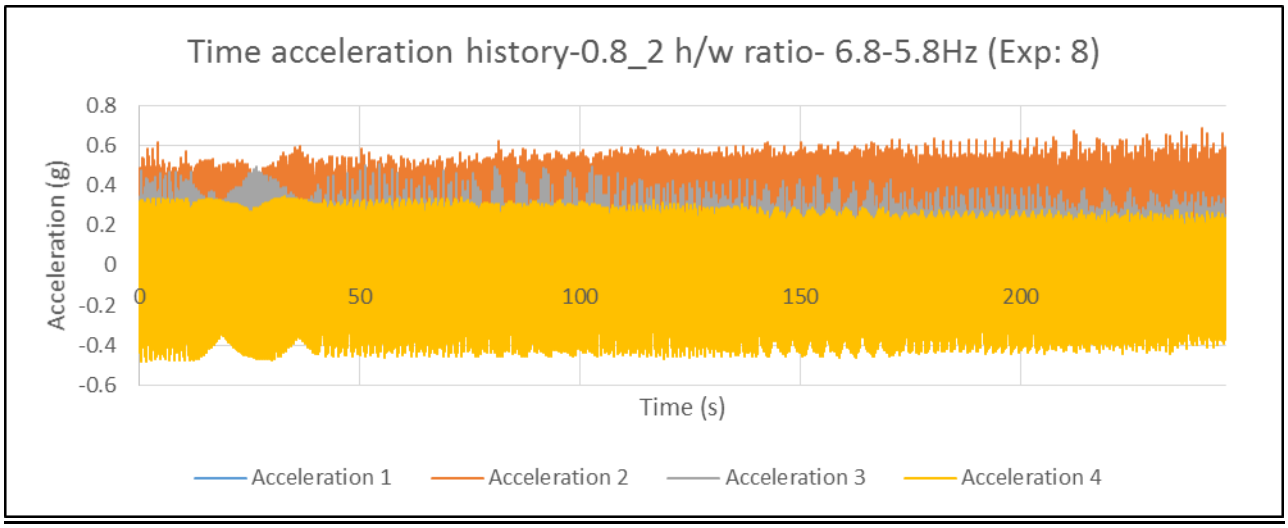
Time acceleration history-0.8_2 h/w ratio- 6.8-5.8Hz (Exp: 8)
Acceleration (g)
0.8
0.6
0.4
0.2
0
-0.2
-0.4
-0.6
0
50
100
150
200
Time (s)
Acceleration 1
Acceleration 2
Acceleration 3
Acceleration 4

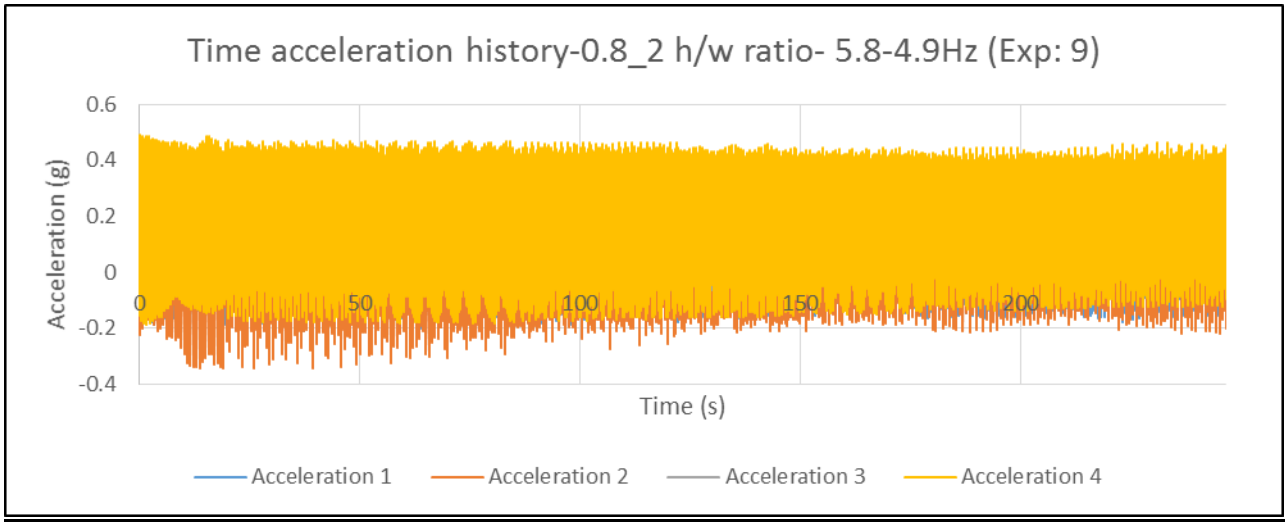
Time acceleration history-0.8_2 h/w ratio- 5.8-4.9Hz (Exp: 9)
Acceleration (g)
0.6
0.4
0.2
0
-0.2
-0.4
0
50
100
150
200
Time (s)
Acceleration 1
Acceleration 2
Acceleration 3
Acceleration 4

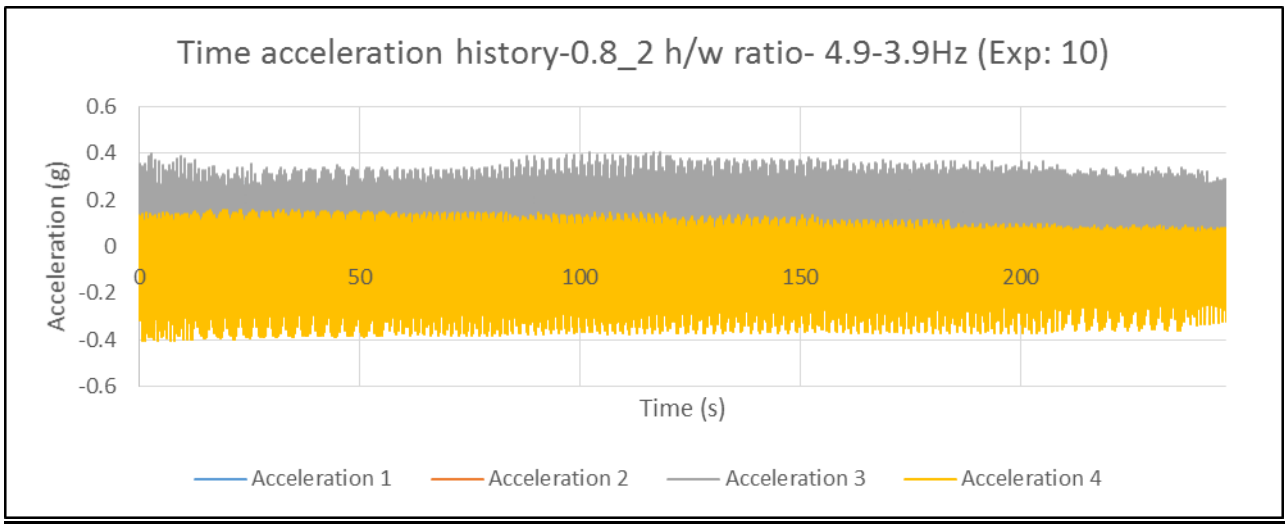
Time acceleration history-0.8_2 h/w ratio- 4.9-3.9Hz (Exp: 10)
Acceleration (g)
0.6
0.4
0.2
0
-0.2
-0.4
-0.6
0
50
100
150
200
Time (s)
Acceleration 1
Acceleration 2
Acceleration 3
Acceleration 4

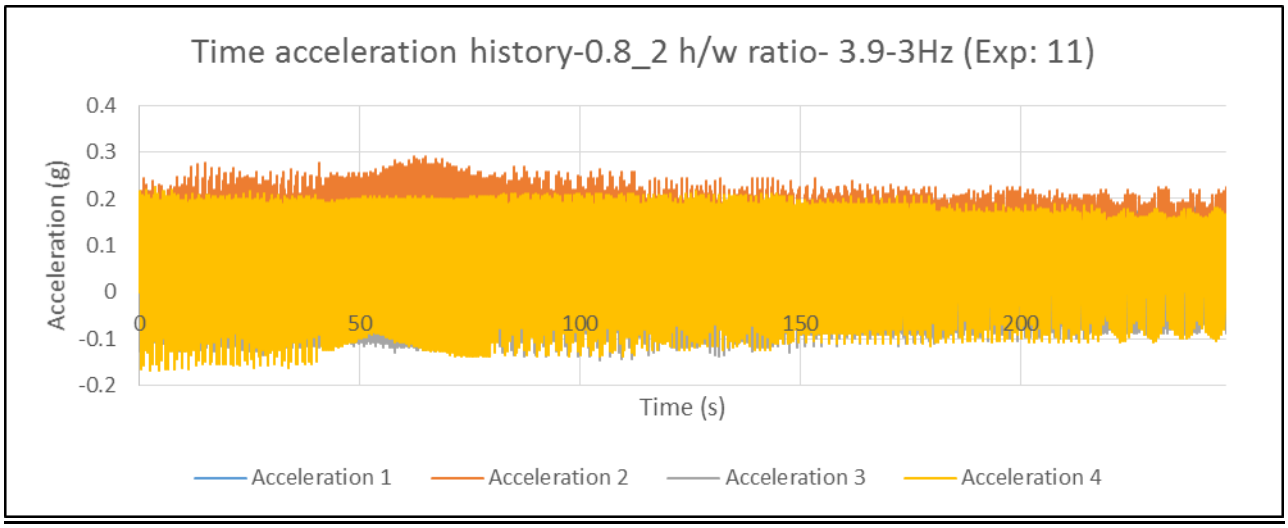
Time acceleration history-0.8_2 h/w ratio- 3.9-3Hz (Exp: 11)
Acceleration (g)
0.4
0.3
0.2
0.1
0
-0.1
-0.2
0
50
100
150
200
Time (s)
Acceleration 1
Acceleration 2
Acceleration 3
Acceleration 4

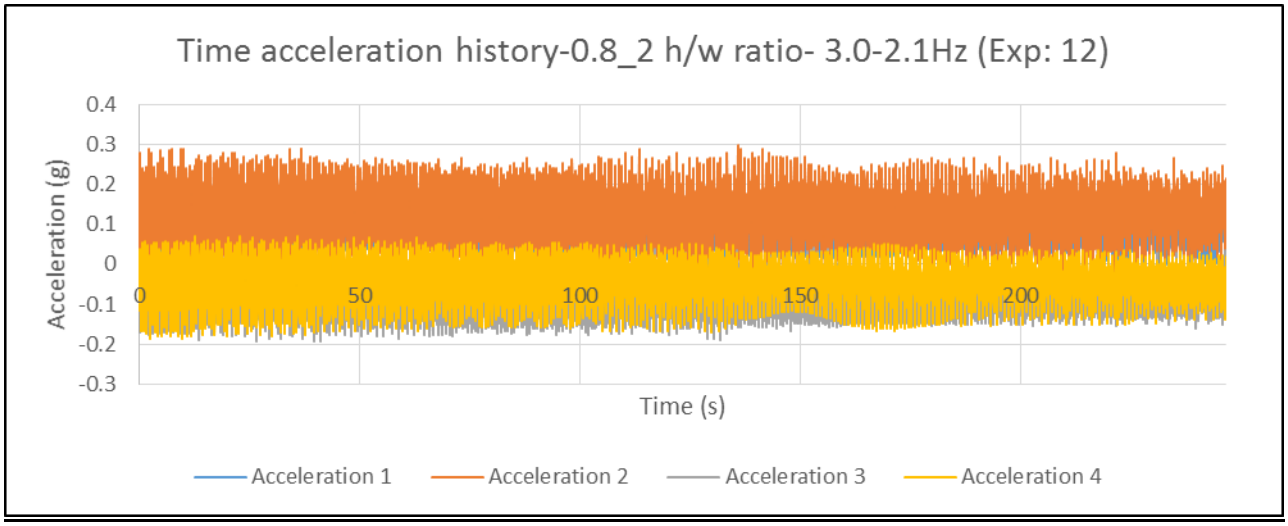

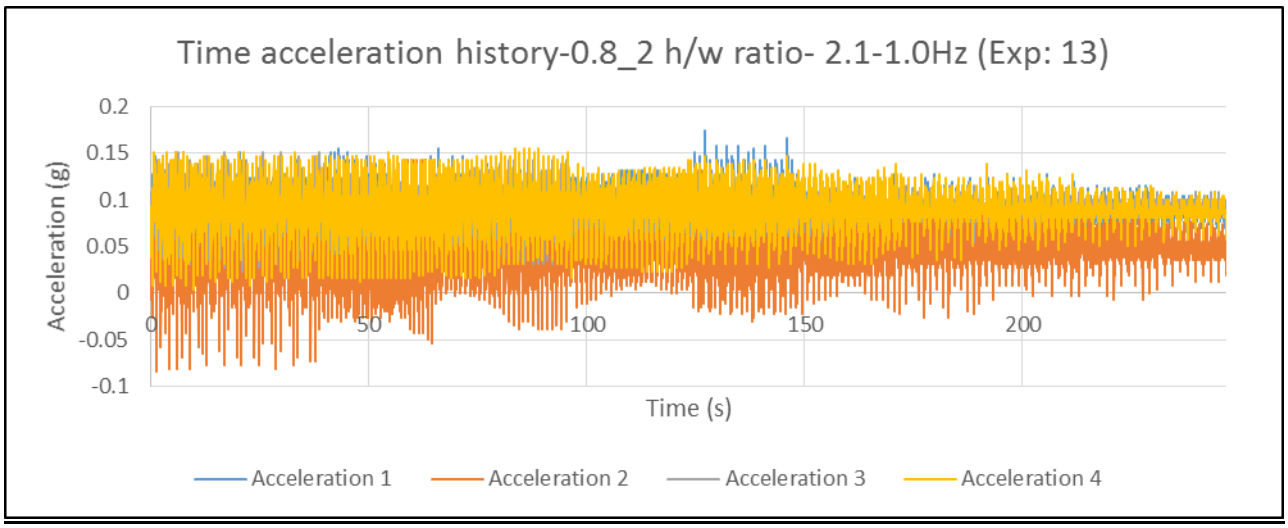

1.0 h/w ratio test

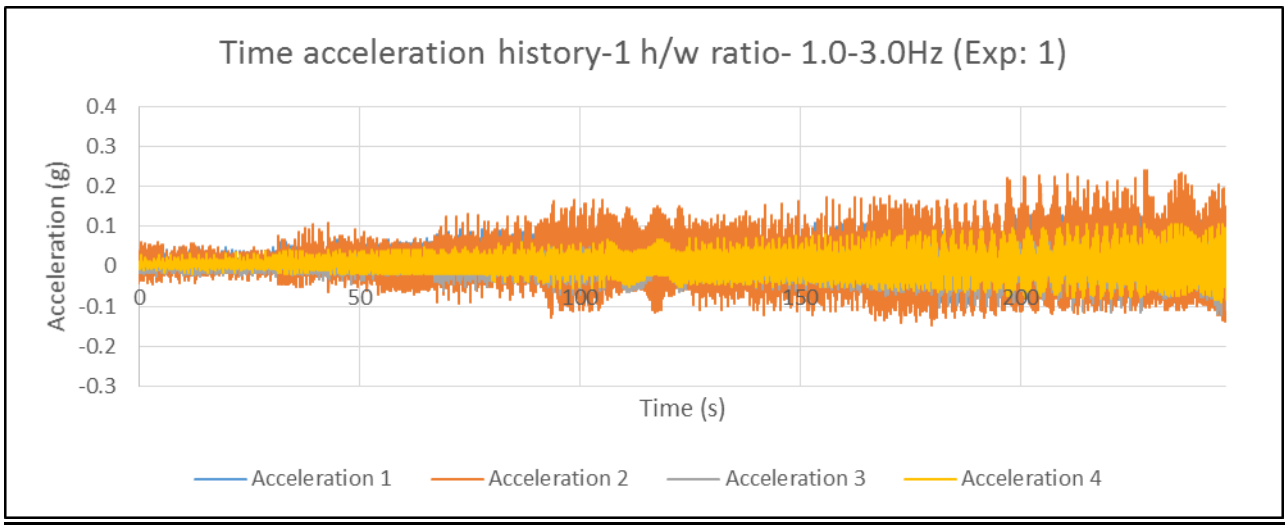

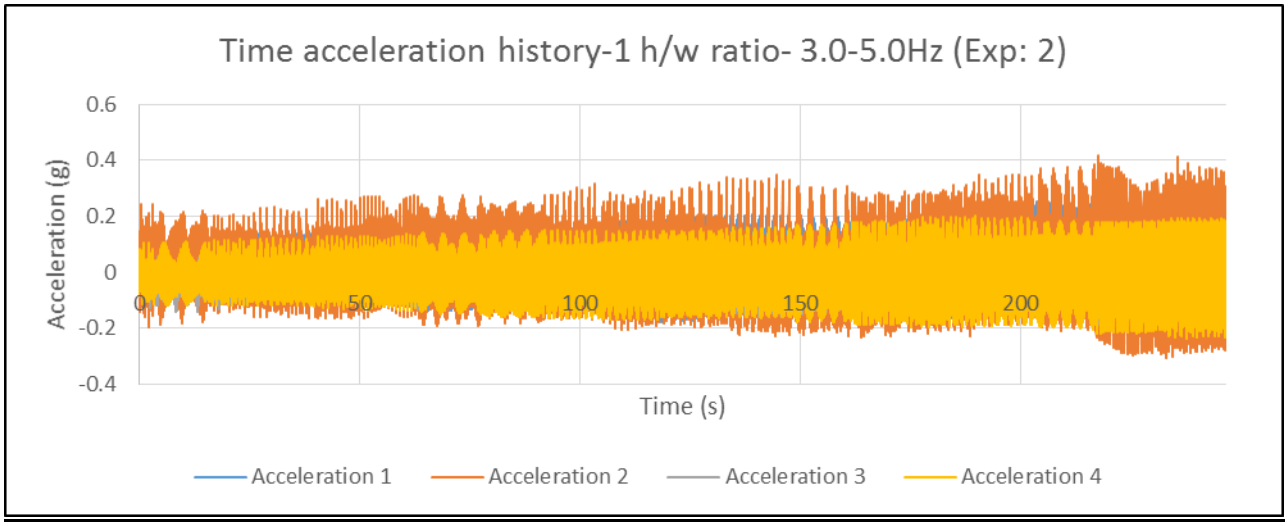

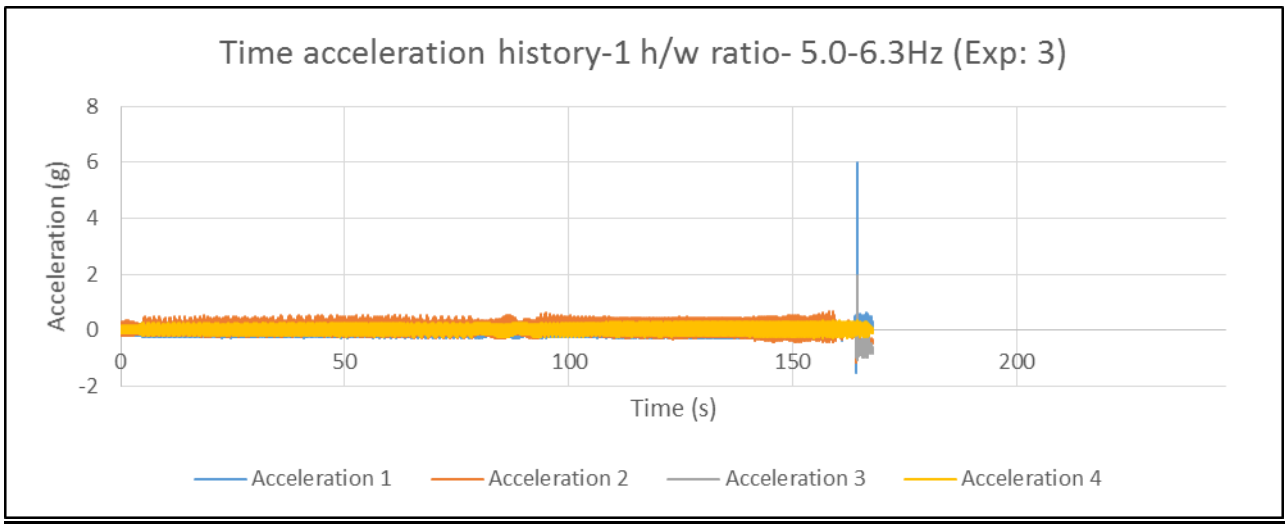

1.2 h/w ratio test

During testing, the data logger shut down and therefore no accelerometer data was available for this test.

Fixed frequency, varying stroke

In all the fixed frequency tests, acceleration 1/0-1 is measures the acceleration from the accelerometer placed on the shake table. Acceleration 1/0-2 measures the acceleration from the accelerometer placed on the apex of the respective arches. All accelerations are measured as a percentage of gravitational acceleration (g=9.81 m/s^2).

2 Hz tests

0.8 h/w ratio arch

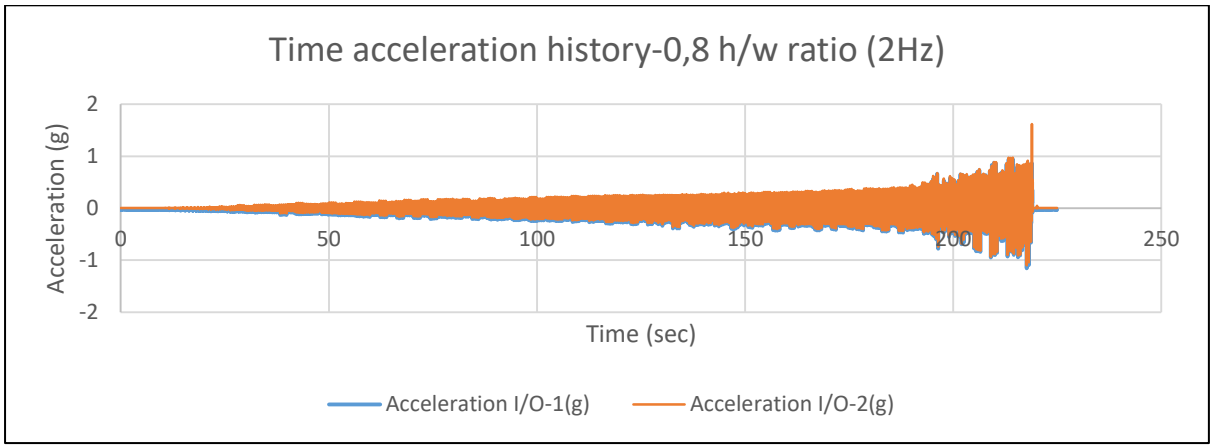

1.0 h/w ratio test

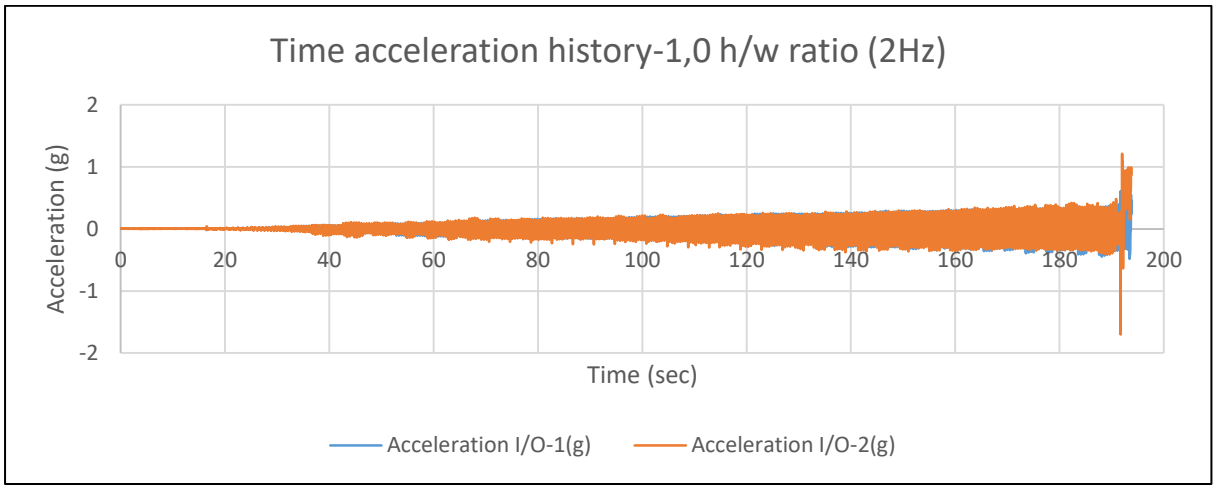

1.2 h/w ratio test

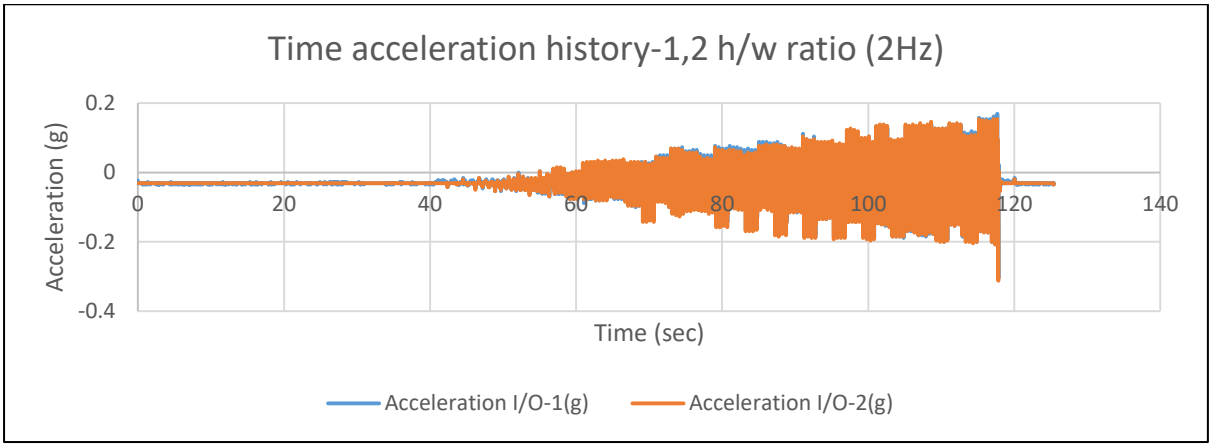

6 Hz tests

0.8 h/w ratio arch

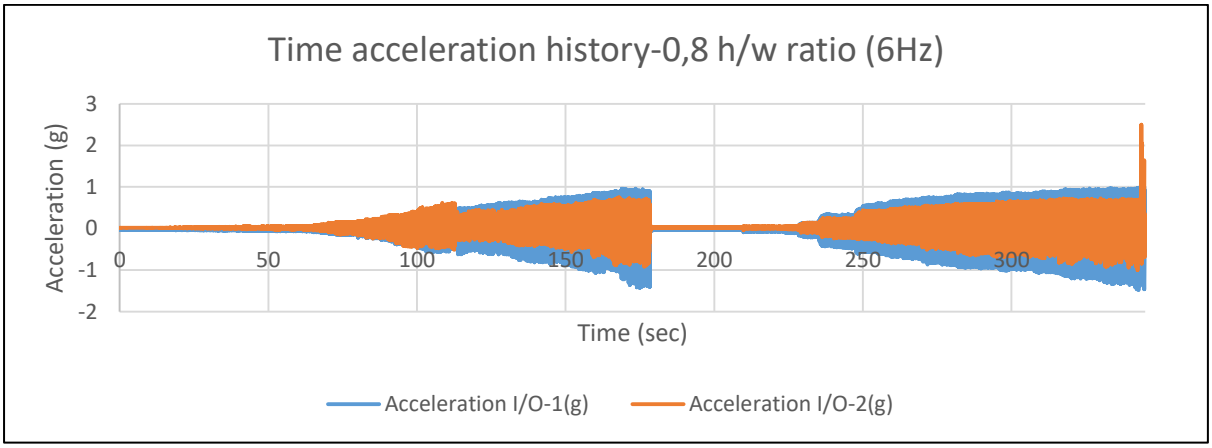

1.0 h/w ratio test

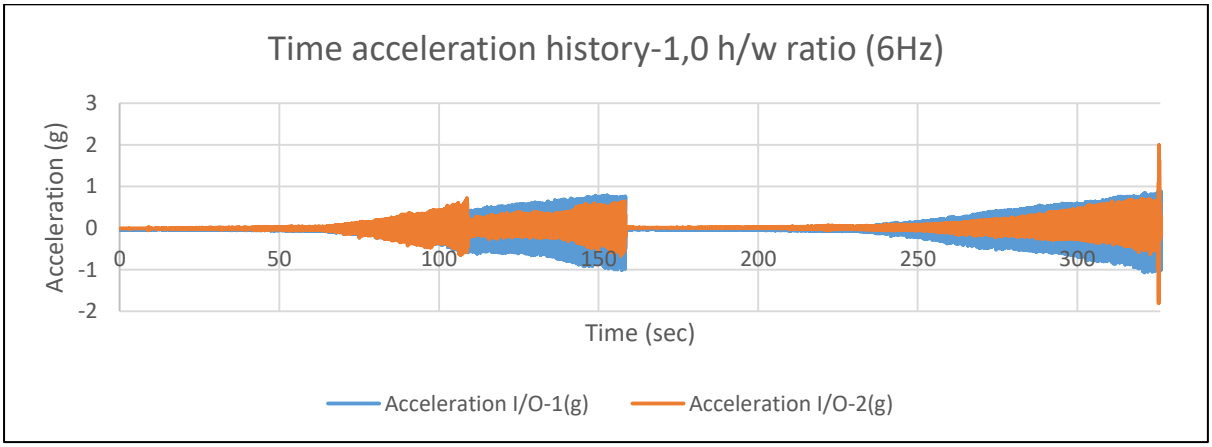

1.2 h/w ratio test

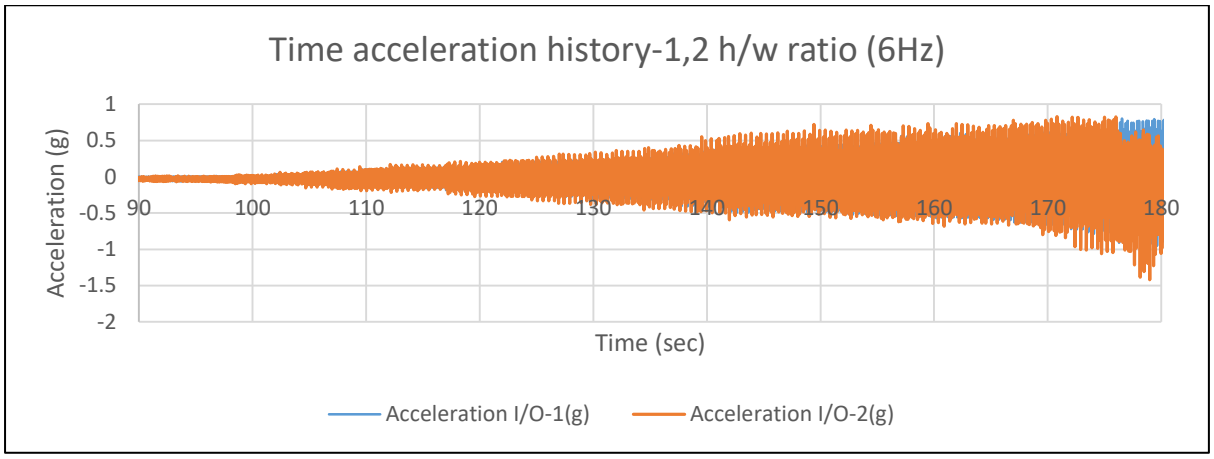

Reinforced tests

Like the unreinforced fixed frequency tests, acceleration 1/0-1 is measures the acceleration from the accelerometer placed on the shake table. Acceleration 1/0-2 measures the acceleration from the accelerometer placed on the apex of the respective arches. All accelerations are measured as a percentage of gravitational acceleration (g=9.81 m/s^2).

Geogrid Alone

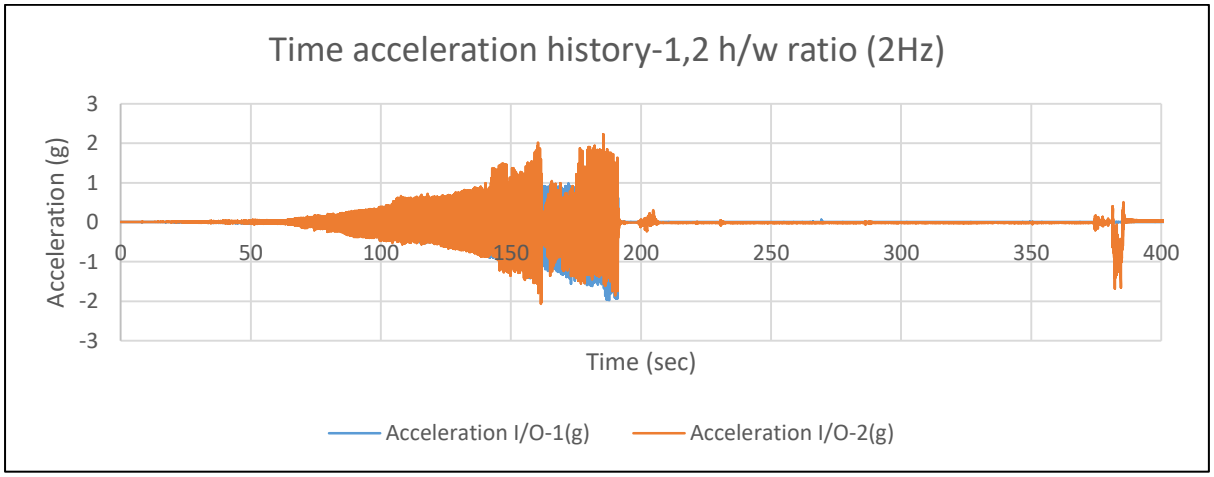

Geogrid with anchors

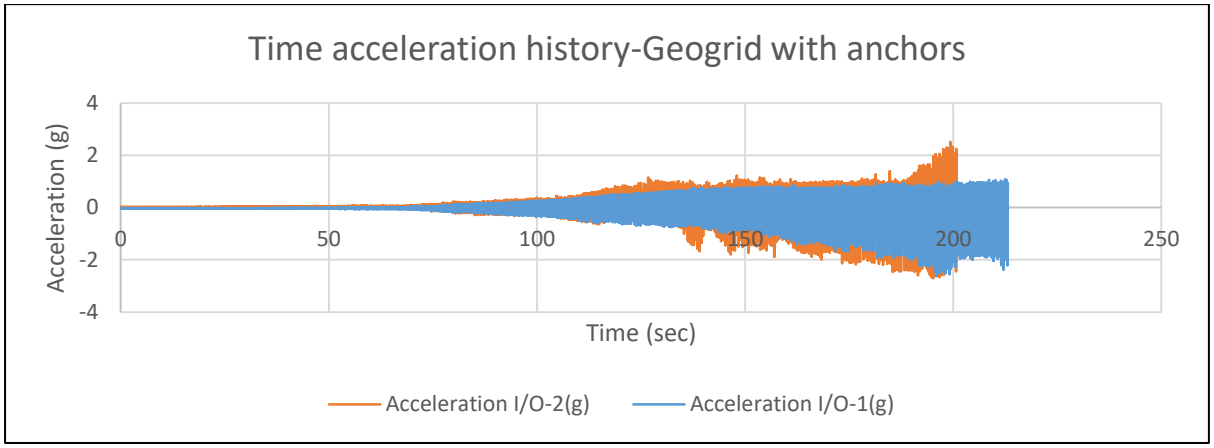

Prestressed geogrid

This time acceleration history was lost during the first test and therefore the test had to be done again. In order to accurately find out if the data correlated with the displacement readings, the structure in its collapsed state was placed kept on the shake table.

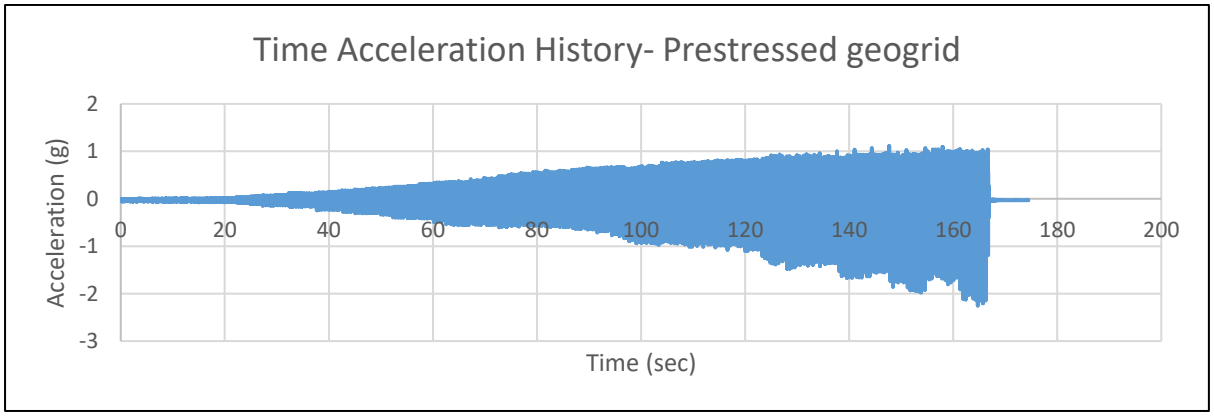

Least Square Approximation

As mentioned in the report, the least squared method was used to smooth out the accelerometer data. The following graphs indicate how the least square method was applied for the various tests. The Excel spread sheet used to compute the least square computation and the macro sheet used in the spread sheet is shown after the graphs below.

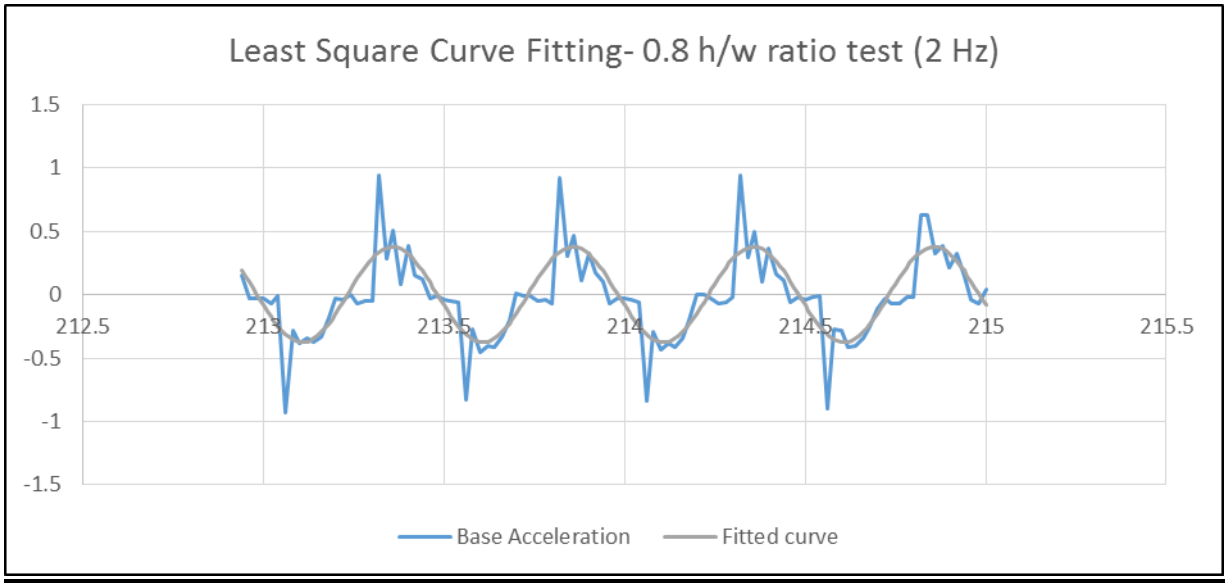

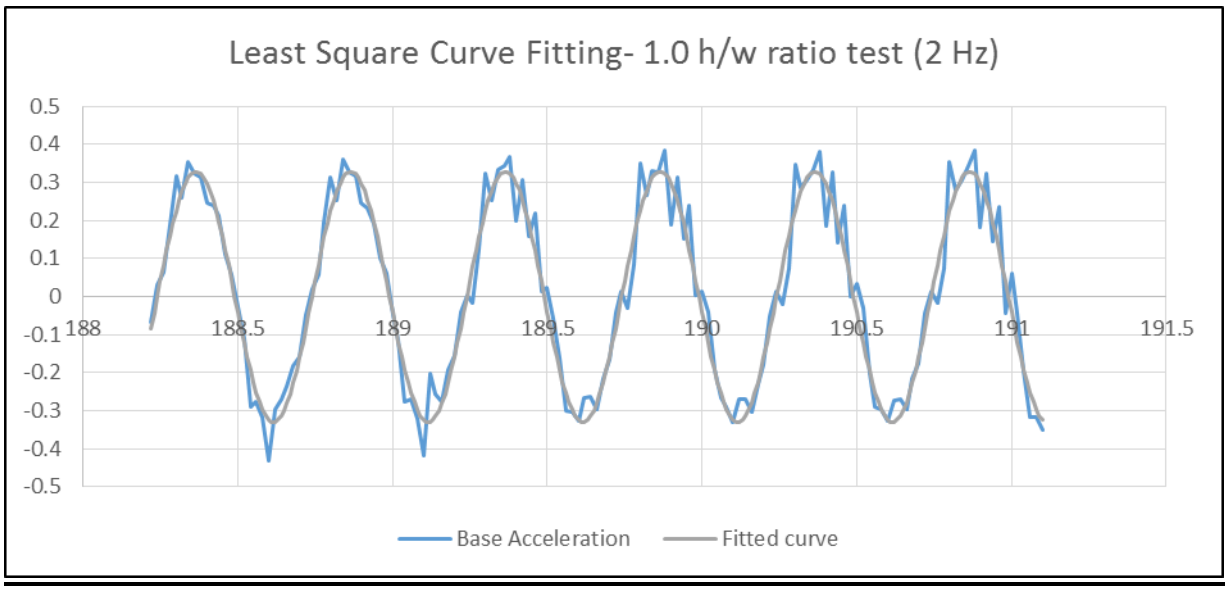

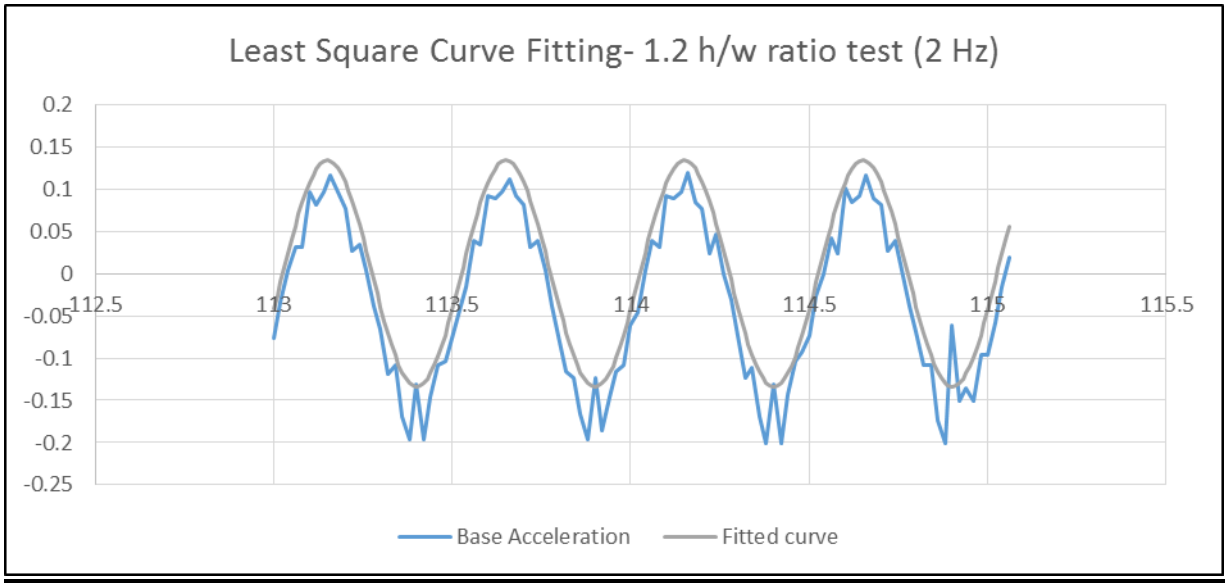
Least Square Curve Fitting- 1.2 h/w ratio test (2 Hz)
0.2
0.15
0.1
0.05
0
-0.05
-0.1
-0.15
-0.2
-0.25
112.5
113
113.5
114
114.5
115
115.5
Base Acceleration
Fitted curve

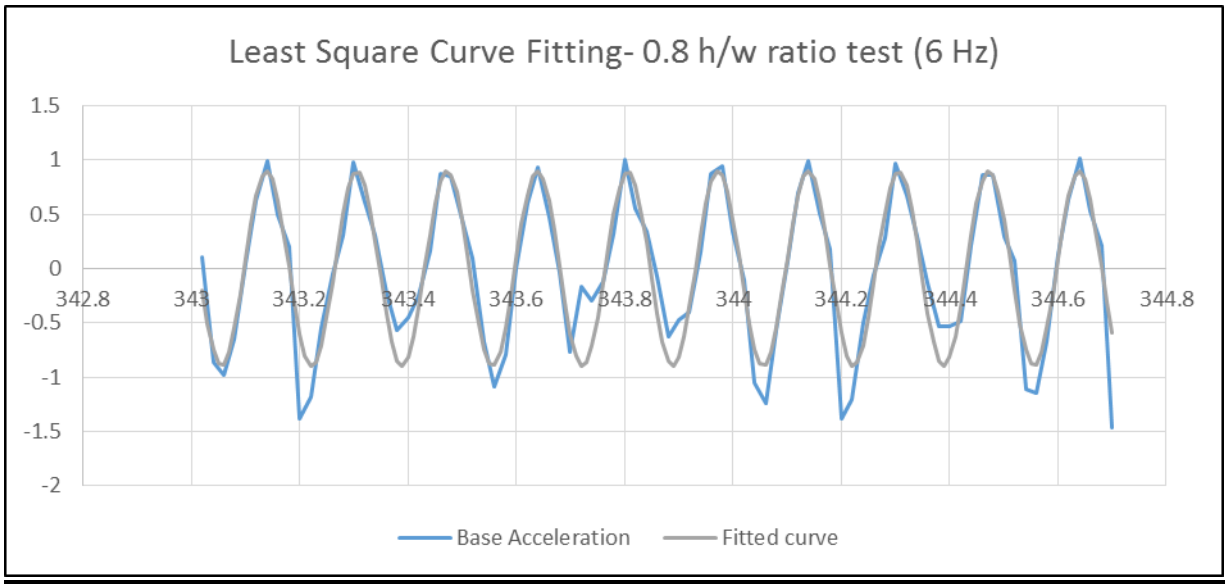
Least Square Curve Fitting- 0.8 h/w ratio test (6 Hz)
1.5
1
0.5
0
-0.5
-1
-1.5
-2
342.8
343
343.2
343.4
343.6
343.8
344
344.2
344.4
344.6
344.8
Base Acceleration
Fitted curve

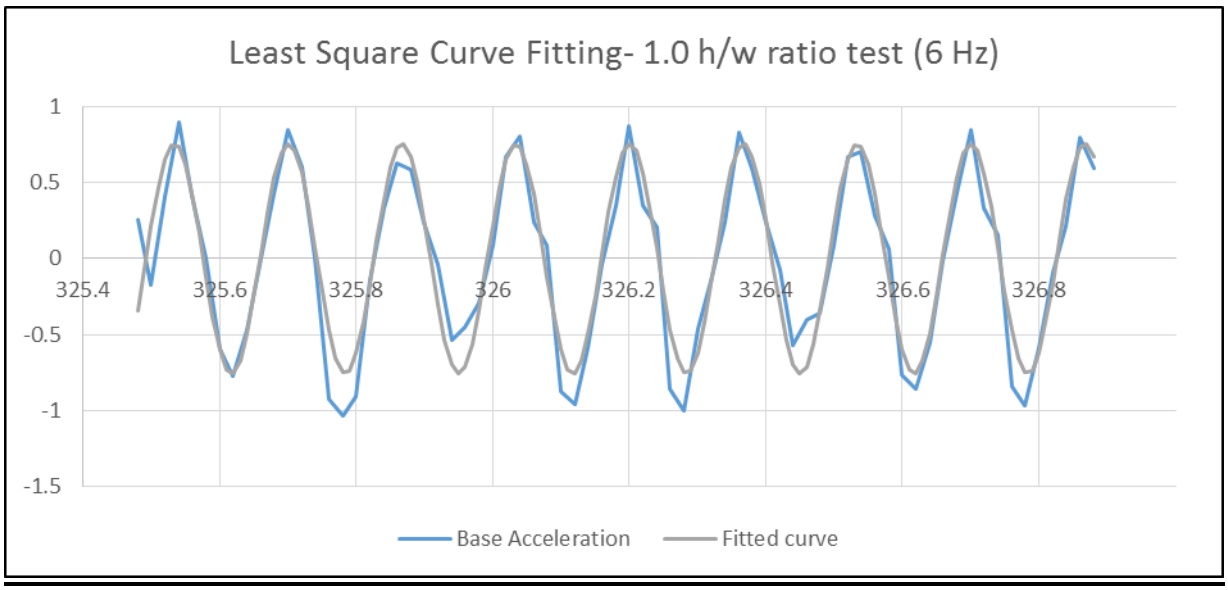
Least Square Curve Fitting- 1.0 h/w ratio test (6 Hz)
1
0.5
0
-0.5
-1
-1.5
325.4
325.6
325.8
326
326.2
326.4
326.6
326.8
Base Acceleration
Fitted curve

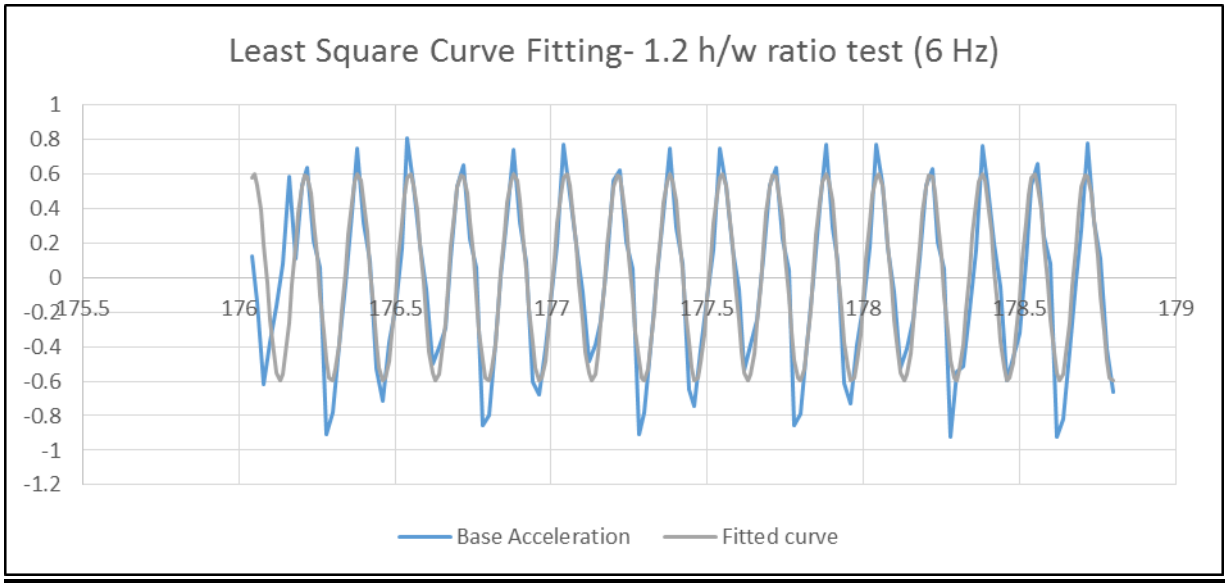
Least Square Curve Fitting- 1.2 h/w ratio test (6 Hz)
1
0.8
0.6
0.4
0.2
0
-0.2
-0.4
-0.6
-0.8
-1
-1.2
175.5
176
176.5
177
177.5
178
178.5
179
Base Acceleration
Fitted curve

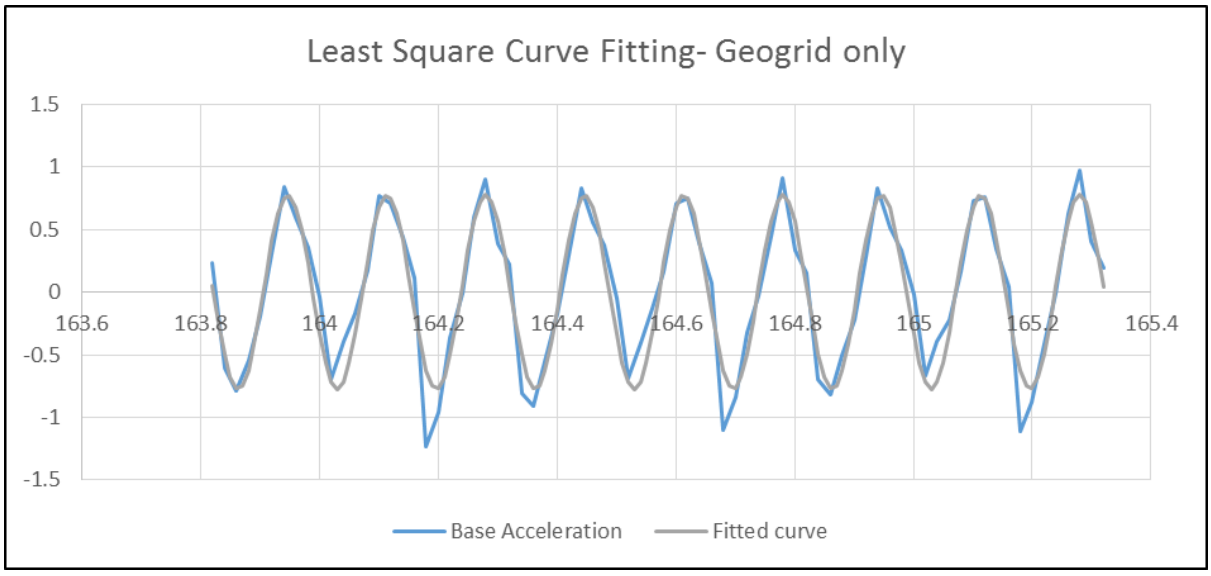
Least Square Curve Fitting- Geogrid only
1.5
1
0.5
0
-0.5
-1
-1.5
163.6
163.8
164
164.2
164.4
164.6
164.8
165
165.2
165.4
Base Acceleration
Fitted curve

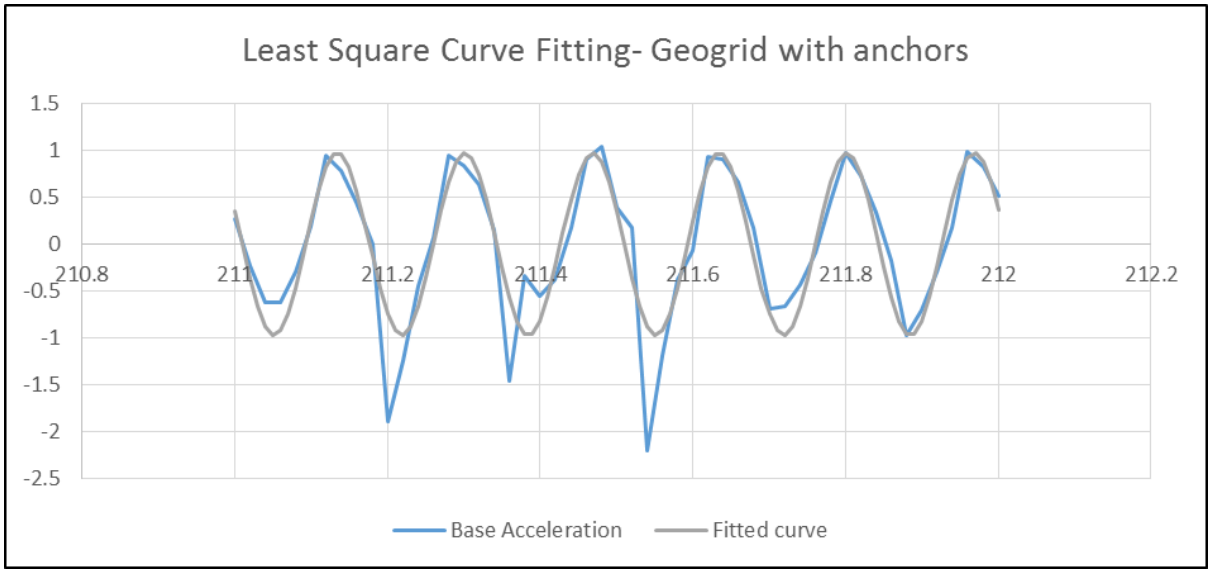
Least Square Curve Fitting- Geogrid with anchors
1.5
1
0.5
0
-0.5
-1
-1.5
-2
-2.5
210.8
211
211.2
211.4
211.6
211.8
212
212.2
Base Acceleration
Fitted curve

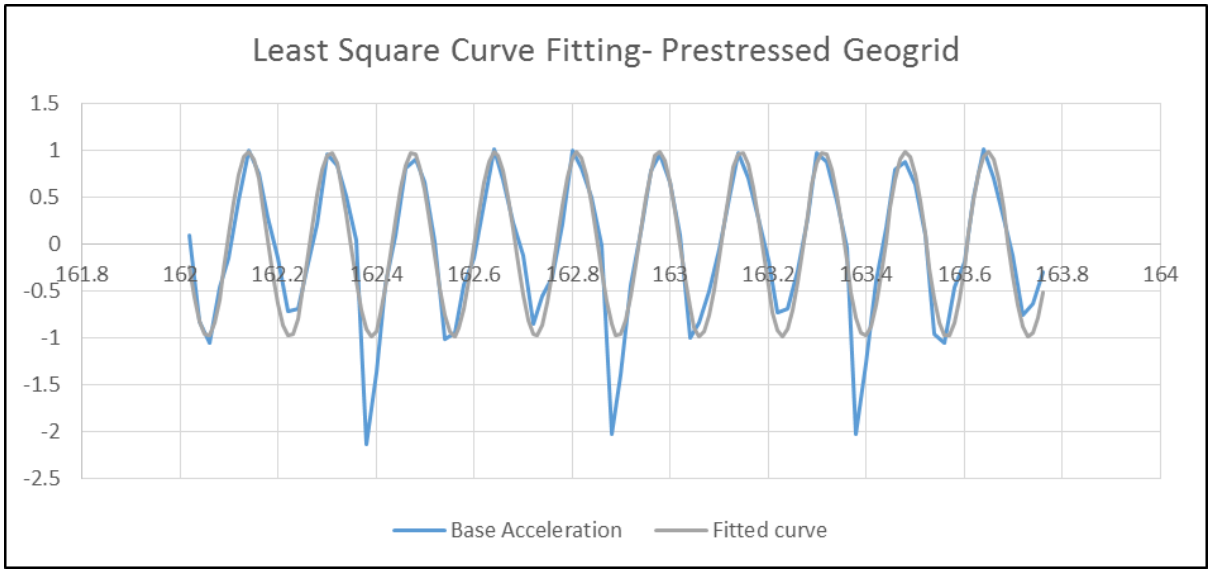
Least Square Curve Fitting- Prestressed Geogrid
1.5
1
0.5
0
-0.5
-1
-1.5
-2
-2.5
161.8
162
162.2
162.4
162.6
162.8
163
163.2
163.4
163.6
163.8
164
Base Acceleration
Fitted curve

INPUT	
A	-8.27002
f	5.999821
Time step	0.01
Max	176.72
SSD	3.11

OUTPUT	
Stroke value	-4.14 mm
Max acc	0.599 g
Test Name	1.2 h/w ratio test (6 Hz)

1)

2)

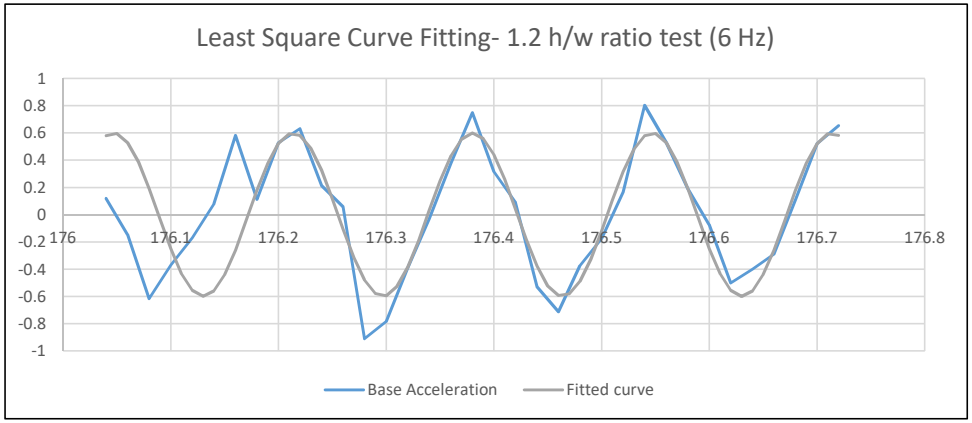

Time	Acc1	Acc2	Model A	Squared deviation 1
176.04	0.11957	0.18514	0.579	0.211
176.06	-0.14657	0.00386	0.528	0.46
176.08	-0.61714	-0.72514	0.191	0.65
176.1	-0.37029	-0.47829	-0.250	0.01
176.12	-0.16971	0.00771	-0.555	0.15
176.14	0.07714	0.13114	-0.559	0.41
176.16	0.58243	0.77914	-0.261	0.71
176.18	0.11186	0.10414	0.179	0.00
176.2	0.52843	0.25071	0.522	0.00
176.22	0.63257	0.50529	0.582	0.00
176.24	0.21214	0.648	0.326	0.01
176.26	0.05786	0.09257	-0.106	0.03
176.28	-0.91029	-0.43586	-0.481	0.18
176.3	-0.783	-0.74829	-0.595	0.04
176.32	-0.38957	-0.44743	-0.387	0.00
176.34	-0.03086	-0.01929	0.031	0.00
176.36	0.378	0.15429	0.433	0.00
176.38	0.74829	0.28929	0.599	0.02
176.4	0.31629	0.74443	0.441	0.02
176.42	0.09257	0.31629	0.044	0.00
176.44	-0.52843	-0.20443	-0.377	0.02
176.46	-0.71357	-0.70971	-0.594	0.01
176.48	-0.37414	-0.38957	-0.488	0.01
176.5	-0.17357	-0.54386	-0.118	0.00
176.52	0.16586	0.12343	0.316	0.02
176.54	0.80229	0.36643	0.579	0.05
176.56	0.52843	0.50529	0.528	0.00
176.58	0.189	0.55929	0.191	0.00
176.6	-0.07329	-0.027	-0.249	0.03
176.62	-0.50143	-0.75986	-0.555	0.00
176.64	-0.40114	-0.57086	-0.559	0.03
176.66	-0.28929	-0.26614	-0.261	0.00
176.68	0.108	-0.20829	0.179	0.01
176.7	0.52071	0.40114	0.522	0.00
176.72	0.65186	0.405	0.582	0.00

Time	Acc fitted
176.04	0.579
176.05	0.595
176.06	0.528
176.07	0.387
176.08	0.191
176.09	-0.032
176.1	-0.250
176.11	-0.433
176.12	-0.555
176.13	-0.599
176.14	-0.559
176.15	-0.441
176.16	-0.261
176.17	-0.044
176.18	0.179
176.19	0.377
176.2	0.522
176.21	0.594
176.22	0.582
176.23	0.488
176.24	0.326
176.25	0.118
176.26	-0.106
176.27	-0.316
176.28	-0.481
176.29	-0.579
176.3	-0.595
176.31	-0.528
176.32	-0.387
176.33	-0.191
176.34	0.031
176.35	0.250
176.36	0.433
176.37	0.555
176.38	0.599
176.39	0.559
176.4	0.441
176.41	0.261
176.42	0.044
176.43	-0.179

Least Square Method- Macro Code

```
Sub Macro3()
'
' Macro3 Macro
'


'
    SolverOk SetCell:="$B$6", MaxMinVal:=2, ValueOf:=0, ByChange:="$B$2,$B$3", _
        Engine:=1, EngineDesc:="GRG Nonlinear"
    SolverOk SetCell:="$B$6", MaxMinVal:=2, ValueOf:=0, ByChange:="$B$2,$B$3", _
        Engine:=1, EngineDesc:="GRG Nonlinear"
    SolverSolve
End Sub
```

APPENDIX B- PREDICTIVE MODEL EXAMPLE

CATENARY CURVE

Block Length =	0.01964	m
Block Weight =	0.095746	kN
Thrust Angle =	61.0846	Deg. (at origin of curve)

Catenary Requirements

Length of curve	0.73	m
h/w ratio	0.4	

Brick Parameters

Block Width	1	m
Block Thickness	0.25	m

Element	Block Length	Block Weight	Left Angle D	Rad. Angle R	Left Thrust x	Left Thrust y	Left Thrust	Right Thrust x	Right Thrust y	Right Thrust	Rad. Angle	Deg. Angle	X	Y
1	0.01964	0.095746	61.0846	1.066127	1.295763	2.345781	2.679867	-1.295763	-2.250034	2.59647	1.048296	60.06296231	0	0
2	0.01964	0.095746	60.06296	1.048296	1.295763	2.250034	2.59647	-1.295763	-2.154288	2.513953	1.029289	58.9738937	0.009496	0.017192
3	0.01964	0.095746	58.97389	1.029289	1.295763	2.154288	2.513953	-1.295763	-2.058542	2.432406	1.008999	57.81135829	0.019298	0.034212
4	0.01964	0.095746	57.81136	1.008999	1.295763	2.058542	2.432406	-1.295763	-1.962796	2.351929	0.98731	56.56872385	0.029421	0.051042
5	0.01964	0.095746	56.56872	0.98731	1.295763	1.962796	2.351929	-1.295763	-1.86705	2.272637	0.964097	55.23871551	0.039883	0.067663
6	0.01964	0.095746	55.23872	0.964097	1.295763	1.86705	2.272637	-1.295763	-1.771304	2.194657	0.939221	53.81337793	0.050704	0.084054
7	0.01964	0.095746	53.81338	0.939221	1.295763	1.771304	2.194657	-1.295763	-1.675558	2.118135	0.912529	52.28404901	0.061902	0.100189
8	0.01964	0.095746	52.28405	0.912529	1.295763	1.675558	2.118135	-1.295763	-1.579811	2.043234	0.883858	50.64135262	0.073498	0.116041
9	0.01964	0.095746	50.64135	0.883858	1.295763	1.579811	2.043234	-1.295763	-1.484065	1.97014	0.853034	48.87522092	0.085513	0.131577
10	0.01964	0.095746	48.87522	0.853034	1.295763	1.484065	1.97014	-1.295763	-1.388319	1.899061	0.819868	46.97496015	0.097968	0.146763
11	0.01964	0.095746	46.97496	0.819868	1.295763	1.388319	1.899061	-1.295763	-1.292573	1.830232	0.784166	44.92937792	0.110886	0.161558
12	0.01964	0.095746	44.92938	0.784166	1.295763	1.292573	1.830232	-1.295763	-1.196827	1.763915	0.745727	42.72699506	0.124286	0.175916
13	0.01964	0.095746	42.727	0.745727	1.295763	1.196827	1.763915	-1.295763	-1.101081	1.700406	0.704352	40.35636854	0.138191	0.189786
14	0.01964	0.095746	40.35637	0.704352	1.295763	1.101081	1.700406	-1.295763	-1.005335	1.640031	0.659849	37.80655532	0.152619	0.203112
15	0.01964	0.095746	37.80656	0.659849	1.295763	1.005335	1.640031	-1.295763	-0.909588	1.583147	0.612048	35.06774524	0.167585	0.21583
16	0.01964	0.095746	35.06775	0.612048	1.295763	0.909588	1.583147	-1.295763	-0.813842	1.530144	0.560811	32.1320831	0.183103	0.227869
17	0.01964	0.095746	32.13208	0.560811	1.295763	0.813842	1.530144	-1.295763	-0.718096	1.48144	0.506053	28.99468097	0.199178	0.239154
18	0.01964	0.095746	28.99468	0.506053	1.295763	0.718096	1.48144	-1.295763	-0.62235	1.437471	0.447761	25.65478827	0.21581	0.2496
19	0.01964	0.095746	25.65479	0.447761	1.295763	0.62235	1.437471	-1.295763	-0.526604	1.398683	0.386015	22.11703691	0.232988	0.25912
20	0.01964	0.095746	22.11704	0.386015	1.295763	0.526604	1.398683	-1.295763	-0.430858	1.365519	0.321012	18.3926173	0.250692	0.267623
21	0.01964	0.095746	18.39262	0.321012	1.295763	0.430858	1.365519	-1.295763	-0.335112	1.338395	0.253076	14.50017947	0.268887	0.275018
22	0.01964	0.095746	14.50018	0.253076	1.295763	0.335112	1.338395	-1.295763	-0.239365	1.317687	0.18267	10.466217	0.287524	0.281215
23	0.01964	0.095746	10.46622	0.18267	1.295763	0.239365	1.317687	-1.295763	-0.143619	1.303698	0.110387	6.324707951	0.306539	0.286132
24	0.01964	0.095746	6.324708	0.110387	1.295763	0.143619	1.303698	-1.295763	-0.047873	1.296647	0.036929	2.115878709	0.325852	0.2897
25	0.01964	0.095746	2.115879	0.036929	1.295763	0.047873	1.296647	-1.295763	0.047873	1.296647	-0.036929	-2.115878709	0.345373	0.291864
26	0.01964	0.095746	-2.115879	-0.036929	1.295763	-0.047873	1.296647	-1.295763	0.143619	1.303698	-0.110387	-6.324707951	0.365	0.292589
27	0.01964	0.095746	-6.324708	-0.110387	1.295763	-0.143619	1.303698	-1.295763	0.239365	1.317687	-0.18267	-10.466217	0.384627	0.291864
28	0.01964	0.095746	-10.46622	-0.18267	1.295763	-0.239365	1.317687	-1.295763	0.335112	1.338395	-0.253076	-14.50017947	0.404148	0.2897
29	0.01964	0.095746	-14.50018	-0.253076	1.295763	-0.335112	1.338395	-1.295763	0.430858	1.365519	-0.321012	-18.3926173	0.423461	0.286132
30	0.01964	0.095746	-18.39262	-0.321012	1.295763	-0.430858	1.365519	-1.295763	0.526604	1.398683	-0.386015	-22.11703691	0.442476	0.281215
31	0.01964	0.095746	-22.11704	-0.386015	1.295763	-0.526604	1.398683	-1.295763	0.62235	1.437471	-0.447761	-25.65478827	0.461113	0.275018
32	0.01964	0.095746	-25.65479	-0.447761	1.295763	-0.62235	1.437471	-1.295763	0.718096	1.48144	-0.506053	-28.99468097	0.479308	0.267623

33	0.01964	0.095746	-28.99468	-0.506053	1.295763	-0.718096	1.48144	-1.295763	0.813842	1.530144	-0.560811	-32.1320831	0.497012	0.25912
34	0.01964	0.095746	-32.13208	-0.560811	1.295763	-0.813842	1.530144	-1.295763	0.909588	1.583147	-0.612048	-35.06774524	0.51419	0.2496
35	0.01964	0.095746	-35.06775	-0.612048	1.295763	-0.909588	1.583147	-1.295763	1.005335	1.640031	-0.659849	-37.80655532	0.530822	0.239154
36	0.01964	0.095746	-37.80656	-0.659849	1.295763	-1.005335	1.640031	-1.295763	1.101081	1.700406	-0.704352	-40.35636854	0.546897	0.227869
37	0.01964	0.095746	-40.35637	-0.704352	1.295763	-1.101081	1.700406	-1.295763	1.196827	1.763915	-0.745727	-42.72699506	0.562415	0.21583
38	0.01964	0.095746	-42.727	-0.745727	1.295763	-1.196827	1.763915	-1.295763	1.292573	1.830232	-0.784166	-44.92937792	0.577381	0.203112
39	0.01964	0.095746	-44.92938	-0.784166	1.295763	-1.292573	1.830232	-1.295763	1.388319	1.899061	-0.819868	-46.97496015	0.591809	0.189786
40	0.01964	0.095746	-46.97496	-0.819868	1.295763	-1.388319	1.899061	-1.295763	1.484065	1.97014	-0.853034	-48.87522092	0.605714	0.175916
41	0.01964	0.095746	-48.87522	-0.853034	1.295763	-1.484065	1.97014	-1.295763	1.579811	2.043234	-0.883858	-50.64135262	0.619114	0.161558
42	0.01964	0.095746	-50.64135	-0.883858	1.295763	-1.579811	2.043234	-1.295763	1.675558	2.118135	-0.912529	-52.28404901	0.632032	0.146763
43	0.01964	0.095746	-52.28405	-0.912529	1.295763	-1.675558	2.118135	-1.295763	1.771304	2.194657	-0.939221	-53.81337793	0.644487	0.131577
44	0.01964	0.095746	-53.81338	-0.939221	1.295763	-1.771304	2.194657	-1.295763	1.86705	2.272637	-0.964097	-55.23871551	0.656502	0.116041
45	0.01964	0.095746	-55.23872	-0.964097	1.295763	-1.86705	2.272637	-1.295763	1.962796	2.351929	-0.98731	-56.56872385	0.668098	0.100189
46	0.01964	0.095746	-56.56872	-0.98731	1.295763	-1.962796	2.351929	-1.295763	2.058542	2.432406	-1.008999	-57.81135829	0.679296	0.084054
47	0.01964	0.095746	-57.81136	-1.008999	1.295763	-2.058542	2.432406	-1.295763	2.154288	2.513953	-1.029289	-58.9738937	0.690117	0.067663
48	0.01964	0.095746	-58.97389	-1.029289	1.295763	-2.154288	2.513953	-1.295763	2.250034	2.59647	-1.048296	-60.06296231	0.700579	0.051042
49	0.01964	0.095746	-60.06296	-1.048296	1.295763	-2.250034	2.59647	-1.295763	2.345781	2.679867	-1.066127	-61.08459783	0.710702	0.034212
50	0.01964	0.095746	-61.0846	-1.066127	1.295763	-2.345781	2.679867	-1.295763	2.441527	2.764065	-1.082877	-62.04428209	0.720504	0.017192
												Width	0.73	8.40E-16
												Height/ width	0.400807	

Hinge Angles

Hinge No	Angle	X	Y	Actual Angle
1	0	0.000	0.000	0.00
2	53	0.1831	0.228	51.40
3	123	0.514	0.250	120.87
4	180	0.730	0.000	180.00

Hinge Coords

	Angle	X	Y
A	0.5047	0.0088	-0.00484
B	0.9587	0.17736	0.23605
C	1.0100	0.50887	0.24113
D	0.5047	0.73875	0.00484

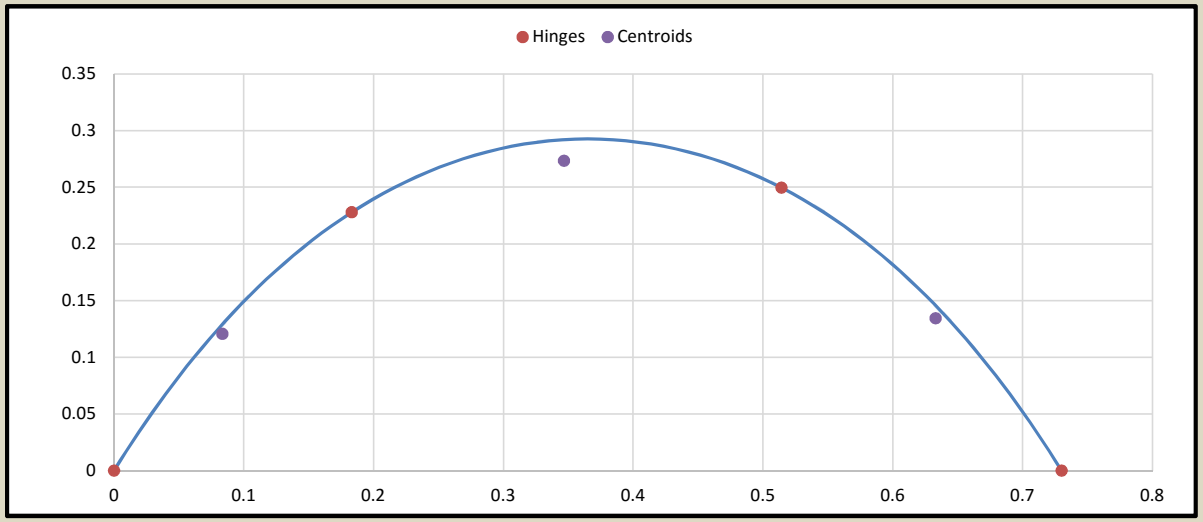

To tables
To ground acceleration

Minimum Ground Acceleration Calculation

Main lines of intersection	
m	c
1.428729	-0.017
-1.027904	0.764
Intersection	
0.318136	0.437189

θ1	1
θ2	1.1976
θ3	0.9937

f blocks per link	
1	15
2	18
3	17

Vert displacements	
Link	Displacement
1	-0.0013
2	0.0006
3	0.0018

Hor Displacements

Link	Displacement
1	0.0022
2	0.0034
3	0.0022

Back

Centroid Locations

Link No	x	y
1	0.0835	0.1206
2	0.3466	0.2734
3	0.6329	0.1345

Horizontal Acceleration Factor

0.1684683	g

Arch Span	0.73	m
H/W ratio	0.4	
Thickness	0.02	m

Length of segment	0.01964	m
Mass of bricks	0.765969	kg
I_G	5.02E-05	$kg.m^2$

To graph and properties

No No	x (m)	y (m)	Radius (m)	Angle (rad)	x' (m)	y' (m)	Ax' (m2)	Ay' (m2)	Radius from hinge (m)	Mom of inertia (kg.m2)
1	0	0	0.365	0	0	0	0	0	0.0000	0.00005
2	0.009496	0.017192	0.355919	2.768606	0.004748	0.008596	1.87E-06	3.38E-06	0.0140	0.00020
3	0.019298	0.034212	0.347391	5.651723	0.014397	0.025702	5.66E-06	1.01E-05	0.0311	0.00079
4	0.029421	0.051042	0.339439	8.64845	0.024359	0.042627	9.57E-06	1.67E-05	0.0500	0.00196
5	0.039883	0.067663	0.332083	11.75659	0.034652	0.059353	1.36E-05	2.33E-05	0.0692	0.00372
6	0.050704	0.084054	0.325341	14.97256	0.045294	0.075859	1.78E-05	2.98E-05	0.0886	0.00606
7	0.061902	0.100189	0.319228	18.29133	0.056303	0.092122	2.21E-05	3.62E-05	0.1080	0.00898
8	0.073498	0.116041	0.31375	21.70646	0.0677	0.108115	2.66E-05	4.25E-05	0.1274	0.01248
9	0.085513	0.131577	0.30891	25.21017	0.079505	0.123809	3.12E-05	4.86E-05	0.1468	0.01656
10	0.097968	0.146763	0.304705	28.79356	0.09174	0.13917	3.6E-05	5.47E-05	0.1662	0.02121
11	0.110886	0.161558	0.301123	32.44684	0.104427	0.15416	4.1E-05	6.06E-05	0.1856	0.02642
12	0.124286	0.175916	0.298143	36.15967	0.117586	0.168737	4.62E-05	6.63E-05	0.2049	0.03220
13	0.138191	0.189786	0.295738	39.92151	0.131239	0.182851	5.16E-05	7.18E-05	0.2241	0.03852
14	0.152619	0.203112	0.293871	43.72205	0.145405	0.196449	5.71E-05	7.72E-05	0.2433	0.04539
15	0.167585	0.21583	0.292498	47.55159	0.160102	0.209471	6.29E-05	8.23E-05	0.2624	0.05277
16	0.183103	0.227869	0.291567	51.40133	0.175344	0.22185	6.89E-05	8.71E-05	0.2813	0.06067
17	0.199178	0.239154	0.291018	55.2637	0.19114	0.233512	3.16E-06	2.22E-06	0.0140	0.00020
18	0.21581	0.2496	0.290788	59.13247	0.207494	0.244377	9.58E-06	6.48E-06	0.0313	0.00080
19	0.232988	0.25912	0.29081	63.0029	0.224399	0.25436	1.62E-05	1.04E-05	0.0505	0.00200
20	0.250692	0.267623	0.291013	66.87163	0.24184	0.263372	2.31E-05	1.39E-05	0.0700	0.00381
21	0.268887	0.275018	0.291329	70.73661	0.25979	0.27132	3.01E-05	1.71E-05	0.0897	0.00621
22	0.287524	0.281215	0.291692	74.59693	0.278206	0.278116	3.74E-05	1.97E-05	0.1093	0.00920
23	0.306539	0.286132	0.292043	78.45257	0.297032	0.283674	4.48E-05	2.19E-05	0.1288	0.01276
24	0.325852	0.2897	0.292333	82.30417	0.316196	0.287916	5.23E-05	2.36E-05	0.1482	0.01688
25	0.345373	0.291864	0.292523	86.15285	0.335613	0.290782	5.99E-05	2.47E-05	0.1675	0.02153
26	0.365	0.292589	0.292589	90	0.355187	0.292226	6.76E-05	2.53E-05	0.1865	0.02669
27	0.384627	0.291864	0.292523	93.84715	0.374813	0.292226	7.53E-05	2.53E-05	0.2053	0.03233
28	0.404148	0.2897	0.292333	97.69583	0.394387	0.290782	8.3E-05	2.47E-05	0.2238	0.03842
29	0.423461	0.286132	0.292043	101.5474	0.413804	0.287916	9.06E-05	2.36E-05	0.2421	0.04493
30	0.442476	0.281215	0.291692	105.4031	0.432968	0.283674	9.81E-05	2.19E-05	0.2600	0.05183
31	0.461113	0.275018	0.291329	109.2634	0.451794	0.278116	0.000106	1.97E-05	0.2776	0.05909
32	0.479308	0.267623	0.291013	113.1284	0.47021	0.27132	0.000113	1.71E-05	0.2950	0.06669

33	0.497012	0.25912	0.29081	116.9971	0.48816	0.263372	0.00012	1.39E-05	0.3120	0.07461
34	0.51419	0.2496	0.290788	120.8675	0.505601	0.25436	0.000127	1.04E-05	0.3288	0.08284
35	0.530822	0.239154	0.291018	124.7363	0.522506	0.244377	3.27E-06	9.6E-05	0.3227	0.07982
36	0.546897	0.227869	0.291567	128.5987	0.53886	0.233512	9.69E-06	9.17E-05	0.3037	0.07071
37	0.562415	0.21583	0.292498	132.4484	0.554656	0.22185	1.59E-05	8.71E-05	0.2846	0.06208
38	0.577381	0.203112	0.293871	136.2779	0.569898	0.209471	2.19E-05	8.23E-05	0.2653	0.05397
39	0.591809	0.189786	0.295738	140.0785	0.584595	0.196449	2.77E-05	7.72E-05	0.2459	0.04638
40	0.605714	0.175916	0.298143	143.8403	0.598761	0.182851	3.32E-05	7.18E-05	0.2265	0.03933
41	0.619114	0.161558	0.301123	147.5532	0.612414	0.168737	3.86E-05	6.63E-05	0.2069	0.03285
42	0.632032	0.146763	0.304705	151.2064	0.625573	0.15416	4.38E-05	6.06E-05	0.1874	0.02694
43	0.644487	0.131577	0.30891	154.7898	0.63826	0.13917	4.87E-05	5.47E-05	0.1678	0.02161
44	0.656502	0.116041	0.31375	158.2935	0.650495	0.123809	5.35E-05	4.86E-05	0.1481	0.01686
45	0.668098	0.100189	0.319228	161.7087	0.6623	0.108115	5.82E-05	4.25E-05	0.1285	0.01270
46	0.679296	0.084054	0.325341	165.0274	0.673697	0.092122	6.27E-05	3.62E-05	0.1089	0.00913
47	0.690117	0.067663	0.332083	168.2434	0.684706	0.075859	6.7E-05	2.98E-05	0.0892	0.00615
48	0.700579	0.051042	0.339439	171.3515	0.695348	0.059353	7.12E-05	2.33E-05	0.0697	0.00377
49	0.710702	0.034212	0.347391	174.3483	0.705641	0.042627	7.52E-05	1.67E-05	0.0502	0.00198
50	0.720504	0.017192	0.355919	177.2314	0.715603	0.025702	7.91E-05	1.01E-05	0.0312	0.00079
51	0.73	0	0.365	180	0.725252	0.008596	8.29E-05	3.38E-06	0.0140	0.00020

Module6 - 1

```
Sub MinValue()
'
' MinValue Macro

Dim b As Double
Dim c As Double
Dim agmin As Double
Dim ag As Double
Dim cmax As Double


Let agmin = 100

cmax = Range("B8").Value - 1.5



For b = Range("B5").Value + 5 To 90 - 1 Step 3
For c = 90 To cmax Step 3

    Range("B6").Value = b
    Range("B7").Value = c
    ag = Range("Q9").Value

    If ag > 0 And ag < agmin Then

    agmin = ag
    bmin = b
    cmin = c

    End If

  Next c

  Next b

Range("B6").Value = bmin
Range("B7").Value = cmin


End Sub
```

Hinge Angles

Hinge No	Angle	X	Y	Actual Angle
1	11.25	0.000	0.000	11.25
2	70.25	6.347	7.431	69.75
3	129	15.999	5.902	128.25
4	168.75	19.616	0.000	168.75

Hinge Coords

	Angle	X	Y
A	0.1963	0.7356	-0.1463
B	1.2174	6.0871	8.1347
C	0.9032	15.534	5.3133
D	0.1963	20.3513	0.1463

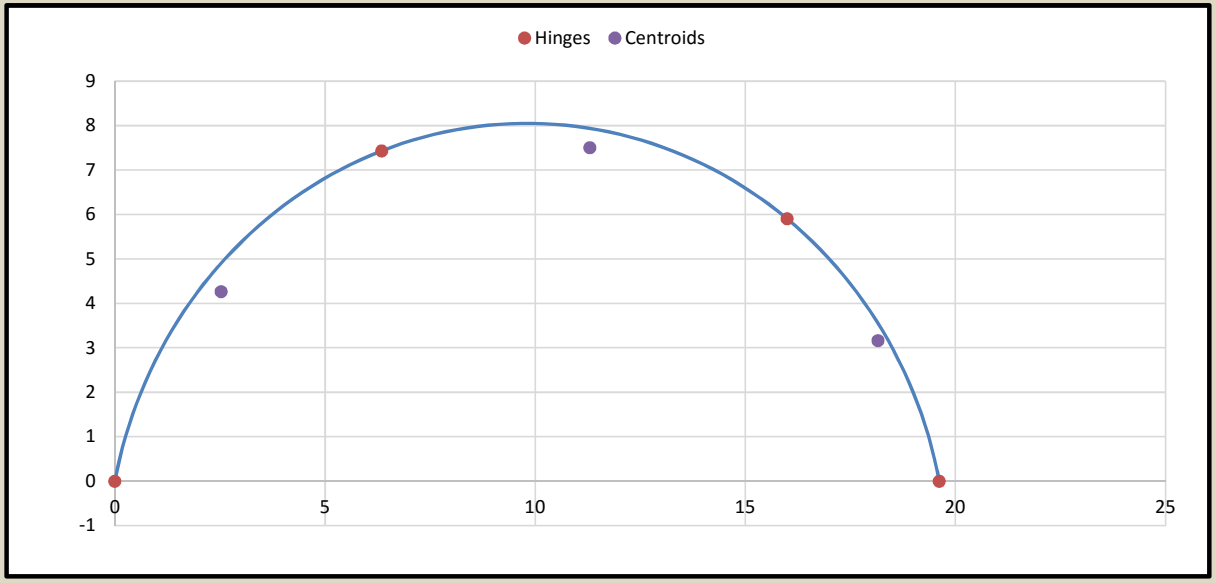

To tables
To ground acceleration

Minimum Ground Acceleration Calculation

Main lines of intersection	
m	c
1.54741	-1.285
-1.07269	21.977
Intersection	
8.878109	12.4534965

θ1	1
θ2	1.916884
θ3	2.6480

No of blocks per link	
1	39
2	39
3	27

Vert displacements	
Link	Displacement
1	-0.0313
2	0.0812
3	0.1015

Hor Displacements

Link	Displacement
1	0.0770
2	0.1657
3	0.1394

Back

Centroid Locations

Link No	x	y
1	2.530	4.2648
2	11.305	7.5020
3	18.157	3.1609

Horizontal Acceleration Factor

0.3542	g

Arch radius	10	m
t/a ratio	0.15	
Thickness	1.5	m
Arch Span	20	m
Embrace angle	157.5	

Length of segment	0.26	m
Density of brick	0.678	kg/m^3
Mass of bricks	0.27	kg
I_G	0.051441	$kg.m^2$

Back

No No	x (m)	y (m)	Angle (rad)	Segment Angle (rad)	x'(m)	y' (m)	Ax' (m2)	Ay' (m2)	Radius from hinge (m)
1	0	0	11.25	1.36	0	0	0	0.000	0.7500
2	0.05443	0.2560711	12.75	1.34	0.027215	0.128036	0.010687	0.050	0.7596
3	0.115544	0.5106297	14.25	1.31	0.084987	0.38335	0.033373	0.151	0.8389
4	0.1833	0.7635013	15.75	1.28	0.149422	0.637065	0.058676	0.250	0.9784
5	0.257653	1.0145125	17.25	1.26	0.220477	0.889007	0.086579	0.349	1.1564
6	0.338552	1.2634914	18.75	1.23	0.298102	1.139002	0.117061	0.447	1.3577
7	0.425939	1.5102674	20.25	1.20	0.382245	1.386879	0.150103	0.545	1.5734
8	0.519757	1.7546712	21.75	1.18	0.472848	1.632469	0.185682	0.641	1.7981
9	0.619941	1.9965353	23.25	1.15	0.569849	1.875603	0.223773	0.737	2.0287
10	0.726421	2.2356942	24.75	1.13	0.673181	2.116115	0.26435	0.831	2.2633
11	0.839125	2.4719837	26.25	1.10	0.782773	2.353839	0.307386	0.924	2.5006
12	0.957976	2.705242	27.75	1.07	0.898551	2.588613	0.35285	1.017	2.7398
13	1.082893	2.9353092	29.25	1.05	1.020435	2.820276	0.400712	1.107	2.9802
14	1.213789	3.1620276	30.75	1.02	1.148341	3.048668	0.450939	1.197	3.2215
15	1.350575	3.3852419	32.25	0.99	1.282182	3.273635	0.503497	1.286	3.4634
16	1.493157	3.6047991	33.75	0.97	1.421866	3.495021	0.558349	1.372	3.7054
17	1.641437	3.8205487	35.25	0.94	1.567297	3.712674	0.615459	1.458	3.9476
18	1.795315	4.0323428	36.75	0.92	1.718376	3.926446	0.674785	1.542	4.1897
19	1.954683	4.2400363	38.25	0.89	1.874999	4.13619	0.736289	1.624	4.4315
20	2.119434	4.4434868	39.75	0.86	2.037059	4.341762	0.799928	1.705	4.6730
21	2.289455	4.6425549	41.25	0.84	2.204445	4.543021	0.865659	1.784	4.9140
22	2.464628	4.8371042	42.75	0.81	2.377041	4.73983	0.933435	1.861	5.1545
23	2.644833	5.0270014	44.25	0.79	2.554731	4.932053	1.003212	1.937	5.3944
24	2.829948	5.2121162	45.75	0.76	2.737391	5.119559	1.07494	2.010	5.6335
25	3.019845	5.3923219	47.25	0.73	2.924897	5.302219	1.148571	2.082	5.8719
26	3.214395	5.5674949	48.75	0.71	3.11712	5.479908	1.224055	2.152	6.1095
27	3.413463	5.7375151	50.25	0.68	3.313929	5.652505	1.30134	2.220	6.3462

28	3.616913	5.9022661	51.75	0.65	3.515188	5.819891	1.380372	2.285	6.5819
29	3.824607	6.0616349	53.25	0.63	3.72076	5.98195	1.461097	2.349	6.8167
30	4.036401	6.2155123	54.75	0.60	3.930504	6.138574	1.543461	2.411	7.0503
31	4.25215	6.3637929	56.25	0.58	4.144276	6.289653	1.627407	2.470	7.2829
32	4.471708	6.506375	57.75	0.55	4.361929	6.435084	1.712877	2.527	7.5143
33	4.694922	6.6431609	59.25	0.52	4.583315	6.574768	1.799812	2.582	7.7445
34	4.92164	6.7740569	60.75	0.50	4.808281	6.708609	1.888154	2.634	7.9735
35	5.151708	6.8989732	62.25	0.47	5.036674	6.836515	1.977841	2.685	8.2012
36	5.384966	7.0178242	63.75	0.45	5.268337	6.958399	2.068812	2.732	8.4275
37	5.621255	7.1305285	65.25	0.42	5.503111	7.074176	2.161005	2.778	8.6524
38	5.860414	7.2370089	66.75	0.39	5.740835	7.183769	2.254356	2.821	8.8760
39	6.102278	7.3371923	68.25	0.37	5.981346	7.287101	2.348802	2.862	9.0980
40	6.346682	7.4310101	69.75	0.34	6.22448	7.384101	2.444278	2.900	9.3185
41	6.593458	7.5183981	71.25	0.31	6.47007	7.474704	0.048453	0.017	0.7630
42	6.842437	7.5992962	72.75	0.29	6.717948	7.558847	0.145791	0.050	0.8541
43	7.093448	7.6736491	74.25	0.26	6.967943	7.636473	0.243961	0.081	1.0120
44	7.34632	7.7414059	75.75	0.24	7.219884	7.707528	0.342896	0.109	1.2106
45	7.600878	7.80252	77.25	0.21	7.473599	7.771963	0.442527	0.134	1.4332
46	7.85695	7.8569496	78.75	0.18	7.728914	7.829735	0.542786	0.157	1.6699
47	8.114358	7.9046574	80.25	0.16	7.985654	7.880803	0.643604	0.177	1.9155
48	8.372927	7.9456106	81.75	0.13	8.243642	7.925134	0.744913	0.194	2.1667
49	8.632479	7.9797813	83.25	0.10	8.502703	7.962696	0.846643	0.209	2.4217
50	8.892837	8.0071461	84.75	0.08	8.762658	7.993464	0.948724	0.221	2.6793
51	9.153822	8.027686	86.25	0.05	9.023329	8.017416	1.051087	0.230	2.9386
52	9.415255	8.0413871	87.75	0.03	9.284538	8.034537	1.15366	0.237	3.1990
53	9.676957	8.04824	89.25	0.00	9.546106	8.044814	1.256375	0.241	3.4602
54	9.938749	8.04824	90.75	-0.03	9.807853	8.04824	1.35916	0.242	3.7218
55	10.20045	8.0413871	92.25	-0.05	10.0696	8.044814	1.461945	0.241	3.9835
56	10.46188	8.027686	93.75	-0.08	10.33117	8.034537	1.564659	0.237	4.2453
57	10.72287	8.0071461	95.25	-0.10	10.59238	8.017416	1.667233	0.230	4.5068
58	10.98323	7.9797813	96.75	-0.13	10.85305	7.993464	1.769595	0.221	4.7680
59	11.24278	7.9456106	98.25	-0.16	11.113	7.962696	1.871676	0.209	5.0288
60	11.50135	7.9046574	99.75	-0.18	11.37206	7.925134	1.973406	0.194	5.2891
61	11.75876	7.8569496	101.25	-0.21	11.63005	7.880803	2.074715	0.177	5.5488
62	12.01483	7.80252	102.75	-0.24	11.88679	7.829735	2.175534	0.157	5.8077
63	12.26939	7.7414059	104.25	-0.26	12.14211	7.771963	2.275793	0.134	6.0659
64	12.52226	7.6736491	105.75	-0.29	12.39582	7.707528	2.375424	0.109	6.3232
65	12.77327	7.5992962	107.25	-0.31	12.64776	7.636473	2.474358	0.081	6.5796
66	13.02225	7.5183981	108.75	-0.34	12.89776	7.558847	2.572528	0.050	6.8350

67	13.26902	7.4310101	110.25	-0.37	13.14564	7.474704	2.669866	0.017	7.0893
68	13.51343	7.3371923	111.75	-0.39	13.39123	7.384101	2.766307	-0.018	7.3426
69	13.75529	7.2370089	113.25	-0.42	13.63436	7.287101	2.861782	-0.057	7.5947
70	13.99445	7.1305285	114.75	-0.45	13.87487	7.183769	2.956228	-0.097	7.8456
71	14.23074	7.0178242	116.25	-0.47	14.11259	7.074176	3.04958	-0.140	8.0953
72	14.464	6.8989732	117.75	-0.50	14.34737	6.958399	3.141773	-0.186	8.3436
73	14.69407	6.7740569	119.25	-0.52	14.57903	6.836515	3.232744	-0.233	8.5906
74	14.92078	6.6431609	120.75	-0.55	14.80742	6.708609	3.322431	-0.284	8.8362
75	15.144	6.506375	122.25	-0.58	15.03239	6.574768	3.410772	-0.336	9.0803
76	15.36356	6.3637929	123.75	-0.60	15.25378	6.435084	3.497708	-0.391	9.3229
77	15.5793	6.2155123	125.25	-0.63	15.47143	6.289653	3.583178	-0.448	9.5640
78	15.7911	6.0616349	126.75	-0.65	15.6852	6.138574	3.667123	-0.508	9.8035
79	15.99879	5.9022661	128.25	-0.68	15.89495	5.98195	3.749487	-0.569	10.0413
80	16.20224	5.7375151	129.75	-0.71	16.10052	5.819891	0.039946	2.285	7.0893
81	16.40131	5.5674949	131.25	-0.73	16.30178	5.652505	0.118978	2.220	6.8350
82	16.59586	5.3923219	132.75	-0.76	16.49859	5.479908	0.196263	2.152	6.5796
83	16.78576	5.2121162	134.25	-0.79	16.69081	5.302219	0.271746	2.082	6.3232
84	16.97087	5.0270014	135.75	-0.81	16.87831	5.119559	0.345378	2.010	6.0659
85	17.15108	4.8371042	137.25	-0.84	17.06098	4.932053	0.417106	1.937	5.8077
86	17.32625	4.6425549	138.75	-0.86	17.23866	4.73983	0.486883	1.861	5.5488
87	17.49627	4.4434868	140.25	-0.89	17.41126	4.543021	0.554659	1.784	5.2891
88	17.66102	4.2400363	141.75	-0.92	17.57865	4.341762	0.62039	1.705	5.0288
89	17.82039	4.0323428	143.25	-0.94	17.74071	4.13619	0.684029	1.624	4.7680
90	17.97427	3.8205487	144.75	-0.97	17.89733	3.926446	0.745533	1.542	4.5068
91	18.12255	3.6047991	146.25	-0.99	18.04841	3.712674	0.804859	1.458	4.2453
92	18.26513	3.3852419	147.75	-1.02	18.19384	3.495021	0.861969	1.372	3.9835
93	18.40192	3.1620276	149.25	-1.05	18.33352	3.273635	0.916821	1.286	3.7218
94	18.53281	2.9353092	150.75	-1.07	18.46736	3.048668	0.969379	1.197	3.4602
95	18.65773	2.705242	152.25	-1.10	18.59527	2.820276	1.019606	1.107	3.1990
96	18.77658	2.4719837	153.75	-1.13	18.71715	2.588613	1.067468	1.017	2.9386
97	18.88928	2.2356942	155.25	-1.15	18.83293	2.353839	1.112932	0.924	2.6793
98	18.99576	1.9965353	156.75	-1.18	18.94252	2.116115	1.155968	0.831	2.4217
99	19.09595	1.7546712	158.25	-1.20	19.04586	1.875603	1.196545	0.737	2.1667
100	19.18977	1.5102674	159.75	-1.23	19.14286	1.632469	1.234636	0.641	1.9155
101	19.27715	1.2634914	161.25	-1.26	19.23346	1.386879	1.270215	0.545	1.6699
102	19.35805	1.0145125	162.75	-1.28	19.3176	1.139002	1.303257	0.447	1.4332
103	19.43241	0.7635013	164.25	-1.31	19.39523	0.889007	1.333739	0.349	1.2106
104	19.50016	0.5106297	165.75	-1.34	19.46628	0.637065	1.361642	0.250	1.0120
105	19.56128	0.2560711	167.25	-1.36	19.53072	0.38335	1.386945	0.151	0.8541

	106	19.61571	0	168.75	-1.36	19.58849	0	1.409631	0.000	0.7767
	107	19.61571	0	168.75	-1.36		0		0.000	
	108	19.61571	0	168.75	-1.36		0		0.000	
	109	19.61571	0	168.75	-1.36		0		0.000	
	110	19.61571	0	168.75	-1.36		0		0.000	
	111	19.61571	0	168.75	-1.36		0		0.000	
	112	19.61571	0	168.75	-1.36		0		0.000	
	113	19.61571	0	168.75	-1.36		0		0.000	
	114	19.61571	0	168.75	-1.36		0		0.000	
	115	19.61571	0	168.75	-1.36		0		0.000	
	116	19.61571	0	168.75	-1.36		0		0.000	
	117	19.61571	0	168.75	-1.36		0		0.000	
	118	19.61571	0	168.75	-1.36		0		0.000	
	119	19.61571	0	168.75	-1.36		0		0.000	
	120	19.61571	0	168.75	-1.36		0		0.000	
	121	19.61571	0	168.75	0.00		0		0.000	

Hyperbolic function form finding

Catenary Requirements

Length of curve	0.75	m
h/w ratio	0.5	
Height of catenary	0.37500	m

a guess	0.232
Final value	0.375

Element No	x value	x	y	y value
1	0	0.375	-0.464013	0
2	0.015	0.36	-0.429045	0.034967
3	0.03	0.345	-0.396464	0.067549
4	0.045	0.33	-0.366134	0.097879
5	0.06	0.315	-0.337927	0.126086
6	0.075	0.3	-0.311726	0.152286
7	0.09	0.285	-0.287423	0.17659
8	0.105	0.27	-0.264914	0.199099
9	0.12	0.255	-0.244107	0.219906
10	0.135	0.24	-0.224915	0.239098
11	0.15	0.225	-0.207257	0.256756
12	0.165	0.21	-0.19106	0.272953
13	0.18	0.195	-0.176256	0.287757
14	0.195	0.18	-0.162784	0.301229
15	0.21	0.165	-0.150586	0.313427
16	0.225	0.15	-0.139613	0.3244
17	0.24	0.135	-0.129819	0.334194
18	0.255	0.12	-0.121162	0.342851
19	0.27	0.105	-0.113607	0.350406
20	0.285	0.09	-0.107121	0.356892
21	0.3	0.075	-0.101679	0.362334
22	0.315	0.06	-0.097257	0.366756
23	0.33	0.045	-0.093836	0.370177
24	0.345	0.03	-0.091403	0.37261
25	0.36	0.015	-0.089947	0.374066
26	0.375	2.22E-16	-0.089462	0.37455
27	0.39	0.015	-0.089947	0.374066
28	0.405	0.03	-0.091403	0.37261
29	0.42	0.045	-0.093836	0.370177
30	0.435	0.06	-0.097257	0.366756
31	0.45	0.075	-0.101679	0.362334
32	0.465	0.09	-0.107121	0.356892
33	0.48	0.105	-0.113607	0.350406

General Parameters

No of elements	50
x incr	0.015
Brick length	0.038049

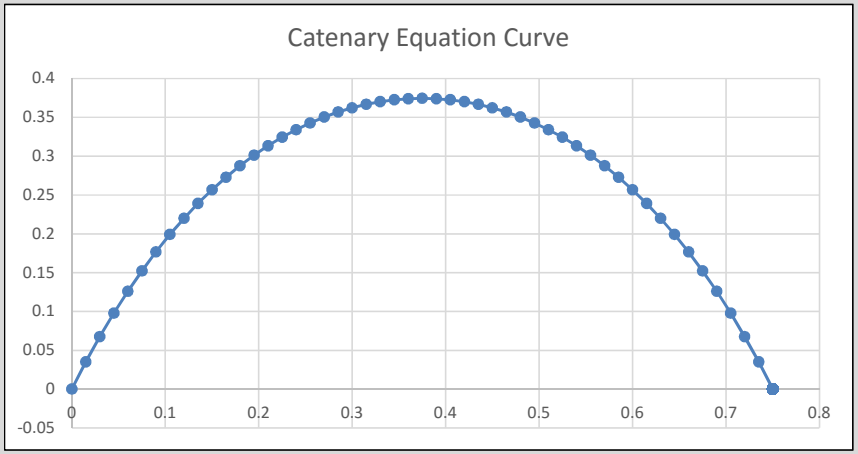

40

34	0.495	0.12	-0.121162	0.342851
35	0.51	0.135	-0.129819	0.334194
36	0.525	0.15	-0.139613	0.3244
37	0.54	0.165	-0.150586	0.313427
38	0.555	0.18	-0.162784	0.301229
39	0.57	0.195	-0.176256	0.287757
40	0.585	0.21	-0.19106	0.272953
41	0.6	0.225	-0.207257	0.256756
42	0.615	0.24	-0.224915	0.239098
43	0.63	0.255	-0.244107	0.219906
44	0.645	0.27	-0.264914	0.199099
45	0.66	0.285	-0.287423	0.17659
46	0.675	0.3	-0.311726	0.152286
47	0.69	0.315	-0.337927	0.126086
48	0.705	0.33	-0.366134	0.097879
49	0.72	0.345	-0.396464	0.067549
50	0.735	0.36	-0.429045	0.034967
51	0.75	0.375	-0.464013	-1.47E-15

APPENDIX C- PSD Matlab© Code

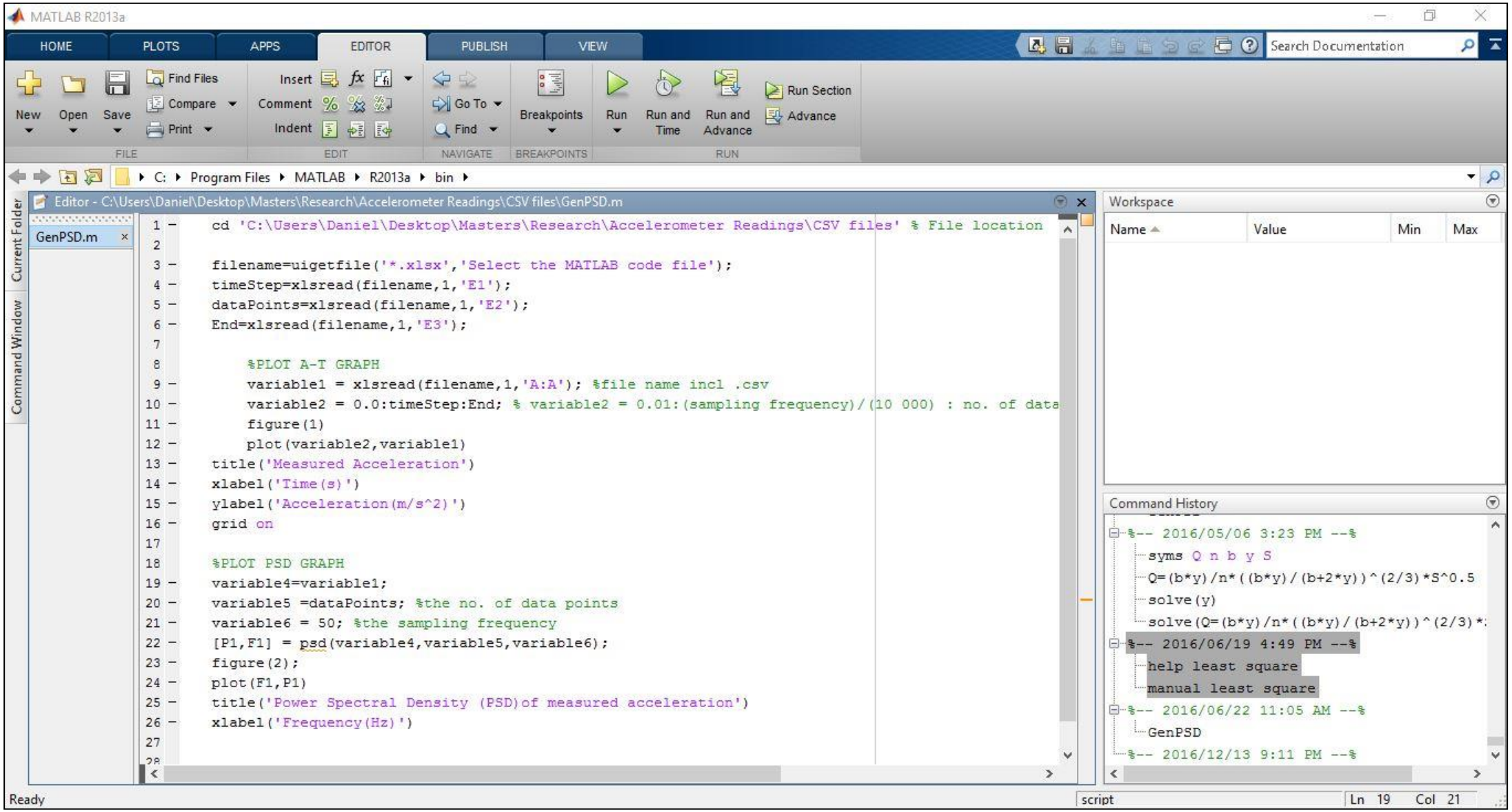
MATLAB R2013a
HOME
PLOTS
APPS
EDITOR
PUBLISH
VIEW
Search Documentation
New
Open
Save
Find Files
Compare
Print
Insert
Comment
Indent
Go To
Find
Breakpoints
Run
Run and Time
Run and Advance
Run Section
Advance
FILE
EDIT
NAVIGATE
BREAKPOINTS
RUN
C: ▸ Program Files ▸ MATLAB ▸ R2013a ▸ bin ▸
Current Folder
Command Window
Editor - C:\Users\Daniel\Desktop\Masters\Research\Accelerometer Readings\CSV files\GenPSD.m
GenPSD.m
1 cd 'C:\Users\Daniel\Desktop\Masters\Research\Accelerometer Readings\CSV files' % File location
2
3 filename=uigetfile('*.xlsx','Select the MATLAB code file');
4 timeStep=xlsread(filename,1,'E1');
5 dataPoints=xlsread(filename,1,'E2');
6 End=xlsread(filename,1,'E3');
7
8 %PLOT A-T GRAPH
9 variable1 = xlsread(filename,1,'A:A'); %file name incl .csv
10 variable2 = 0.0:timeStep:End; % variable2 = 0.01:(sampling frequency)/(10 000) : no. of data
11 figure(1)
12 plot(variable2,variable1)
13 title('Measured Acceleration')
14 xlabel('Time(s)')
15 ylabel('Acceleration(m/s^2)')
16 grid on
17
18 %PLOT PSD GRAPH
19 variable4=variable1;
20 variable5 =dataPoints; %the no. of data points
21 variable6 = 50; %the sampling frequency
22 [P1,F1] = psd(variable4,variable5,variable6);
23 figure(2);
24 plot(F1,P1)
25 title('Power Spectral Density (PSD)of measured acceleration')
26 xlabel('Frequency(Hz)')
27
Workspace
Name
Value
Min
Max
Command History
%-- 2016/05/06 3:23 PM --%
syms Q n b y S
Q=(b*y)/n*((b*y)/(b+2*y))^(2/3)*S^0.5
solve(y)
solve(Q=(b*y)/n*((b*y)/(b+2*y))^(2/3)*
%-- 2016/06/19 4:49 PM --%
help least square
manual least square
%-- 2016/06/22 11:05 AM --%
GenPSD
%-- 2016/12/13 9:11 PM --%
Ready
script
Ln 19
Col 21